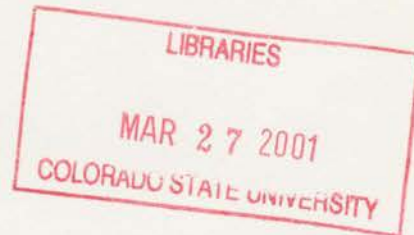


NSF Grants ATM-9726464

National Science Foundation

DISSERTATION ON THE RELATIONSHIPS  
BETWEEN CONVECTIVE STORM KINEMATICS,  
MICROPHYSICS, AND LIGHTNING

by Timothy J. Lang



**Colorado  
State  
University**

**DEPARTMENT OF  
ATMOSPHERIC SCIENCE**

PAPER NO. 700

**DISSERTATION**  
**ON THE RELATIONSHIPS BETWEEN CONVECTIVE STORM**  
**KINEMATICS, MICROPHYSICS, AND LIGHTNING**

by

**Timothy J. Lang**

Department of Atmospheric Science  
Colorado State University  
Fort Collins, CO 80523

**Research Supported by**  
**National Science Foundation**  
under Grant ATM-9726464

Fall 2000

Atmospheric Science Paper No. 700



U18402 0470746

83 293CSU 1646  
08/01 XL2  
38-000-01 GBC



QC  
852  
.C6  
no. 700  
ATMOS

DISSERTATION

**ON THE RELATIONSHIPS BETWEEN CONVECTIVE STORM  
KINEMATICS, MICROPHYSICS, AND LIGHTNING**

Submitted by

**Timothy James Lang**

Department of Atmospheric Science

In partial fulfillment of the requirements

for the Degree of Doctor of Philosophy

Colorado State University

Fort Collins, Colorado

Spring 2001

COLORADO STATE UNIV. LIBRARIES

COLORADO STATE UNIVERSITY

December 1, 2000

WE HEREBY RECOMMEND THAT THE DISSERTATION PREPARED UNDER OUR SUPERVISION BY TIMOTHY JAMES LANG ENTITLED ON THE RELATIONSHIPS BETWEEN CONVECTIVE STORM KINEMATICS, MICROPHYSICS, AND LIGHTNING BE ACCEPTED AS FULFILLING IN PART REQUIRMENTS FOR THE DEGREE OF DOCTOR OF PHILOSOPHY.

Committee on Graduate Work

---

---

---

---

Adviser

---

Department Head

## ABSTRACT

### ON THE RELATIONSHIPS BETWEEN CONVECTIVE STORM KINEMATICS, MICROPHYSICS, AND LIGHTNING

Combined multiparameter radar, dual-Doppler, thermodynamic sounding, and lightning observations of 11 thunderstorms (6 from the mid-latitudes, 5 from the tropics) are presented. The thunderstorms span a wide spectrum of intensities, from weak monsoon-type to severe tornadic, and include both unicellular and multicellular convection. In general, the kinematically strongest storms featured lower production of negative cloud-to-ground lightning (typically  $< 1 \text{ min}^{-1}$  flash rates for large portions of the storms' lifetimes) when compared with more moderate convection, in accord with an elevated charge mechanism. The only significant differences between intense storms that produced predominately positive cloud-to-ground (CG) lightning for a significant portion of their lifetimes (PPCG storms), and intense storms that produced little CG lightning of any polarity (low-CG storms), was that PPCG storms featured much larger volumes of significant updrafts (both  $> 10 \text{ m s}^{-1}$  and  $> 20 \text{ m s}^{-1}$ ) and produced greater amounts of precipitation (both rain and hail). Otherwise, peak updrafts and vertical air mass fluxes were very similar between the two types of storms, and both types were linked by anomalously low production of negative CG lightning. It is suggested that PPCG storms may be caused by enhanced lower positive charge created by the larger volume of significant updrafts. Since both PPCG and low-CG storms are capable of being severe, anomalously low production of negative CG lightning (regardless of positive CG flash rate) may be a useful signature for use in the "nowcasting" of severe convection.

Timothy James Lang  
Department of Atmospheric Science  
Colorado State University  
Fort Collins, Colorado  
Spring 2001

## **ACKNOWLEDGEMENTS**

I would like to thank the following people and organizations for their crucial help and support: my adviser, Dr. Steven Rutledge; my committee, Dr. William Cotton, Dr. Richard Johnson, and Dr. Ray Robinson; the CSU Radar Meteorology group, especially Paul Hein, Margi Cech, Dr. Larry Carey, Dr. Walt Petersen, and Dr. Rob Cifelli; the CSU CHILL radar staff; the NCAR S-Pol radar staff; the NASA TOGA radar staff; the NASA Marshall Space Flight Center, especially Dr. Rich Blakeslee; New Mexico Tech, especially Dr. Paul Krehbiel; and Ray McAnelly. This work was supported under National Science Foundation grant ATM-9726464.

## TABLE OF CONTENTS

<u>Chapter/Section Title</u>	<u>Page</u>
<b>1. INTRODUCTION</b>	<b>1</b>
1.1 Background	1
1.2 Hypotheses	3
<b>2. DATA AND METHODOLOGY</b>	<b>8</b>
2.1 Overview	8
2.2 Observational Platforms	9
2.2a CSU-CHILL Radar	9
2.2b Pawnee Radar	10
2.2c SPOL Radar	10
2.2d TOGA Radar	10
2.2e Field Change Meters	10
2.2f National Lightning Detection Network	11
2.2g TRMM/LBA Advanced Lightning Direction Finder Network	11
2.2h New Mexico Tech VHF Lightning Mapper	12
2.2i Thermodynamic Soundings	12
2.3 Methodology	13
2.3a Radar Scan Strategy	13
2.3b Multiparameter Radar Analysis	13
2.3c Dual-Doppler Radar Analysis	17
2.3d Lightning Analysis	19
2.3e Sounding Analysis	20
2.3f Synthesis	20
<b>3. CHILL-PAWNEE AND STEPS MID-LATITUDE THUNDERSTORMS</b>	<b>28</b>
3.1 Overview of Storms	28
3.1a 1 July 1998	28
3.1b 15 July 1998	30
3.1c 21 July 1998	32
3.1d 25 July 1998	34
3.1e 30 July 1998	36
3.1f 29 June 2000	37
3.1g Summary	39
3.2 Comparison of Storm Environments	40
3.3 Vertical Structure	43
3.4 Testing of Elevated Charge Mechanism	49
3.5 Testing of PPCG Mechanisms	51
3.5a Tilted Dipole	51
3.5b Inverted Dipole	52
3.5c Precipitation Unshielding	53
3.6 Testing of Separated Updraft-Downdraft Mechanism	53
3.7 Summary	56

<b>4. TRMM/LBA TROPICAL THUNDERSTORMS</b>	<b>132</b>
4.1 Overview of Storms	132
4.1a 26 January 1999	132
4.1b 13 February 1999	134
4.1c 15 February 1999	136
4.1d 17 February 1999	138
4.1e 20 February 1999	140
4.1f Summary	142
4.2 Comparison of Storm Environments	142
4.3 Vertical Structure	144
4.4 Testing of Elevated Charge Mechanism	148
4.5 Testing of PPCG Mechanisms	150
4.6 Testing of Separated Updraft-Downdraft Mechanism	150
4.7 Summary	151
<b>5. SYNTHESIS AND DISCUSSION</b>	<b>211</b>
5.1 Synthesis of Mid-Latitude and Tropical Results	211
5.1a Kinematic Intensity versus Cloud-to-Ground Lightning Production	211
5.1b Precipitation Intensity versus Cloud-to-Ground Lightning Production	214
5.1c Radar Reflectivity Intensity versus Cloud-to-Ground Lightning Production	215
5.1d Kinematic Intensity versus Precipitation and Reflectivity Intensities	216
5.2 Energy and Charge Considerations	217
5.3 Discussion and Conclusions	218
5.4 Suggestions for Future Research	223
<b>BIBLIOGRAPHY</b>	<b>234</b>

## LIST OF TABLES

<u>Table Caption</u>	<u>Page</u>
Table 2.1: Specifics of the radars used in this study.	22
Table 2.2: Overview of the algorithm used to calculate rain and hail rates from CSU-CHILL and SPOL multiparameter radar data.	23
Table 2.3: Overview of the dual-Doppler algorithms employed in this study.	24
Table 3.1: Summary of kinematic, microphysical, and lightning observations for the mid-latitude cases.	59
Table 3.2: CAPE (in $\text{J kg}^{-1}$ ) and shear (in $\text{m s}^{-1}$ ) calculations for the mid-latitude cases.	60
Table 3.3: Best correlation coefficients for reflectivity versus vertical wind speed, considering various regions of the mid-latitude storms. Also shown are the times of the radar volumes in which the best correlations were found (L – local/MDT; Z – UTC).	61
Table 4.1: Summary of kinematic, microphysical, and lightning observations for the tropical cases.	153
Table 4.2: CAPE (in $\text{J kg}^{-1}$ ) and shear (in $\text{m s}^{-1}$ ) calculations for the tropical cases.	154
Table 4.3: Best correlation coefficients for reflectivity versus vertical wind speed, considering various regions of the tropical thunderstorms. Also shown are the times of the radar volumes in which the best correlations were found (Z – UTC).	155
Table 5.1: Total kinetic energy (in $10^{13}$ J) contained in the vertical motions of the thunderstorms in this study.	225

## LIST OF FIGURES

<u>Figure Caption</u>	<u>Page</u>
Figure 1.1: Schematic representation of the impact of the elevated charge mechanism on lightning flash rates.	6
Figure 1.2: Schematic representations of the three mechanisms proposed to explain PPCG thunderstorms. The top-left panel depicts the tilted dipole mechanism. The top-right panel depicts the inverted dipole or enhanced lower positive charge mechanism. The bottom panels depict the precipitation unshielding mechanism. From Williams (2000).	7
Figure 2.1: Schematic map of the operational area of the CHILL-Pawnee dual-Doppler network. Pictured are the two dual-Doppler lobes. Landmarks include the two radars (CHILL and Pawnee) as well as nearby cities and airports (map courtesy of P. Kennedy).	25
Figure 2.2: Schematic map of the STEPS operational area. Pictured are the two dual-Doppler lobes (bold circles) formed by CHILL and SPOL. Also shown are major elevation contours. Landmarks include the three project radars (CHILL, SPOL, and Goodland/KGLD) as well as nearby cities, airports, and other regional NEXRAD radars. The shaded areas include other dual-Doppler and triple-Doppler lobes formed by the CHILL-SPOL-KGLD network (map courtesy of Dr. J. Miller).	26
Figure 2.3: Schematic map of the TRMM/LBA operational area. Shown are the locations of the radars (SPOL and TOGA), sounding site, rain gauge networks, ALDF sensors, and profiler. Also shown are nearby cities and geographical regions. Topography is color-coded. Black circles show the maximum ranges of both radars. The red dashed circles show the dual-Doppler lobes (map courtesy of Dr. W. Petersen).	27
Figure 3.1: Horizontal cross-section of CHILL radar reflectivity at 0.5 km AGL, at 1850 MDT on 1 July 1998. Distances are relative to CHILL	62
Figure 3.2: Time-height cross-section of peak CHILL radar reflectivity for the 1 July 1998 storm. Values are in dBZ.	63
Figure 3.3: Time-height cross-section of maximum vertical velocity for the 1 July 1998 storm. Values are in $\text{m s}^{-1}$ .	64
Figure 3.4: Volume of 1 July 1998 storm containing updrafts within respective bins as a function of time.	65
Figure 3.5: Rain production by the 1 July 1998 storm as a function of time. Values are at 0.5 km AGL. Moderate rain is 20-60 $\text{mm h}^{-1}$ , and heavy rain is greater than 60 $\text{mm h}^{-1}$ .	66

Figure 3.6: Hail production by the 1 July 1998 storm as a function of time. Values are at 0.5 km AGL.	67
Figure 3.7: CG flash rate as a function of time for the 1 July 1998 storm.	68
Figure 3.8: Horizontal cross-section of CHILL radar reflectivity at 0.5 km AGL, at 1925 MDT on 1 July 1998. Also shown are ground strike positions (plus signs for positives, minus signs for negatives) of NLDN CGs that occurred during 1920-1930 MDT. Distances are relative to CHILL.	69
Figure 3.9: Horizontal cross-section of CHILL radar reflectivity at 0.5 km AGL, at 1804 MDT on 15 July 1998. Distances are relative to CHILL.	70
Figure 3.10: Time-height cross-section of peak CHILL radar reflectivity for the 15 July 1998 storm. Values are in dBZ.	71
Figure 3.11: Time-height cross-section of maximum vertical velocity for the 15 July 1998 storm. Values are in $\text{m s}^{-1}$ .	72
Figure 3.12: Volume of 15 July 1998 storm containing updrafts within respective bins as a function of time.	73
Figure 3.13: Rain production by the 15 July 1998 storm as a function of time. Values are at 0.5 km AGL. Moderate rain is 20-60 $\text{mm h}^{-1}$ , and heavy rain is greater than 60 $\text{mm h}^{-1}$ .	74
Figure 3.14: Hail production by the 15 July 1998 storm as a function of time. Values are at 0.5 km AGL.	75
Figure 3.15: CG flash rate as a function of time for the 15 July 1998 storm.	76
Figure 3.16: a) Horizontal cross-section of CHILL radar reflectivity at 0.5 km AGL, at 1804 MDT on 15 July 1998. Also shown are ground strike positions (plus signs for positives, minus signs for negatives) of NLDN CGs that occurred during 1800-1810 MDT. b) Same as a) except for radar at 1840 MDT and CG lightning during 1840-1850 MDT. Distances are relative to CHILL.	77
Figure 3.17: Horizontal cross-section of CHILL radar reflectivity at 0.5 km AGL, at 1531 MDT on 21 July 1998. Distances are relative to CHILL.	78
Figure 3.18: Time-height cross-section of peak CHILL radar reflectivity for the 21 July 1998 storm. Values are in dBZ.	79
Figure 3.19: Time-height cross-section of maximum vertical velocity for the 21 July 1998 storm. Values are in $\text{m s}^{-1}$ .	80
Figure 3.20: Volume of 21 July 1998 storm containing updrafts within respective bins as a function of time.	81
Figure 3.21: Rain production by the 21 July 1998 storm as a function of time. Values are at 0.5 km AGL. Moderate rain is 20-60 $\text{mm h}^{-1}$ , and heavy rain is greater than 60 $\text{mm h}^{-1}$ .	82
Figure 3.22: Hail production by the 21 July 1998 storm as a function of time. Values are at 0.5 km AGL.	83
Figure 3.23: CG flash rate as a function of time for the 21 July 1998 storm.	84

Figure 3.24: Horizontal cross-section of CHILL radar reflectivity at 0.5 km AGL, at 1516 MDT on 21 July 1998. Also shown are ground strike positions (plus signs for positives, minus signs for negatives) of NLDN CGs that occurred during 1509-1519 MDT. Distances are relative to CHILL.	85
Figure 3.25: Total flash rate as a function of time for the 21 July 1998 storm.	86
Figure 3.26: Horizontal cross-section of CHILL radar reflectivity at 0.5 km AGL, at 1625 MDT on 25 July 1998. Distances are relative to CHILL.	87
Figure 3.27: Time-height cross-section of peak CHILL radar reflectivity for the 25 July 1998 storm. Values are in dBZ.	88
Figure 3.28: Time-height cross-section of maximum vertical velocity for the 25 July 1998 storm. Values are in $\text{m s}^{-1}$ .	89
Figure 3.29: Volume of 25 July 1998 storm containing updrafts within respective bins as a function of time.	90
Figure 3.30: Rain production by the 25 July 1998 storm as a function of time. Values are at 0.5 km AGL. Moderate rain is $20\text{-}60 \text{ mm h}^{-1}$ , and heavy rain is greater than $60 \text{ mm h}^{-1}$ .	91
Figure 3.31: Hail production by the 25 July 1998 storm as a function of time. Values are at 0.5 km AGL.	92
Figure 3.32: CG flash rate as a function of time for the 25 July 1998 storm.	93
Figure 3.33: Horizontal cross-section of CHILL radar reflectivity at 0.5 km AGL, at 1640 MDT on 25 July 1998. Also shown are ground strike positions (plus signs for positives, minus signs for negatives) of NLDN CGs that occurred during 1640-1650 MDT. Distances are relative to CHILL.	94
Figure 3.34: Total flash rate as a function of time for the 25 July 1998 storm.	95
Figure 3.35: Horizontal cross-section of CHILL radar reflectivity at 0.5 km AGL, at 1716 MDT on 30 July 1998. Distances are relative to CHILL.	96
Figure 3.36: Time-height cross-section of peak CHILL radar reflectivity for the 30 July 1998 storm. Values are in dBZ.	97
Figure 3.37: Time-height cross-section of maximum vertical velocity for the 30 July 1998 storm. Values are in $\text{m s}^{-1}$ .	98
Figure 3.38: Volume of 30 July 1998 storm containing updrafts within respective bins as a function of time.	99
Figure 3.39: Rain production by the 30 July 1998 storm as a function of time. Values are at 0.5 km AGL. Moderate rain is $20\text{-}60 \text{ mm h}^{-1}$ , and heavy rain is greater than $60 \text{ mm h}^{-1}$ .	100
Figure 3.40: Horizontal cross-section of CHILL radar reflectivity at 0.5 km AGL, at 2325 UTC on 29 June 2000. Distances are relative to CHILL.	101
Figure 3.41: Time-height cross-section of peak CHILL radar reflectivity for the 29 June 2000 storm. Values are in dBZ.	102

Figure 3.42: Time-height cross-section of maximum vertical velocity for the 29 June 2000 storm. Values are in $\text{m s}^{-1}$ .	103
Figure 3.43: Volume of 29 June 2000 storm containing updrafts within respective bins as a function of time.	104
Figure 3.44: Rain production by the 29 June 2000 storm as a function of time. Values are at 0.5 km AGL. Moderate rain is $20\text{-}60 \text{ mm h}^{-1}$ , and heavy rain is greater than $60 \text{ mm h}^{-1}$ .	105
Figure 3.45: Hail production by the 29 June 2000 storm as a function of time. Values are at 0.5 km AGL	106
Figure 3.46: CG flash rate as a function of time for the 29 June 2000 storm.	107
Figure 3.47: Horizontal cross-section of CHILL radar reflectivity at 0.5 km AGL, at 2343 UTC on 29 June 2000. Also shown are ground strike positions (plus signs for positives, minus signs for negatives) of NLDN CGs that occurred during 2340-2350 UTC. Distances are relative to CHILL.	108
Figure 3.48: Two minutes of LMA data for the 29 June 2000 storm, centered on 23:23:54 UTC. The top panel shows VHF signals as a function of time and altitude. The bottom left panel shows a plan view of the signals. The panels immediately above and to its right show projections of the data onto vertical planes in the east-west and north-south directions, respectively. The remaining panel shows an altitude histogram of signals that occurred during the time period. Warmer colors denote more recent signals.	109
Figure 3.49: a) Average positive vertical air mass flux as a function of height at the times of peak updrafts for the mid-latitude storms. b) Standard deviation of positive vertical air mass flux as a function of height at the times of peak updrafts for the mid-latitude storms.	110
Figure 3.50: Cumulative frequency by altitude diagrams (CFADs) of CHILL radar reflectivity (a) and dual-Doppler-derived vertical velocity (b) for the 1 July 1998 storm at 1850 MDT. The dashed lines denote the approximate boundaries of the mixed phase region.	111
Figure 3.51: Cumulative frequency by altitude diagrams (CFADs) of CHILL radar reflectivity (a) and dual-Doppler-derived vertical velocity (b) for the 15 July 1998 storm at 1804 MDT. The dashed lines denote the approximate boundaries of the mixed phase region.	112
Figure 3.52: Cumulative frequency by altitude diagrams (CFADs) of CHILL radar reflectivity (a) and dual-Doppler-derived vertical velocity (b) for the 21 July 1998 storm at 1531 MDT. The dashed lines denote the approximate boundaries of the mixed phase region.	113
Figure 3.53: Cumulative frequency by altitude diagrams (CFADs) of CHILL radar reflectivity (a) and dual-Doppler-derived vertical velocity (b) for the 25 July 1998 storm at 1625 MDT. The dashed lines denote the approximate boundaries of the mixed phase region.	114

- Figure 3.54: Cumulative frequency by altitude diagrams (CFADs) of CHILL radar reflectivity (a) and dual-Doppler-derived vertical velocity (b) for the 30 July 1998 storm at 1716 MDT. The dashed lines denote the approximate boundaries of the mixed phase region. 115
- Figure 3.55: Cumulative frequency by altitude diagrams (CFADs) of CHILL radar reflectivity (a) and dual-Doppler-derived vertical velocity (b) for the 29 June 2000 storm at 2325 UTC. The dashed lines denote the approximate boundaries of the mixed phase region. 116
- Figure 3.56: Vertical cross-sections of CHILL radar reflectivity (shaded), along with differential reflectivity (solid line) and vertical velocity (dashed). a) Cross-section taken at 16 km north, at 1850 MDT on 1 July 1998. b) Same as a) except at 21 km north. Distances are relative to CHILL. 117
- Figure 3.57: Vertical cross-section of CHILL radar reflectivity (shaded), along with differential reflectivity (solid line) and vertical velocity (dashed). a) Cross-section is taken at 30 km north, at 1804 MDT on 15 July 1998. b) Same as a) except at 8 km north. Distances are relative to CHILL. 118
- Figure 3.58: Vertical cross-section of CHILL radar reflectivity (shaded), along with differential reflectivity (solid line) and vertical velocity (dashed). Cross-section is taken at 2 km north, at 1840 MDT on 15 July 1998. Distances are relative to CHILL. 119
- Figure 3.59: Vertical cross-section of CHILL radar reflectivity (shaded), along with differential reflectivity (solid line) and vertical velocity (dashed). Cross-section is taken at 23 km north, at 1531 MDT on 21 July 1998. Distances are relative to CHILL. 120
- Figure 3.60: Vertical cross-section of CHILL radar reflectivity (shaded), along with differential reflectivity (solid line) and vertical velocity (dashed). a) Cross-section is taken at 24 km north, at 1516 MDT on 21 July 1998. b) Same as a) except at 50 km north. Distances are relative to CHILL. 121
- Figure 3.61: Vertical cross-section of CHILL radar reflectivity (shaded), along with differential reflectivity (solid line) and vertical velocity (dashed). Cross-section is taken at 39 km north, at 1625 MDT on 25 July 1998. Distances are relative to CHILL. 122
- Figure 3.62: Vertical cross-section of CHILL radar reflectivity (shaded), along with differential reflectivity (solid line) and vertical velocity (dashed). a) Cross-section is taken at 27 km north, at 1640 MDT on 25 July 1998. b) Same as a) except at 11 km south. Distances are relative to CHILL. 123
- Figure 3.63: Vertical cross-section of CHILL radar reflectivity (shaded), along with differential reflectivity (solid line) and vertical velocity (dashed). Cross-section is taken at 25 km north, at 1716 MDT on 30 July 1998. Distances are relative to CHILL. 124
- Figure 3.64: Vertical cross-section of CHILL radar reflectivity (shaded), along with differential reflectivity (solid line) and vertical velocity (dashed). a) Cross-section is taken at 51 km north, at 2312 UTC on 29 June 2000. b) Taken at 35 km north, at 2343 UTC on 29 June. Distances are relative to CHILL. 125
- Figure 3.65: Horizontal cross-section of CHILL radar reflectivity (shaded) and vertical velocity (solid line) at 4.5 km AGL for the 1 July 1998 storm. a) At 1850 MDT. b) At 1925 MDT. 126

Figure 3.66: Horizontal cross-section of CHILL radar reflectivity (shaded) and vertical velocity (solid line) at 4.5 km AGL for the 15 July 1998 storm. a) At 1804 MDT. b) At 1840 MDT.	127
Figure 3.67: Horizontal cross-section of CHILL radar reflectivity (shaded) and vertical velocity (solid line) at 4.5 km AGL for the 21 July 1998 storm. a) At 1516 MDT. b) At 1531 MDT.	128
Figure 3.68: Horizontal cross-section of CHILL radar reflectivity (shaded) and vertical velocity (solid line) at 4.5 km AGL for the 25 July 1998 storm. a) At 1625 MDT. b) At 1640 MDT.	129
Figure 3.69: Horizontal cross-section of CHILL radar reflectivity (shaded) and vertical velocity (solid line) at 4.5 km AGL for the 30 July 1998 storm at 1716 MDT.	130
Figure 3.70: Horizontal cross-section of CHILL radar reflectivity (shaded) and vertical velocity (solid line) at 4.5 km AGL for the 29 June 2000 storm.	131
Figure 4.1: Horizontal cross-section of SPOL radar reflectivity at 0.5 km AGL, at 2030 UTC on 26 January 1999. Distances are relative to SPOL.	156
Figure 4.2: Time-height cross-section of peak SPOL radar reflectivity for the 26 January 1999 storm. Values are in dBZ.	157
Figure 4.3: Time-height cross-section of maximum vertical velocity for the 26 January 1999 storm. Values are in $\text{m s}^{-1}$ .	158
Figure 4.4: Volume of 26 January 1999 storm containing updrafts within respective bins as a function of time.	159
Figure 4.5: Rain production by the 26 January 1999 storm as a function of time. Values are at 0.5 km AGL. Moderate rain is $20\text{-}60 \text{ mm h}^{-1}$ , and heavy rain is greater than $60 \text{ mm h}^{-1}$ .	160
Figure 4.6: CG flash rates as functions of time for the 26 January 1999 storm.	161
Figure 4.7: Horizontal cross-section of SPOL radar reflectivity at 0.5 km AGL, at 2010 UTC on 26 January 1999. Also shown are ground strike positions (plus signs for positives, minus signs for negatives) of BLDN CGs that occurred during 2010-2020 UTC. Distances are relative to SPOL.	162
Figure 4.8: Total flash rate as a function of time for the 26 January 1999 storm.	163
Figure 4.9: Horizontal cross-section of SPOL radar reflectivity at 0.5 km AGL, at 1733 UTC on 13 February 1999. Distances are relative to SPOL.	164
Figure 4.10: Time-height cross-section of peak SPOL radar reflectivity for the 13 February 1999 storm. Values are in dBZ.	165
Figure 4.11: Time-height cross-section of maximum vertical velocity for the 13 February 1999 storm. Values are in $\text{m s}^{-1}$ .	166
Figure 4.12: Volume of 13 February 1999 storm containing updrafts within respective bins as a function of time.	167

Figure 4.13: Rain production by the 13 February 1999 storm as a function of time. Values are at 0.5 km AGL. Moderate rain is 20-60 mm h <sup>-1</sup> , and heavy rain is greater than 60 mm h <sup>-1</sup> .	168
Figure 4.14: CG flash rates as functions of time for the 13 February 1999 storm.	169
Figure 4.15: Horizontal cross-section of SPOL radar reflectivity at 0.5 km AGL, at 1833 UTC on 13 February 1999. Also shown are ground strike positions (plus signs for positives, minus signs for negatives) of BLDN CGs that occurred during 1830-1840 UTC. Distances are relative to SPOL.	170
Figure 4.16: Horizontal cross-section of SPOL radar reflectivity at 0.5 km AGL, at 2030 UTC on 15 February 1999. Distances are relative to SPOL.	171
Figure 4.17: Time-height cross-section of peak SPOL radar reflectivity for the 15 February 1999 storm. Values are in dBZ.	172
Figure 4.18: Time-height cross-section of maximum vertical velocity for the 15 February 1999 storm. Values are in m s <sup>-1</sup> .	173
Figure 4.19: Volume of 15 February 1999 storm containing updrafts within respective bins as a function of time.	174
Figure 4.20: Rain production by the 15 February 1999 storm as a function of time. Values are at 0.5 km AGL. Moderate rain is 20-60 mm h <sup>-1</sup> , and heavy rain is greater than 60 mm h <sup>-1</sup> .	175
Figure 4.21: CG flash rates as functions of time for the 15 February 1999 storm.	176
Figure 4.22: Horizontal cross-section of SPOL radar reflectivity at 0.5 km AGL, at 2050 UTC on 15 February 1999. Also shown are ground strike positions (plus signs for positives, minus signs for negatives) of BLDN CGs that occurred during 2050-2100 UTC. Distances are relative to SPOL.	177
Figure 4.23: Total flash rate as a function of time for the 15 February 1999 storm.	178
Figure 4.24: Horizontal cross-section of SPOL radar reflectivity at 0.5 km AGL, at 1750 UTC on 17 February 1999. Distances are relative to SPOL.	179
Figure 4.25: Time-height cross-section of peak SPOL radar reflectivity for the 17 February 1999 storm. Values are in dBZ.	180
Figure 4.26: Time-height cross-section of maximum vertical velocity for the 17 February 1999 storm. Values are in m s <sup>-1</sup> .	181
Figure 4.27: Volume of 17 February 1999 storm containing updrafts within respective bins as a function of time.	182
Figure 4.28: Rain production by the 17 February 1999 storm as a function of time. Values are at 0.5 km AGL. Moderate rain is 20-60 mm h <sup>-1</sup> , and heavy rain is greater than 60 mm h <sup>-1</sup> .	183
Figure 4.29: CG flash rates as functions of time for the 17 February 1999 storm.	184

Figure 4.30: Horizontal cross-section of SPOL radar reflectivity at 0.5 km AGL, at 1730 UTC on 17 February 1999. Also shown are ground strike positions (plus signs for positives, minus signs for negatives) of BLDN CGs that occurred during 1730-1740 UTC. Distances are relative to SPOL.	185
Figure 4.31: Total flash rate as a function of time for the 17 February 1999 storm.	186
Figure 4.32: Horizontal cross-section of SPOL radar reflectivity at 0.5 km AGL, at 1848 UTC on 20 February 1999. Distances are relative to SPOL.	187
Figure 4.33: Time-height cross-section of peak SPOL radar reflectivity for the 20 February 1999 storm. Values are in dBZ.	188
Figure 4.34: Time-height cross-section of maximum vertical velocity for the 20 February 1999 storm. Values are in $\text{m s}^{-1}$ .	189
Figure 4.35: Volume of 20 February 1999 storm containing updrafts within respective bins as a function of time.	190
Figure 4.36: Rain production by the 20 February 1999 storm as a function of time. Values are at 0.5 km AGL. Moderate rain is 20-60 $\text{mm h}^{-1}$ , and heavy rain is greater than 60 $\text{mm h}^{-1}$ .	191
Figure 4.37: CG flash rates as functions of time for the 20 February 1999 storm.	192
Figure 4.38: Horizontal cross-section of SPOL radar reflectivity at 0.5 km AGL, at 1859 UTC on 20 February 1999. Also shown are ground strike positions (plus signs for positives, minus signs for negatives) of BLDN CGs that occurred during 1900-1910 UTC. Distances are relative to SPOL.	193
Figure 4.39: a) Average positive vertical air mass flux as a function of height at the times of peak updrafts for the tropical storms. b) Standard deviation of positive vertical air mass flux as a function of height at the times of peak updrafts for the tropical storms.	194
Figure 4.40: Cumulative frequency by altitude diagrams (CFADs) of SPOL radar reflectivity (a) and dual-Doppler-derived vertical velocity (b) for the 26 January 1999 storm at 2030 UTC. The dashed lines denote the approximate boundaries of the mixed phase region.	195
Figure 4.41: Cumulative frequency by altitude diagrams (CFADs) of SPOL radar reflectivity (a) and dual-Doppler-derived vertical velocity (b) for the 13 February 1999 storm at 1733 UTC. The dashed lines denote the approximate boundaries of the mixed phase region.	196
Figure 4.42: Cumulative frequency by altitude diagrams (CFADs) of SPOL radar reflectivity (a) and dual-Doppler-derived vertical velocity (b) for the 15 February 1999 storm at 2030 UTC. The dashed lines denote the approximate boundaries of the mixed phase region.	197
Figure 4.43: Cumulative frequency by altitude diagrams (CFADs) of SPOL radar reflectivity (a) and dual-Doppler-derived vertical velocity (b) for the 17 February 1999 storm at 1750 UTC. The dashed lines denote the approximate boundaries of the mixed phase region.	198

Figure 4.44: Cumulative frequency by altitude diagrams (CFADs) of SPOL radar reflectivity (a) and dual-Doppler-derived vertical velocity (b) for the 20 February 1999 storm at 1848 UTC. The dashed lines denote the approximate boundaries of the mixed phase region.	199
Figure 4.45: Vertical cross-section of SPOL radar reflectivity (shaded), along with differential reflectivity (solid line) and vertical velocity (dashed). a) Cross-section taken at 35 km north, at 2030 UTC on 26 January 1999. b) Same as a) except at 85 km north. Distances are relative to SPOL.	200
Figure 4.46: Vertical cross-section of SPOL radar reflectivity (shaded), along with differential reflectivity (solid line) and vertical velocity (dashed). Cross-section taken at 45 km north, at 1733 UTC on 13 February 1999. Distances are relative to SPOL.	201
Figure 4.47: Vertical cross-section of SPOL radar reflectivity (shaded), along with differential reflectivity (solid line) and vertical velocity (dashed). Cross-section taken at 24 km north, at 2030 UTC on 15 February 1999. Distances are relative to SPOL.	202
Figure 4.48: Vertical cross-section of SPOL radar reflectivity (shaded), along with differential reflectivity (solid line) and vertical velocity (dashed). Cross-section taken at 17 km north, at 1750 UTC on 17 February 1999. Distances are relative to SPOL.	203
Figure 4.49: Vertical cross-section of SPOL radar reflectivity (shaded), along with differential reflectivity (solid line) and vertical velocity (dashed). a) Cross-section taken at 72 km north, at 1739 UTC on 20 February 1999. b) Same as a) except at 60 km north, at 1848 UTC. Distances are relative to SPOL.	204
Figure 4.50: Vertical cross-section of SPOL radar reflectivity (shaded), along with differential reflectivity (solid line) and vertical velocity (dashed). Cross-section taken at 25 km north, at 1859 UTC on 20 February 1999. Distances are relative to SPOL.	205
Figure 4.51: Horizontal cross-section of SPOL radar reflectivity (shaded) and vertical velocity (solid line) at 5.0 km AGL for the 26 January 1999 storm at 2030 UTC.	206
Figure 4.52: Horizontal cross-section of SPOL radar reflectivity (shaded) and vertical velocity (solid line) at 5.0 km AGL for the 13 February 1999 storm at 1733 UTC.	207
Figure 4.53: Horizontal cross-section of SPOL radar reflectivity (shaded) and vertical velocity (solid line) at 5.0 km AGL for the 15 February 1999 storm at 2030 UTC.	208
Figure 4.54: Horizontal cross-section of SPOL radar reflectivity (shaded) and vertical velocity (solid line) at 5.0 km AGL for the 17 February 1999 storm at 1750 UTC.	209
Figure 4.55: Horizontal cross-section of SPOL radar reflectivity (shaded) and vertical velocity (solid line) at 5.0 km AGL for the 20 February 1999 storm at 1848 UTC.	210
Figure 5.1: a) Kinematic intensity index versus peak negative CG flash rate for all the storms in this study. b) Same as a) except for positive CG flash rate. Blue points denote mid-latitude cases, red points denote tropical cases.	226
Figure 5.2: a) Rain intensity index versus peak negative CG flash rate for all the storms in this study. b) Same as a) except for positive CG flash rate. Blue points denote mid-latitude cases, red points denote tropical cases.	227
Figure 5.3: a) Hail intensity index versus peak negative CG flash rate for the mid-latitude storms in this study. b) Same as a) except for positive CG flash rate.	228

Figure 5.4: a) Reflectivity intensity index versus peak negative CG flash rate for all the storms in this study. b) Same as a) except for positive CG flash rate. Blue points denote mid-latitude cases, red points denote tropical cases.	229
Figure 5.5: Kinematic intensity index versus rain intensity index for all the storms in this study. Blue points denote mid-latitude cases, red points denote tropical cases.	230
Figure 5.6: Kinematic intensity index versus hail intensity index for the mid-latitude storms in this study.	231
Figure 5.7: Kinematic intensity index versus reflectivity intensity index for all the storms in this study. Blue points denote mid-latitude cases, red points denote tropical cases.	232
Figure 5.8: Schematic diagram of possible charge structures within the updraft regions of ordinary, low-CG, and PPCG thunderstorms. Negative charge is denoted by blue negative signs, positive charge by red plus signs. Updrafts are denoted by vector arrows, with the length of the arrow corresponding to the strength of the updraft.	233

## CHAPTER 1

### INTRODUCTION

#### *1. Background*

How do convective storm microphysical and dynamical processes affect lightning production? This is a fundamental question in atmospheric electricity research, but it is a difficult question to answer, as there are a variety of convective storm types as well as different lightning patterns, as manifested in cloud-to-ground lightning flash rates, dominant polarity of cloud-to-ground lightning, total and intracloud lightning flash rates, the ratio of intracloud to cloud-to-ground lightning, and so on. Indeed, with the advent of lightning data for operational use in the “nowcasting” of thunderstorms, in particular severe thunderstorms, this question takes on additional weight. Answers to this question may provide better insights into the probability of severe weather, such as large hail and tornadoes.

Past research by a number of different scientists has shown that “typical” convection (e.g., a single-cell airmass storm, or perhaps a cell within a multicell complex) lasts less than two hours and becomes electrically active after vigorous convective growth associated with ice-phase development (Workman and Reynolds 1949; Mazur et al. 1986; Goodman et al. 1988; Williams et al. 1989b; Weber et al. 1993; Carey and Rutledge 1996). Its first flashes are typically intracloud (IC) flashes (Workman and Reynolds 1949; Livingston and Krider 1978; Goodman et al. 1988; Williams et al. 1989b; Maier and Krider 1986), and cloud-to-ground (CG) lightning flashes tend not to occur until the main core of the cell descends to lower altitudes (Larson and Stansbury 1974; MacGorman et al. 1989; Goodman et al. 1988, 1989; Williams et al. 1989b; Carey and Rutledge 1996). Thus, CG flashes typically peak after the ICs. Typical peak total flash rates are around  $10 \text{ min}^{-1}$  (Livingston and Krider 1978; Piepgrass et al. 1982; Williams et al. 1989a,b; Carey and Rutledge 1996), with CGs averaging around  $2 \text{ min}^{-1}$  and sometimes as high as  $10 \text{ min}^{-1}$  (Maier

and Krider 1982; Peckham et al. 1984; Williams et al. 1989b; Carey and Rutledge 1996). In typical warm season convection, over 90% of CG lightning is of negative polarity (i.e., transferring predominantly negative charge to ground; Orville 1994; Orville and Silver 1997).

By contrast, many severe thunderstorms feature high total lightning flash rates (greater than  $15 \text{ min}^{-1}$ , and often greater than  $30 \text{ min}^{-1}$ ). These storms also can produce very little CG lightning (often  $< 1 \text{ min}^{-1}$  and sometimes no CGs for 10 minutes or more), which means they can have high IC lightning flash rates, and thus a high IC:CG ratio. This ratio may even take on values of infinity for brief periods of time. These so-called “low-CG” storms are a topic of recent interest (MacGorman et al. 1989; Billingsley and Biggerstaff 1994; Maddox et al. 1997; Lang et al. 2000).

In addition, research in recent years has focused on the phenomenon of predominantly positive CG producing (PPCG) severe storms (Reap and MacGorman 1989; Branick and Doswell 1992; Curran and Rust 1992; Seimon 1993; MacGorman and Burgess 1994; Stolzenburg 1994; Carey and Rutledge 1998). These are storms that, under typical definitions, produce positive polarity flashes as greater than half of their total CG lightning flash rates. PPCG storms usually are severe, and can have high IC flash rates.

What really distinguishes low-CG from PPCG storms? Both have the potential for severity. Both tend to have high IC flash rates and high IC:CG ratios. Both lack significant production of negative CGs. But PPCG storms can produce significant numbers of positive CGs and low-CG storms do not. The large number of similarities between the two types of storms suggest that these storms perhaps lay on a continuum, with low-CG storms on one end and very significant PPCG storms on another. A storm’s position on the continuum then would be set primarily by the strength of whatever mechanism causes storms to become PPCG. Say for example that mechanism is a tilted dipole, where upper positive charge is displaced laterally by a high shear environment, so that it is exposed to ground rather than shielded by the main negative charge center, resulting in more positive CGs. Then a pure low-CG storm might be an intense storm that developed in somewhat less shear (although still significant shear since it is intense) than a pure PPCG storm. This is just one of many examples which will be systematically investigated in this dissertation.

Before any such continuum can be discussed, a better understanding is needed of the kinematic, microphysical, and environmental differences between low-CG and PPCG storms, if there are any, and the

differences between these storms and more general convection. The best way to do this is through radar and lightning observations of a variety of storms. By examining how lightning output changes as a function of things like vertical mass flux in updrafts/downdrafts, updraft/downdraft magnitudes and structure, hail/rain production, and general microphysical structure, we can better understand how storm microphysics and dynamics may affect lightning production.

## *2. Hypotheses*

MacGorman et al. (1989) first suggested that low-CG storms might be caused by an elevated charge mechanism. Here, intense updrafts loft the main negative charge layer to greater altitudes than normal. For a variety of reasons, most notably the reduced electric field between the main negative charge and ground due to the greater spatial separation, a reduction in the CG lightning flash rate (and in particular negative CG flash rate) would be expected. However, the total lightning (and thus IC) flash rate skyrockets due to stronger charging overall. Figure 1.1 presents these concepts in a schematic diagram. For normal convection, as kinematic (updraft) intensity increases, the storm electrifies more and negative CG lightning flash rate increases. However, at the high end of kinematic intensity, the negative charge becomes elevated enough that negative CG flash rates are reduced back to values typical of weak convection, even as total flash rate continues to climb.

Later research, such as Lang et al. (2000), found CG flash rate to be anti-correlated with storm intensity as measured by a multiparameter radar, which supports this hypothesis. In addition, balloon-borne electric field meter data presented in the suite of papers by Stolzenburg et al. (1998a-c) directly show a correlation between updraft speed and elevation of the negative charge layer. Finally, a modeling study by Ziegler and MacGorman (1994) supports the concept of the elevated charge mechanism. Based on these initial successes, this mechanism deserves further testing and refinement. In particular more case studies in a variety of climatic regimes need to be examined to see if these early insights are borne out.

There are basically three proposed mechanisms to explain PPCG storms. The tilted-dipole mechanism (explained above; MacGorman and Nielsen 1991; Branick and Doswell 1992), the inverted-dipole process, and the precipitation unshielding mechanism. The inverted-dipole mechanism suggests that in PPCG storms the lower positive charge layer may become so large that it effectively causes the classic dipole

structure of thunderstorms to become inverted, with negative charge atop positive charge. The lower positive charge then would favor positive CGs over negative CGs (MacGorman and Nielsen 1991; Williams et al. 1991). The precipitation-unshielding mechanism suggests that in intense storms the precipitation mass flux can become so large that the negative charge center is effectively rained out of the storm as the storm pulses in strength (Carey and Rutledge 1998). After every pulse the upper positive charge layer is exposed to ground, favoring positive CGs. The large precipitation mass flux also could lead to a large precipitation current (which tends to be negative), which means that the role of negative CGs in neutralizing charge may be diminished. Such a mechanism could explain the dearth of negative CGs in PPCG (and even low-CG) storms as well. A schematic depiction of the three proposed PPCG mechanisms can be seen in Figure 1.2.

Another mechanism that could be active in addition to or in place of the elevated charge mechanism, and which has received very little testing whatsoever, is the separated updraft/downdraft mechanism. Numerous studies have shown that, in typical storms, the main precipitation core falls through at least a portion of the main updraft. This gives that precipitation access to supercooled liquid water (SLW) that is being generated and lofted by the storm updraft. The noninductive charging mechanism (NIC) that has been studied by such researchers as Takahashi (1978) suggests that a colliding mixture of precipitation-sized ice particles, ice crystals, and SLW will develop significant charge separation as the large and small ice particles rebound. At slightly subfreezing temperatures, say  $> -10$  °C, graupel should develop positive charge. This results in a lower positive charge region underneath the main negative charge region, which typically resides somewhere in the  $-10$  °C to  $-20$  °C layer. Recent research by Dr. E. P. Krider (personal communication) and others (e.g., Clarence and Malan 1957; Williams et al. 1985; Williams et al. 1989b) has shown that this lower positive charge region could be very important in providing a downward bias for negative CGs which begin in the main negative charge layer. In stronger storms with higher shear, however, the updraft and downdraft are more separated, and the main precipitation core of the storm may fall mostly through the downdraft, which will feature comparatively little SLW. Indeed, this juxtaposition of the updraft and downdraft promotes and sustains supercellular activity (e.g., Klemp 1987). This may imply less NIC and perhaps no lower positive charge to assist with negative CG production. Hence, lower negative CG flash rates associated with more strongly sheared storms may result.

These hypotheses will be tested in a variety of different ways, by utilizing a very unique data set. This data set features combined dual-Doppler, multiparameter radar, and lightning observations of 11 different cases. The cases vary from weak monsoon-type storms, to “garden variety” convection, to relatively intense storms, then finally to severe and even tornadic thunderstorms. Both unicellular and multicellular convective storms are represented. Six cases are from the mid-latitudes, and five are from the tropics. The breadth and scale of this data set are unprecedented, and it provides a wealth of information to understand how convective storm microphysics and dynamics may influence lightning production.

Chapter 2 describes this data set, as well as the methodology employed in this study. Chapter 3 reports on five 1998 mid-latitude cases from the CHILL-Pawnee radar network in northeast Colorado, as well as an additional case that occurred near the Colorado/Kansas border in June 2000 (a severe tornadic storm). Chapter 4 reports on five cases of tropical convection in Brazil observed during January-February 1999. Chapter 5 synthesizes the previous chapters’ results into a coherent set of observations and conclusions, and summarizes the results of this study.

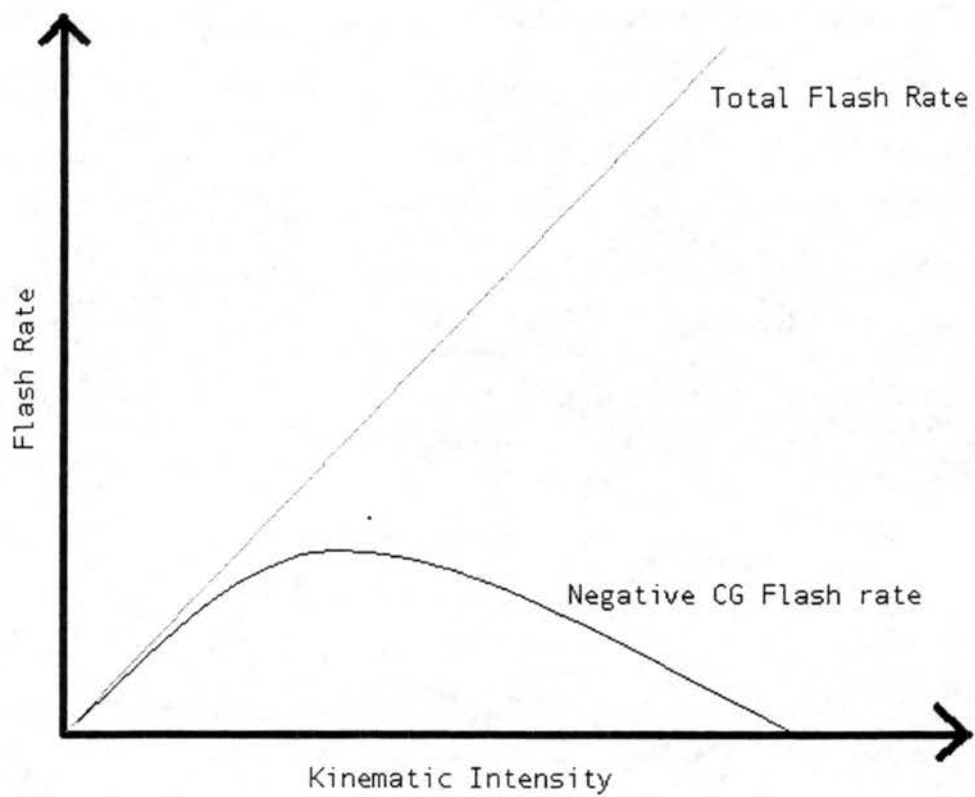


Figure 1.1: Schematic representation of the impact of the elevated charge mechanism on lightning flash rates.

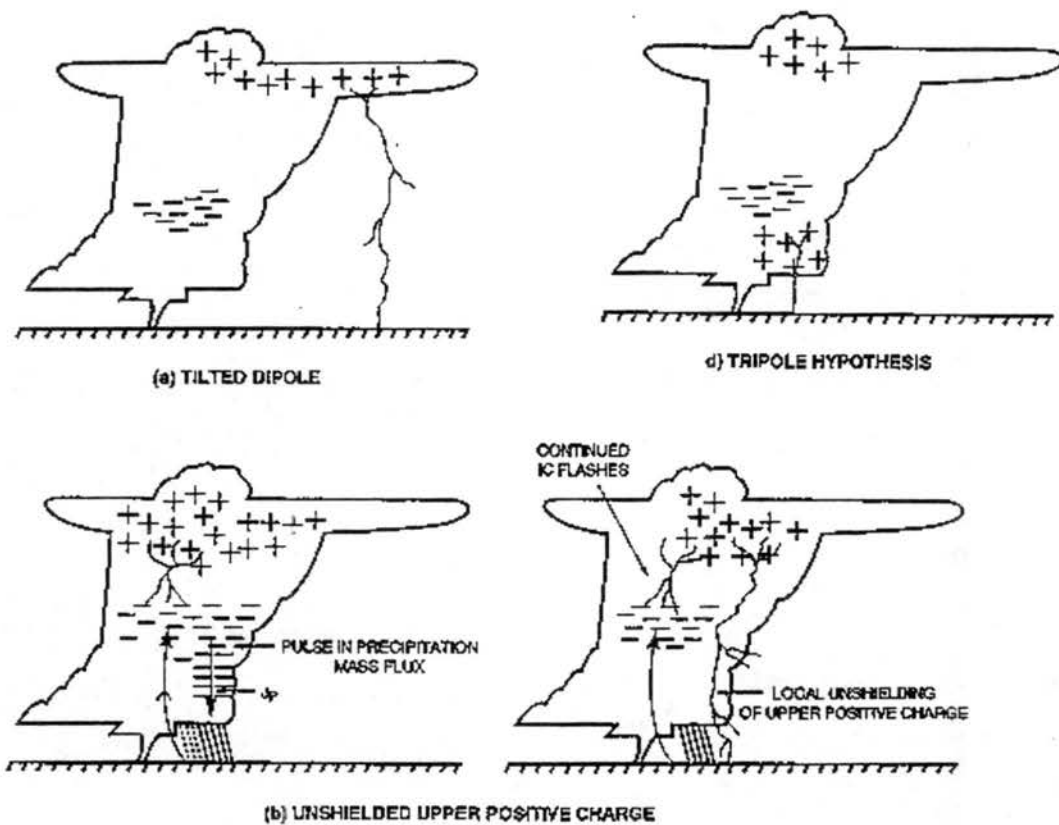


Figure 1.2: Schematic representations of the three mechanisms proposed to explain PPCG thunderstorms. The top-left panel depicts the tilted dipole mechanism. The top-right panel depicts the inverted dipole or enhanced lower positive charge mechanism. The bottom panels depict the precipitation unshielding mechanism. From Williams (2000).

## CHAPTER 2

### DATA AND METHODOLOGY

#### *1. Overview*

This study contains five case studies (1, 15, 21, 25, and 30 July 1998) of thunderstorms from the mid-latitudes utilizing the CHILL-Pawnee dual-Doppler radar network in northeast Colorado. This is the only permanent research dual-Doppler network in the United States. It came into operation during the summer of 1998, with the installation of the Pawnee radar. Previously, the CSU-CHILL radar operated alone in this region.

In addition, to broaden the scope of the analysis, there are five cases (26 Jan, 13, 15, 17 and 20 Feb 1999) from the tropics, specifically from the Tropical Rainfall Measuring Mission/Large-Scale Biosphere-Atmosphere Experiment (TRMM/LBA; Rutledge et al. 2000) field project in the southwestern Amazon region of Brazil. TRMM/LBA was one of several validation campaigns to support the TRMM satellite, which maps tropical rainfall using a combination of active and passive microwave sensors. TRMM/LBA was the only such campaign carried out in a tropical continental region. TRMM/LBA occurred in the state of Rondonia during January and February of 1999.

Finally, there is a solitary case (29 June 2000) from the Severe Thunderstorm Electrification and Precipitation Study (STEPS). STEPS occurred during the summer of 2000 in eastern Colorado/western Kansas. The project combined an unprecedented scale of electrical, radar, in situ, and sounding observations of U.S. High Plains convection.

These cases were selected to span a broad spectrum of convection weakly from electrified to PPCG and low-CG intense storms. Furthermore, the choice of both mid-latitude and tropical cases provides for additional contrast between these two regimes. Each case typically features 1-2 hours of combined dual-

Doppler and multiparameter radar data. Each has access to CG lightning data (ground strike location, polarity, peak current, multiplicity). Field change meters (FCMs) provide some information on total lightning flash rates for at least a portion of most of the cases (CHILL-Pawnee and TRMM/LBA). The STEPS case features data from a VHF lightning mapper, which provides higher quality total/IC lightning data than do FCMs. Finally, all cases have some thermodynamic sounding data to characterize convective available potential energy (CAPE) and environmental wind shear.

The CHILL-Pawnee cases feature multiparameter radar data from the CSU-CHILL radar, and when combined with Pawnee data, dual-Doppler coverage of storm kinematics. The TRMM/LBA cases feature multiparameter radar data from the NCAR SPOL radar, and dual-Doppler coverage when combined with data from the TOGA radar. The STEPS case was covered by the CSU-CHILL (located near Burlington, CO, for STEPS) and the SPOL radars. FCMs provided total lightning coverage for the CHILL-Pawnee and TRMM/LBA cases. The National Lightning Detection Network (NLDN) provided CG lightning data for CHILL-Pawnee and STEPS cases. A network of combined direction finder (DF) and time-of-arrival (TOA) sensors provided CG data for TRMM/LBA cases. This network was installed and maintained by NASA Marshall Space Flight Center personnel. A time-of-arrival (TOA) VHF lightning mapper provided total lightning data for the STEPS case. Thermodynamic soundings were available for all cases. In the following sections, each of these observational platforms will be described in more detail.

## *2. Observational Platforms*

### *a) CSU-CHILL Radar*

The CSU-CHILL radar is a dual-linearly-polarized S-band Doppler radar (Brunkow et al. 2000). See Table 2.1 for specifications. The multiparameter variables measured by the CSU-CHILL radar include horizontal reflectivity ( $Z_h$ ), radial velocity ( $V_r$ ), differential reflectivity ( $Z_{dr}$ ), linear depolarization ratio (LDR), correlation coefficient at zero lag ( $\rho_{hv}$ ), and differential phase ( $\Psi_{dp}$ ). These variables give information on the size, shape, orientation, thermodynamic phase, and radial velocity of hydrometeors in a bulk sense. For a thorough review of these variables see Doviak and Zrnich (1993). The CHILL radar normally resides near Greeley, CO, but was located near Burlington, CO, for the STEPS project.

*b) Pawnee Radar*

The Pawnee radar is an S-band Doppler radar whose specifications are summarized in Table 2.1. Figure 2.1 shows the dual-Doppler network created by the CHILL-Pawnee pair. In this study, the Pawnee radar data were used to provide Doppler information for dual-Doppler syntheses with the CHILL radar.

*c) SPOL Radar*

The SPOL radar is a dual-linearly-polarized S-band Doppler radar whose specifications are summarized in Table 2.1. SPOL data products are very similar to those provided by CHILL. See Figure 2.2 for a map of the dual-Doppler network created by the CHILL-SPOL pair during STEPS.

*d) TOGA Radar*

The TOGA radar is a C-band Doppler radar whose specifications are summarized in Table 2.1. Figure 2.3 shows the dual-Doppler network created by the SPOL-TOGA pair. In this study, the TOGA radar data were used to provide Doppler information for dual-Doppler syntheses with the SPOL radar.

*e) Field Change Meters*

FCMs detect electrostatic field changes due to lightning. Thus, they can be used to measure total flash rates for a given storm. The sensors used in the CHILL-Pawnee and TRMM/LBA cases had a nominal range of 40 km. However, this detection range varied with time, and detection efficiency was a strong function of range. Thus, flash rates can be heavily influenced by storms moving into and out of range of the FCM. Sensors were periodically subject to enhanced noise and/or reduced sensitivity due to mechanical and electronic problems, as well as weather (sensitive to wind and rain). In addition, FCMs provide no direction or range information, so multiple cells within range cannot be distinguished. At best, they provide a first guess at total lightning flash rates for a short period in a particular storm's lifetime. During these times CGs (detected by other instruments) can be subtracted from the total flash rate to provide rough IC flash rates as well as the IC:CG ratio.

Three FCMs were deployed during the CHILL-Pawnee cases: one at CHILL, one at Pawnee, and one at Christman Field, which is roughly at the center of the western dual-Doppler lobe. There were two FCMs

deployed during the TRMM/LBA cases: one at SPOL and one at TOGA. However, the TOGA FCM malfunctioned during all of the studied TRMM/LBA cases, and hence no TOGA FCM data were used in this study. No FCMs were deployed during STEPS, as more sophisticated means were employed to measure total lightning.

*f) National Lightning Detection Network*

The National Lightning Detection Network detects CG lightning within the continental United States. Available data for all flashes include ground strike location, peak current and polarity (positive or negative), and multiplicity (number of return strokes). Recently, the NLDN was upgraded to its current combination of direction-finding and time-of-arrival technology. As a result of this upgrade, detection efficiencies in northeastern Colorado are projected to have improved to 90% or better (80% or better in the STEPS domain), with a median location accuracy of 0.5 km (Cummins et al. 1998).

An unexpected result of this upgrade was the inclusion of a previously undetected population of weak positive flashes. These discharges may not be true positive CGs; instead, many could be IC discharges that are being falsely identified as positive CGs. It has been suggested that some detected positive discharges with peak currents under 10 kA may be IC discharges (Cummins et al. 1998). Therefore, such flashes were not included in CG flash rates for the CHILL-Pawnee and STEPS storms.

*g) TRMM/LBA Advanced Lightning Direction Finder Network*

The Advanced Lightning Direction Finder (ALDF) network in Brazil was comprised of four Improved Accuracy from Combined Technology (IMPACT) sensors. IMPACT sensors utilize both magnetic direction finding (DF) and time-of-arrival (TOA) technology to locate ground strike positions of CG flashes. Like the NLDN, peak current, polarity, and multiplicity also are measured. When all four sensors were operational, estimated detection efficiency within the LBA dual-Doppler lobes was 70-80% or better, with a median location accuracy of 1-2 km (Dr. R. Blakeslee, personal communication). However, during the TRMM/LBA cases in this study, the entire network was not completely functional. At times, only 2-3 stations were available for CG detections. This would cause particularly the flash locations to have significantly greater errors. Detection efficiency would not be significantly degraded, however. Similar to

the NLDN, positive CGs with peak currents less than 15 kA were not included in the analysis of LBA storms.

*h) New Mexico Tech VHF Lightning Mapper*

The New Mexico Tech Lightning Mapping Array (LMA) was operated in the STEPS project area from mid-May to mid-August, 2000. Thirteen measurement stations were deployed over a four-county area in northwestern Kansas and eastern Colorado. LMA coverage included and extended well beyond the CHILL-SPOL dual-Doppler lobes. The system locates the sources of impulsive VHF radio signals from lightning by measuring the time that the signals arrive at the different receiving stations. Each station listens for lightning signals in an unused television channel (Channel 3, 60-66 MHz), and arrival times are measured with an accuracy of 50 ns. Synthesis of the time-of-arrival (TOA) measurements allows three-dimensional reproduction of the lightning inside storms. For more discussion of the TOA lightning mapping method see Proctor (1981).

*i) Thermodynamic Soundings*

CHILL-Pawnee cases utilized standard semi-daily National Weather Service (NWS) soundings from Denver, CO. Typically, the 0000 UTC (1800 MDT, local evening) sounding was used, as it usually was the closest to convective initiation times. If the 0000 UTC sounding was incomplete or missing, then the 1200 UTC (0600 MDT, local morning) sounding from the previous UTC day (i.e., that morning) was used. Because these NWS soundings were not in the immediate vicinity of convective areas scanned in the CHILL-Pawnee cases, model-produced soundings from the Regional Atmospheric Modeling System (RAMS; Pielke et al. 1992, Nachamkin et al. 1999) supplemented these NWS soundings where possible.

During TRMM/LBA, VIZ soundings were released every three hours from the Abracos Hill observation site, which is very near the TOGA radar. These soundings were used to characterize the thermodynamic environment for the TRMM/LBA cases.

Mobile GLASS soundings were available for the STEPS case. These were used instead of the NWS soundings due to better proximity in time and space to the convection of interest.

### 3. Methodology

#### *a) Radar Scan Strategy*

In all cases, the only radar scans used for analysis purposes were plan position indicator (PPI) sector volumes. These scans are well suited for high-quality dual-Doppler and multiparameter analyses. The general strategy for all cases was the full coverage of all relevant echoes by both radars in a manner consistent with convective time scales. Hence, sector volumes typically varied between four and six minutes in length, enclosed at least 30 dBZ echo and larger, and “topped” the storm. For the CHILL-Pawnee cases, the radars synchronized their scans automatically via timers. In all other cases, radars were synchronized manually via direct radio or telephone communications. This generally resulted in the radars scanning no more than 30 seconds apart. Sometimes, particularly in the TRMM/LBA cases, radars were more than a minute apart due to poor communication links. These times will be noted when TRMM/LBA dual-Doppler results are presented. Sector volumes did not always follow one another, as range height indicator (RHI) scans and surveillance scans could be interspersed at times. This lowered temporal resolution was especially true in the TRMM/LBA data, as there were other project goals than just standard PPI dual-Doppler/multiparameter sectors.

#### *b) Multiparameter Radar Analysis*

Multiparameter radar data can be used to characterize rain and ice mixing ratios in each storm of interest. Information on precipitation rates (both water and ice phases), mass fluxes, and general microphysical structure can be determined for each radar echo volume.

Multiparameter radar data (from SPOL and CHILL, all cases) were first carefully edited for clutter, sidelobe, and other spurious echo. To accomplish this, CHILL data were thresholded on  $Z_h$  ( $< 0$  dBZ gates were deleted) and  $\rho_{hv}$  ( $< 0.7$  gates were deleted). This eliminated most unwanted echo. The rest was removed by hand using Research Data Support System (RDSS) software developed at the National Center for Atmospheric Research (NCAR; Oye and Carbone, 1981). Before calculating specific differential phase ( $K_{dp}$ ), differential phase data were edited in a manner similar to the method of Ryzhkov and Zrnich (1998). The standard deviation of the differential phase field was calculated for each gate using a 21-point running filter. Gates that had standard deviations greater than a specific threshold were not used in  $K_{dp}$  calculations.

In areas where the radar reflectivity was equal to or greater than 35 dBZ the standard deviation threshold was 18°, and it was 6° elsewhere. As long as the number of consecutive bad gates were no more than two, bad data gates interspersed with good data were filled via linear interpolation. In addition, gates surrounding good data were similarly padded, up to a maximum of 10 gates on either side of the good data, for the purpose of further filtering (see the next step). The resulting differential phase field was filtered again using a 21-point finite impulse response (FIR) filter to suppress effects from non-Rayleigh backscatter effects (Hubbert and Bringi, 1995).  $K_{dp}$  was then:

$$K_{dp} = \frac{1}{2} \frac{d\Phi_{dp}}{dr},$$

where  $r$  is range and  $\Phi_{dp}$  the filtered differential phase field. This derivative was evaluated via the finite difference method.

SPOL data were edited in a similar manner, except that all variables (not just differential phase) were filtered using the differential phase standard deviation method. The standard deviation thresholds were significantly stricter than with the CHILL data (3° for > 35 dBZ, 9° otherwise). Additionally, the data were thresholded on a  $\rho_{hv}$  threshold (0.95 for < 35dBZ, 0.8 otherwise). No reflectivity threshold was required as the above thresholds were sufficient to eliminate nearly all spurious echo. CHILL data could not be subjected to these strict thresholding methods because they removed a lot of seemingly good data (i.e., large portions of significant storm cores). The reasons why the SPOL differential phase data seemed “cleaner” than the CHILL data were not investigated thoroughly, but could be due to lower noise in the differential phase field. The correlation coefficient threshold was higher because tropical data typically do not show significant reductions in  $\rho_{hv}$  due to the lack of significant hail. However, the same thresholds appeared to work well for the mid-latitude STEPS case covered by SPOL. It is likely that raising the  $\rho_{hv}$  threshold for the CHILL data also could have been done without compromising the data.

Differential reflectivity biases were determined on a case-by-case basis by looking at histograms of high elevation angle (> 15°) PPI scans. If the average differential reflectivity value in areas outside major cores was significantly different than zero, then the difference was assumed to be due to bias, and the  $Z_{dr}$  field was adjusted accordingly.

Sidelobe contamination in the  $Z_{dr}$ , LDR, and  $\rho_{hv}$  fields (Herzogh and Carbone, 1984) was accounted for in a subjective manner, as these fields were not used in any objective analyses. Generally, these fields were examined to gain a better idea of the microphysical structure of the storms, and to supplement inferences from any objective multiparameter data analyses. For these purposes, data in areas of strong reflectivity gradients were under considerable scrutiny. However, since the CHILL and SPOL are high-quality research radars with well-matched sidelobe patterns, sidelobe contamination was not a major concern.

SPOL and CHILL data were gridded using the NCAR REORDER package. A Cressman (1959) filter was used, either with a fixed or variable radius of influence. For CHILL data, a variable radius of influence of  $1^\circ$  was used. SPOL data often used a fixed radius of influence of 1.5 km in the horizontal and 1.0 km in the vertical because older gridding methods were “grandfathered” into this study. However, a  $1^\circ$  variable radius was used at times when this fixed radius of influence failed to account for data far from the radar. Grid boundaries were chosen so as to contain the dual-Doppler lobe in which convection was occurring, unless convection was very isolated and a smaller grid could be used. Grid spacing was 1.0 km in the horizontal and 0.5 km in the vertical. CHILL-Pawnee data were gridded up to 16 km AGL (above ground level), and STEPS and tropical data up to 20 km AGL. Mid-latitude grids were defined relative to CHILL, and tropical grids were defined relative to SPOL.

The multiparameter data analysis focused on two objectives: 1) calculate near-surface rain and hail rates, and thus make estimates of storm-total mass flux for each precipitation type, and 2) distinguish between different hydrometeor types in a subjective bulk sense.

Table 2.2 summarizes how rain and hail rates/fluxes were calculated. At a particular grid point, if  $K_{dp}$  was greater than  $0.25^\circ \text{ km}^{-1}$  (noise level), then it was used to calculate rain rate via the method of Sachidananda and Zmic (1987). If the specific differential phase was less than this threshold, then a radar reflectivity-rain rate (Z-R) relationship was used to calculate the rain rate. In the mid-latitudes, the Z-R from Jones (1955) was chosen. In the tropics, a preliminary Z-R developed by analysis of SPOL and rain gauge data (Dr. L. Carey, personal communication) was used. If the relevant Z-R gave a rain rate greater than  $20 \text{ mm h}^{-1}$ , then it was assumed that the reflectivity was almost entirely due to hail at that point, and the rain rate was set to zero.

The hail rate was calculated by first using  $K_{dp}$  to determine the reflectivity factor (in  $\text{mm}^6 \text{m}^{-3}$ ) due to rain at a grid point by substituting the  $K_{dp}$ -R relationship from Sachidananda and Zrnica (1987) into the relevant Z-R. The resulting rain reflectivity factor was subtracted from the total  $Z_h$ , with the remainder being the reflectivity factor due to hail. This was input into the hail reflectivity-hail rate (Z-H) relationship of Carey and Rutledge (1998), which was based on the Cheng and English (1983) hail size distribution, to determine hail rate in  $\text{mm h}^{-1}$  liquid equivalent. However, if the hail reflectivity was not within 7 dB of the rain reflectivity, then the hail rate was assumed negligible, after Balakrishnan and Zrnica (1990). Note that this method assumes Rayleigh scattering by hail, which may not be valid for S-band radars like CHILL and SPOL, especially when the hail is large.

There are some important sources of error in these radar-derived precipitation rates. Differential phase provides superior estimates of rain rate, especially at high rain rates ( $> 60 \text{ mm h}^{-1}$ ), but is still subject to errors on the order of 10-20% based on raindrop size distribution and drop size-shape relationship variation, as well as radar estimation errors (Chandrasekar et al., 1990). Radar reflectivity-rain rate relationships provide comparable errors, but only when rain rates are low ( $< 20 \text{ mm h}^{-1}$ ); otherwise they are much larger (Chandrasekar et al., 1990). Thus, 10-20% serves as a lower bound for errors in rainfall estimates, with an upper bound around 30-40% for those times when assumptions are grossly violated. These errors will affect rain rate calculations as well as the hail rate calculations. In addition, hail rate calculations are subject to further errors. After the initial rain rate calculation, the computation of reflectivity factor due to rain is subject to errors on the order of a few dB (Doviak and Zrnica, 1993). The choice of the Cheng and English (1983) hailstone size distribution may not be valid in all instances, and furthermore, as mentioned above, the assumption of Rayleigh scattering for hail is not always valid, especially for large hail. Hail rate is inherently difficult to measure properly via in situ methods, so it is difficult to accurately quantify the magnitude of the error associated with these radar-inferred hail rates. However, estimates of error magnitudes on the order of 50% or more probably are not unreasonable, especially in regions where the assumptions about hail size distribution and Rayleigh scattering are not valid. For example, the given algorithm could significantly overestimate hail rate during those times that hail reflectivity is caused mostly by a few large hailstones, rather than the broader distribution predicted by Cheng and English (1983).

Precipitation fluxes were computed by summing all the precipitation rates over the whole horizontal grid at a specific vertical level (usually the lowest level – 0.5 km above ground level, or AGL – in this case). Fluxes were calculated for the entire storm complex, not individual cells.

### *c) Dual-Doppler Radar Analysis*

Dual-Doppler syntheses give information on the magnitudes and spatial variability of updrafts and downdrafts, as well as vertical air mass fluxes, for every radar volume of each case.

Pawnee and TOGA radar data, not being multiparameter, typically were thresholded on noise-corrected power and total power if needed, then remaining spurious echo (particularly sidelobe echo and clutter) was removed by hand. For each set of volumes, radial velocities for both radars (CHILL/Pawnee, SPOL/TOGA, or CHILL/SPOL) were carefully edited to eliminate any velocity aliasing. Pawnee data were interpolated to a CHILL-centric grid using a variable radius of influence of  $1.2^\circ$  (slightly larger than CHILL's due to Pawnee's greater beamwidth). TOGA data were interpolated to an SPOL-centric grid using either a fixed radius of influence (1.5 km horizontal, 1.0 km vertical), or if that failed to properly grid the data, a variable radius of influence set at  $1.6^\circ$  (TOGA's beamwidth being larger than SPOL's). In the STEPS case, SPOL data were interpolated to a CHILL-centric grid.

For the actual dual-Doppler syntheses, slightly different methods were employed depending on the project (CHILL-Pawnee, LBA, or STEPS). These differences arose through the "grandfathering" of different methods from studies that occurred prior to the present one. Based on tests utilizing the same method for a few volumes from different projects, it is not believed that these different methods significantly affected the comparisons of cases from different projects.

Each set of volumes was synthesized using the CEDRIC package developed by NCAR. The specifics of the dual-Doppler syntheses for all cases can be found in Table 2.3. For CHILL-Pawnee syntheses, the required inter-beam angle was  $30^\circ$  for the radial velocities to be combined to create a first estimate of the horizontal wind field (west-east: U, south-north: V). LBA and STEPS syntheses required a crossing angle of only  $22.16^\circ$ .

During synthesis, data were shifted relative to a specific time (to account for advection during the sampling interval) using an estimate of storm motion gathered from perusal of the radar data. For CHILL-

Pawnee cases this time was set as the midpoint of the current set of scans, since the radars were always in near-perfect synchronization. For other cases it was set at the beginning of the principal radar's (SPOL in LBA, CHILL in STEPS) scan.

The U and V fields resulting from the synthesis were filtered using a Leise filter. Then, to determine vertical velocity ( $W$ ), the first step was to correct the initial estimates of U and V for the vertical fallspeed of the precipitation using a reflectivity-terminal fall velocity ( $Z-V_t$ ) relationship and geometric factors from the synthesis. The reflectivity field from the principal radar (CHILL in all mid-latitude cases, SPOL for LBA) was used for calculations of  $V_t$ . After this is done, the horizontal divergence calculated from the corrected U and V was numerically integrated downward from the top level (zero vertical velocity is the upper boundary condition) only to the next level in the column to obtain a first estimate of the vertical air motion. The U and V at this next level were corrected for this air motion, again using the geometric factors, then the divergence was recalculated and the integration downward was repeated, but from the top level to the next level in the column. Once the solution converged, an integration step then was done from this level to the next level, and so on. At each integration step from one level to the next, the above-described iteration was done until the solution converged. Convergence criteria usually were met after two or three cycles. This is the Lax-Wendroff iterative scheme for solving partial differential equations, in particular the continuity equation, where the desired quantity,  $W$ , appears in the partial derivatives for all three directions. For more on multiple Doppler analyses see Bohne and Srivastava (1975), Ray (1978), and Ray (1980).

Once the final U, V, and W fields were determined, they were output in gridded form. Key uses of the dual-Doppler syntheses were: calculation of maximum and average  $W$  (positive and/or negative) at all height levels, calculation of storm volume containing vertical velocities in excess of (or less than) a particular threshold, multiplication of  $W$  with air density (determined from soundings) to estimate vertical air mass flux, and correlation of vertical velocity with reflectivity and other multiparameter variables and derivatives.

In dual-Doppler analyses, errors in vertical wind estimation can result from two main issues: poor sampling of convergence, and an incorrect  $Z-V_t$  relationship. Convergence errors are minimized with the top-down integration approach employed in this study, since such errors are weighted by air density.

Sensitivity studies with different  $Z-V_r$  relationships were done, and peak vertical velocities were found to vary about 10-20% depending on the relationship used. Overall, it is not believed that in this study errors in vertical velocity estimation significantly exceeded 20%.

#### *d) Lightning Analysis*

CG lightning data (time, strike location, peak current, multiplicity) from the NLDN (mid-latitude) and ALDF (Brazil; also known as the Brazil Lightning Detection Network or BLDN) were used to compute both positive and negative CG lightning flash rates during the entire radar analysis period of each case. CG ground strike locations were compared to plots of radar reflectivity at periodic times to identify strikes that were not close (subjectively chosen, but typically > 10 km away) to any radar echo. These strikes were not included in flash rates. As noted above, positive CGs with peak currents less than 10 kA (15 kA for the BLDN) were not included in CG flash rates.

Standard FCM data give voltage strength as a function of time. Flashes then manifest themselves as rapid changes in the voltage signal. Flashes were detected in the FCM data by thresholding on both the signal-to-noise ratio (SNR) and the peak-to-peak (PP) voltage change in the signal. The SNR threshold basically tests on the ratio of the maximum PP voltage change to the minimum PP change within a given time period. The threshold used varied from case to case, but was set such that no flashes were detected in data from clear air times (no storms within 40 km). The additional PP change threshold ensures that in low-noise situations, a minor noise blip does not register as a flash. This threshold also varied on a case-to-case basis and was set using clear air data. Once a flash was detected, 500 ms were required to pass before another flash could be detected, to account for multiple strokes. Visual inspection of the FCM data via a plotting package was used to confirm that the objective analysis was performing well. With detected flashes and flash times, total lightning flash rates were computed. When storms were particularly well situated (i.e., close, with low noise) relative to the FCM in question, the CG flash rate (via NLDN/ALDF) was subtracted from the total flash rate to give IC flash rate, and the IC:CG ratio was computed.

Full LMA data for the STEPS case were not yet available at the time of analysis. In fact, only about two minutes of data near the time the storm went tornadic are available. Furthermore, the VHF signals during this time were continuous and filled a substantial volume of the storm, making actual calculations of flash

rates difficult, if not misleading. Therefore, LMA data were analyzed in a fairly raw form, with just locations and times of VHF sources.

*e) Sounding Analysis*

Limited sounding data were available in the mid-latitude cases. Model-generated soundings from RAMS were used to supplement these observational data, and to confirm that they were relevant to the environments in which the storms developed. Regular soundings in the immediate vicinity of the main observational area were available in the tropical cases. Soundings were used to determine important temperature levels (useful in radar analyses) and air density profiles (useful in determining vertical mass fluxes), and to estimate CAPE and shear.

*f) Synthesis*

For all cases, time series of all available measurements (radar and lightning) were developed. This allowed for easy comparison of the storms over a significant portion of their life cycles. In addition, storms were compared at key times in their life cycles, such as time of peak updraft, time of peak CG lightning, etc. Storms were compared both quantitatively (through things like fluxes and rates) and qualitatively (through things like general microphysical/dynamical structure).

Lightning output as a function of storm dynamics, as derived from dual-Doppler syntheses, was determined. This implied examining positive/negative CG flash rates, and where possible, total/IC lightning flash rates and IC:CG ratios, as functions of: 1) vertical air mass fluxes in updrafts; 2) overall strength and sizes of updrafts; and 3) correlation of updrafts with major precipitation cores.

Lightning output also was examined as a function of multiparameter radar-derived estimates of microphysical variables, such as: 1) rain and hail/ice rates and mass fluxes at the surface and elsewhere; 2) size/area of the storm producing rain and/or hail; and 3) radar reflectivity structure and intensity of each storm.

These comparisons were performed for all the mid-latitude cases as a whole, and hypotheses were tested using the results of the comparisons (Chapter 3). The tropical data were subjected to a similar process

(Chapter 4). Finally, the mid-latitude and tropical data were synthesized into a combined data set to confirm whether or not hypotheses were applicable to only one regime or both (Chapter 5).

Table 2.1: Specifics of the radars used in this study.

<b>Radar Characteristic</b>	<b>CSU-CHILL</b>	<b>Pawnee</b>	<b>SPOL</b>	<b>TOGA</b>
<i>Wavelength (cm)</i>	11.01	10.99	10.71	5.3
<i>Polarization</i>	Linear, H & V	Linear, V	Linear, H & V	Linear, H
<i>Peak power (kW)</i>	800-1000	380	>1000	250
<i>3 dB Beamwidth (°)</i>	1.10	1.60	0.91	1.65
<i>Noise Power (dBm)</i>	-114.0	-109.0	-115.5	-113.0

Table 2.2: Overview of the algorithm used to calculate rain and hail rates from CSU-CHILL and SPOL multiparameter radar data.

<p>If <math>K_{dp} \geq 0.25 \text{ } ^\circ \text{ km}^{-1}</math>:</p> $R(K_{dp}) = 40.683 \bullet (K_{dp})^{0.866}$	(Sachidananda and Zmic, 1987)
<p>If <math>K_{dp} &lt; 0.25 \text{ } ^\circ \text{ km}^{-1}</math> and <math>1 \text{ mm h}^{-1} &lt; R(Z_h) &lt; 20 \text{ mm h}^{-1}</math>:</p> $Z_h = 486 \bullet R(Z_h)^{1.37}$ $Z_h = 163 \bullet R(Z_h)^{1.49}$	<p>(Jones, 1955) – mid-latitudes</p> <p>(Preliminary LBA Z-R) - tropics</p>
<p>Hail (<math>\text{mm h}^{-1}</math> liquid equivalent):</p> $H(K_{dp}, Z_{hail}) = \frac{88.0}{\exp\left[5.38 \times 10^{-6} Z_{hail} \left\{K_{dp}\right\}^{-0.297}\right]}$	(Carey and Rutledge, 1998)

Table 2.3: Overview of the dual-Doppler algorithms employed in this study.

Dual-Doppler	CHILL-Pawnee	TRMM/LBA	STEPS
<i>Minimum Crossing Angle</i> (°)	30	22.16	22.16
<i>Z-V<sub>r</sub> Relationship</i> $V_r = -A \cdot 10^{BZ_h} \cdot \left( \frac{\rho_0}{\rho_z} \right)^{0.4}$ $(\rho_z = e^{-0.1z})$	A= 1.5, B=0.0105	A=0.817, B=0.0063 (above freeze altitude)  A=2.6. B=0.0107 (below freeze altitude)	A= 1.5, B=0.0105
<i>Integration</i>	Downward	Downward	Downward
<i>Boundary Conditions</i>	W=0 at storm top	W=0 at storm top, sponge	W=0 at storm top, sponge
<i>Convergence Criterion</i> (difference between horizontal and vertical convergence at each level)	0.01	0.005	0.005

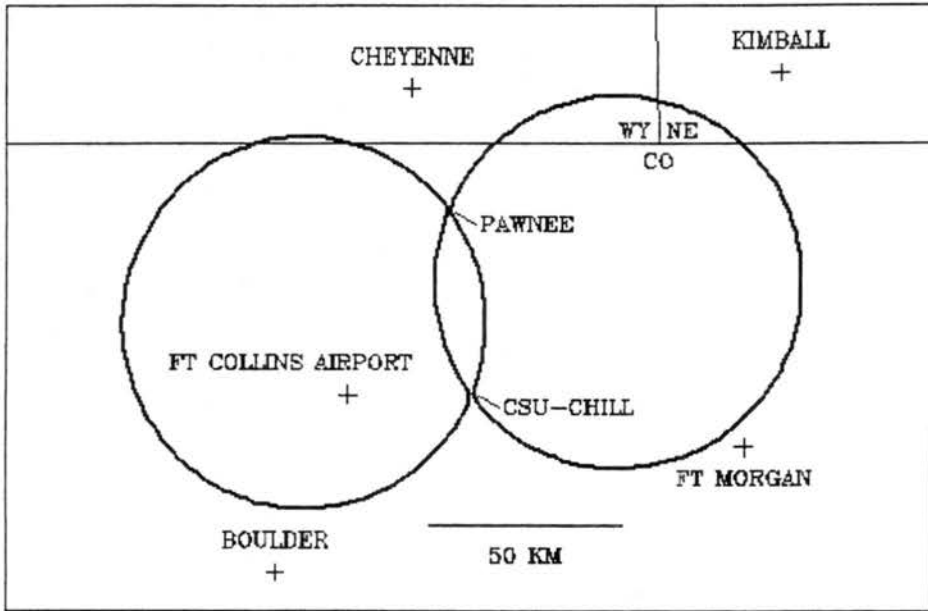


Figure 2.1: Schematic map of the operational area of the CHILL-Pawnee dual-Doppler network. Pictured are the two dual-Doppler lobes. Landmarks include the two radars (CHILL and Pawnee) as well as nearby cities and airports (map courtesy of P. Kennedy).

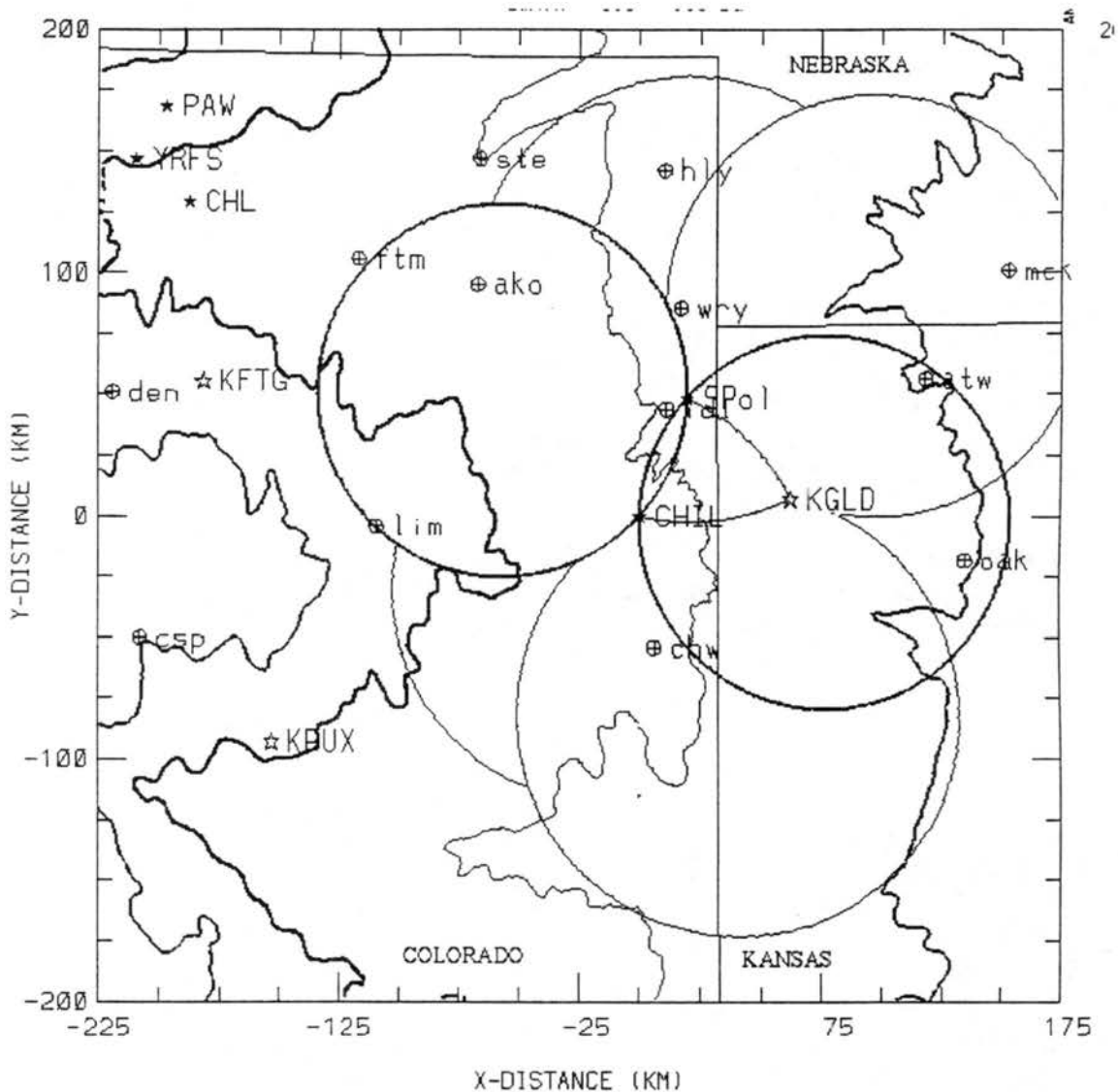


Figure 2.2: Schematic map of the STEPS operational area. Pictured are the two dual-Doppler lobes (bold circles) formed by CHILL and SPOL. Also shown are major elevation contours. Landmarks include the three project radars (CHILL, SPOL, and Goodland/KGLD) as well as nearby cities, airports, and other regional NEXRAD radars. The shaded areas include other dual-Doppler and triple-Doppler lobes formed by the CHILL-SPOL-KGLD network (map courtesy of Dr. J. Miller).

## TRMM-LBA Instrumentation Network

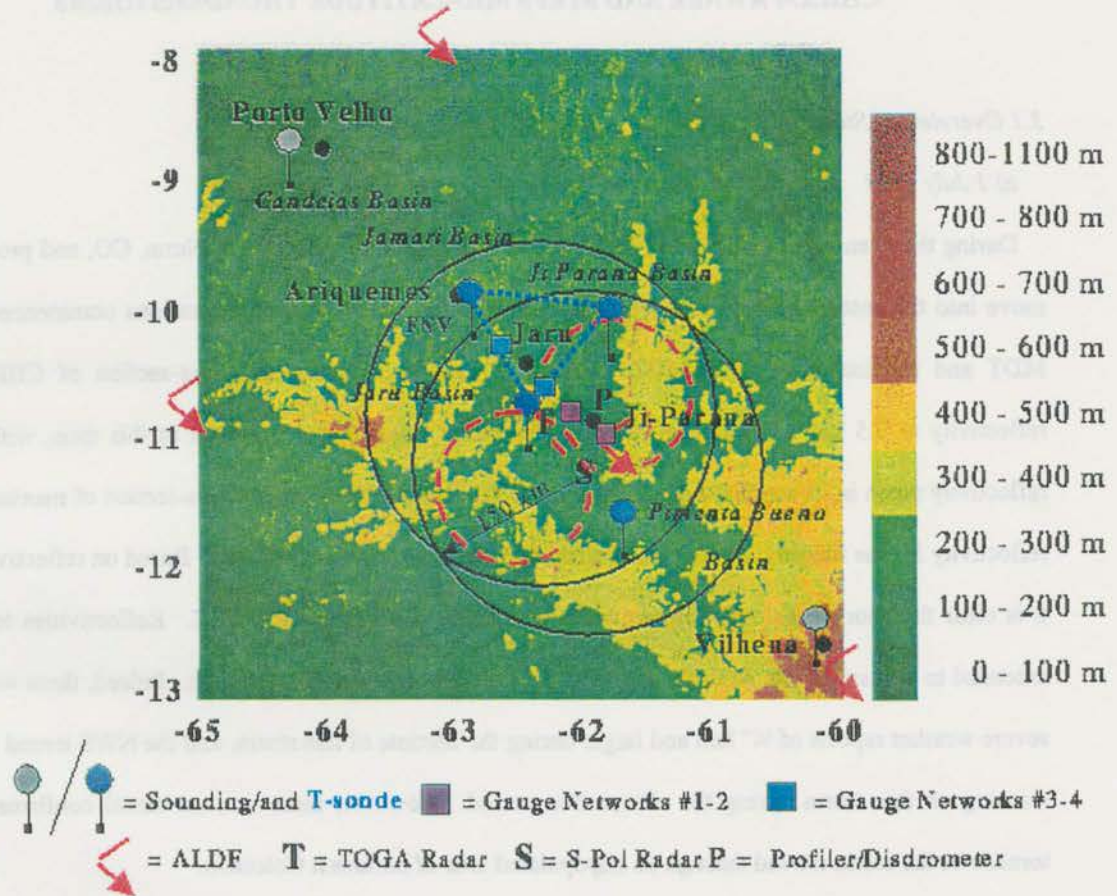


Figure 2.3: Schematic map of the TRMM/LBA operational area. Shown are the locations of the radars (SPOL and TOGA), sounding site, rain gauge networks, ALDF sensors, and profiler. Also shown are nearby cities and geographical regions. Topography is color-coded. Black circles show the maximum ranges of both radars. The red dashed circles show the dual-Doppler lobes (map courtesy of Dr. W. Petersen).

## CHAPTER 3

### CHILL-PAWNEE AND STEPS MID-LATITUDE THUNDERSTORMS

#### *3.1 Overview of Storms*

##### *a) 1 July 1998*

During the evening of 1 July 1998 (MDT), a severe hailstorm passed near Nunn, CO, and proceeded to move into the eastern CHILL-Pawnee dual-Doppler lobe. Dual-Doppler operations commenced at 1838 MDT and terminated at 2030 MDT. Figure 3.1 shows a horizontal cross-section of CHILL radar reflectivity at 0.5 km AGL at 1850 MDT. The storm resembled a supercell at this time, with a weak reflectivity notch in its southeast quadrant. Figure 3.2 shows a time-height cross-section of maximum radar reflectivity for the roughly 2-hour period when this storm was studied in detail. Based on reflectivity alone, it is clear this storm was very intense, with reflectivity peaking over 70 dBZ. Reflectivities to 60 dBZ extended to at least 10 km AGL for a substantial portion of the storm's lifetime. Indeed, there were a few severe weather reports of  $\frac{3}{4}$ " hail and larger during the lifetime of this storm, and the NWS issued a tornado warning on this storm during the observation period. However, there was no visual confirmation of a tornado as the storm moved through an unpopulated area of northeast Colorado.

Figure 3.3 shows a time-height cross-section of peak updraft, as determined by the dual-Doppler syntheses. For the early period of the storm, maximum updrafts were in excess of  $30 \text{ m s}^{-1}$ , peaking at times to  $40 \text{ m s}^{-1}$  or more. After 1940 MDT the storm was poorly positioned for dual-Doppler geometry and therefore vertical velocities should be interpreted with caution.

Figure 3.4 shows the volume of the storm containing updraft speeds within various increments as a function of time. While the vast majority of the updraft portion of the storm contained fairly moderate updrafts (less than  $10 \text{ m s}^{-1}$ ), a substantial volume contained significantly stronger velocities. In fact, over

100 km<sup>3</sup> of the storm contained updrafts in excess of 30 m s<sup>-1</sup> during the early phase, with over 300 km<sup>3</sup> of the storm containing W between 20 and 30 m s<sup>-1</sup>.

Figure 3.5 shows rain area and rain mass flux at 0.5 km AGL for this storm as functions of time. Moderate (20-60 mm h<sup>-1</sup>) rain covered 300-500 km<sup>2</sup> for essentially all of the analysis period. Heavy (greater than 60 mm h<sup>-1</sup>) rain covered on the order of 100 km<sup>2</sup> for most of the same period. Rain mass flux generally varied within 6-10 · 10<sup>6</sup> kg s<sup>-1</sup>, which is substantial especially when compared to intense Colorado storms studied by Lang (1997) as well as Carey and Rutledge (1998). Note mass flux contains a contribution from light (less than 20 mm h<sup>-1</sup>) rain as well. Figure 3.6 is the same as Figure 3.5 except for hail, and with no distinction between different hailfall intensities. Hail area generally varied between 50 and 150 km<sup>2</sup>, with hail flux varying between 1 and 4.5 · 10<sup>5</sup> kg s<sup>-1</sup>. These values also are substantial compared to previous precipitation area and mass flux studies (Lang 1997; Carey and Rutledge 1998).

Figure 3.7 shows positive and negative CG flash rates as functions of time for the 1 July 1998 storm. Peak total CG flash rates (mostly made up of negative CGs) were approximately 20 per 10-minute period, or 2 min<sup>-1</sup>. These peaks occurred during 1840-1850 MDT and 1920-1940 MDT. Otherwise, CG flash rates were substantially lower, well under 1 min<sup>-1</sup>. This especially was true between 1850 and 1920 MDT, representing a substantial portion of the storm's intense early phase. During these times positive CGs were ~50% of total CGs, although their absolute rates were very low. Moreover, even during peak CG times like 1920-1940 MDT, most of these CGs were associated with weaker ancillary convection, not the main storm. This point is illustrated in Figure 3.8, which shows a horizontal cross-section of radar reflectivity from the 1925 MDT volume of the CHILL radar at 0.5 km AGL, along with ground strike positions and polarities of NLDN-detected CGs that occurred between 1920 and 1930 MDT. The main cell was fairly devoid of CGs, whereas the ancillary echo contained most of the CGs. This pattern was repeated during other peak CG times. At best this storm had a peak CG flash rate comparable to average CG flash rates from other storms (e.g., Peckham et al. 1984). Thus, the main storm is identified as a low-CG storm. The percentage of positive CGs in the main storm is higher than normal (~50%) but this was accomplished mostly through a reduction of negative CGs, not any significant increase in positive ground flashes.

Unfortunately, only the CHILL FCM (field change meter) was operated during this storm, and the storm was a fair distance away from CHILL (~40 km or more). Moreover, the CHILL FCM suffered from a

noise source that plagued it during the entire summer of 1998. Thus, the FCM detected typically less than one flash per minute, which is anomalously low compared to other storms of this caliber (e.g., Lang et al. 2000). Due to the quality of the data, no quantitative inferences about total flash rate can be made about this storm. However, it is suspected that this storm adhered to the standard severe storm pattern of total flash rates well in excess of  $15 \text{ min}^{-1}$ .

In summary, the storm of 1 July 1998 was a severe low-CG supercell that featured an intense radar reflectivity structure, updrafts in excess of  $40 \text{ m s}^{-1}$ , and substantial rain and hail. It remains one of the most intense storms ever observed by CHILL, and was one of the strongest storms examined in this study.

#### *b) 15 July 1998*

On 15 July 1998, a line of convective cells developed and moved into the eastern dual-Doppler lobe. The system developed into a small but intense squall line, with leading convection and trailing stratiform precipitation. Dual-Doppler operations commenced at 1728 MDT and terminated at 1952 MDT after most of the convective line had moved out of the eastern lobe. Figure 3.9 shows a horizontal cross-section of CHILL radar reflectivity at 0.5 km AGL at 1804 MDT. Note that the radars had a difficult time scanning the entire storm, evidenced by truncated reflectivities along 60 km north of CHILL. This was true throughout the analysis period, as the storm was very large. Figure 3.10 shows a time-height cross-section of maximum radar reflectivity for the roughly 2.5-hour analysis period of this storm. Like 1 July 1998, this storm was very intense, with 60 dBZ and greater up to 10 km AGL at times, following a rapid intensification of the storm immediately prior to 1800 MDT. There were a few severe weather reports of  $\frac{3}{4}$ " hail and larger during the lifetime of this storm, as well as wind gusts over 50 knots.

Figure 3.11 shows a time-height cross-section of peak updraft, as determined by the dual-Doppler syntheses. For nearly the entire first half of the analysis period, maximum updrafts exceeded  $30 \text{ m s}^{-1}$  and at times greater than  $40 \text{ m s}^{-1}$ , much like the 1 July storm. There are two such peaks of  $> 30 \text{ m s}^{-1}$ , separated by a short interlude of weaker updrafts. After 1840 MDT the storm became less well positioned in the eastern lobe and reasonable dual-Doppler coverage was not possible.

Figure 3.12 shows the volume of the 15 July 1998 storm containing updraft speeds within various bins as a function of time. The vast majority of the updraft portion of the storm contained fairly moderate updrafts

(less than  $10 \text{ m s}^{-1}$ ), in fact well over  $10,000 \text{ km}^3$ . This number is so much larger than the number from 1 July because the storm is so much larger than 1 July. But again, like 1 July, a substantial volume contained significantly stronger velocities. At times, specifically right after 1800 MDT and around 1830 MDT, up to  $100 \text{ km}^3$  of the storm contained updrafts in excess of  $30 \text{ m s}^{-1}$ , with up to  $800 \text{ km}^3$  of the storm containing updrafts between 20 and  $30 \text{ m s}^{-1}$ . In general, the volume numbers are as large or larger than those for the 1 July 1998 storm, reflecting the 15 July 1998 storm's massive size and squall line nature.

Figure 3.13 shows rain area and rain mass flux at 0.5 km AGL for this storm as functions of time. During the early phase, moderate rain covered  $300\text{-}500 \text{ km}^2$ . These numbers grew larger toward the end of the analysis period as the trailing stratiform precipitation area increased in both size and intensity. Heavy rain covered up to  $200 \text{ km}^2$  for most of the early period, and tracked the moderate rain values during the later stage of the storm. Rain mass flux generally varied up to  $10 \cdot 10^6 \text{ kg s}^{-1}$  during this early period, comparable to 1 July 1998. It then grew to values over  $20 \cdot 10^6 \text{ kg s}^{-1}$  as the stratiform region developed and matured. Figure 3.14 is the same as Figure 3.13 except for hail. Hail area varied near  $50 \text{ km}^2$ , with hail flux tracking it near between  $5 \cdot 10^5 \text{ kg s}^{-1}$ . Both blossomed to much larger values as the storm grew in size during its later periods. Note especially the rapid growth beginning near 1800 MDT, around the same time the reflectivity and updraft significantly intensified. Around this time, the storm was very comparable to 1 July in terms of hail production, if it was not producing more hail.

Figure 3.15 shows positive and negative CG flash rates as functions of time for the 15 July 1998 storm. Here the most significant difference between 1 and 15 July manifests itself. From 1750 to 1820 MDT, the positive CG flash rate for this storm averaged near  $4 \text{ min}^{-1}$ , with negative CG flash rate a more modest  $1 \text{ min}^{-1}$  or less. Both CG flash rates generally declined to lower values later, with a total CG flash rate between 1 and  $2 \text{ min}^{-1}$  for the rest of the analysis period. While these values are near average relative to more ordinary convection (e.g., Peckham et al. 1984), considering the significant size of the storm it is surprising that flash rates were not higher during these later periods. These results suggest that the storm at this time was a low-CG producer. The 30-minute spike in positive CGs coincides well with the major intensification that occurred near 1800 MDT, and suggests that the 15 July 1998 had PPCG (predominantly positive CG producing) characteristics during the early portion of its lifetime.

Figure 3.16a shows a horizontal cross-section of radar reflectivity from 1804 MDT at 0.5 km AGL, along with ground strike positions and polarities of NLDN-detected CGs that occurred between 1800 and 1810 MDT. Notice how most of the positive CGs are clustered near the northeastern portion of the line (at least the part that was scanned), while the lower-reflectivity weaker southern cells are essentially devoid of CGs. Figure 3.16b shows the same except for the radar volume at 1840 MDT and CGs during 1840-1850 MDT. While the main cell appeared to be as intense as before, the CG flash rate, in particular the positive CG flash rate, had dropped considerably.

The Pawnee FCM was operated during this storm, and it appeared to show nearly continuous flash activity, with estimated total flash rates near 1 per second. However, this activity continued even as the storm moved out of the 40-km nominal range of the instrument after 1800 MDT. It is not likely that the FCM could have detected such distant flashes. Wind and rain at the FCM site may have contributed to this noisiness. Given the intensity of the storm compared to other storms for which total flash rates are available (e.g., Lang et al. 2000), a flash rate near 1 per second is not unreasonable, but given the quality of the data this estimate needs to be viewed with caution.

In summary, the storm of 15 July 1998 was a severe squall line that featured both low-CG and PPCG characteristics, depending on which time and which particular cells were observed. The storm featured an intense radar reflectivity structure, updrafts in excess of  $40 \text{ m s}^{-1}$ , and substantial rain and hail. Along with 1 July 1998 this storm ranks near the top of the intensity scale of the cases in this study.

#### *c) 21 July 1998*

Compared to the previous two storms, the storm of 21 July 1998 was weaker, yet it was a significant hailstorm that developed in the west lobe near the town of Wellington, CO. Dual-Doppler operations commenced at 1439 MDT and terminated at 1621 MDT. Figure 3.17 shows a horizontal cross-section of CHILL radar reflectivity at 0.5 km AGL at 1531 MDT. Figure 3.18 shows a time-height cross-section of maximum radar reflectivity for the roughly 2-hour analysis period of this storm. The storm featured peak reflectivities over 60 dBZ, plus 50 dBZ over 8 km AGL. However, this storm is clearly not of the same magnitude as the previous two storms examined. There were no severe weather reports for the analysis period of this storm.

Figure 3.19 shows a time-height cross-section of peak updraft, as determined by the dual-Doppler syntheses. This figure solidifies the second-tier status of the storm, with a peak updraft of just over  $15 \text{ m s}^{-1}$  occurring several times during the storm's lifetime.

Figure 3.20 shows the volume of the storm containing updraft speeds within various bins as a function of time. Like the first two storms, the vast majority of the updraft portion of the storm contained moderate updrafts (less than  $10 \text{ m s}^{-1}$ ), but only 200-300  $\text{km}^3$  contained updrafts in excess of  $10 \text{ m s}^{-1}$  at peak.

However, Figure 3.21 shows that the rain area and rain mass flux at 0.5 km AGL for the 21 July 1998 storm compared favorably to the previous two storms. Moderate rain typically covered 400-600  $\text{km}^2$ , with heavy rain usually covering 100-200  $\text{km}^2$ . Rain mass flux was on the order of  $10 \cdot 10^6 \text{ kg s}^{-1}$ . Figure 3.22 shows that hail area was highly variable and typically less than 20  $\text{km}^2$ , with hail flux under  $4 \cdot 10^4 \text{ kg s}^{-1}$  and also highly variable. Thus, while the storm produced comparable rain, its hail production lagged that of the 1 and 15 July cases.

Figure 3.23 depicts positive and negative CG flash rates as functions of time for the 21 July 1998 storm. Here, the difference between the previous low-CG/PPCG storms and lesser convection is shown in stark contrast. Positive CG flash rates were negligible when compared to negative CG flash rates, which were generally over  $10 \text{ min}^{-1}$  and peaked near  $20 \text{ min}^{-1}$  around 1510 MDT. The average negative CG flash rate from this storm is substantially larger than the peak total CG flash rates from the previous two storms. In fact, this storm produced CGs at a rate well above the average for typical storms (e.g., Peckham et al. 1984), much less low-CG ones.

Figure 3.24 shows a horizontal cross-section of radar reflectivity from the 1516 MDT volume of the CHILL radar at 0.5 km AGL, along with ground strike positions and polarities of NLDN-detected CGs that occurred between 1509 and 1519 MDT. CGs occurred throughout the region of the storm, except for a weaker cell to the extreme northwest.

The Christman Field FCM was operated during this storm from 1515 to 1630 MDT. Figure 3.25 shows total flash rate as a function of time. The best estimates were during the early part of the FCM coverage, when the storm was closer to the FCM. Total flash rates were at best  $2\text{-}3 \text{ min}^{-1}$ , which is significantly less than the total CG flash rate during the same time period. This shows how limited the FCMs were at detecting flashes. They clearly were not detecting even the majority of CGs, much less ICs. Based on the

FCM and NLDN data, a reasonable guess is that, at least during 1515-1530 MDT when the storm was closest to the Christman Field FCM, the IC flash rate was fairly low relative to the CG flash rate, with an IC:CG ratio near 1:1, if not less.

In summary, the storm of 21 July 1998 was a significant hailstorm that featured a fairly intense radar reflectivity structure, updrafts in excess of  $15 \text{ m s}^{-1}$ , heavy rain, and moderate amounts of hail. The storm produced negative CGs almost exclusively, at a rate well above the average for typical storms from past studies. Total flash rate was fairly modest and the IC:CG ratio probably was fairly low, if not less than 1:1. The 21 July 1998 storm was clearly a tier or two below the intensity of the 1 and 15 July storms.

#### *d) 25 July 1998*

The storm of 25 July 1998 was a significant multicell storm that passed through the eastern dual-Doppler lobe. Dual-Doppler operations commenced at 1540 MDT and terminated at 1710 MDT. Figure 3.26 shows a horizontal cross-section of CHILL radar reflectivity at 0.5 km AGL at 1625 MDT. Obviously, the term "multicell" is used loosely. The 25 July storm perhaps is described best as a collection of cells, some related and some not, which populated the eastern lobe for about an hour and a half. Figure 3.27 shows a time-height cross-section of maximum radar reflectivity for the roughly 1.5-hour analysis period of this storm. The storm is comparable to 21 July, with peak reflectivity over 60 dBZ, and 50 dBZ up to 8 km AGL. No severe weather reports were recorded for the analysis period of this storm.

Figure 3.28 shows a time-height cross-section of peak updraft, as determined by the dual-Doppler syntheses. During the early part of the analysis period, the Pawnee radar failed to top the strongest cells, and thus estimates of peak updrafts were poor. Once the storm was topped, after 1600 MDT, strong updrafts were evident with two peaks of greater than  $25 \text{ m s}^{-1}$ . Recall that, since this storm really was just a collection of cells, this figure is just showing the impact of the strongest cells. Overall, peak updrafts were stronger than 21 July but not as strong as 1 and 15 July.

Figure 3.29 shows the volume of the storm containing updraft speeds within various bins as a function of time. Once again, the vast majority of the updraft portion of the storm contained moderate updrafts (less than  $10 \text{ m s}^{-1}$ ), but at peak approximately  $150 \text{ km}^3$  contained updrafts in excess of  $20 \text{ m s}^{-1}$ . Thus, updraft volumes were larger than 21 July.

Figure 3.30 shows that the 25 July rain area and rain mass flux at 0.5 km AGL were comparable to previous storms. Moderate rain typically covered 300-700 km<sup>2</sup>, with heavy rain covering about 50-200 km<sup>2</sup>. Once again, rain mass flux was on the order of  $10 \cdot 10^6$  kg s<sup>-1</sup>. Figure 3.31 shows highly variable hail area, ranging from about 5 to 45 km<sup>2</sup>. Hail flux varied up to  $4.5 \cdot 10^4$  kg s<sup>-1</sup>. Thus, the 25 July storm produced comparable rain to the previous three storms. Its hail production lagged that of 1 and 15 July but was slightly larger than that of 21 July.

Figure 3.32 shows positive and negative CG flash rates as functions of time for the 25 July 1998 storm. Like 21 July, positive CG flash rates were fairly low, but negative CG flash rates were more modest than 21 July, though still higher than 1 and 15 July. Negative CG flash rate varied near 2 min<sup>-1</sup>, peaking near 10 min<sup>-1</sup> around 1640 MDT. These rates were very close to reported CG flash rates from the past studies mentioned above, although they are storm total so any particular cell featured fewer CGs.

Figure 3.33 depicts a horizontal cross-section of radar reflectivity from the 1640 MDT volume of the CHILL radar at 0.5 km AGL, along with ground strike positions and polarities of NLDN-detected CGs that occurred between 1640 and 1650 MDT. Most of the significant cells produced substantial numbers of negative CGs, except for the cell to the extreme southwest.

The CHILL FCM was operated during this storm from 1535 to 1655 MDT. Figure 3.34 shows total flash rate as a function of time. The best estimates were during 1600-1645 MDT, as some cells moved closest to the CHILL. Total flash rates were 8 min<sup>-1</sup> at peak (1610 MDT), and unlike 21 July this value exceeded the CG flash rate at this time, which was near 2 min<sup>-1</sup>, yielding an IC flash rate of 6 min<sup>-1</sup>. Hence, the IC:CG ratio around 1610 MDT was about 3:1, in line with previous estimates of IC:CG ratio for typical convection (e.g., Price and Rind 1993). Of course, this would be a lower bound, since not every cell that was producing CGs at this time was within range of the CHILL FCM. Because of this, the true IC:CG ratio (and IC flash rate) likely was higher than 3:1.

In summary, the storm of 25 July 1998 was collection of cells that featured a fairly intense radar reflectivity structure, peak updrafts in excess of 25 m s<sup>-1</sup> at peak, heavy rain, and moderate amounts of hail. The storm produced CGs in line with the average for typical storms from past studies. Total flash rate was fairly modest and the IC:CG ratio probably was comparable to other typical convective storms. The 25

July 1998 storm was not as intense as the 1 and 15 July storms, and perhaps was slightly more intense than the 21 July storm, at least in terms of peak updraft.

*e) 30 July 1998*

The storm of 30 July 1998 was a shallow monsoonal-like storm that developed in the western lobe. Dual-Doppler operations commenced at 1712 MDT and terminated at 1818 MDT. Figure 3.35 shows a horizontal cross-section of CHILL radar reflectivity and horizontal dual-Doppler wind vectors at 0.5 km AGL at 1716 MDT. Figure 3.36 shows a time-height cross-section of maximum radar reflectivity for the roughly 1-hour analysis period of this storm. The storm is clearly very weak when compared to the previous storms, with peak reflectivity barely over 50 dBZ, and 10 dBZ just exceeding 10 km AGL. No severe weather reports were recorded for the analysis period of this storm.

Figure 3.37 shows a time-height cross-section of peak updraft, as determined by the dual-Doppler syntheses. Peak updrafts exceeded  $10 \text{ m s}^{-1}$  only during the early portion of the analysis period. Figure 3.38 shows the volume of the storm containing updraft speeds within various bins as a function of time. Most of the updraft portion of the storm barely exceeded  $5 \text{ m s}^{-1}$ .

Figure 3.39 depicts the rain area and rain mass flux at 0.5 km AGL for the 30 July 1998. Although values were a bit lower than the previous storms, they are generally within a factor of two. Moderate rain typically covered 300-500  $\text{km}^2$ , with heavy rain covering less than 100  $\text{km}^2$ . Rain mass flux varied between 5 and  $10 \cdot 10^6 \text{ kg s}^{-1}$ . The storm did not produce significant quantities of hail. Therefore, hail area and hail flux are not shown. Thus, while the storm produced less rain than the previous storms, its production was not too different (i.e., within a factor of two at worst). However, hail production was negligible.

During the analysis period, the storm produced only two CGs, both of which occurred during the period 1715-1720 MDT. Both were positive CGs with peak currents in excess of 10 kA. The Christman Field FCM was in range of the storm, and was operated during the analysis period. It detected three flashes total, two during 1730-1735 MDT, and one during 1735-1740 MDT. The Christman FCM did not detect the NLDN CGs. The three detected flashes likely were ICs.

In summary, the storm of 30 July 1998 was a weakly electrified monsoonal storm with a shallow radar reflectivity structure, updrafts generally less than  $10 \text{ m s}^{-1}$ , a fair amount of heavy rain, and negligible hail. The storm produced very little lightning in general. The 30 July 1998 storm was the least intense storm examined in this study, and it serves as the study's electrical "null" case.

*f) 29 June 2000*

On 29 June 2000, a severe supercell moved through the eastern STEPS dual-Doppler lobe and was scanned by the CSU-CHILL and SPOL radars. Dual-Doppler observations lasted for a few hours, but in this study only the one-hour period from 2259 to 2357 UTC (MDT equals UTC minus 6 hours) was analyzed. Around the midpoint of this time period, 2330 UTC, the storm produced a tornado. Figure 3.40 shows a horizontal cross-section of CHILL radar reflectivity at 2325 UTC, near the time the storm became tornadic. Figure 3.41 shows a time-height cross-section of maximum radar reflectivity for the analysis period of this storm. Prior to 2330, the storm was intense, with 50 dBZ up to 10 km AGL. However, after this time the storm intensified rapidly, with 60 dBZ reaching  $\geq 10 \text{ km AGL}$ . This clearly put the storm into a class with 1 and 15 July 1998, based on reflectivity alone.

Figure 3.42 shows a time-height cross-section of peak updraft, as determined by the dual-Doppler syntheses. The most notable feature in this plot is the fact that the peak updraft exceeded  $50 \text{ m s}^{-1}$  near the time of the tornado. Prior to the tornado, maximum updrafts generally were in excess of  $30 \text{ m s}^{-1}$  and at times exceeded  $40 \text{ m s}^{-1}$ . After 2330 UTC, storm updrafts weakened somewhat before re-intensifying to over  $40 \text{ m s}^{-1}$  again toward the end of the analysis period. These vertical velocities exceeded the highest values that even the intense 1 and 15 July storms produced.

Figure 3.43 shows the volume of the 29 June 2000 storm containing updraft speeds within various bins as a function of time. Values tended to rise with time as the storm intensified. Well over  $2 \cdot 10^4 \text{ km}^3$  of the updraft portion of the storm contained fairly moderate updrafts (less than  $10 \text{ m s}^{-1}$ ). This number exceeds even the gargantuan 15 July 1998 storm. Moreover, after the 2330 intensification,  $200 \text{ km}^3$  or more of the storm contained updrafts in excess of  $30 \text{ m s}^{-1}$ , with around  $800 \text{ km}^3$  of the storm containing updrafts between 20 and  $30 \text{ m s}^{-1}$ . Thus, particularly at the high end, this storm contained a greater volume of 20+

$\text{m s}^{-1}$  updraft than either 1 or 15 July. However, prior to the intensification, such updrafts were seen in more modest volumes.

Figure 3.44 shows rain area and rain mass flux at 0.5 km AGL for this storm as functions of time. Here, the storm's intensification manifested itself once again. Prior to 2330, moderate rain covered 300-500  $\text{km}^2$  but its area grew larger as the storm intensified. Heavy rain started off covering less than 100  $\text{km}^2$  but later grew to nearly 400  $\text{km}^2$ . Likewise, rain mass flux started below  $10 \cdot 10^6 \text{ kg s}^{-1}$  during this early period, and then grew to over  $20 \cdot 10^6 \text{ kg s}^{-1}$  as the storm intensified. Thus, this storm produced comparable or more rainfall when compared the other mid-latitude storms. Figure 3.45 is the same as Figure 3.44 except for hail. Interestingly enough, the storm was producing a much larger area of hail than heavy rain at the start of the analysis period, in fact over 200  $\text{km}^2$ . This area declined a bit before growing to over 300  $\text{km}^2$  after 2330. Hail flux followed this decline-and-recover behavior, growing to over 1 million  $\text{kg s}^{-1}$  near the end. This storm's hail production falls between that of 1 and 15 July.

Figure 3.46 shows positive and negative CG flash rates with time. During the early period CGs were almost non-existent, but the positive CG flash rate began increasing at 2310 UTC, reaching a peak of just over  $2 \text{ min}^{-1}$  at 2340. The negative CG flash rate was variable but never exceeded 5 in a 10-minute period. Once again, it appears that the 2330 time marks a transition in the storm, from low-CG prior to more PPCG-like later.

Figure 3.47 shows a horizontal cross-section of radar reflectivity from the 2343 UTC volume of the CHILL radar at 0.5 km AGL, along with ground strike positions and polarities of NLDN-detected CGs that occurred between 2340 and 2350 UTC. All CGs were positive, and were clustered around the main cell. Weaker convection to the northeast featured no CGs.

The STEPS LMA was operated during this storm, but only 2 minutes of data, centered near 2324 UTC, are analyzed in this study. This time is near the time of maximum updraft as well as the time of the tornado. Figure 3.48 shows VHF signals from this storm that were detected by the LMA. The top panel plots signals as a function of time and height. Although activity was basically continuous, these signals tended to be grouped into short bursts that represent the major flashes within the storm. Just by subjectively counting these short bursts a total flash rate of over  $30 \text{ min}^{-1}$ , which is very high, can be estimated roughly. The lower left panel shows a plan view of the signals that occurred during the 2-minute

period. The main storm is in the western half of the domain, with a minor cell (corresponding to the closest northeast cell in Figure 3.47) that produced fewer signals to the northeast. This northeast cell produced very few CGs overall, and based on this two-minute period of data it appears that it wasn't particularly electrified in general. In the main storm, VHF signals from lightning filled a substantial area, but with a distinctive hole, which corresponds to the location of the main updraft. The panels immediately above and to the right of the plan view show projections of the data onto vertical planes in the east-west and north-south directions, respectively. Most signals occurred above 5 km, which is not surprising since according to the NLDN no CGs occurred during this time period. The final panel (center-right) of Figure 3.48 shows an altitude histogram of all the signals that occurred during the 2-minute period. Most of the VHF signals were clustered near 10 km, indicative of IC lightning.

In summary, the storm of 29 June 2000 was a tornadic supercell that featured low-CG characteristics in early on in the analysis period, and then more PPCG characteristics later. The storm featured an intense radar reflectivity structure, updrafts in excess of  $50 \text{ m s}^{-1}$ , and substantial rain and hail. What little total flash rate data are available suggest near-continuous flashing within the storm. Overall, this storm compares favorably to 1 and 15 July 1998 in terms of intensity.

#### *g) Summary*

To summarize the results of this section, the storm of 1 July 98 was a low-CG severe supercell. The 15 July 98 storm was a PPCG/low-CG severe squall line. The storms of 21 and 25 July 98 were indicative of more typical High Plains convection, and featured average to high negative CG flash rates, with very few positive CGs. The 30 July 98 storm was a weakly electrified monsoonal storm, and the 29 June 2000 storm was a low-CG/PPCG tornadic supercell.

Table 3.1 summarizes some of the key observations from this set of storms. The storms of 1 and 15 July were by far the most intense storms of the CHILL-Pawnee set by virtually any measure – reflectivity structure, strongest drafts, largest hail production, etc. Based on the results presented so far, 15 July 1998 had larger peak volumes of significant updrafts, although 1 July 1998 had a larger peak vertical velocity. The 15 July 1998 storm also produced larger amounts of rain and hail. This is interesting to note, since the 15 July 1998 storm had a much larger peak positive CG flash rate than 1 July. Another interesting thing to

point out is that the 15 July 1998 storm was not necessarily more intense than 1 July (in terms of peak reflectivity, peak height of the 30 dBZ contour, peak updraft; i.e., the non-area -and non-volume-based measures), just larger.

The 29 June 2000 storm from STEPS had larger volumes of significant updrafts than either 1 or 15 July 1998 (particularly 1 July), but its rain production (in terms of heavy rain area and rain mass flux) was comparable to 15 July, and it had a smaller peak hail area than 15 July. The peak vertical velocity on 29 June 2000 was larger than any other mid-latitude storm, although not significantly larger than that of 1 July 1998 considering the 10-20% error expected in vertical velocity measurements. The 29 June 2000 storm produced very few negative CGs, but it had a peak positive CG flash rate that fell between the 1 and 15 July 1998 storms. Thus, 29 June 2000 was the largest of the most intense storms, but not necessarily that much stronger (in terms of, say, peak vertical velocity) than the other two.

The 21 and 25 July cases were less intense than the severe storms (1 and 15 July 1998, 29 June 2000) by just about every measure, but produced far more negative CGs. In particular the 21 July storm produced negative CG flashes at a consistent rate that was well above average, and it was less intense overall than 25 July 1998, which had CG flash rates that were very typical of ordinary convection. Interestingly, however, both 21 and 25 July 1998 produced more rain than the 1 July 1998 low-CG storm. The monsoonal storm of 30 July was the least intense of the set and also had the lowest lightning output, with very few CGs or ICs.

### *3.2 Comparison of Storm Environments*

Table 3.2 shows convective available potential energy (CAPE) and wind shear for each of the dates in this study. For the CHILL-Pawnee cases, NWS soundings from Denver were used to calculate these values. If it was available and complete, the afternoon (0000 UTC, 1800 MDT) sounding was used since this was nearest to the convective initiation times. However, complete afternoon soundings were not available for 15 and 25 July, and thus morning (1200 UTC, 0600 MDT) soundings were used instead for those days. A mobile GLASS sounding system was available for the STEPS case, and a sounding taken at 2022 UTC on 29 June 2000 was used since it was closest to the convection in time, while also immediately preceding it.

The first column in Table 3.2 shows a straight calculation of CAPE for all dates, assuming no mixed layer and based on irreversible processes. That is, simply the positive area of the sounding, starting with a surface air parcel. The 1 July 1998 sounding featured over  $1500 \text{ J kg}^{-1}$  in CAPE, which is enough for moderate convection (Bluestein 1993, chapter 3) but is a bit low considering the strength of the convection on that day. The 15 July 1998 sounding featured no CAPE at all, and 21 July had just  $28.4 \text{ J kg}^{-1}$ . These values are too low considering both days, in particular 15 July, featured intense convection. However, recall that 15 July only had a morning sounding. The 21 July 1998 sounding, taken at 1800 MDT, is well past the time that convection occurred that day, as storms started in the early afternoon along the Front Range. Thus, these two soundings were not entirely representative of the immediate pre-storm environments. The 25 July 1998 sounding contained approximately  $470 \text{ J kg}^{-1}$  of CAPE, which normally should only be enough for at least weak convection. However, recall that the 25 July 1998 sounding was taken in the morning. The 30 July sounding contained about  $510 \text{ J kg}^{-1}$  of CAPE, which is enough for weak convection, which is precisely what occurred on that day. The 29 June 2000 M-GLASS sounding was of better quality than the NWS soundings, in that it featured far more data points, and thus a more accurate estimate of CAPE. From this sounding the CAPE was estimated to be over  $2000 \text{ J kg}^{-1}$ , which is certainly sufficient for intense convection.

Since the initial estimates of CAPE were so poor, some soundings were adjusted and the resulting values are shown in the second column of Table 3.2. The morning soundings on 15 and 25 July were adjusted to include known surface temperatures and dewpoints from the afternoon. In the case of 15 July, the surface temperature and dewpoint from the time of maximum heating in the afternoon was used. The rest of the temperature and dewpoint values in the layer below 700 mb were adjusted to reflect these changes. Temperatures were adjusted to form a roughly dry adiabatic lapse rate in this layer, with mixing ratio roughly conserved. These changes resulted in an increase of CAPE to over  $2000 \text{ J kg}^{-1}$ , which is far more in line with the convection observed that day.

The 21 July sounding contained a small inversion in the sub-700 mb layer, which was one cause of the low CAPE. This inversion was removed by making a roughly linear decrease in temperature between the surface and 700 mb. The resulting CAPE was nearly  $800 \text{ J kg}^{-1}$ , which still seems a bit low considering the convection on this day.

In the case of 25 July, there was a partial sounding in the afternoon which contained information below 700 mb in height. This afternoon information was used instead of the morning information in the lowest layer of the atmosphere, resulting in a significant increase in CAPE, to over 2700 J kg<sup>-1</sup>. This is very high considering the intensity of convection on that day.

The third column in Table 3.2 shows predicted CAPEs for the CHILL-Pawnee cases from the Colorado State University RAMS forecast model. These were 24-hour forecasts from the previous day's 0000 UTC run, valid the same time that the afternoon NWS soundings were. With the exception of 30 July 1998, all of the soundings were extracted from the gridpoint that corresponded to 40.40 degrees north and 104.54 degrees west, which is very close the location of the CSU-CHILL radar. The 30 July 1998 forecast predicted rain at 0000 UTC at this gridpoint, so a dry gridpoint slightly northeast of this location was used instead (40.61 °N, 104.25 °W).

RAMS predicted nearly 2000 J kg<sup>-1</sup> of CAPE for 1 July 1998, which is more than the Denver NWS sounding observed. However, this predicted CAPE is more in line with the strength of the convection observed that day. By contrast, RAMS predicted lower CAPE on 15 July 1998, approximately 1400 J kg<sup>-1</sup>, than what the adjusted NWS sounding from that day contained. However, the RAMS sounding was certainly more in line with the convection observed that day than the unadjusted NWS sounding, which had no energy. RAMS predicted about 1000 J kg<sup>-1</sup> on 21 July 1998, which is more reasonable than the lower CAPEs seen in the adjusted and unadjusted NWS soundings that day. RAMS predicted over 2200 J kg<sup>-1</sup> of CAPE on 25 July 1998, which high considering that other days had more intense convection yet lower predicted CAPEs. However, this predicted CAPE is less than what the adjusted NWS sounding contained. On 30 July 1998, the RAMS prediction did not compare favorably with the observed convective strength, nor did it compare favorably to the NWS sounding from that day. The roughly 1500 J kg<sup>-1</sup> contained in the RAMS sounding seems too high compared to the shallowness of the convection on that day, particularly since the NWS sounding contained a more reasonable value of approximately 500 J kg<sup>-1</sup>. RAMS forecasts were not used for 29 June 2000 since higher quality sounding data were available on that day,

Overall, based on the adjusted and predicted CAPEs, the storms with the weakest updrafts (21 and 30 July) tended to feature the lowest CAPE values. Excepting 25 July 1998, the storms with the strongest updrafts (1 and 15 July, 29 June) featured the largest values of CAPE. However, CAPE observations did

not always correlate exactly to convective strength, so it is uncertain how much can be inferred from these particular soundings. In addition, using the formula,  $w_{\max} = \sqrt{2 * CAPE}$ , all of the adjusted CAPEs for each particular case give theoretical updraft speed maximums well in excess of what was observed.

Similar problems befell the shear calculations. The essence of the problem was that the NWS soundings reported too few data points. If just a couple of them were bad, the whole sounding was made nearly corrupt. Column 3 in Table 3.2 shows the magnitude of the shear vector between the surface and 400 mb, which is roughly 6 km AGL in Colorado. Thus, these values are basically the shear over the lowest 6 km, a value often used when predicting convective organization (Bluestein 1993, chapter 3). Again, morning soundings were used on 15 and 25 July 1998. The environment on 29 June 2000 featured the strongest shear, over  $20 \text{ m s}^{-1}$ , with 1 July 1998 second. Notably, 15 and 25 July 1998 featured very little shear, less than 21 July or even 30 July. However, perhaps upper level shear is important, since sheared anvils could expose upper positive charge to ground, enhancing positive CGs (the tilted dipole mechanism). Thus, the magnitude of the shear vector also was calculated between 400 and 200 mb. This is roughly between 6 and 11 km AGL. Column 4 in Table 3.2 displays these values. Once again, 29 June 2000 featured the most upper-level shear, followed surprisingly by 30 July, then 21, 15, 25, and finally 1 July. Note none of these shear calculations involved any pressure weighting.

Again, due to quality control issues, not too much should be inferred from these shear calculations. However, it is interesting to note that the two supercell storms (1 July and 29 June) featured the most low-level shear, and the two PPCG storms (15 July and 29 June 2000) had greater upper-level shear than the low-CG storm of 1 July. However, both 21 and 30 July had greater upper-level shear than 15 July, yet featured few positive CGs.

### *3.3 Vertical Structure*

To gain better insight into how each of the storms differed from one another, this study focused on 1-2 key periods in each storm's lifetime. One of those times was the time of a significant peak in updraft speed (if not the outright maximum updraft for the entire case). Radar volumes that corresponded to this time were 1850 MDT on 1 July 1998, 1804 MDT on 15 July 1998, 1531 MDT on 21 July 1998, 1625 MDT on 25 July 1998, 1716 MDT on 30 July 1998, and 2325 UTC on 29 June 2000.

One parameter of potential importance to thunderstorm electrification is vertical air mass flux, particularly positive (upward) vertical air mass flux. In essence, this is just the product of air density and positive vertical velocity. Vertical air mass flux is important since the greater mass of air flowing through a unit area in a unit time, the greater mass of condensate potentially available for collisions that cause electrical charging. Also, larger mass fluxes would provide for better maintenance of mixing ratios of precipitation-sized particles important for electrification, as well as more efficient gravitationally based charge separation after rebounding collisions. A final advantage of air mass flux is that it is easily calculated in atmospheric models and has relevance to mass budget calculations.

Figure 3.49a shows average positive vertical air mass flux as a function of height for each storm at their times of peak updraft. The 1 and 15 July 1998 storms, as well as 29 June 2000, clearly had greater fluxes than the other storms, particularly in the lower half of the storm volumes. The mixed phase region (defined as 0 to  $-40$  °C) generally spanned between 3 and 9 km AGL for all the storms, and here 1 and 15 July, as well as 29 June, generally exceeded the other storms' fluxes by a large margin (up to a factor of two), especially near the base of the mixed phase region. The 30 July storm had a larger positive flux than 21 or 25 July below the mixed phase region, but 21 and 25 July had larger positive fluxes within the mixed phase region itself. The 21 July 1998 storm had a somewhat larger flux in this region than 25 July, despite the fact that 25 July featured higher peak vertical velocities.

However, complicating the results from Figure 3.49a is the fact that the standard deviations of the vertical air mass fluxes (Figure 3.49b) typically were as large or larger than the means, for all storms. This is to be expected, though, since most updrafts were confined to relatively small cores, while the bulk of the ambient positive vertical velocities were more moderate ( $< 10 \text{ m s}^{-1}$ ). The 1 and 15 July storms, as well as 29 June, had significantly larger standard deviations than the other storms, reflecting the fact that they had stronger updrafts in those cores. Thus, it can be argued that they would have larger positive vertical air mass fluxes in their updraft cores, when compared to, say, 21 or 25 July.

The next set of figures show cumulative frequency by altitude diagrams (CFADs) of CHILL radar reflectivity and dual-Doppler-derived vertical velocity for these key times in each storm. These CFADs are a variation of the contoured frequency by altitude diagrams introduced by Yuter and Houze (1995). CFADs show the frequency of occurrence of a particular radar variable above a certain threshold at each

vertical grid level. For instance, a value of 10% for 30 dBZ reflectivity at 4.5 km AGL means that, at that level, 10% of the storm contained 30 dBZ or greater. CFADs give a better idea of storm intensity than just peak values. In the CFADs produced in this study, bin size was 2 dBZ for reflectivity, and was  $2 \text{ m s}^{-1}$  for vertical velocity. In the CFAD analyses, close attention was paid to the mixed phase region (0 to  $-40 \text{ }^\circ\text{C}$ ), a region where ice and water can coexist, conditions necessary for significant non-inductive charging (NIC). Significant precipitation in this region means more mass is available for collisions and thus electrical charging. Significant positive vertical velocity in this area means more throughput and a larger supply of supercooled liquid water, and thus more charging. For the mid-latitude cases the mixed phase region was roughly between 3 and 9 km AGL, as determined by soundings.

Figure 3.50 shows CFADs of CHILL radar reflectivity (Figure 3.50a) and dual-Doppler-derived vertical velocity (Figure 3.50b) for the 1 July storm at 1850 MDT. Figure 3.51 shows the same but for 15 July 1998 at 1804 MDT. Figure 3.52 shows the same for 21 July 1998 at 1531 MDT, and Figure 3.53 shows the same for 25 July 1998 at 1625 MDT. Figure 3.54 shows CFADs for 30 July 1998 at 1716 MDT, and Figure 3.55 shows CFADs for 29 June 2000 at 2325 UTC.

Depending on the level, approximately 2-5% of the 1 July 1998 storm contained reflectivity values of 50 dBZ or greater throughout the mixed phase region, and 15-25% of the storm contained 30 dBZ or greater. The 15 July 1998 storm compared more than favorably, with over 5% containing 50 dBZ or more and 25-35% containing 30 dBZ or greater in the same region. The vertical velocity frequencies for these storms were equally impressive, with 5% of the 1 July storm containing  $10 \text{ m s}^{-1}$  or greater updraft in the mixed phase region, and up to 1% containing  $30 \text{ m s}^{-1}$  or more. In the same region, the 15 July 1998 storm had up to 10% containing  $10 \text{ m s}^{-1}$  or greater, but generally less than 0.5% containing  $30 \text{ m s}^{-1}$  or more.

The 21 July 1998 storm had a weaker reflectivity structure, with less than 2% containing 50 dBZ and greater in the mixed phase region, although 10-25% still contained 30 dBZ and greater. Generally, less than 2% of the 21 July storm contained updraft of  $10 \text{ m s}^{-1}$  or larger in the same region. Mixed phase reflectivity in 25 July was highly variable, with anywhere from 2 to 25% of the grid levels containing 30 dBZ and greater, and 2% or less containing 50 dBZ and greater. The 25 July 1998 storm had up to 2% of its mixed phase volume with  $10 \text{ m s}^{-1}$  or larger updraft, but it had less than 0.5% containing  $20 \text{ m s}^{-1}$  or larger.

The 30 July 1998 storm was the weakest. Even at the 1716 MDT peak some grid levels in the mixed phase region failed to contain even 30 dBZ, with the lower grid levels having at best 15% with 30 dBZ or greater. No 50 dBZ contour existed in the mixed phase region. Very little, 0.1% or less, of the storm contained  $10 \text{ m s}^{-1}$  or larger updraft, and then only in the lowest part of the mixed phase region.

The 29 June 2000 storm showed similar characteristics to 1 and 15 July 1998 in the CFADs. Roughly 0.5 to 2% of the storm contained 50 dBZ or greater in the mixed phase region. This is a bit low compared to 1 and 15 July but recall this CFAD is from 2325 UTC, right before reflectivities intensified significantly. In the mixed phase region, 15-25% of the storm contained 30 dBZ or greater, comparable to the other storms. Over 5% of the 29 June storm contained updrafts in excess of  $10 \text{ m s}^{-1}$  in the critical mixed phase region. Roughly 1% contained  $20 \text{ m s}^{-1}$  or greater in the same part, and less than 0.5% contained  $30 \text{ m s}^{-1}$  or greater. These numbers compare favorably to those from 1 and 15 July.

With the exception of 30 July 1998, these CFADs were overall more intense than those presented for Florida thunderstorms by Yuter and Houze (1995). This was true whether considering peak values of reflectivity and vertical velocity at each altitude, and the percentage of the storm that contained high reflectivities and vertical velocities at each altitude.

The vertical structure of the storms was examined in still more detail. Figure 3.56a shows a vertical cross-section, at 16 km north of CHILL, of radar reflectivity, differential reflectivity, and updraft speeds for the 1 July 1998 storm at 1850 MDT. This is through the southern portion of the storm, co-located with the most intense updraft. Updrafts exceeded  $40 \text{ m s}^{-1}$ , with 50 dBZ extending above 10 km. A significant bounded weak echo region (BWER) was apparent in the vicinity of the updraft. Offset to the west of the updraft was the lower core region, with large raindrops as evidenced by co-located high  $Z_{dr}$ . A vertical cross-section taken at the same time at 21 km north (Figure 3.56b) shows depressed  $Z_{dr}$  in the core region, suggesting that the major hailshaft in the storm was situated there. At 21 km north, the updraft and the BWER were not as pronounced, although a large column of positive  $Z_{dr}$  extended above the altitude of the freezing level, which was around 3.5 km AGL, on the eastern side of the core. This so-called " $Z_{dr}$  column" suggests that significant supercooled liquid water was being lofted by the updraft at this time.

Figure 3.57 is the same as Figure 3.56 except for the 15 July 1998 storm at 1804 MDT. Figure 3.57a goes through 30 km north, the location of the main core of the storm. The updraft exceeded  $30 \text{ m s}^{-1}$  and a

significant BWER also was apparent, with 50 dBZ over 10 km. A  $Z_{dr}$  column extended to a very high altitude, over 6 km AGL, along the eastern edge of the core. Thus, while peak updraft was a bit lower than 1 July, the  $Z_{dr}$  column extended to a higher altitude. Other than these differences, based on these cross-sections the two storms appeared very similar in intensity. Figure 3.57b goes through 8 km north, which is the location of the southern cell that was producing apparently no CGs during this time. The cell apparently still was in the developing stage, with peak reflectivity aloft rather than at the ground. The cell also was somewhat less intense than the northern cell, although it was not topped properly so vertical velocity estimates were not as reliable. Peak reflectivity and reflectivity contour heights were lower, with no BWER, although a  $Z_{dr}$  column extended to nearly 5 km AGL.

Figure 3.58 depicts a vertical cross-section (at 2 km north of CHILL) of the same radar variables as before, but for 1840 MDT on 15 July 1998. Around this time the storm featured more low-CG characteristics (or at least produced fewer CGs overall), and the cross-section goes through the main core of the storm. Peak updrafts were a bit larger than before, above  $40 \text{ m s}^{-1}$ , and 50 dBZ again extended above 10 km AGL. A  $Z_{dr}$  column extended to 6 km AGL. No pronounced BWER was present, although a small reflectivity notch on the eastern edge of the core certainly showed some weak echo characteristics.

Figure 3.59 shows a vertical cross-section, at 23 km north of CHILL, of radar reflectivity, differential reflectivity, and positive vertical velocity for the 21 July 1998 storm, at 1531 MDT. The 50 dBZ contour extended to nearly 9 km AGL. The core featured depressed  $Z_{dr}$ , indicative of hail, although there was no obvious differential reflectivity column with this storm. The peak vertical velocity was just over  $10 \text{ m s}^{-1}$  and there was no weak echo region. Figure 3.60 shows vertical cross-sections for the same storm 15 minutes earlier, at 1516 MDT. Around this time the storm was at maximum CG production. Figure 3.60a goes through the main core of the storm, at 24 km north. Here there appeared to be a weak echo region, with a notch around 26 km west of the CHILL, but it probably was just a gap between two cells, one mature cell around 30 km west, and one developing cell around 24 km west. The updraft maximum (which was greater than  $10 \text{ m s}^{-1}$ ) appeared to be associated with the developing cell, which is not surprising. The tallest  $Z_{dr}$  contours, around 4 km AGL, were near the developing cell as well. Overall, reflectivities were about as intense as 1531 MDT, with 50 dBZ to 9 km AGL. Figure 3.60b goes through 50 km north, the

location of the cell that was nearly devoid of CGs around this time (see Figure 3.24). This cell was clearly far less intense than the main cell, in terms of vertical reflectivity structure alone.

Figure 3.61 shows a vertical cross-section, at 39 km north of CHILL, of the 25 July 1998 storm at 1625 MDT, the time of maximum updraft. The 50 dBZ contour extended to just over 5 km AGL, with no weak echo region. However, the vertical velocity exceeded  $20 \text{ m s}^{-1}$  and positive  $Z_{dr}$  values extended to 5 km AGL. Figure 3.62 shows vertical cross-sections of the same storm, this time at 1640 MDT, the time of maximum CG output. Figure 3.62a is through 27 km north of CHILL, in the most active region of CG production (see Figure 3.33). This cell was very comparable to the one in Figure 3.61, in terms of vertical reflectivity structure, differential reflectivity structure, and updraft. However, the  $20 \text{ m s}^{-1}$  contour covered a slightly smaller area in the 1640 MDT cell, and the 40 dBZ contour at 1640 MDT extended to a slightly lower altitude, 8 km versus 9 km AGL at 1625 MDT. Thus, the main part of the storm perhaps weakened slightly during the 15-minute period separating the two times, lowering the main negative charge region and favoring more CGs. Figure 3.62b is a cross-section through 11 km south of CHILL. Recall from Figure 3.33 that this was an apparently intense cell that produced only two negative CGs in the 10-minute period. The cross-section shows that this cell was a tier below in intensity compared to the main cell, either at 1625 or 1640 MDT. The 50 dBZ contour extended just above 3 km AGL, with positive differential reflectivity extending to a similar level. Also, the cell was smaller in overall size than the previous two cells. Unfortunately, this cell was not scanned properly by both radars so a dual-Doppler solution was not available to estimate updraft velocity. This cell was the closest one to CHILL, and thus the most likely of all the cells to have contributed to the total flash rate measured by the CHILL FCM around 1640 MDT. The FCM detected 39 flashes from 1640 to 1650 MDT, so the average total flash rate during this period was about four per minute. This is not a substantial flash rate, even factoring in the poor FCM detection efficiency. Thus, this southernmost cell likely was not intense enough to be significantly electrified, hence the relatively low CG and total flash rates for this cell.

Figure 3.63 is vertical cross-section for the 30 July 1998 storm, this one taken at 25 km north of CHILL at 1716 MDT. The main cell for this storm clearly was very shallow and weak compared to most of the other cells seen in the previous cross-sections.

Figure 3.64 shows vertical cross-sections of the 29 June 2000 storm at two significant times, 2312 UTC (Figure 3.64a) when both negative and positive CG flash rates were extremely low, and 2343 UTC (Figure 3.64b) when the positive CG flash rate had increased significantly. The 2312 cross-section was taken at 51 km north of CHILL, through the updraft core of the main cell. Reflectivities were not that intense, compared to 1 and 15 July, although a new 50 dBZ core was forming to the west and reached to nearly 10 km AGL. This new core coincided nicely with the location of the strongest updraft core, which had speeds in excess of  $30 \text{ m s}^{-1}$ . There was some  $Z_{dr}$  suppression in the mature precipitation core just to the east, but a column of positive differential reflectivities reached 4 km AGL right under the updraft core. Thus, while the updrafts were comparable to 1 and 15 July, reflectivities and the  $Z_{dr}$  column were not as impressive, and actually were more comparable to the 21 and 25 July storms. However, by 2343 UTC on 29 June 2000 (cross-section taken through 35 km north of CHILL), the reflectivity and differential reflectivity structures had intensified, with a large swath of 50 dBZ over 10 km, 60 dBZ to nearly 8 km AGL, and a  $Z_{dr}$  column over 5 km. The updraft region broadened in size as well, with  $30 \text{ m s}^{-1}$  or greater forming two distinct cores within the updraft region. Unlike 1 and 15 July, however, at neither time did the storm exhibit an obvious BWER.

#### *3.4 Testing of Elevated Charge Mechanism*

The elevated charge hypothesis (MacGorman et al. 1989) predicts that the storms with the strongest drafts should feature the lowest negative CG lightning flash rates, and the highest IC:CG ratios. The observations presented herein are consistent with this hypothesis. Based on the vertical velocity CFADs (Figures 50-55), vertical air mass fluxes (Figure 3.49), as well as the peak updraft figures (Figures 3.3, 3.11, 3.19, 3.28, 3.37, and 3.42) and the updraft volume figures (Figures 3.4, 3.12, 3.20, 3.29, 3.38, and 3.43), the mid-latitude storms can be subjectively ranked in terms of updraft intensity. The 30 July 1998 storm was clearly the weakest. The storm of 21 July was substantially stronger, but was weaker than 25 July 1998. The storms of 1 and 15 July were much stronger than the other CHILL-Pawnee storms, but are difficult to rank relative to one another. The 1 July storm featured greater vertical velocities (as well as greater volume and frequency) at the high end, but 15 July 1998 was greater in the more moderate updraft region of  $10\text{-}20 \text{ m s}^{-1}$ . The lone STEPS case (29 June 2000) had stronger peak updrafts, and larger volumes

of intense updrafts, than either 1 or 15 July, but only in its later stages. Comparatively weaker updrafts were present prior to the intensification period.

Based on CG lightning flash rates (Figures 3.7, 3.15, 3.23, 3.32 and 3.46), the three storms with the strongest drafts (1 and 15 July, 29 June) also featured the lowest negative CG lightning flash rates, excepting 30 July 1998. The 30 July storm featured the lowest CG flash rates (positive or negative), but also produced the least amount of total (IC+CG) lightning. By contrast, the available total lightning data suggest that 15 July and 29 June were the most electrified. However, recall that there are some doubts as to the 15 July 1998 total lightning data, and the 1 July 1998 data weren't viable at all so no estimates were made for that storm. What this means is that, as best as could be determined, the storms with the strongest drafts also featured the highest IC:CG ratios.

By contrast, 25 July 1998 featured somewhat weaker (though still fairly intense) updrafts, and a more typical CG lightning flash rate, as well as IC:CG ratio. Interestingly, the storm of 21 July 1998 tended to have slightly weaker updrafts than 25 July 1998, but produced more negative CGs, the most of any storm in fact. The available data also suggest that 21 July 1998 had a very low IC:CG ratio.

Placing the mid-latitude storms on a spectrum, increasing updraft intensity increases negative CG lightning output as one moves from the least intense storm (30 July 1998) to one of moderate intensity (21 July 1998). Moving up in updraft intensity to a storm like 25 July 1998, negative CG lightning flash rate drops somewhat, but the IC:CG ratio increases. However, once updraft intensity becomes very strong negative CGs become nearly absent, even as total flash rate continues to climb (1 and 15 July, 29 June). This leads to very high IC:CG ratios in the storms with the most intense updrafts. The flash rates and ratios in this spectrum can be thought of in either the peak or average sense.

The elevated charge hypothesis is consistent with this observed spectrum. Storms with very weak updrafts should not electrify significantly (e.g., 30 July). Then as updraft strength increases the storm should electrify more, but with a weighting toward negative CGs (e.g., 21 July). As storm updrafts continue to increase, one should pass through more typical lightning patterns (e.g., 25 July), and then at the level of extreme updrafts the total lightning flash rate should be substantial, and weighted almost entirely toward ICs (e.g., 1 and 15 July, 29 June). Without in situ charge measurements a final determination

cannot be made, but the radar and lightning data from these 6 cases support the basic tenets of the elevated charge mechanism.

### *3.5 Testing of PPCG Mechanisms*

It is difficult to test the proposed PPCG mechanisms (tilted and inverted dipole, precipitation unshielding) without adequate in situ charge measurements. These were made in only one case, 29 June 2000, and those data were not available for analysis by the completion of this study. However, some speculation on each mechanism's viability can be made, based on the current set of observations.

#### *a) Tilted Dipole*

In the two storms that are best characterized as PPCG, 15 July and 29 June, there is some limited evidence to favor a tilted dipole. For example, both 29 June and 15 July had stronger upper-level shear than the low-CG storm of 1 July. However, as noted earlier, the 21 July 1998 storm, which featured substantial negative CGs and few positive CGs, had stronger upper-level shear than 15 July 1998. Examining horizontal radar cross-sections and NLDN CG lightning from the storms at their peak positive CG output (Figures 3.16 and 3.47) the ground-strike locations of the positive CGs in general were positioned outside the main 60 dBZ cores of these storms. This was true even during the lower CG output period of 15 July, around 1840 MDT (Figure 3.16b). However, many positive CGs were still within the 50 dBZ contours in these plots. Moreover, many positive CGs came to ground not that far from a 60 dBZ core, often within 10 km (e.g., Figure 3.47). Since ground-strike position does not necessarily correspond to the flash origin, or even mean flash location, it cannot be ruled out that a substantial portion of the positive CGs in these storms started within the main core and not the adjacent anvil. Finally, while 29 June 2000 positive CGs during 2340-2350 UTC (the time of peak positive CG flash rate) showed some evidence of coming to ground in the downshear (eastern) part of the storm (Figure 3.47), as the tilted dipole mechanism would suggest, Figure 3.16 (a, b) shows no such preferential behavior for 15 July 1998, with positive CGs coming to ground in all directions from the main 60 dBZ core. Thus, if the tilted dipole mechanism was active in these storms, it did not manifest itself very obviously. Another thing to note

about the tilted dipole mechanism is that it does not attempt to explain the dearth of negative CGs in PPCG (or low-CG) storms.

*b) Inverted Dipole*

From Figures 3.14 and 3.15, it can be seen that the 15 July 1998 storm reached its peak positive CG flash rate as the hail production by the storm increased significantly. Positive CGs peaked during 1750-1820 MDT, while hail area and mass flux began their increase after 1750 MDT, and reached a peak immediately after 1820 MDT. This time period was also coincident with a significant increase in vertical velocity (Figures 3.11 and 3.12) as well as rain production (Figure 3.13). The 29 June 2000 storm featured similar behavior, with positive CGs (Figure 3.46) largely tracking the increases in hail (Figure 3.45), rain (Figure 3.44), and volumes of significant updraft (Figure 3.43) during the latter two-thirds of the observation period. In addition, for both storms the positive CG flash rate peak roughly coincided with (15 July) or immediately lagged (29 June 2000) the rapid ascent of the 60 dBZ reflectivity contour (Figures 3.10 and 3.41). The Carey and Rutledge (1998) precipitation identification matrix was applied to these storms to identify large (> 2 cm) hail near the surface (0.5 km AGL). The matrix identifies regions containing large hail primarily by looking for enhanced LDR values. The matrix found no large hail during 15 July 1998, but did identify up to 69 km<sup>2</sup> of large hail during 29 June 2000 (2351 UTC radar volume). The large hail area on 29 June (not shown) generally tracked the intensification of the storm, much like the other radar-derived variables did.

These observations are at times convergent with and divergent with the PPCG case study of Carey and Rutledge (1998). By examining a PPCG storm that occurred in northeast Colorado on 7 June 1995, those researchers found that large hail and positive CG lightning were anticorrelated in time, with peaks in positive CGs occurring 20-35 minutes after peaks in large hail. For the 29 June 2000 case examined in this study, large hail and positive CGs were largely coincident. However, like Carey and Rutledge (1998), the positive CG peaks during the storms of 15 July and 29 June occurred as the rain and hail production underwent significant increases. If positive charge formed on these hail/graupel particles as they descended through the charge-reversal layer (0 to -10 °C) then these observations are broadly consistent with an inverted dipole, since the enhanced lower positive charge then could allow for a greater positive CG flash

rate. In addition, a very preliminary analysis of the LMA data from the 29 June case suggests that the lightning were consistent with a major layer of positive charge underlying the main negative charge; that is, an inverted dipole (Dr. P. Krehbiel, personal communication). An inverted dipole might also explain the lack of negative CGs in 29 June and 15 July during their peak positive CG output, although it doesn't necessarily explain the lack of CGs in general when these storms were not PPCG. In addition, given the microphysical and kinematic similarities between these storms and the 1 July 1998 low-CG storm, it is unclear why 1 July 1998 shouldn't have an inverted dipole and enhanced positive CGs as well.

### *c) Precipitation Unshielding*

As mentioned before, the positive CG lightning peaked as the rain and hail production of the 15 July and 29 June storms increased significantly. This is broadly consistent with precipitation unshielding upper level positive charge. However, other storms, most notably 1, 21, and 25 July 1998, featured substantial precipitation (particularly rain in the cases of 21 and 25 July) as well, and sparse positive CG lightning. In those cases, though, no major intensification was observed during the analysis periods. As best as could be determined, the storms typically fluctuated around a given intensity level, or diminished in intensity during the analysis times. Thus, it appears that if a mechanism like precipitation unshielding was active, it was only active during major intensification periods in the storms.

### *3.6 Testing of Separated Updraft-Downdraft Mechanism*

To test the separated updraft-downdraft hypothesis, simple correlations were performed between CHILL reflectivity and vertical velocity. If the proposed mechanism were active, then one might expect a strong negative correlation between reflectivity and vertical velocity in the most intense storms, so that the cores (areas of substantial reflectivity) were primarily in downdrafts. Correlations were performed for all volumes on all days. For a given radar volume, correlations were done over the entire radar volume, only in the region of 30 dBZ and greater (to ignore everything except major cores), only in the region of  $-10$  to  $0$  °C (since this would be the most important region of positive charging), and in 30 dBZ and greater plus in the region of  $0$  to  $-10$  °C. The best correlations found are summarized in Table 3.3. For all of the storms, the absolute value of the correlation coefficient generally was less than 0.6, and often the correlation was

positive, not negative as one might expect if the mechanism were active. In fact, correlations often switched sign in storms as they evolved, and much of the time correlations were well below the best values. In addition, depending on the region considered, the best correlation often moved between different times for a given storm.

Particular attention was paid to the low-CG or PPCG storms of 1 and 15 July, as well as 29 June, since these storms featured the lowest negative CG flash rates of the set (excluding the weakly electrified 30 July case). The best correlations from 1 July are all negative, consistent with the separated updraft-downdraft mechanism, but do not even reach  $-0.5$ . Moreover, often the correlations were much lower, close to zero in fact (not shown). The results for 15 July were even more mixed, with the best correlations often positive, meaning updrafts were tending to be co-located with precipitation cores. The best correlation seen was  $0.764$ , considering the intersection of the  $0$  to  $-10$  °C region with the region of  $30$  dBZ and greater, but this was late (1937 MDT), when little if any of the main convective line remained in the dual-Doppler lobe. Moreover, as the storm evolved the correlations often fluctuated between positive and negative values (not shown).

The 29 June 2000 storm showed the most promise, with the best correlations all negative and better than  $-0.5$ . Moreover, correlations became increasingly negative as the storm intensified with time (not shown). This is reflected in the fact that all the best correlations for 29 June 2000 occurred late in the analysis period (2343 UTC or later). Thus, there did appear to be a tendency for the updrafts and precipitation cores to be offset from one another in 29 June, although the storm featured little negative CG lightning throughout the analysis period and the best correlations were achieved later in the period. In addition, both 1 and 15 July featured similarly low negative CG lightning production and neither achieved the quality of correlations that 29 June did.

However, perhaps just looking at straight correlations is not the best way to look at this issue, as correlations look for a linear relationship, meaning the maximum reflectivity is expected to be co-located with the maximum downdraft. However, the separated updraft-downdraft mechanism merely requires that the main core be in a region of downdraft, not necessarily a major downdraft core. To examine this possibility, horizontal cross-sections of CHILL reflectivity and vertical velocity were examined. The cross-sections were taken through  $4.5$  km AGL, which is located within the key  $-10$  to  $0$  °C region. Figure 3.65

shows cross-sections for the key times of 1850 (the time of maximum updraft, Figure 3.65a) and 1925 MDT (the time of maximum CG production, Figure 3.65b) on 1 July 1998. In general, the major precipitation cores were offset horizontally from the major updraft cores, consistent with what was seen in Figure 3.56. Figure 3.66 shows cross-sections for the 15 July 1998 storm, at 1804 MDT (updraft maximum/positive CG maximum, Figure 3.66a) and 1840 MDT (CG minimum/updraft maximum, Figure 3.66b). While dual-Doppler solutions were not available for the entire storm at 1840 MDT, once again the updraft cores were offset from the precipitation cores. This is consistent with the vertical cross-sections in Figures 3.57 and 3.58. Thus, the necessary conditions for the updraft-downdraft mechanism to be active appear to have been met in these storms at these key times. Indeed, these storms did feature low negative CG flash rates.

However, Figure 3.67 muddies the waters a bit. It shows cross-sections from the 21 July 1998 storm, at 1516 MDT (CG maximum, Figure 3.67a) and 1531 MDT (updraft maximum, Figure 3.67b). While updrafts were less intense than the previous two storms, they still tended to be offset from the major precipitation cores, which is not consistent with the separated updraft-downdraft mechanism because the storm produced so many negative CGs.

Figure 3.68 shows cross-sections for the 25 July 1998 storm. The key times examined were 1625 MDT (updraft maximum, Figure 3.68a) and 1640 MDT (CG maximum, Figure 3.68b). Here the updraft cores tended to be situated within the major precipitation cores, which is consistent with the updraft-downdraft mechanism since the 25 July 1998 storm produced more CGs than 1 or 15 July. Figure 3.69 shows a cross-section for the 30 July 1998 storm at 1716 MDT, the time of maximum updraft. Once again, the storm shows its overall weakness relative to the others. What little significant updraft there was seems to have been co-located with a precipitation core. However, the lack of substantial precipitation mass in the mixed phase region likely was what affected this storm's electrical output, so the separated updraft-downdraft mechanism would not likely apply to this case.

Figure 3.70 shows a cross-section of the 29 June 2000 storm at 2325 UTC. At 4.5 km AGL, the updraft core clearly was displaced west of the main precipitation core (which was near 50 km north and 70 km east of CHILL), meeting the necessary requirements for the separated updraft-downdraft mechanism.

Thus, the testing of the separated updraft-downdraft mechanism yields mixed results. Overall, correlations between reflectivity and vertical velocity for all storms tended to be weak, and not always negative in the low-CG/PPCG storms. Although the stronger storms (1 and 15 July, 29 June) with low negative CG flash rates did show some offset between precipitation and updraft, so did a weaker, more prolific CG producer like 21 July 1998.

### 3.7 Summary

Radar, lightning, and sounding data from six convective storms were analyzed, compared, and contrasted. Several proposed mechanisms to explain the observed lightning patterns were tested. Of these, the most successful was the elevated charge mechanism, which posits that stronger updrafts loft the main negative charge region to higher altitudes, favoring ICs over CGs. At the extreme end of very intense updrafts, ICs should completely dominate over CGs, particularly negative CGs. At the other end, weakly electrified storms should feature little lightning of any kind. Between these extremes should lay storms with moderate updrafts, and more typical CG lightning flash rates and IC:CG ratios. The available data fit this proposed spectrum very well, with the strongest storms (1 and 15 July 1998, 29 June 2000) indeed featuring the highest IC:CG ratios and lowest negative CG lightning flash rates. Storms with more moderate updrafts (21 and 25 July 1998) featured higher negative CG flash rates and lower IC:CG ratios, and the weakest storm (30 July 1998) featured little lightning of any kind.

The strongest storms also manifested themselves in the radar reflectivity and hail data. In addition to having the strongest updrafts, they also tended to have the most intense radar reflectivities, as well as produce the most hail. Interestingly, however, all storms tended to produce comparable rainfall, regardless of their overall intensities. This suggests that while radar reflectivity structure and hail production may be used as proxies for updraft strength, rainfall production may not. In addition, given the fact that this set of storms featured markedly different lightning patterns within it, rainfall appears to not play a significant role electrically, in the sense that it is not correlated with total or CG lightning flash rate, on a storm-by-storm basis. This tends to undercut any sort of hypothesis that predicts precipitation (i.e., rain) current to significantly affect lightning.

The separated updraft-downdraft mechanism argues that in storms where precipitation is falling largely outside of updrafts, particularly in the important positive charging region of 0 to  $-10^{\circ}\text{C}$ , significant charging should not occur (due to suppression of supercooled liquid water) and negative CG lightning flashes should be suppressed. As such, this mechanism could act either in concert with, or instead of, the elevated charge mechanism. However, the available data show mixed results for the testing of this hypothesis. While storms with low negative CG flash rates did in fact tend to show precipitation cores offset from updraft cores – the necessary precondition for this mechanism to be active – so did a more prolific negative CG producer like 21 July 1998. Thus, it appears that the elevated charge mechanism more successfully explains reduced negative CG flash rates in intense storms than the separated updraft-downdraft mechanism. However, it should be noted that the number of cases presented here is too small to make definitive statistical conclusions.

The PPCG mechanisms (tilted dipole, inverted dipole, precipitation unshielding) could not be adequately tested due to lack of in situ charge data. However, the tilted dipole mechanism, which posits that upper-level positive charge is displaced laterally in storms with strong shear - thereby exposing it to ground and enhancing positive CG flash rates – is not well supported by the available radar and lightning data.

The inverted dipole mechanism suggests that significant positive charge lies beneath the main negative charge region in an intense thunderstorm, causing positive CGs to increase as significant precipitation reaches the ground. This is thought to occur much like negative CG flash rates increase as cores in normal polarity storms reach the ground (e.g., Carey and Rutledge 1996). Positive CG flash rates did increase as significant precipitation reached the ground in the PPCG storms of 15 July 1998 and 29 June 2000. However, in 15 July, positive CGs later decreased even as significant precipitation continued to fall. Also, the kinematic and microphysical sibling of these PPCG storms, 1 July 1998, produced very little positive CG lightning.

The precipitation unshielding mechanism predicts that positive CGs are enhanced after cores fall out of intense storms, exposing the upper positive charge to ground and increasing positive CG flash rate. Again, positive CGs should increase as precipitation intensifies at the ground, much like with the inverted dipole mechanism, and very similar to what was observed in the PPCG storms observed in this study. However, the precipitation unshielding mechanism could account for the later reduction in positive CGs during 15

July, since once the upper positive charge layer discharged itself there would be less impetus for more positive CGs. At least, the charge within it might have been reduced enough that positive CGs were less common, even though ICs still may have been prevalent.

Comparing the PPCG and low-CG storms within this data set, enhanced positive CG lightning flash rates occurred when storms (15 July 1998 and 29 June 2000) underwent a significant intensification. After this intensification positive CG rates tended to drop (in the case of 15 July 1998), even though the storm remained very strong, with fast updrafts, intense reflectivities, and substantial hail production. In terms of these three things, the low-CG storm of 1 July 1998 was of comparable intensity to the PPCG storms. And during both its PPCG and low-CG periods, the 15 July 1998 storm remained very strong. It may be that enhanced positive CG lightning can be associated with a major intensification in a storm, and after that intensification, the storm remains strong but can revert to low-CG status. A storm may even be strong and low-CG prior to this intensification, much like 29 June 2000. No intensification was observed during 1 July, as the storm remained strong throughout the observation period, and positive CGs were not enhanced in that storm.

To summarize, the elevated charge mechanism explains the spectrum of negative CG and IC:CG ratio observations in the mid-latitude storms. The PPCG storms are perhaps best explained via an inverted dipole or precipitation unshielding mechanism, although in situ electrical charge data are lacking so definitive conclusions cannot be made. However, enhanced positive CGs may only occur near the time of intensification, and not necessarily afterward, when the storm can revert to low-CG status. In this study, the PPCG storms also at times exhibited low-CG characteristics, and they did not differ significantly in intensity (in terms of updraft, reflectivity, and hail) between these times. Moreover the one true low-CG storm (1 July 1998) was just as intense as the PPCG storms. All of these storms were severe. Thus, it is concluded that what can distinguish intense or severe convection from more ordinary convection is not necessarily enhanced positive CG flash rates, but instead a dearth of negative CGs, and a high IC:CG ratio.

Table 3.1: Summary of kinematic, microphysical, and lightning observations for the mid-latitude cases.

	1 Jul 98	15 Jul 98	21 Jul 98	25 Jul 98	30 Jul 98	29 Jun 00
Peak $Z_h$ (dBZ)	72.6	67.5	65.0	66.6	53.8	70.7
Peak Height 30 dBZ (km AGL)	14.5	14.0	13	15	6.5	16.0
Peak $W$ ( $m s^{-1}$ )	45.9	40.8	19.1	29.9	12.4	51.3
Peak Volume $W > 10 m s^{-1}$ ( $km^3$ )	1667.0	3023.0	325.5	764.5	12.5	4123.0
Peak Volume $W > 20 m s^{-1}$ ( $km^3$ )	521.5	868.0	0.0	130.5	0.0	1165.5
Peak Area Heavy Rain ( $km^2$ )	150.0	377.0	193.0	172.0	67.0	391.0
Peak Rain Mass Flux ( $10^6 kg s^{-1}$ )	10.8	22.3	12.6	12.1	8.2	20.7
Peak Area Hail ( $km^2$ )	168	490	24	45	3	330
Peak -CG Flash Rate (flashes per 10 minutes)	18	16	188	93	0	5
Peak +CG Flash Rate (flashes per 10 minutes)	6	44	3	6	2	21
Peak Total Flash Rate (flashes per 5 minutes)	NA	NA	18	40	2	$\sim 30 min^{-1}$ or more

Table 3.2: CAPE (in  $\text{J kg}^{-1}$ ) and shear (in  $\text{m s}^{-1}$ ) calculations for the mid-latitude cases.

	<b>Standard CAPE</b>	<b>Adjusted CAPE</b>	<b>RAMS-Predicted CAPE</b>	<b>Sfc-400 mb Shear</b>	<b>400-200 mb Shear</b>
<b>1 July 1998</b>	1596.4	1596.4	1936.0	16.09	4.84
<b>15 July 1998</b>	0.0	2237.0	1397.0	6.69	13.34
<b>21 July 1998</b>	28.4	779.8	1011.0	12.64	15.33
<b>25 July 1998</b>	469.8	2768.4	2246.0	2.00	5.40
<b>30 July 1998</b>	510.2	510.2	1498.0	13.75	20.79
<b>29 June 2000</b>	2169.6	2169.6	NA	21.24	21.34

Table 3.3: Best correlation coefficients for reflectivity versus vertical wind speed, considering various regions of the mid-latitude storms. Also shown are the times of the radar volumes in which the best correlations were found (L – local/MDT; Z – UTC).

	All of Storm	> 30 dBZ	0 to -10 °C	0 to -10 °C & > 30dBZ
<b>1 July 1998</b>	-0.408 (1844L)	-0.347 (1844L)	-0.452 (2005L)	-0.405 (2025L)
<b>15 July 1998</b>	-0.374 (1752L)	0.562 (1937L)	0.373 (1728L)	0.764 (1937L)
<b>21 July 1998</b>	-0.374 (1439L)	0.475 (1606L)	-0.350 (1439L)	0.474 (1606L)
<b>25 July 1998</b>	-0.386 (1650L)	0.575 (1550L)	-0.503 (1650L)	0.578 (1550L)
<b>30 July 1998</b>	0.216 (1804L)	0.327 (1804L)	0.124 (1804L)	0.246 (1804L)
<b>29 June 2000</b>	-0.552 (2343Z)	-0.573 (2357Z)	-0.541 (2343Z)	-0.587 (2357Z)

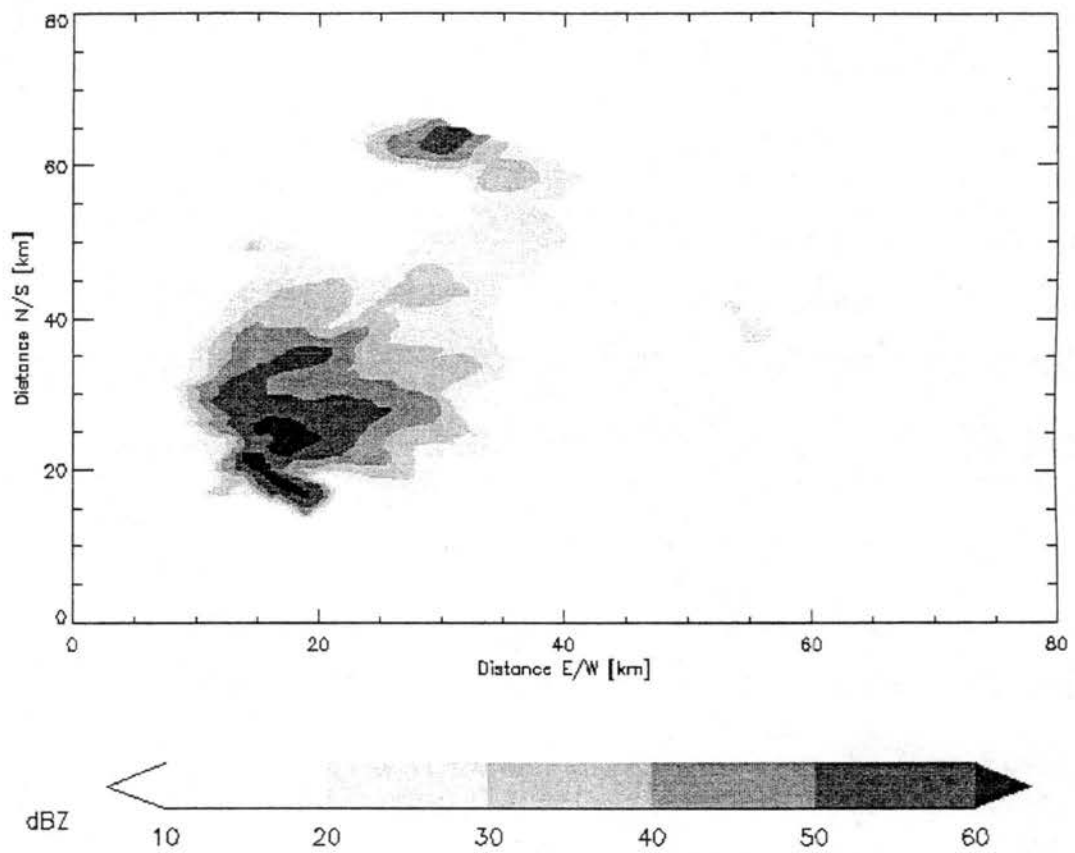


Figure 3.1: Horizontal cross-section of CHILL radar reflectivity at 0.5 km AGL, at 1850 MDT on 1 July 1998. Distances are relative to CHILL.

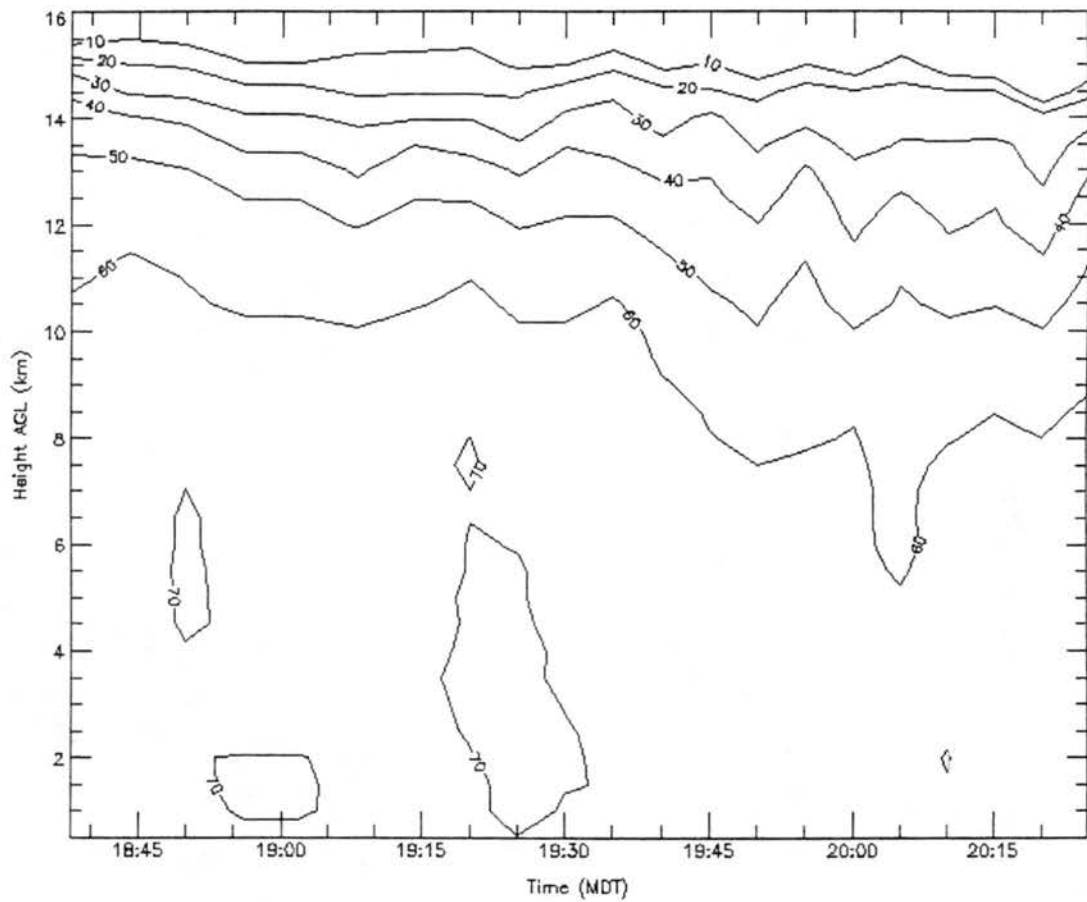


Figure 3.2: Time-height cross-section of peak CHILL radar reflectivity for the 1 July 1998 storm. Values are in dBZ.

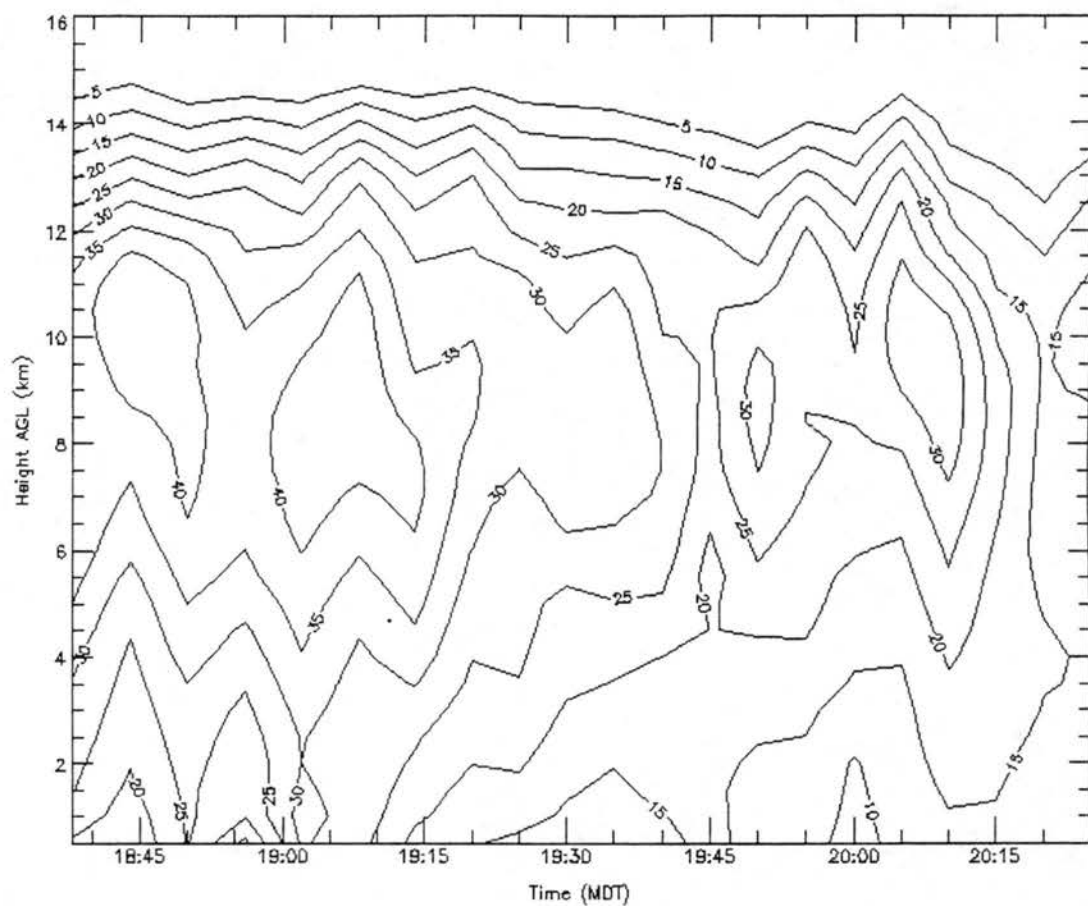


Figure 3.3: Time-height cross-section of maximum vertical velocity for the 1 July 1998 storm. Values are in  $\text{m s}^{-1}$ .

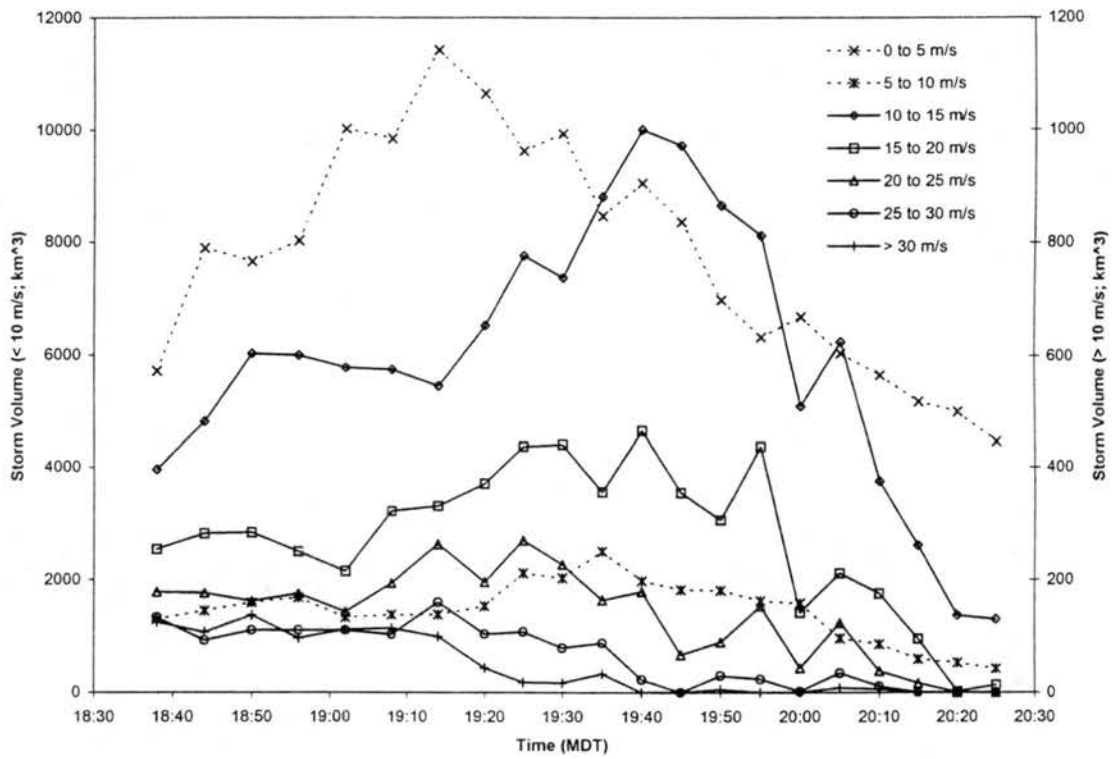


Figure 3.4: Volume of 1 July 1998 storm containing updrafts within respective bins as a function of time.

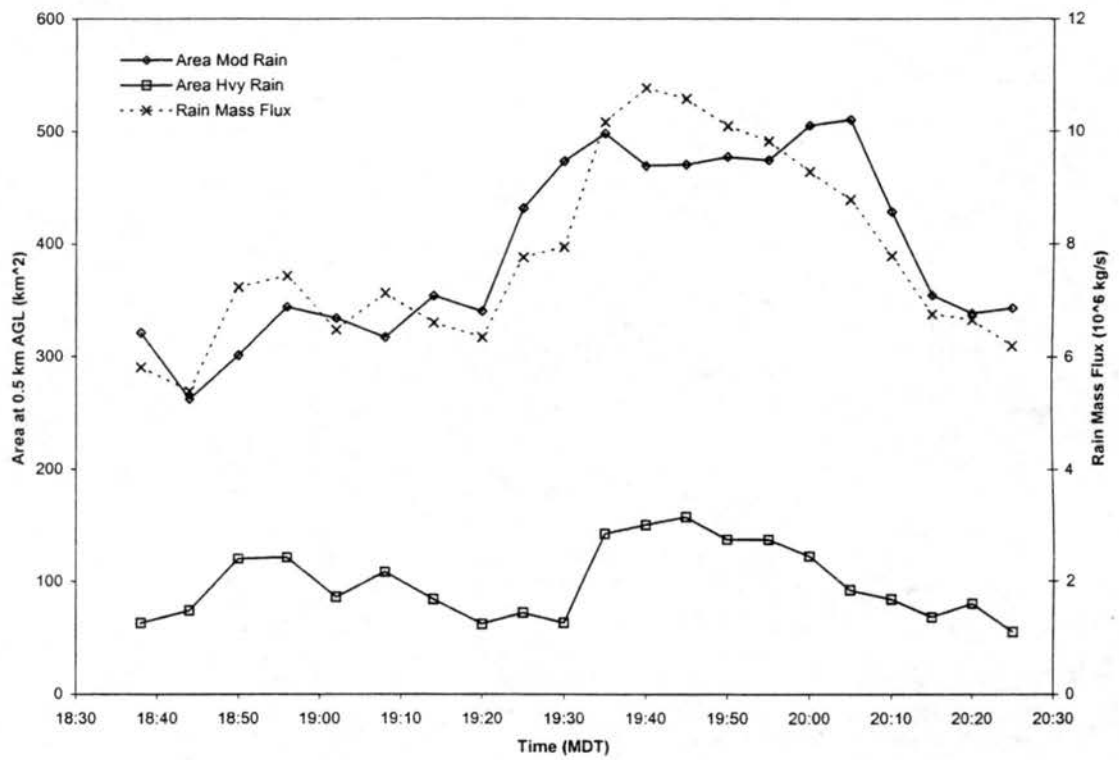


Figure 3.5: Rain production by the 1 July 1998 storm as a function of time. Values are at 0.5 km AGL. Moderate rain is 20-60 mm h<sup>-1</sup>, and heavy rain is greater than 60 mm h<sup>-1</sup>.

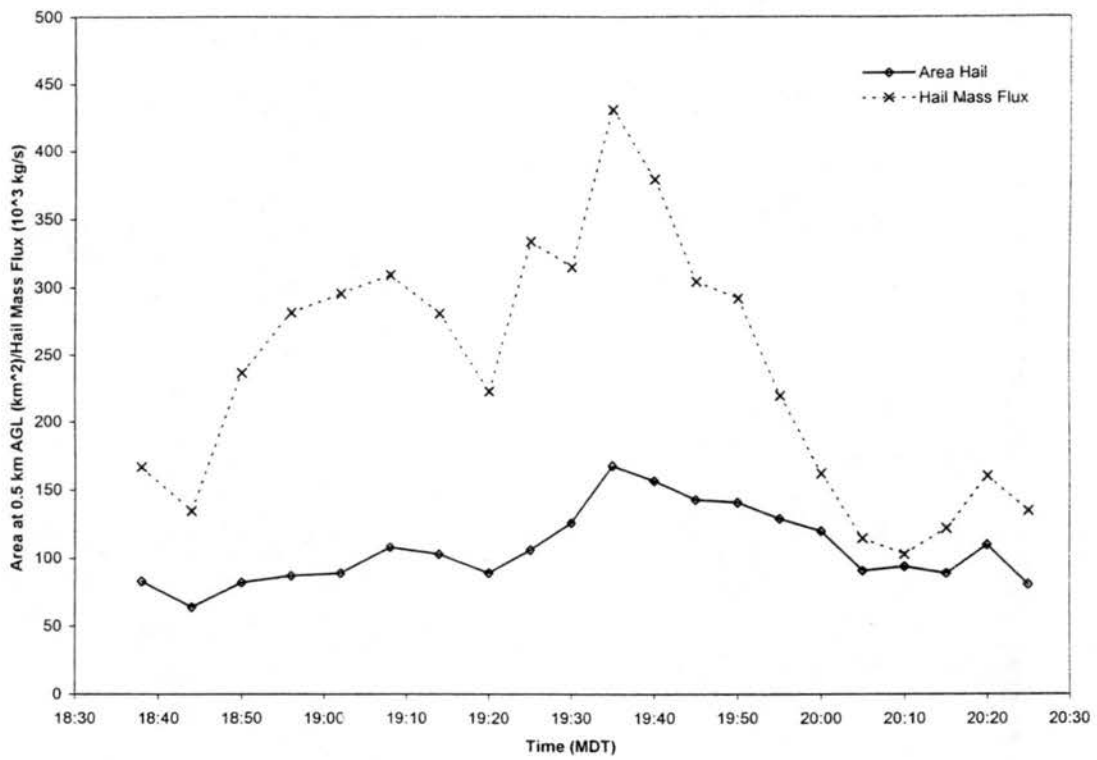


Figure 3.6: Hail production by the 1 July 1998 storm as a function of time. Values are at 0.5 km AGL.

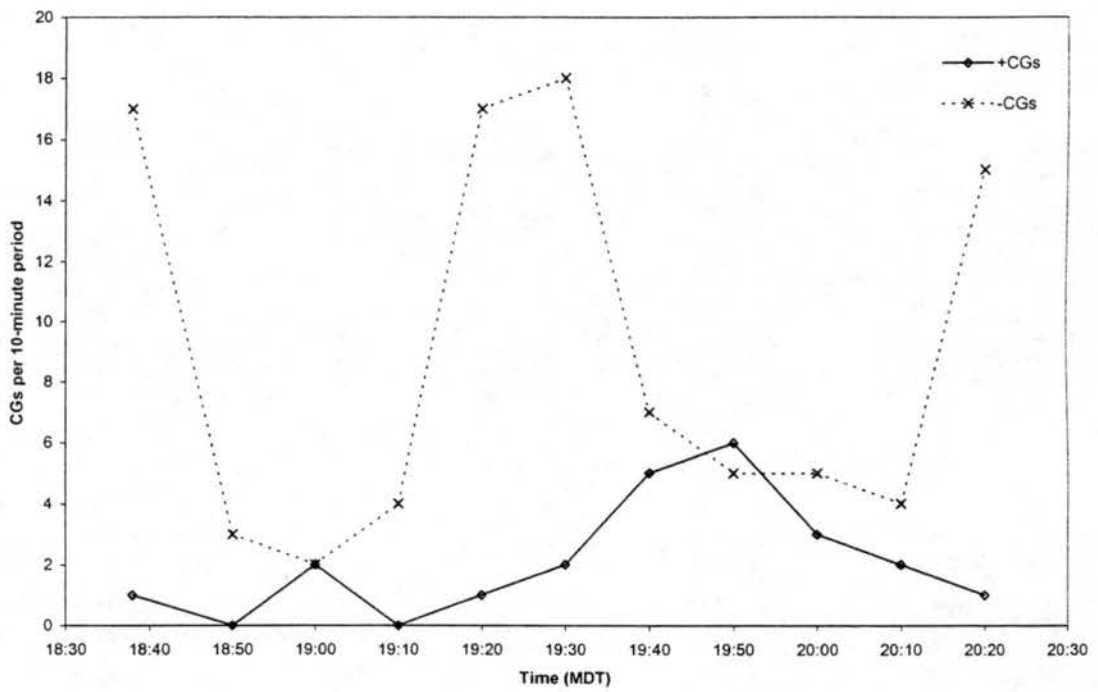


Figure 3.7: CG flash rate as a function of time for the 1 July 1998 storm.

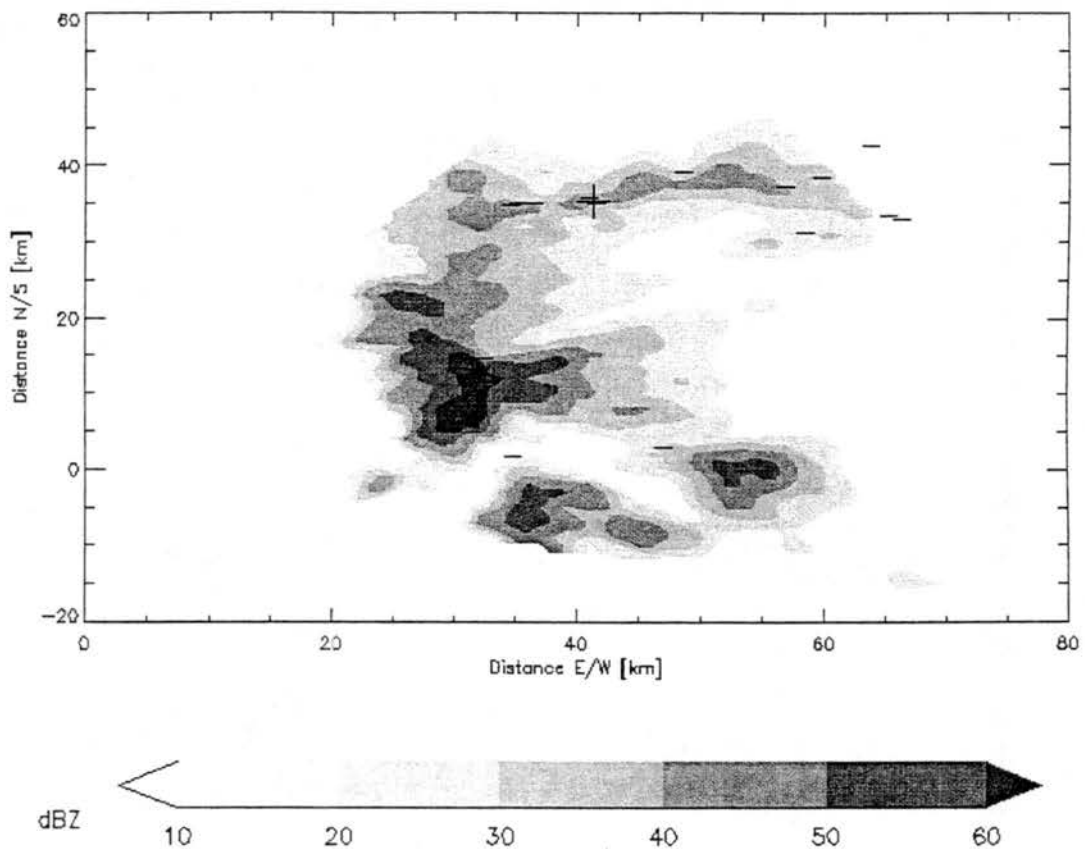


Figure 3.8: Horizontal cross-section of CHILL radar reflectivity at 0.5 km AGL, at 1925 MDT on 1 July 1998. Also shown are ground strike positions (plus signs for positives, minus signs for negatives) of NLDN CGs that occurred during 1920-1930 MDT. Distances are relative to CHILL.

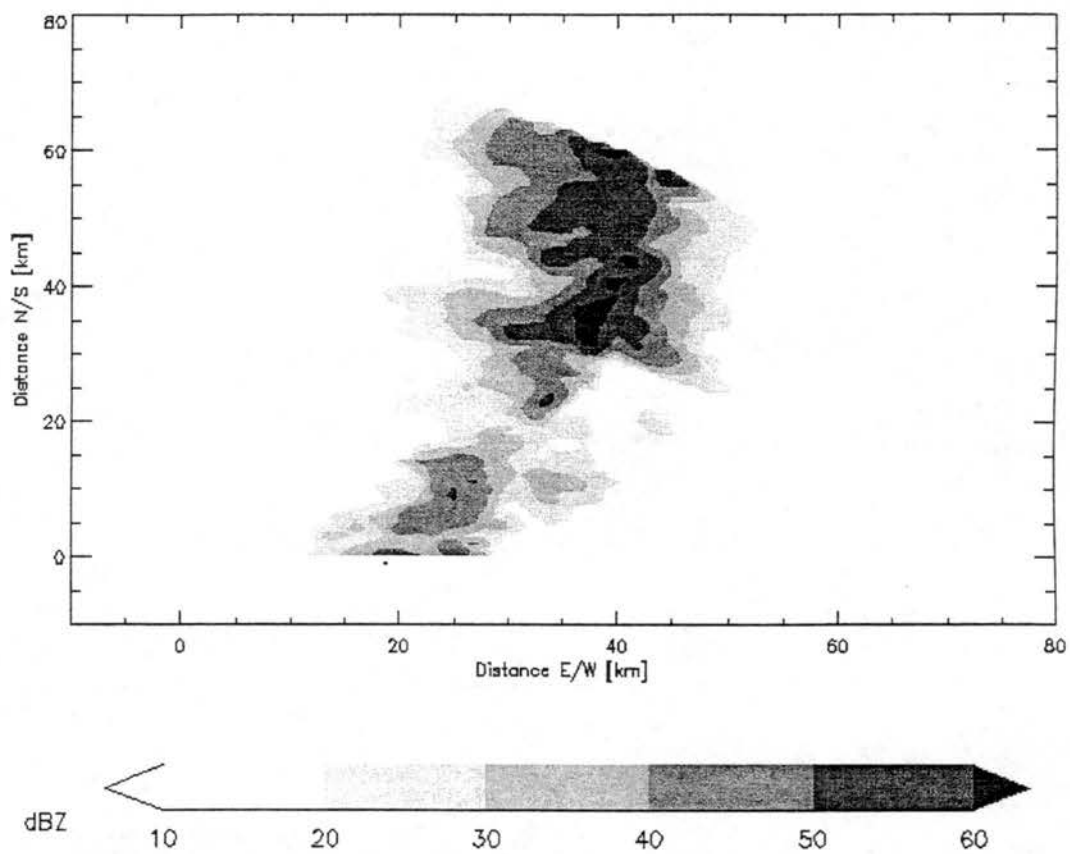


Figure 3.9: Horizontal cross-section of CHILL radar reflectivity at 0.5 km AGL, at 1804 MDT on 15 July 1998. Distances are relative to CHILL.

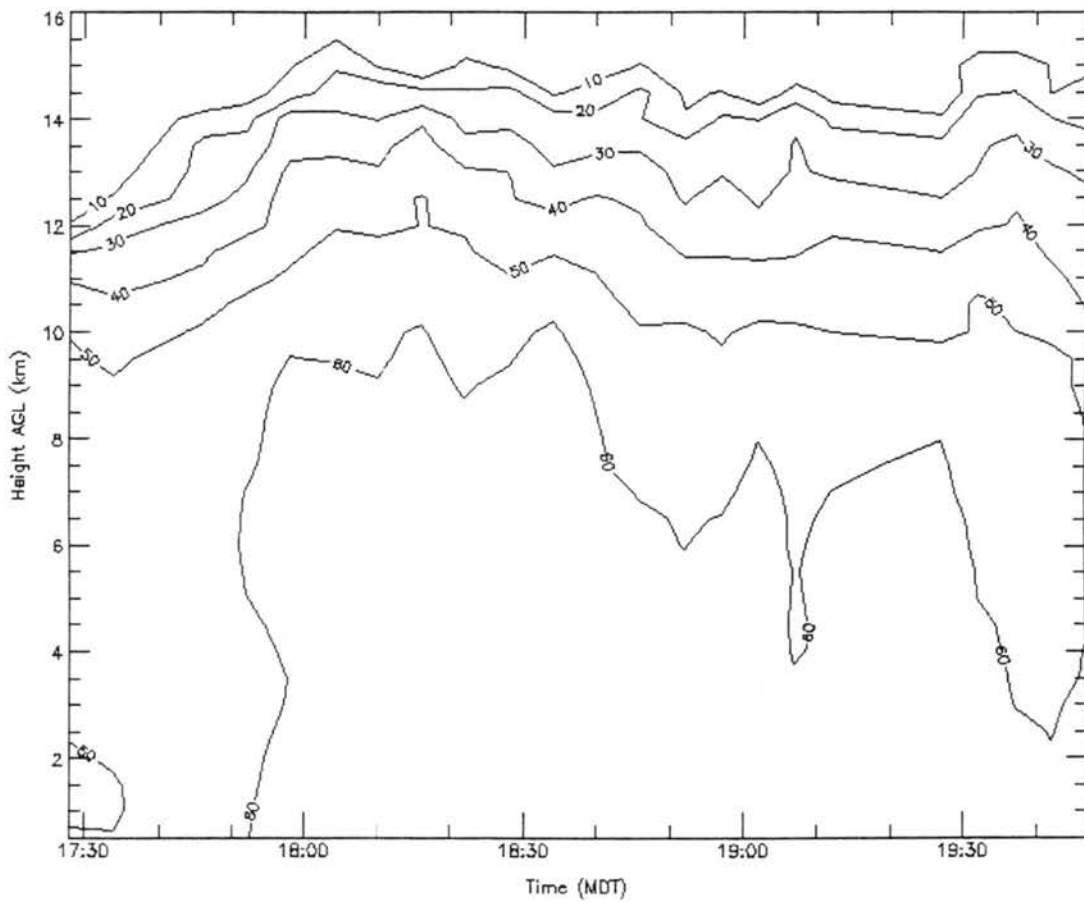


Figure 3.10: Time-height cross-section of peak CHILL radar reflectivity for the 15 July 1998 storm. Values are in dBZ.

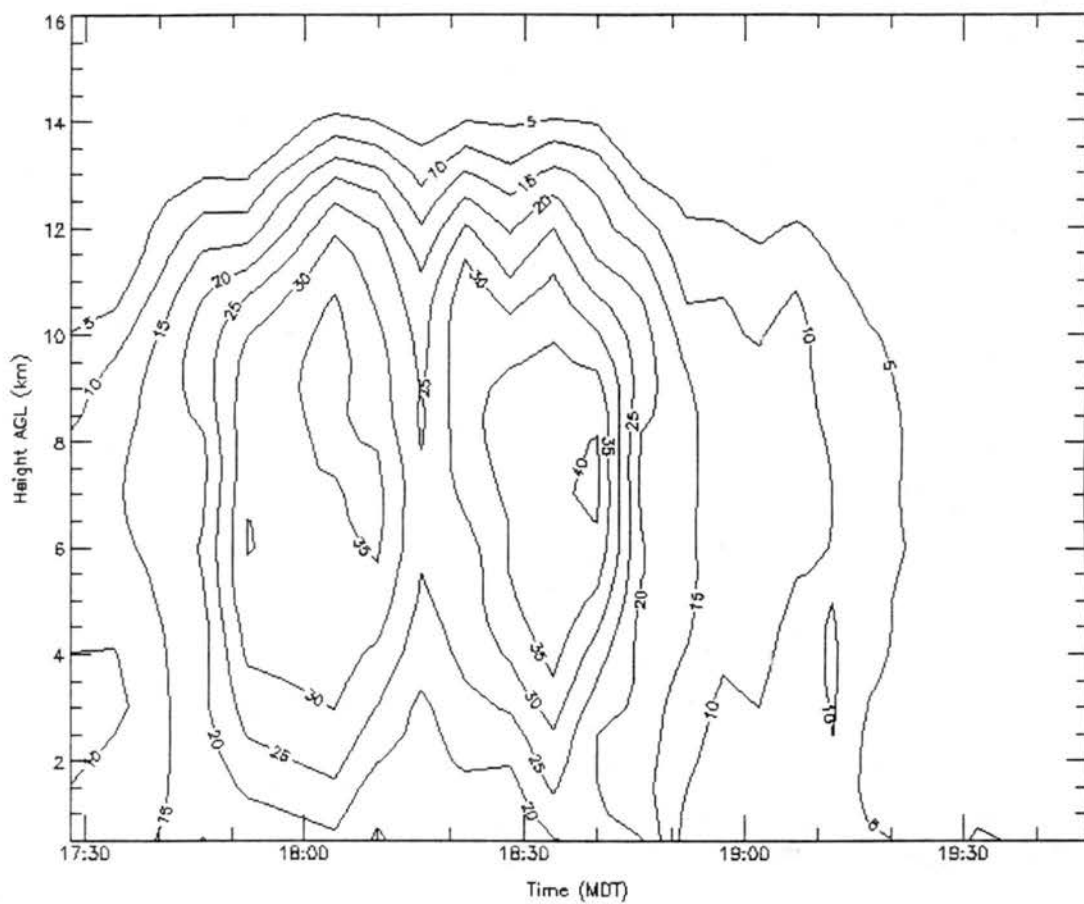


Figure 3.11: Time-height cross-section of maximum vertical velocity for the 15 July 1998 storm. Values are in  $\text{m s}^{-1}$ .

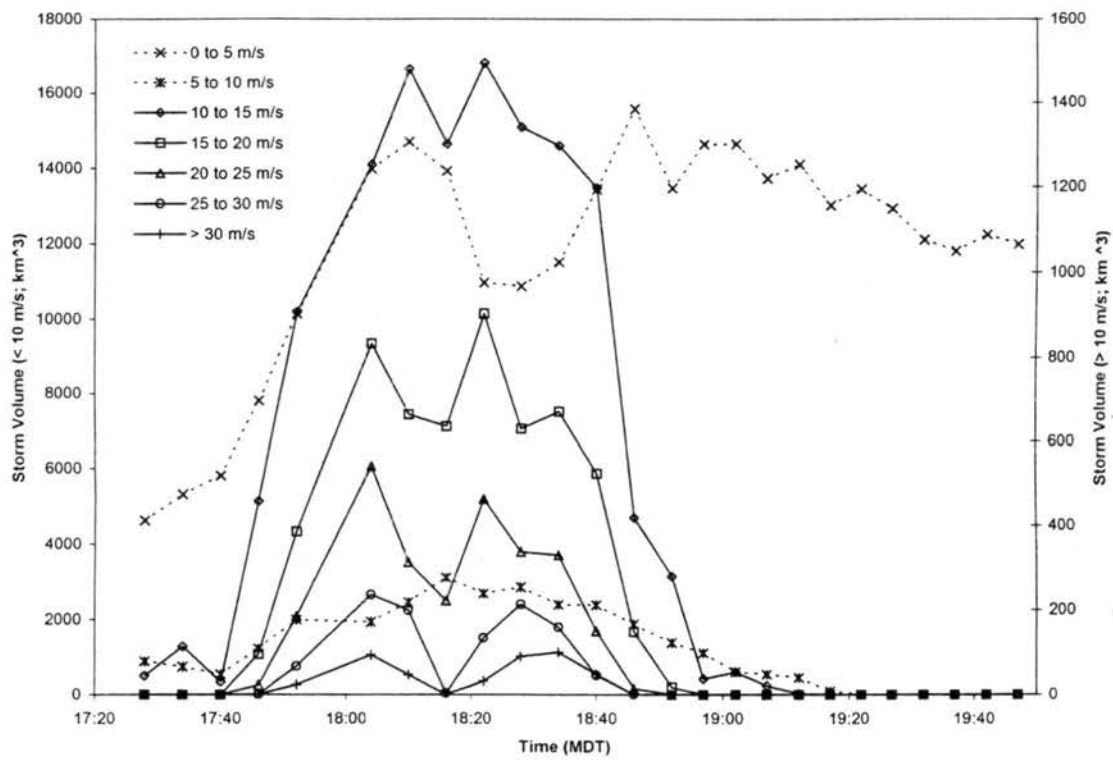


Figure 3.12: Volume of 15 July 1998 storm containing updrafts within respective bins as a function of time.

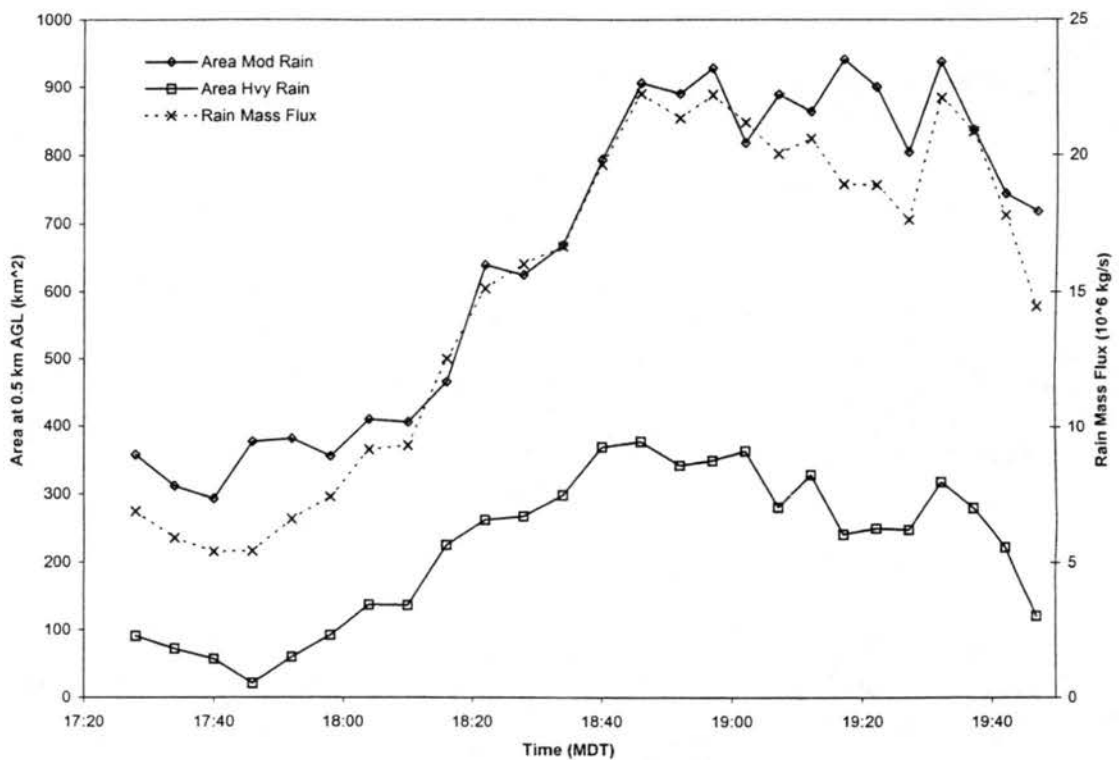


Figure 3.13: Rain production by the 15 July 1998 storm as a function of time. Values are at 0.5 km AGL. Moderate rain is 20-60 mm h<sup>-1</sup>, and heavy rain is greater than 60 mm h<sup>-1</sup>.

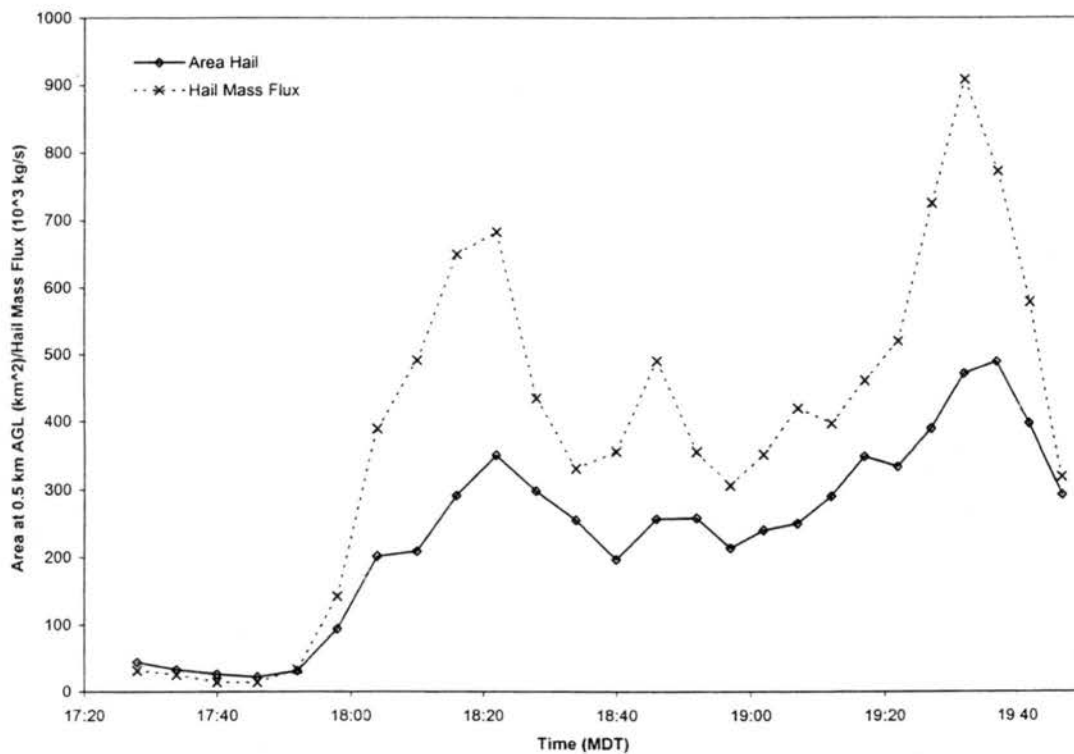


Figure 3.14: Hail production by the 15 July 1998 storm as a function of time. Values are at 0.5 km AGL.

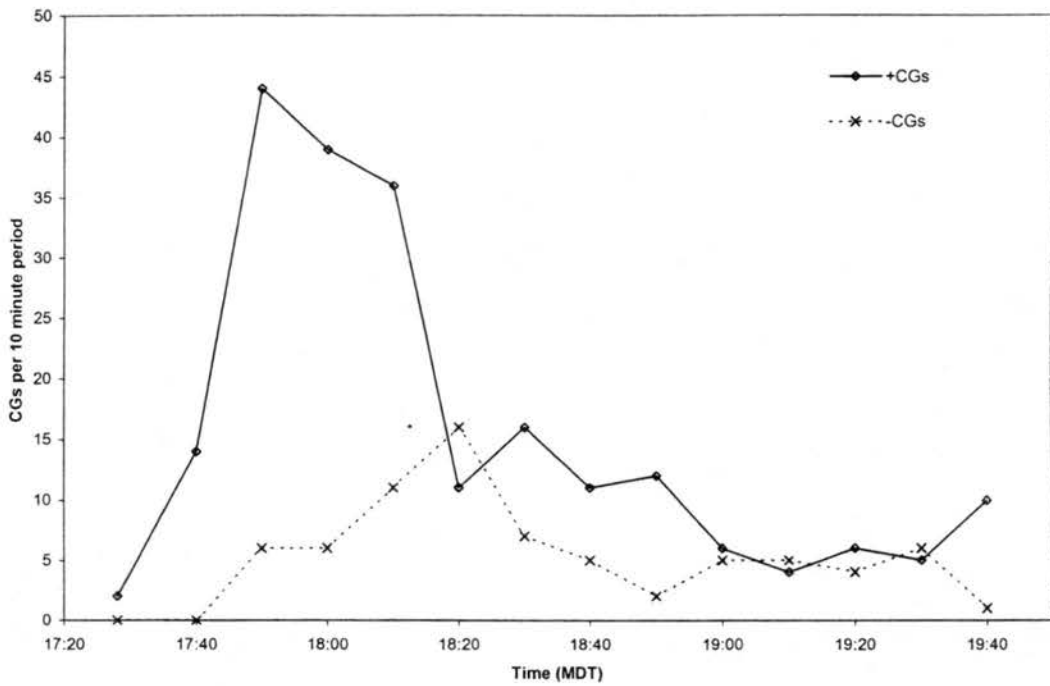
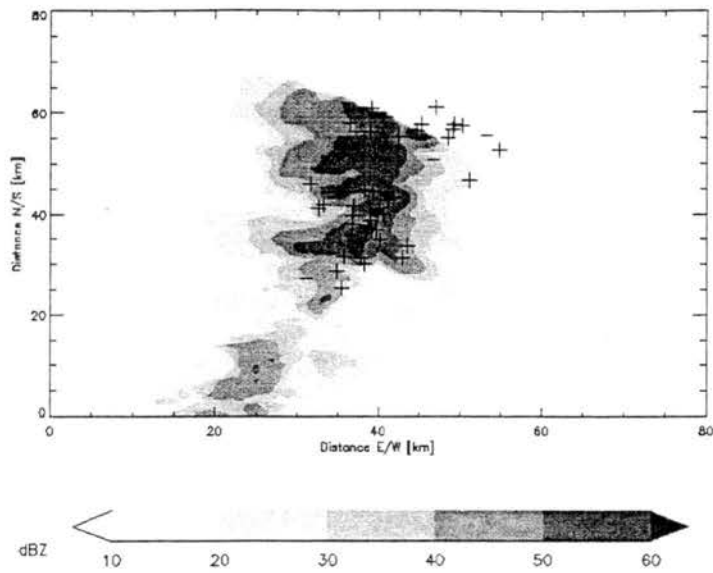


Figure 3.15: CG flash rate as a function of time for the 15 July 1998 storm.

a.



b.

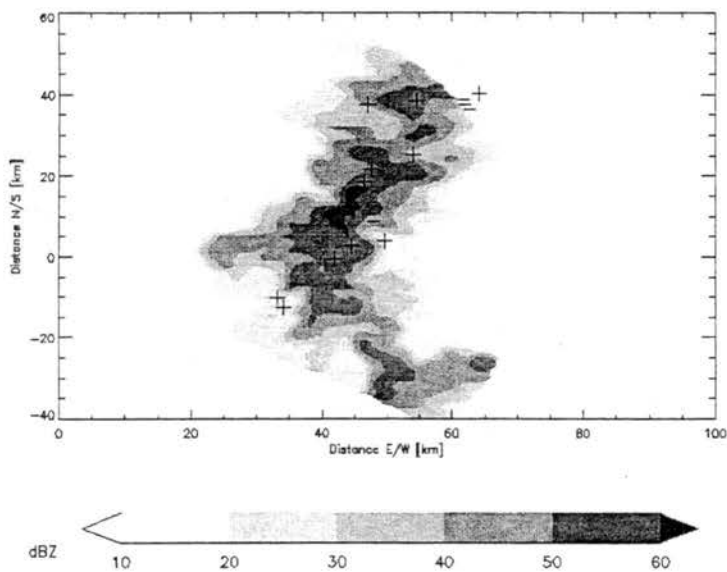


Figure 3.16: a) Horizontal cross-section of CHILL radar reflectivity at 0.5 km AGL, at 1804 MDT on 15 July 1998. Also shown are ground strike positions (plus signs for positives, minus signs for negatives) of NLDN CGs that occurred during 1800-1810 MDT. b) Same as a) except for radar at 1840 MDT and CG lightning during 1840-1850 MDT. Distances are relative to CHILL.

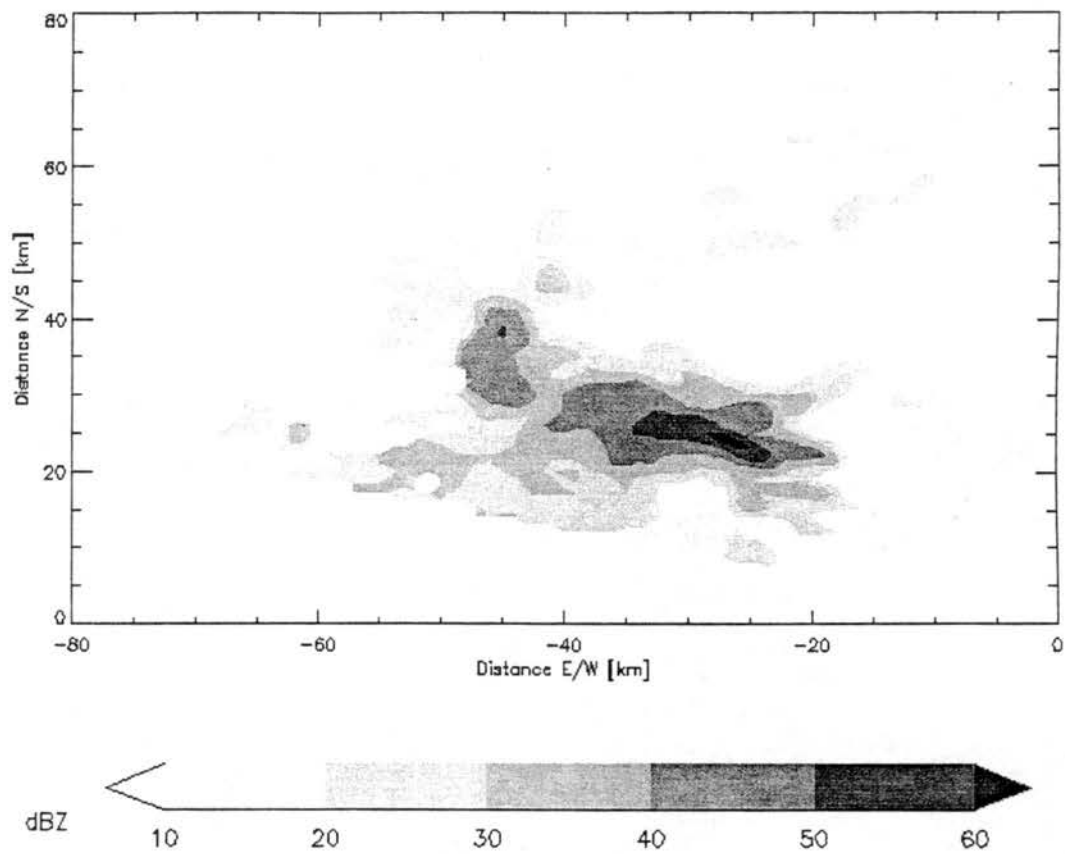


Figure 3.17: Horizontal cross-section of CHILL radar reflectivity at 0.5 km AGL, at 1531 MDT on 21 July 1998. Distances are relative to CHILL.

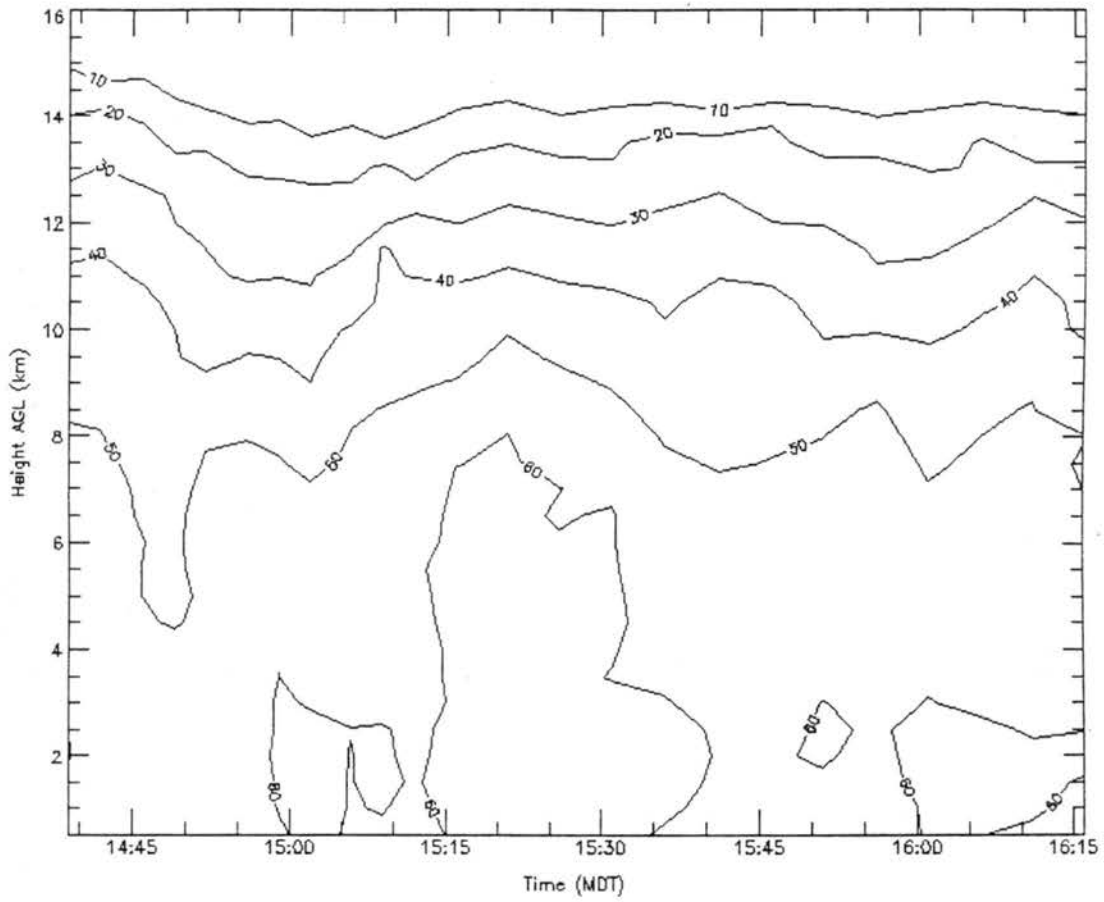


Figure 3.18: Time-height cross-section of peak CHILL radar reflectivity for the 21 July 1998 storm. Values are in dBZ.

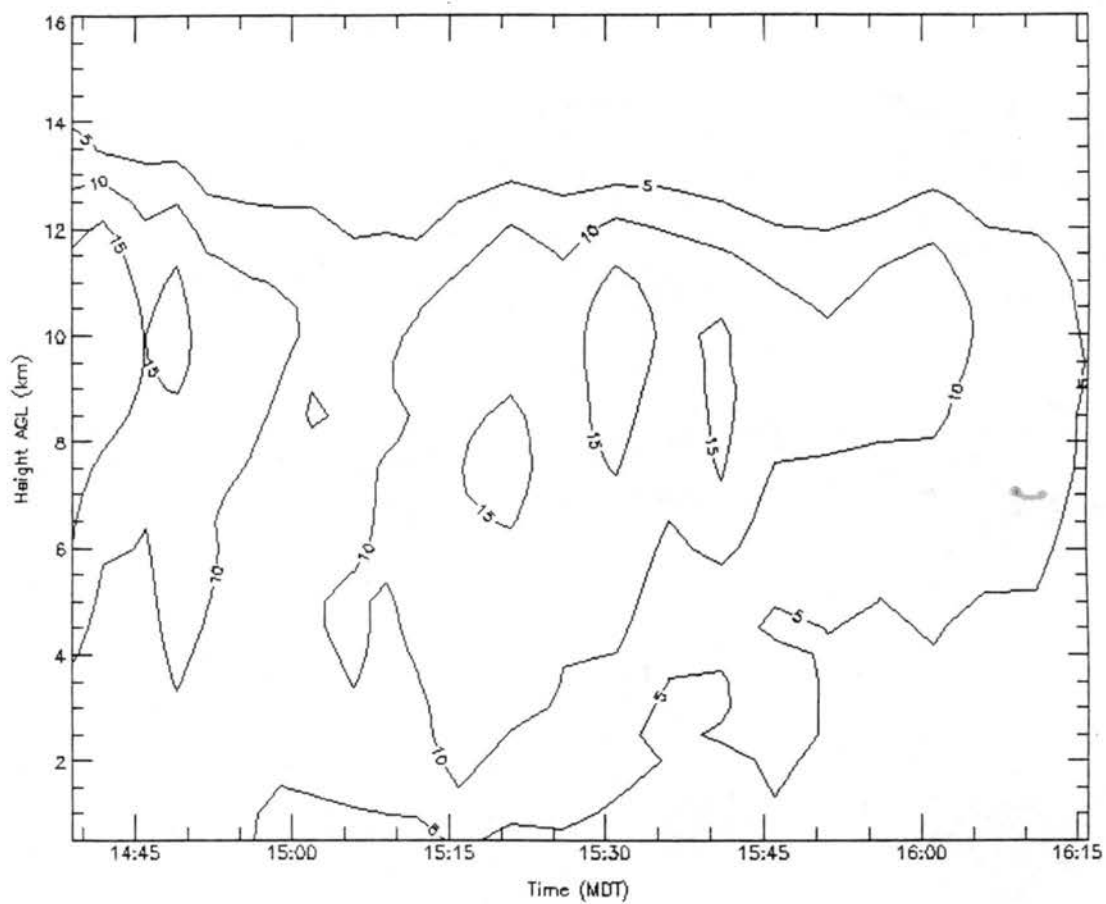


Figure 3.19: Time-height cross-section of maximum vertical velocity for the 21 July 1998 storm. Values are in  $\text{m s}^{-1}$ .

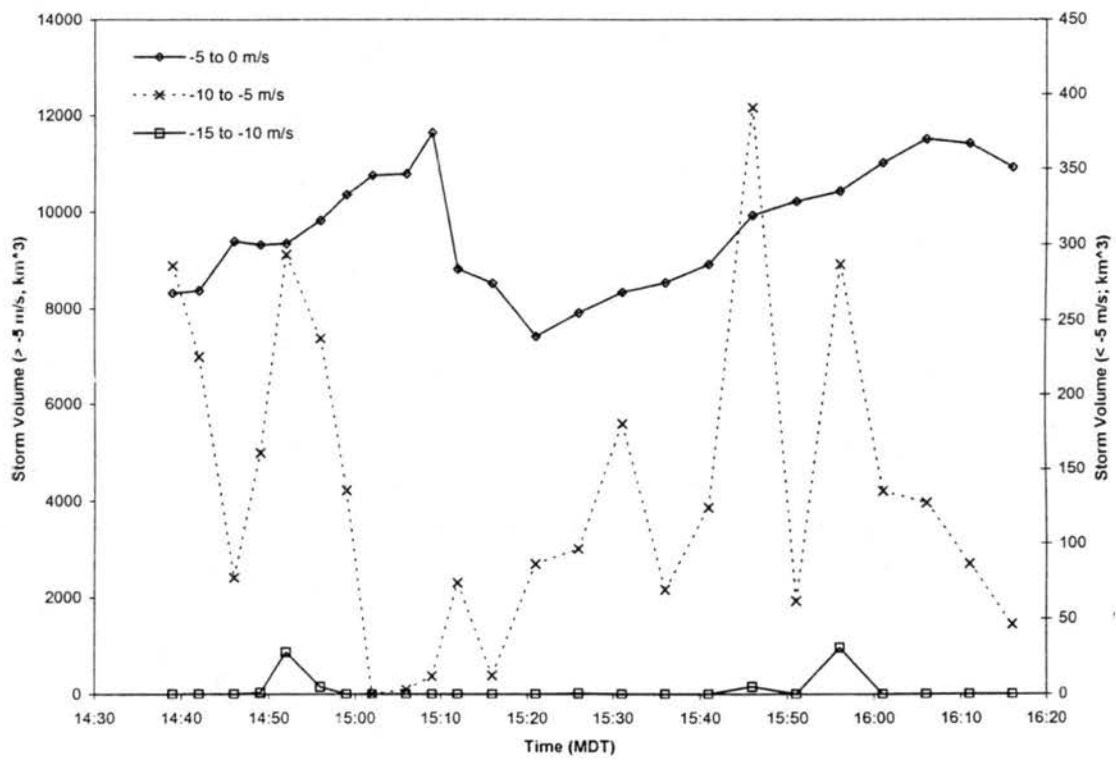


Figure 3.20: Volume of 21 July 1998 storm containing updrafts within respective bins as a function of time.

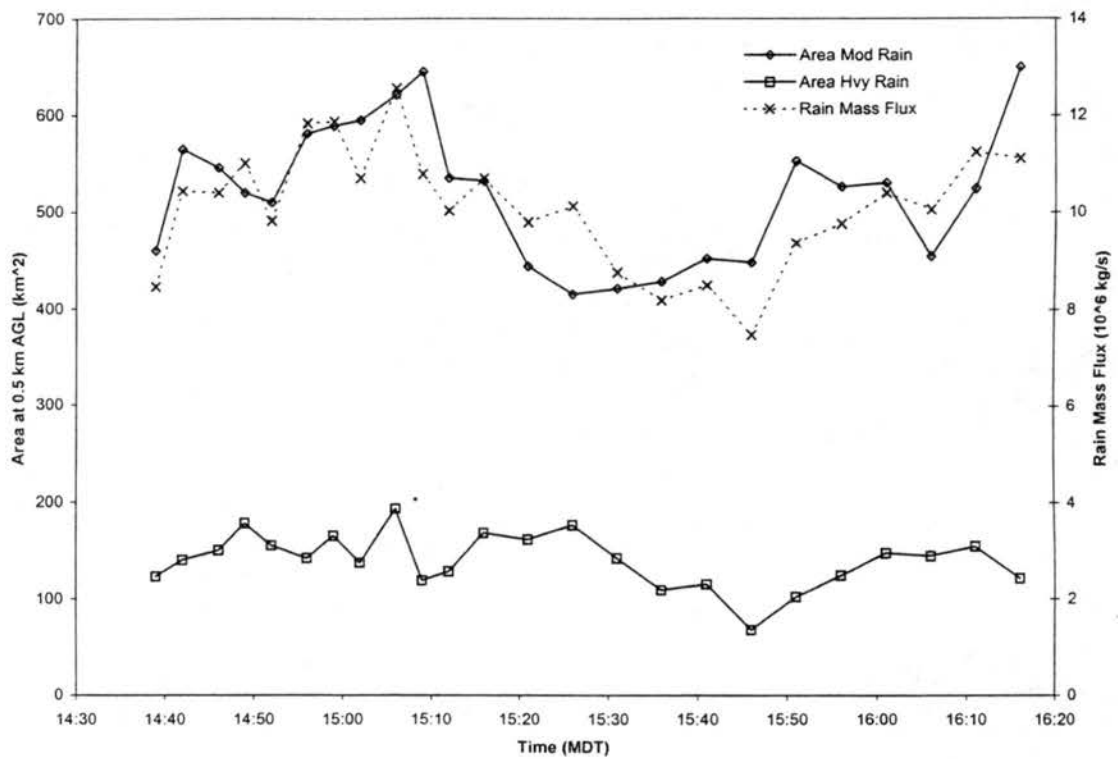


Figure 3.21: Rain production by the 21 July 1998 storm as a function of time. Values are at 0.5 km AGL. Moderate rain is 20-60 mm h<sup>-1</sup>, and heavy rain is greater than 60 mm h<sup>-1</sup>.

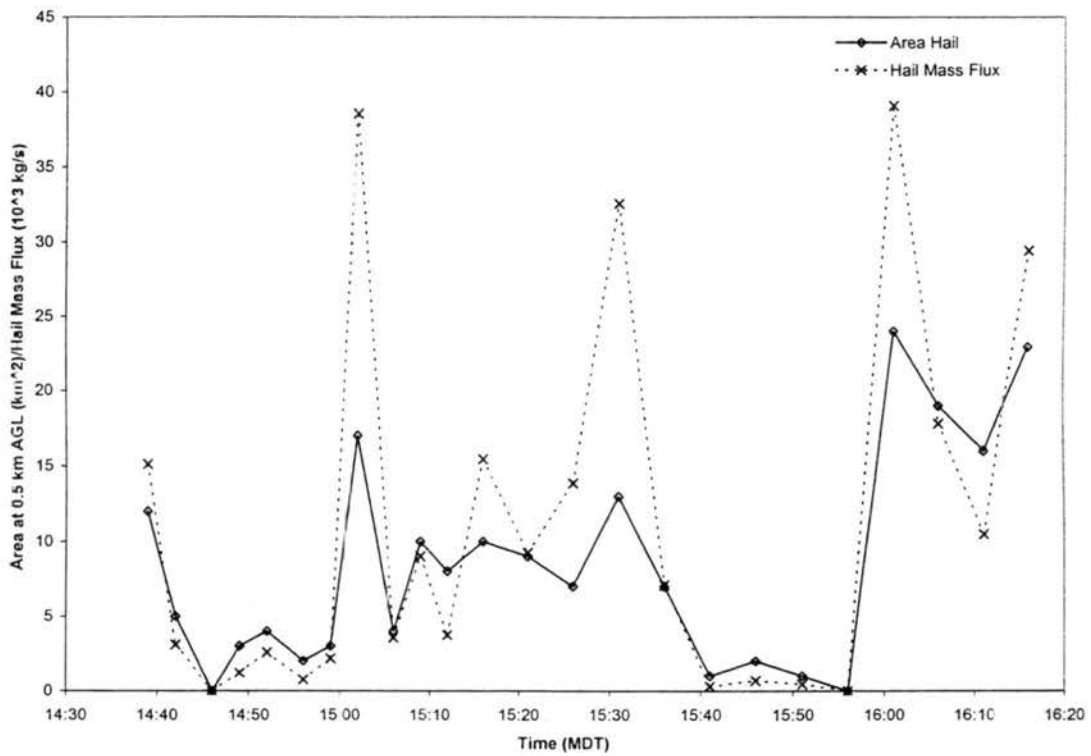


Figure 3.22: Hail production by the 21 July 1998 storm as a function of time. Values are at 0.5 km AGL.

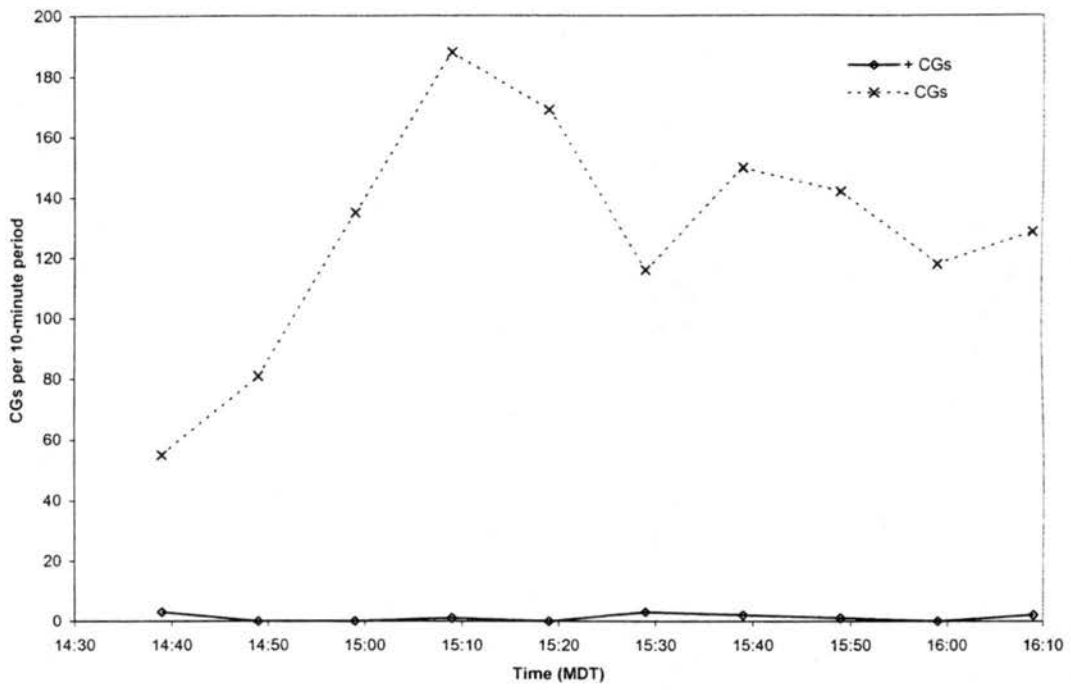


Figure 3.23: CG flash rate as a function of time for the 21 July 1998 storm.

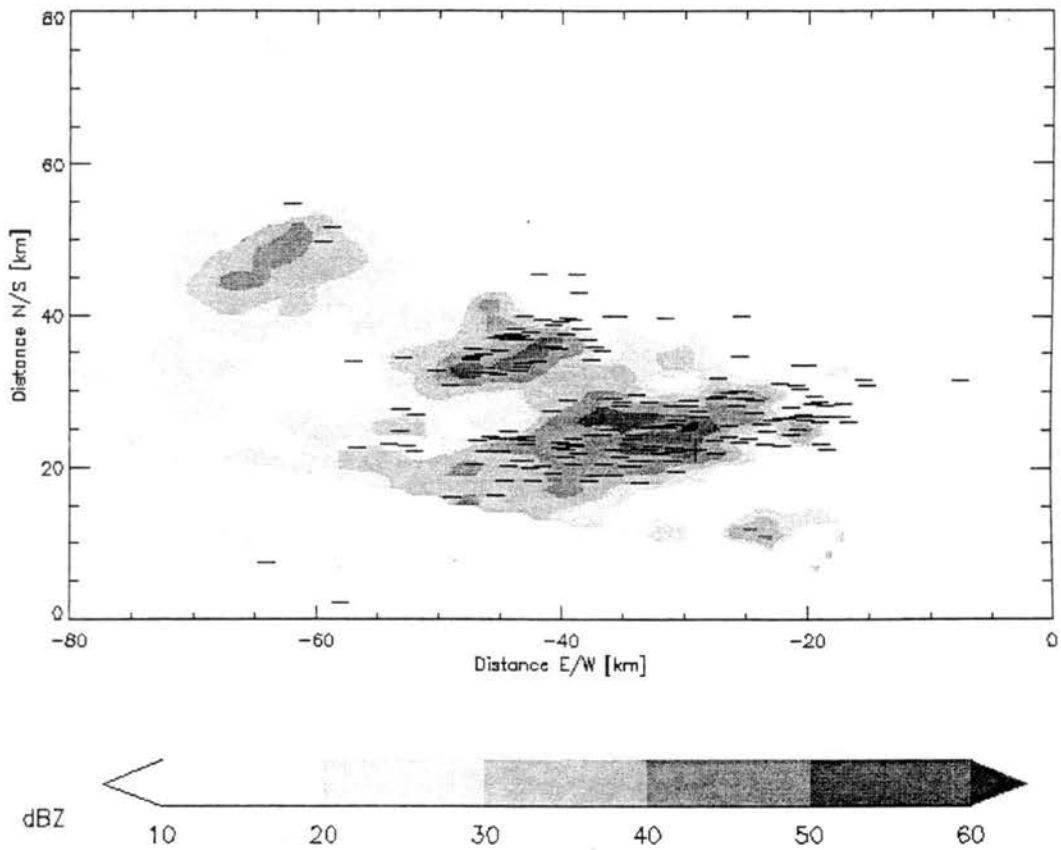


Figure 3.24: Horizontal cross-section of CHILL radar reflectivity at 0.5 km AGL, at 1516 MDT on 21 July 1998. Also shown are ground strike positions (plus signs for positives, minus signs for negatives) of NLDN CGs that occurred during 1509-1519 MDT. Distances are relative to CHILL.

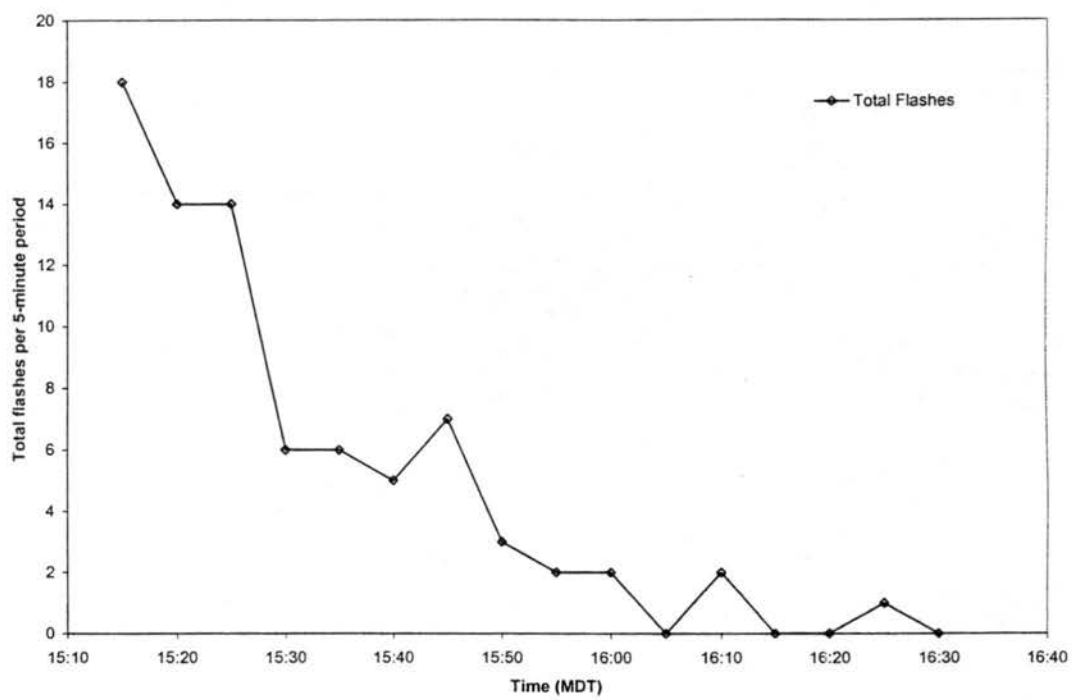


Figure 3.25: Total flash rate as a function of time for the 21 July 1998 storm.

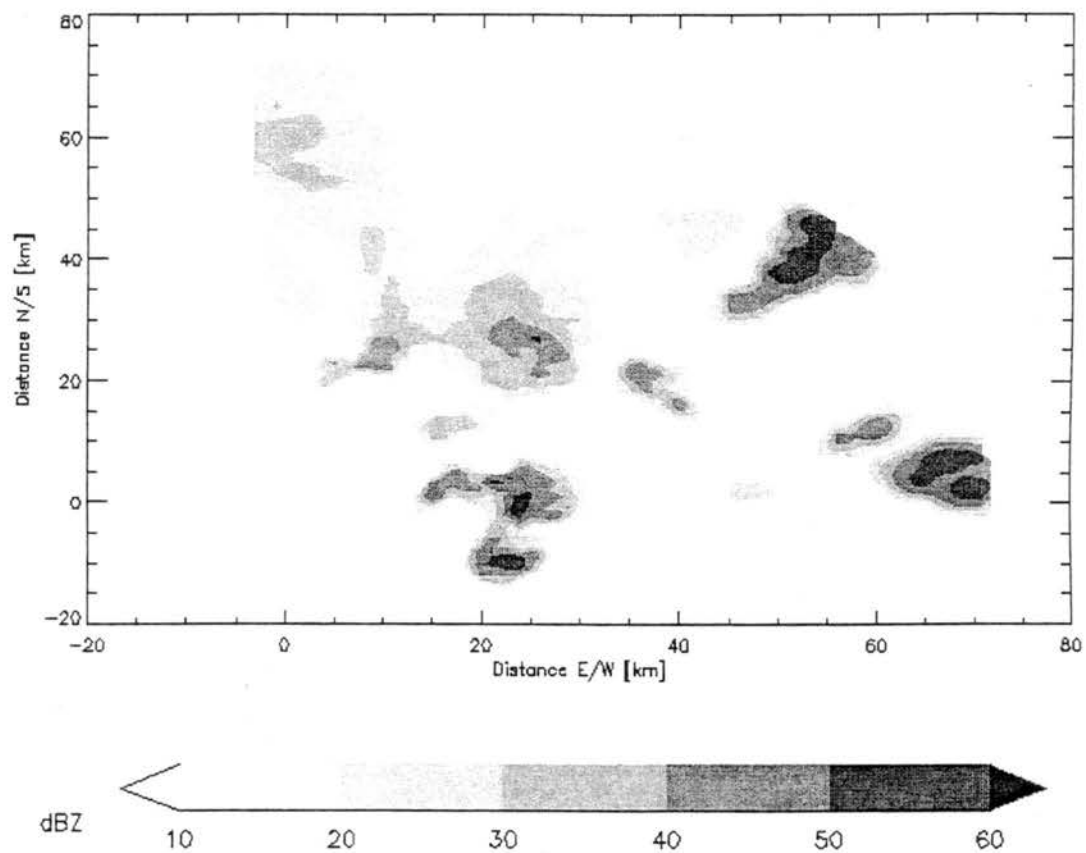


Figure 3.26: Horizontal cross-section of CHILL radar reflectivity at 0.5 km AGL, at 1625 MDT on 25 July 1998. Distances are relative to CHILL.

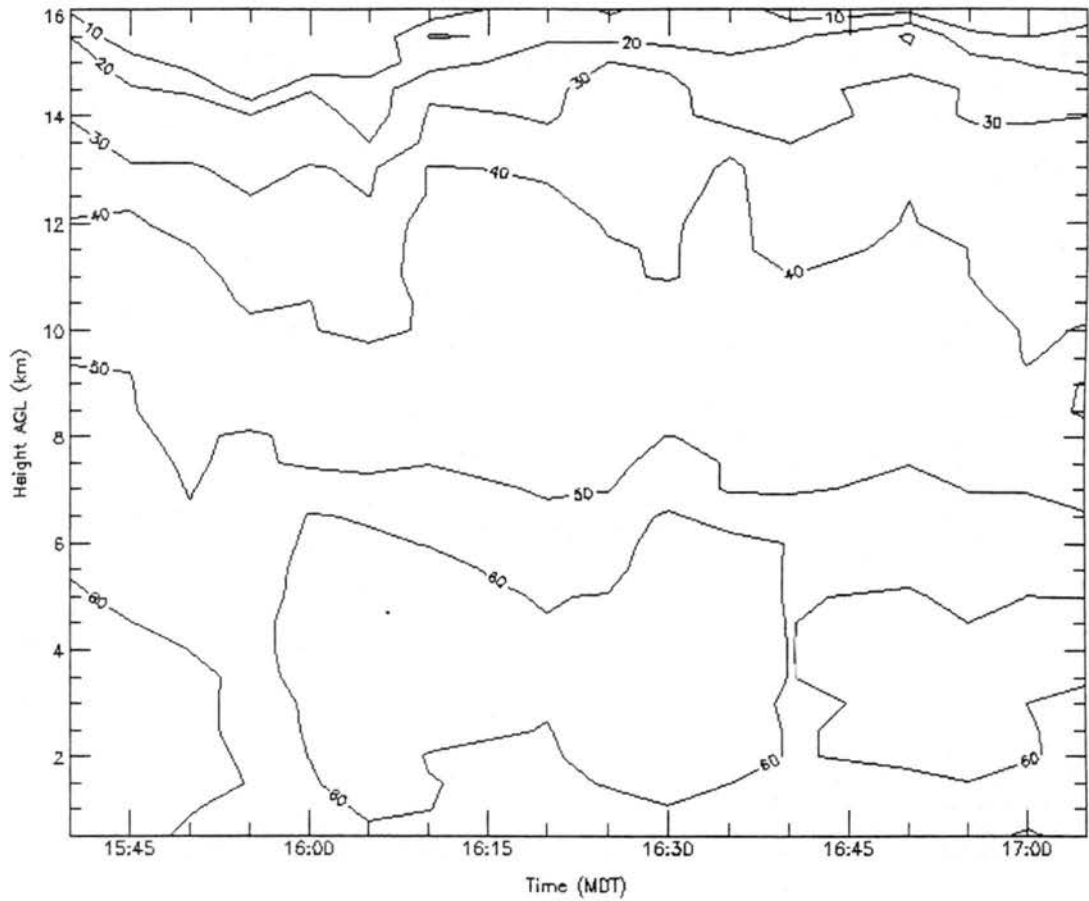


Figure 3.27: Time-height cross-section of peak CHILL radar reflectivity for the 25 July 1998 storm. Values are in dBZ.

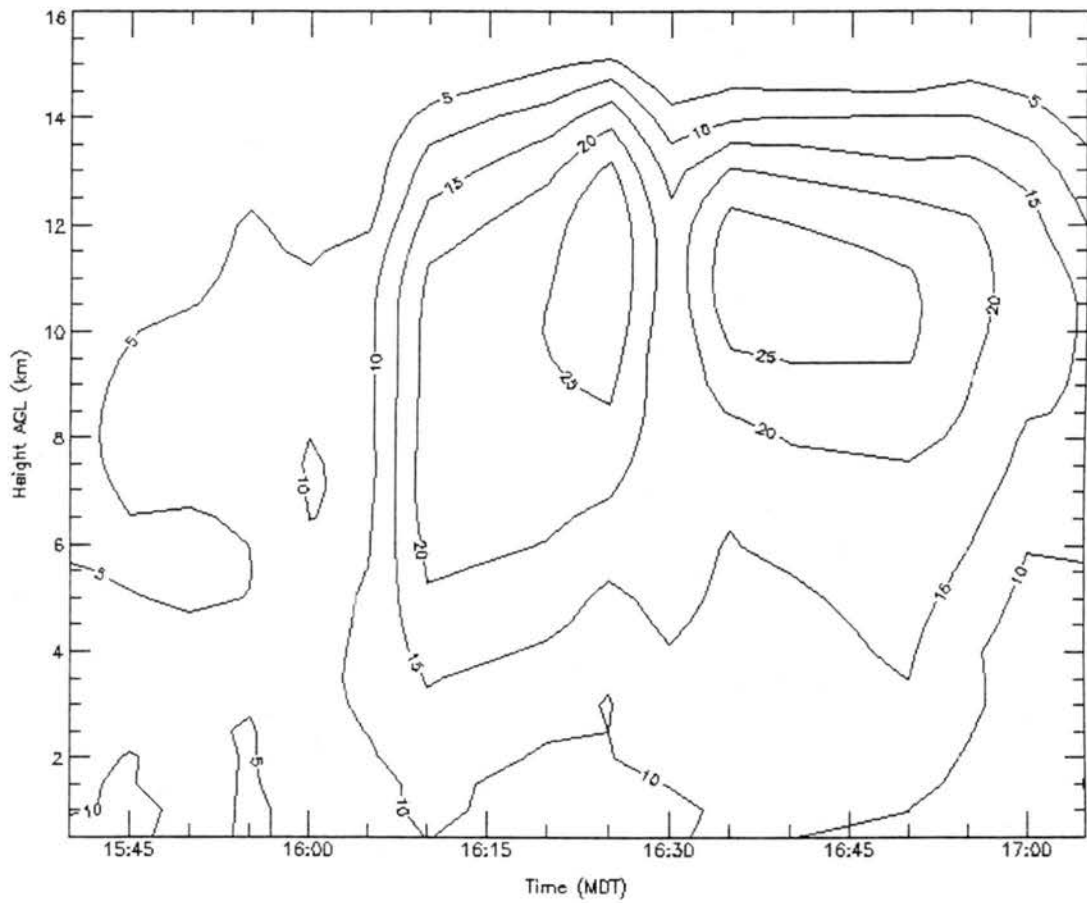


Figure 3.28: Time-height cross-section of maximum vertical velocity for the 25 July 1998 storm. Values are in  $\text{m s}^{-1}$ .

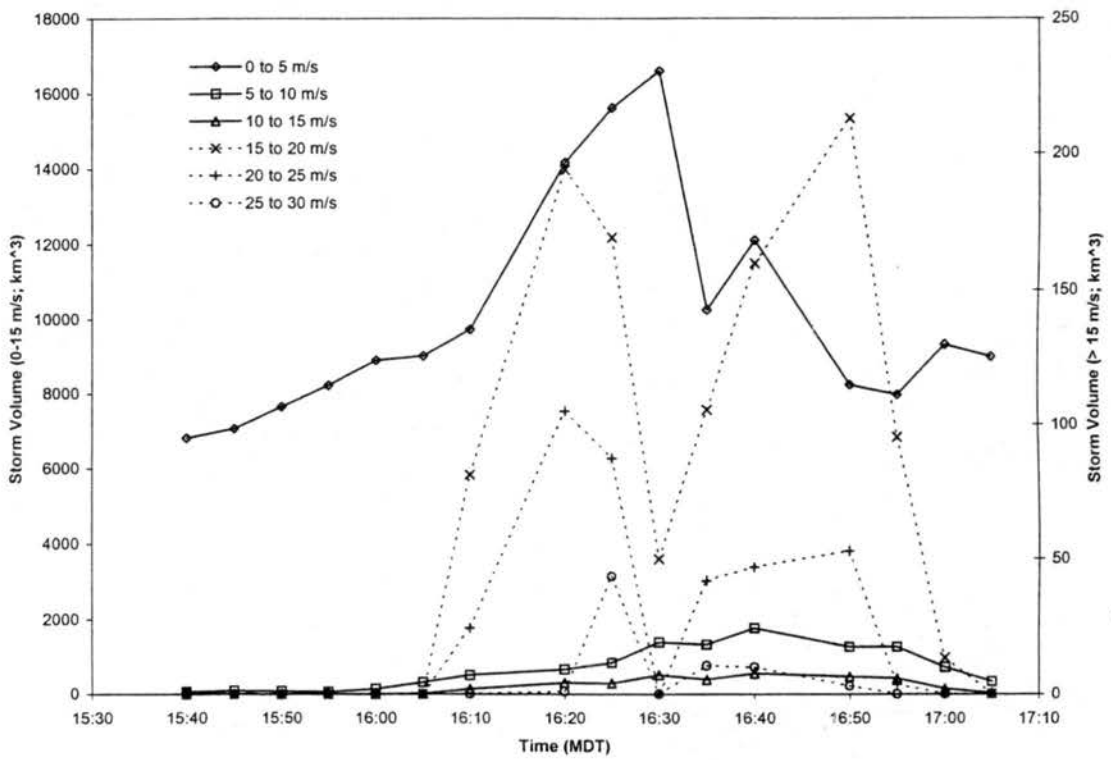


Figure 3.29: Volume of 25 July 1998 storm containing updrafts within respective bins as a function of time.

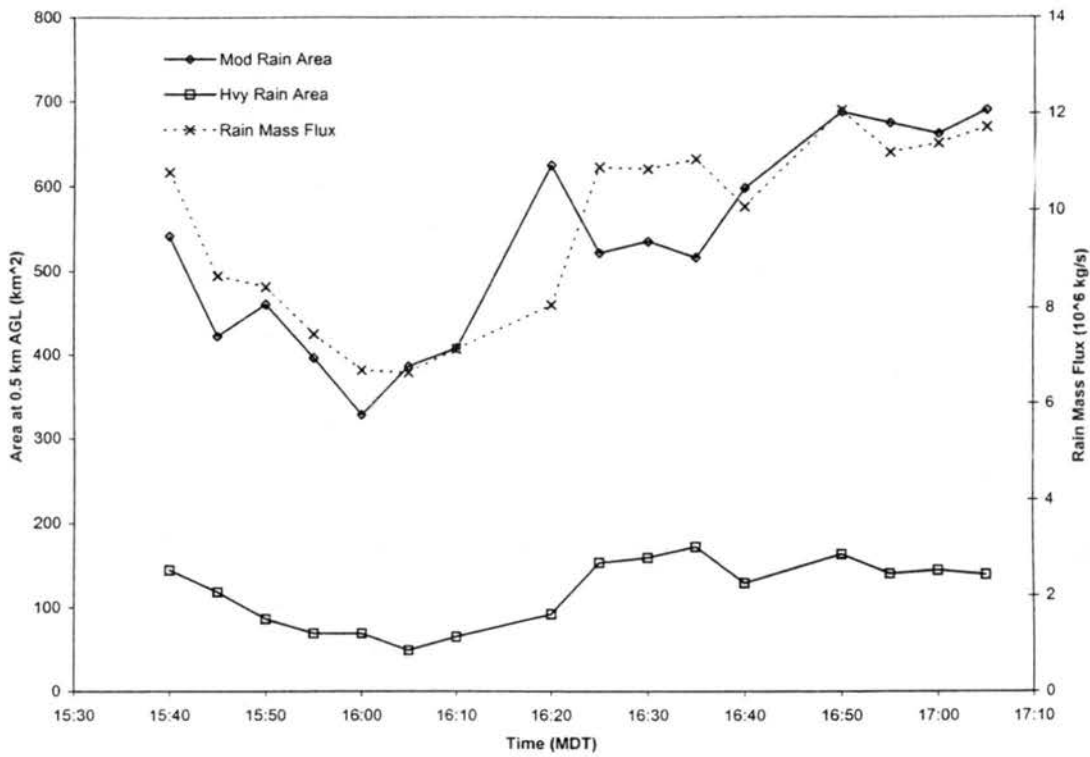


Figure 3.30: Rain production by the 25 July 1998 storm as a function of time. Values are at 0.5 km AGL. Moderate rain is 20-60 mm h<sup>-1</sup>, and heavy rain is greater than 60 mm h<sup>-1</sup>.

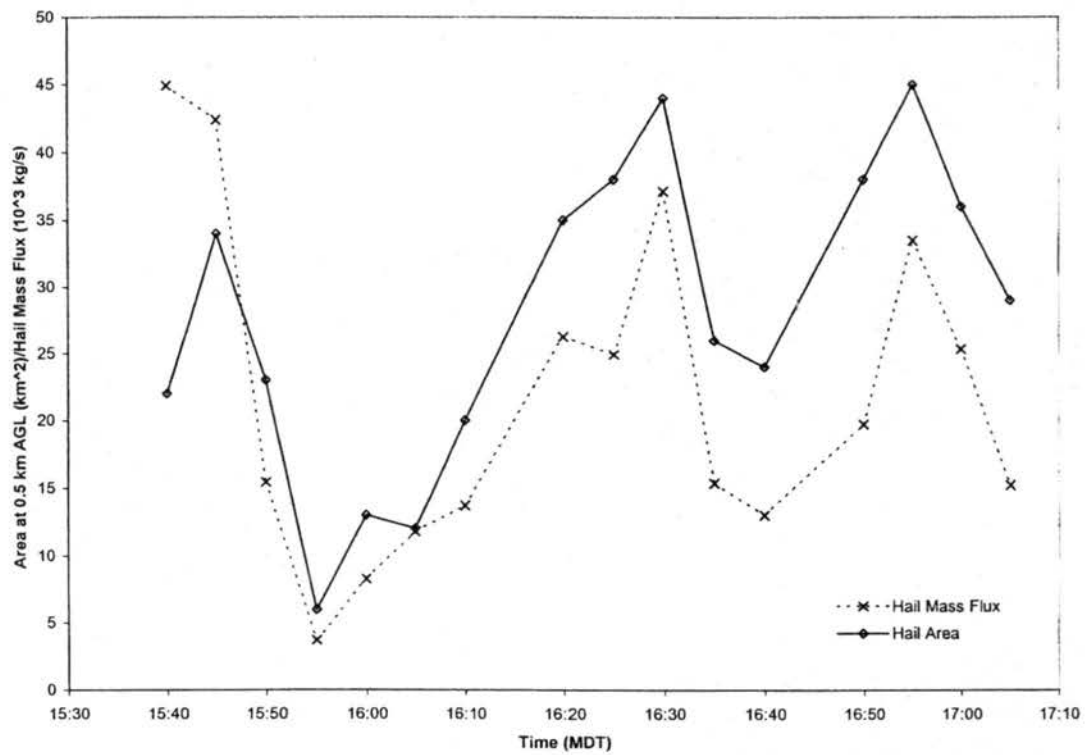


Figure 3.31: Hail production by the 25 July 1998 storm as a function of time. Values are at 0.5 km AGL.

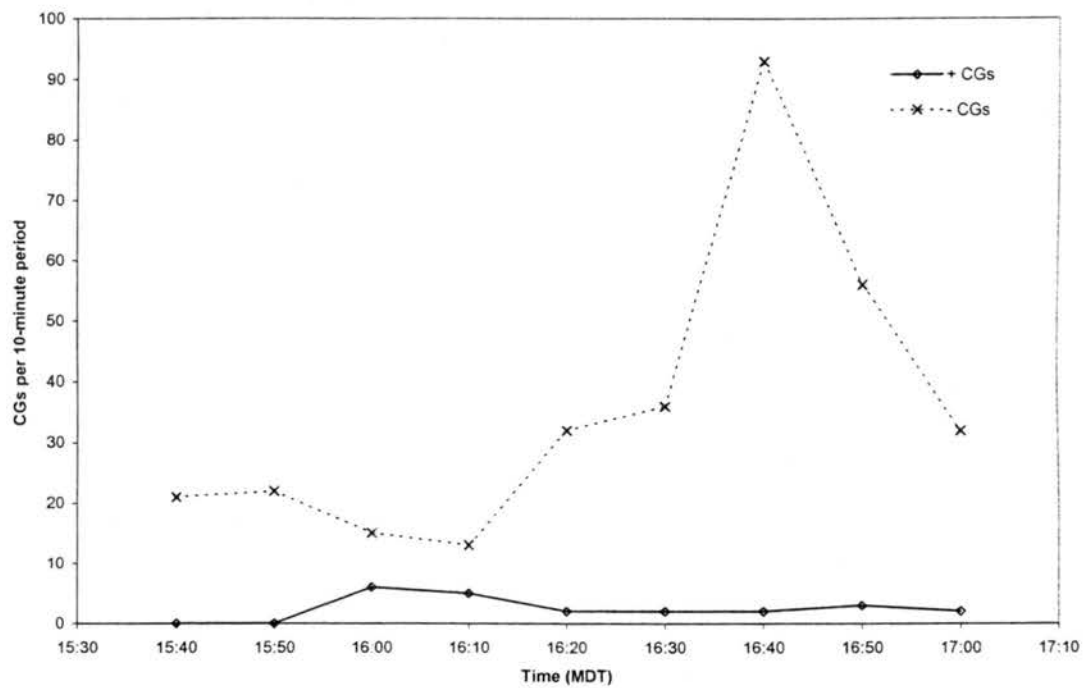


Figure 3.32: CG flash rate as a function of time for the 25 July 1998 storm.

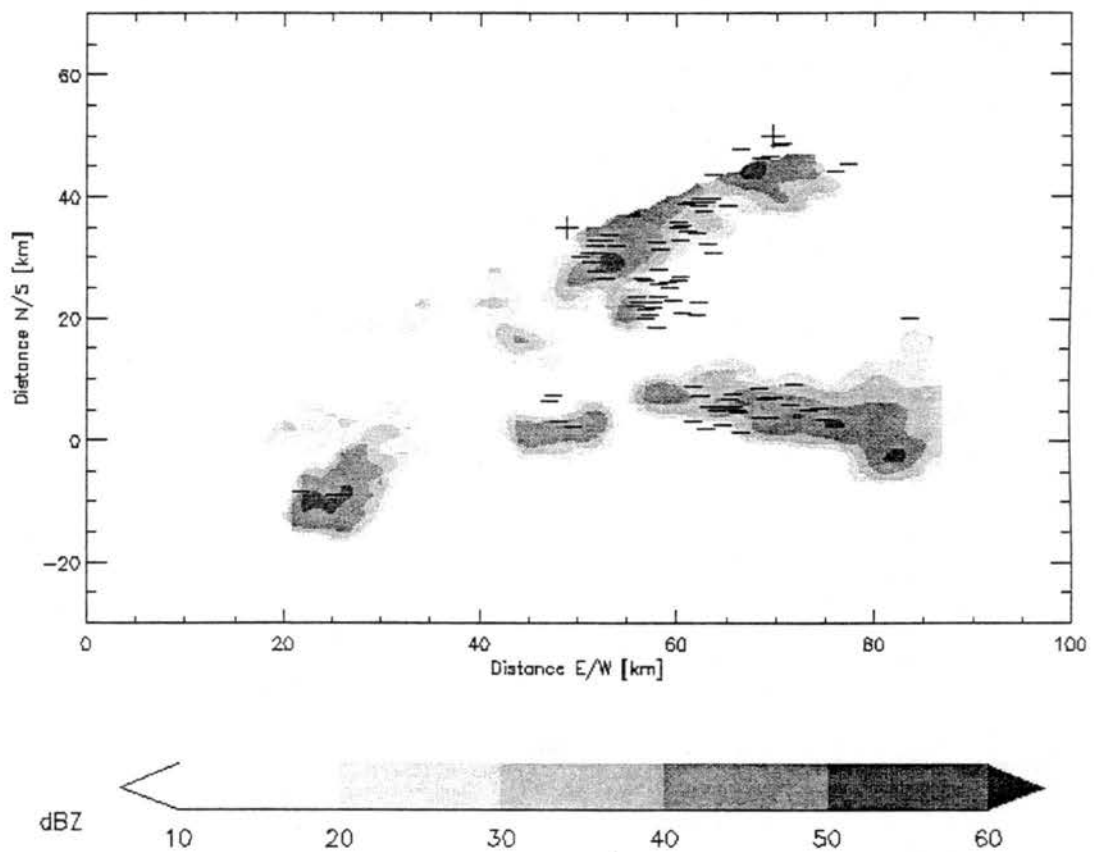


Figure 3.33: Horizontal cross-section of CHILL radar reflectivity at 0.5 km AGL, at 1640 MDT on 25 July 1998. Also shown are ground strike positions (plus signs for positives, minus signs for negatives) of NLDN CGs that occurred during 1640-1650 MDT. Distances are relative to CHILL.

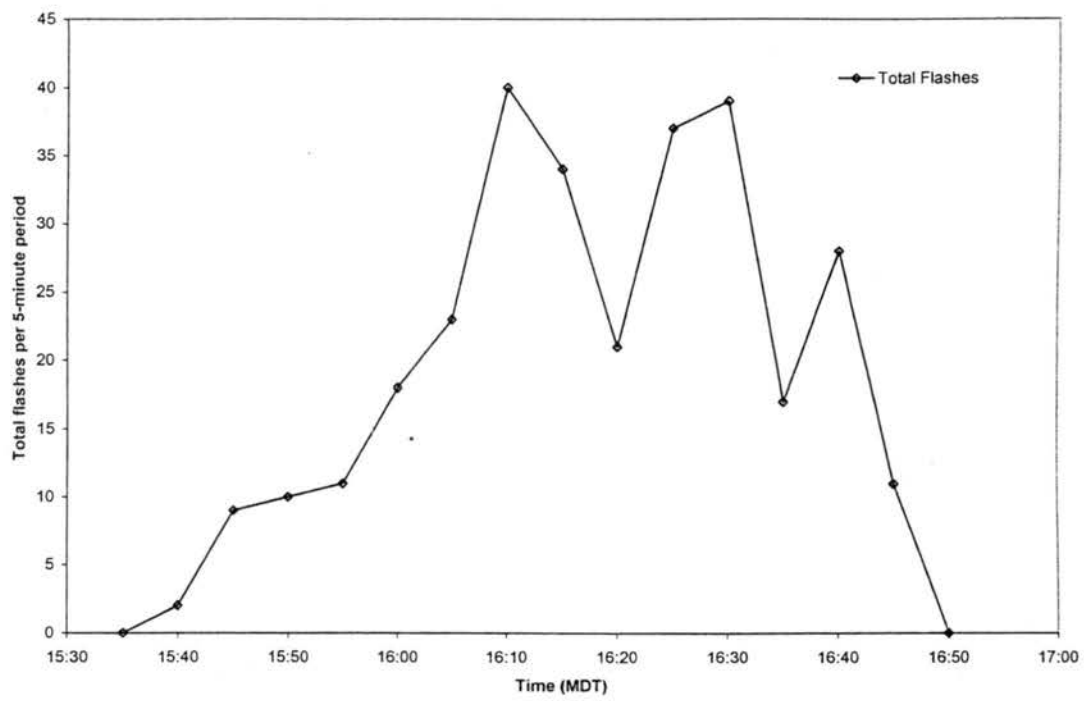


Figure 3.34: Total flash rate as a function of time for the 25 July 1998 storm.

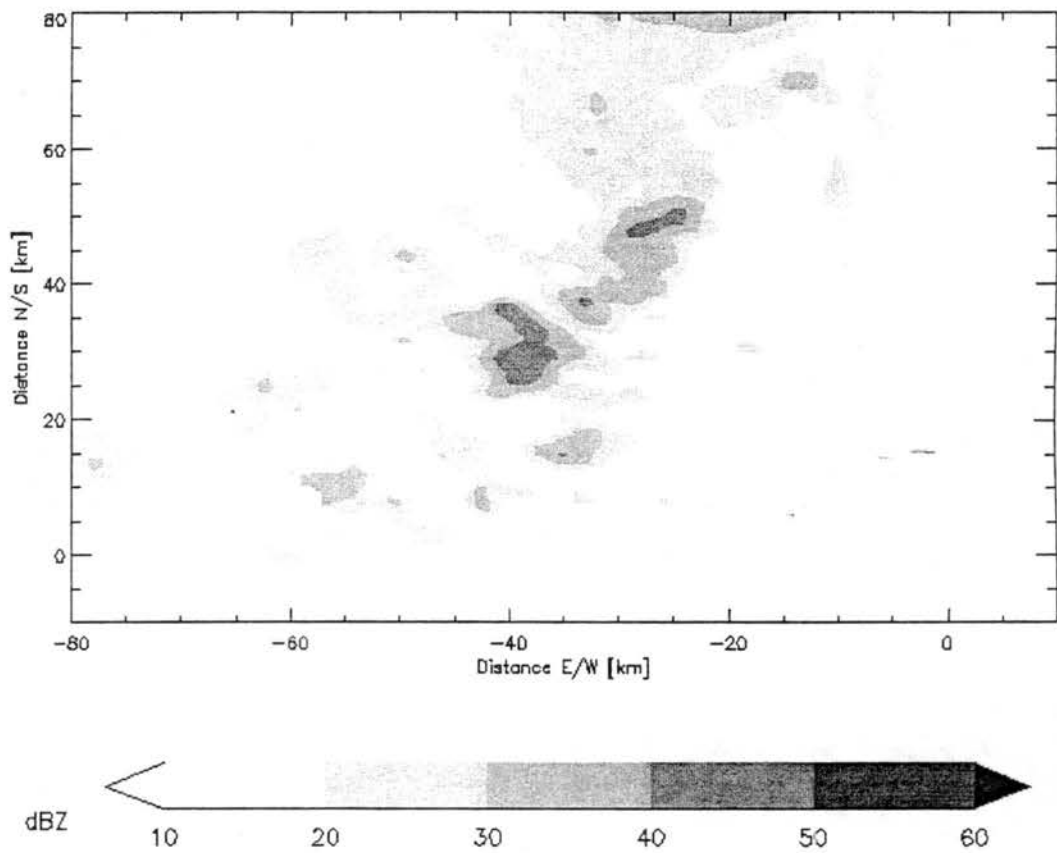


Figure 3.35: Horizontal cross-section of CHILL radar reflectivity at 0.5 km AGL, at 1716 MDT on 30 July 1998. Distances are relative to CHILL.

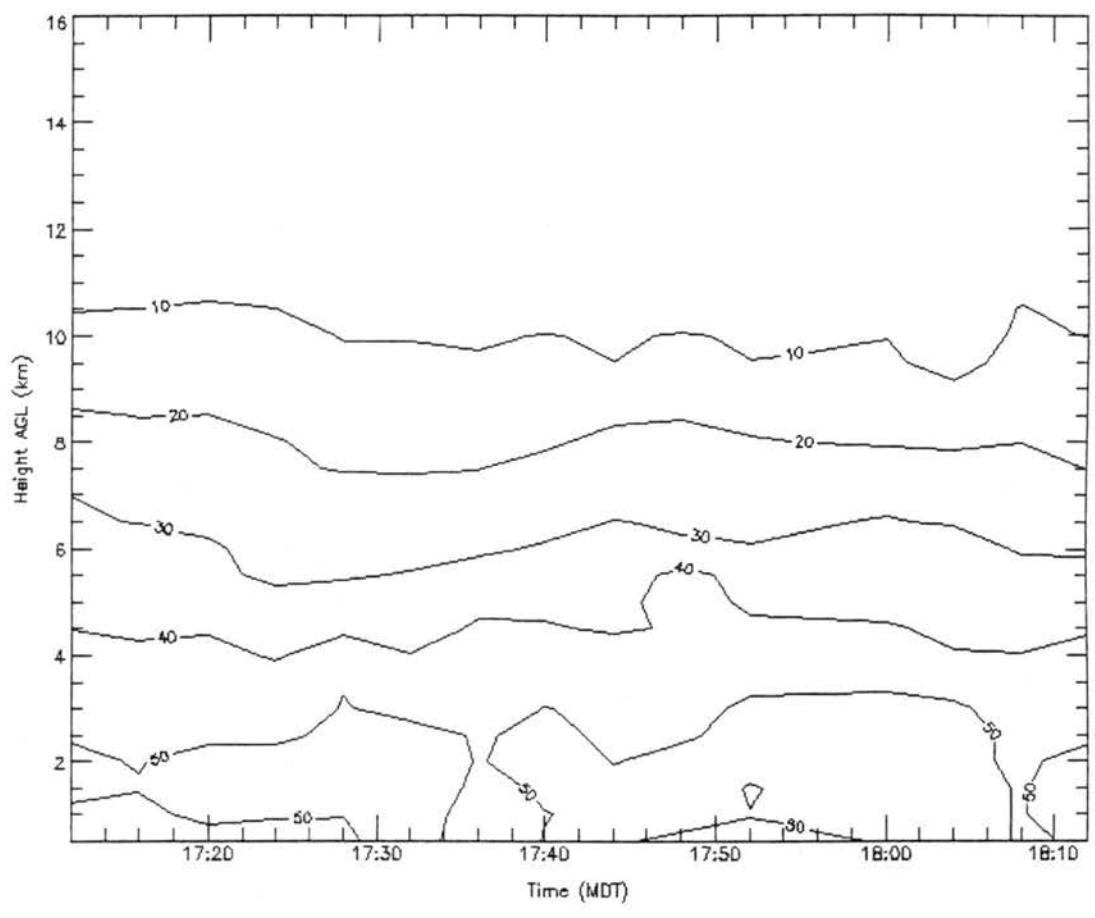


Figure 3.36: Time-height cross-section of peak CHILL radar reflectivity for the 30 July 1998 storm. Values are in dBZ.

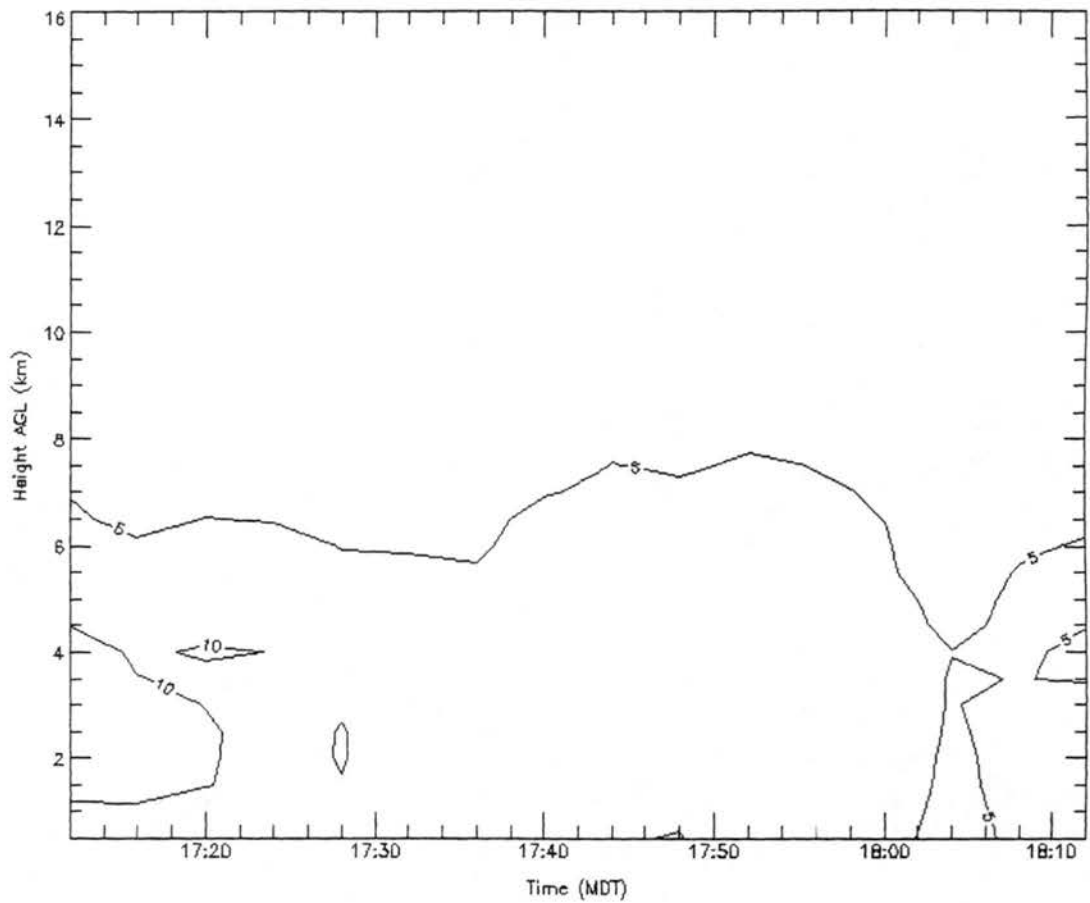


Figure 3.37: Time-height cross-section of maximum vertical velocity for the 30 July 1998 storm. Values are in  $\text{m s}^{-1}$ .

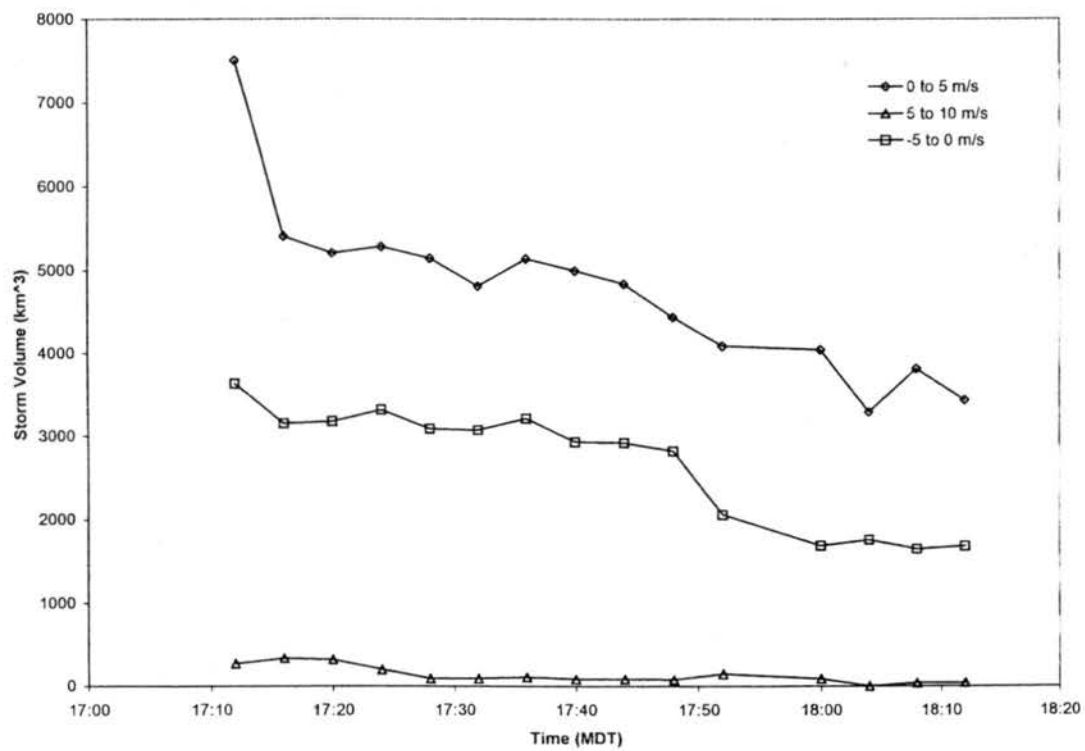


Figure 3.38: Volume of 30 July 1998 storm containing updrafts within respective bins as a function of time.

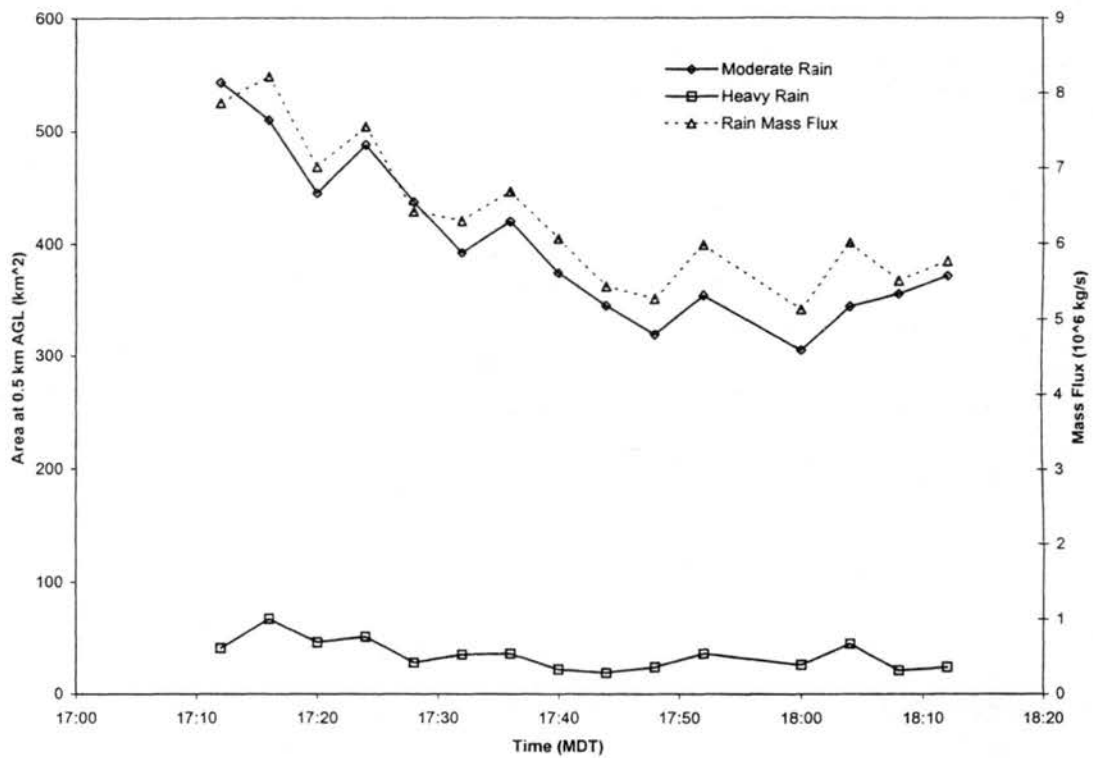


Figure 3.39: Rain production by the 30 July 1998 storm as a function of time. Values are at 0.5 km AGL. Moderate rain is 20-60 mm h<sup>-1</sup>, and heavy rain is greater than 60 mm h<sup>-1</sup>.

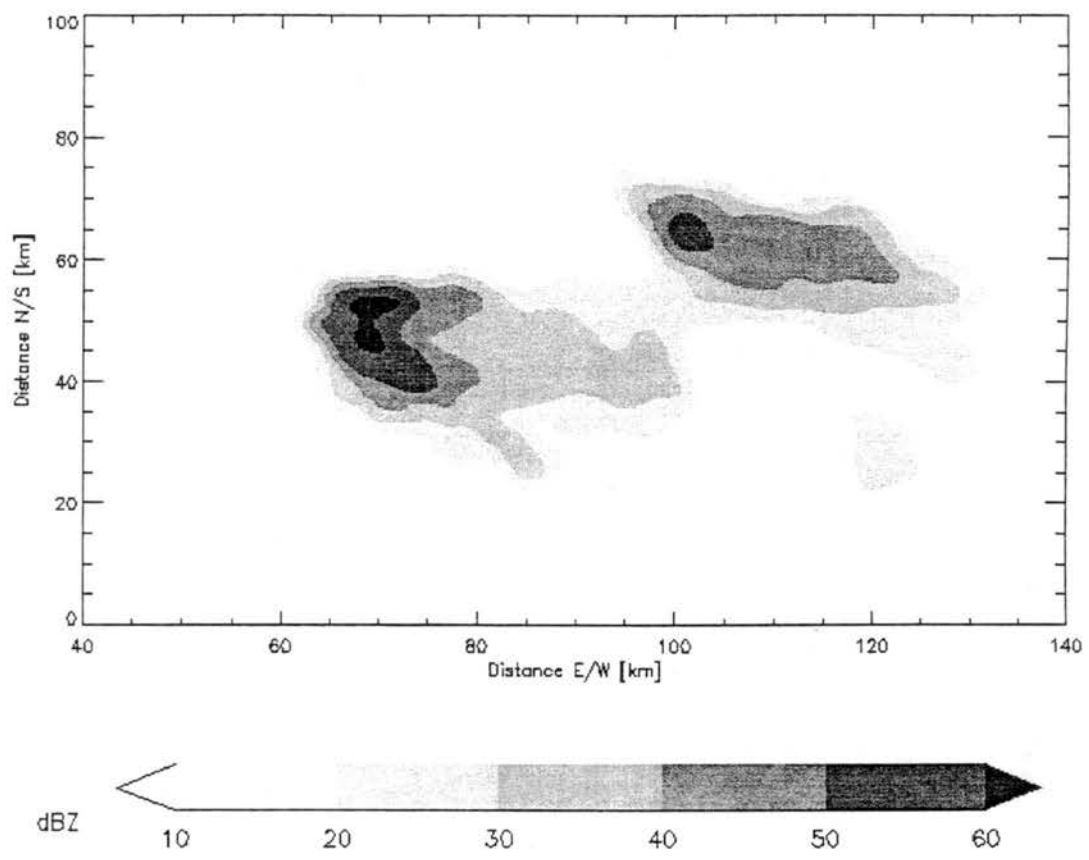


Figure 3.40: Horizontal cross-section of CHILL radar reflectivity at 0.5 km AGL, at 2325 UTC on 29 June 2000. Distances are relative to CHILL.

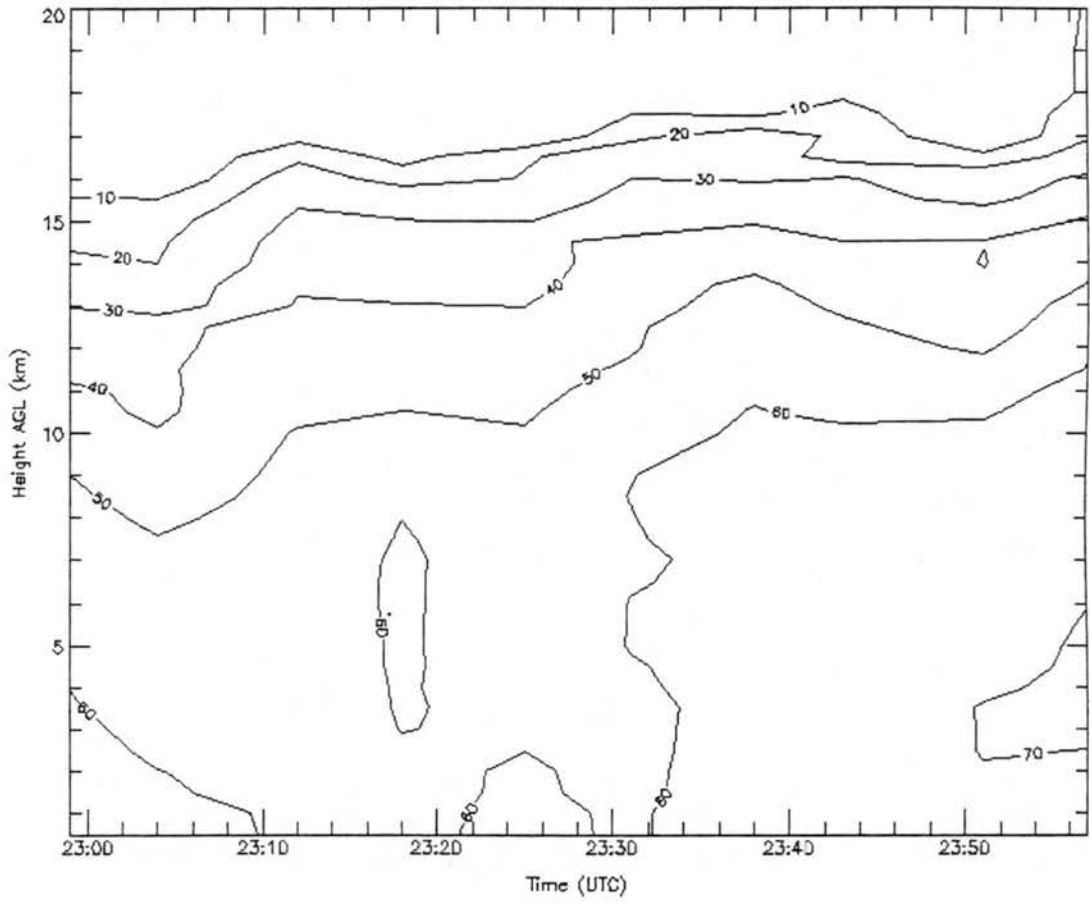


Figure 3.41: Time-height cross-section of peak CHILL radar reflectivity for the 29 June 2000 storm. Values are in dBZ.

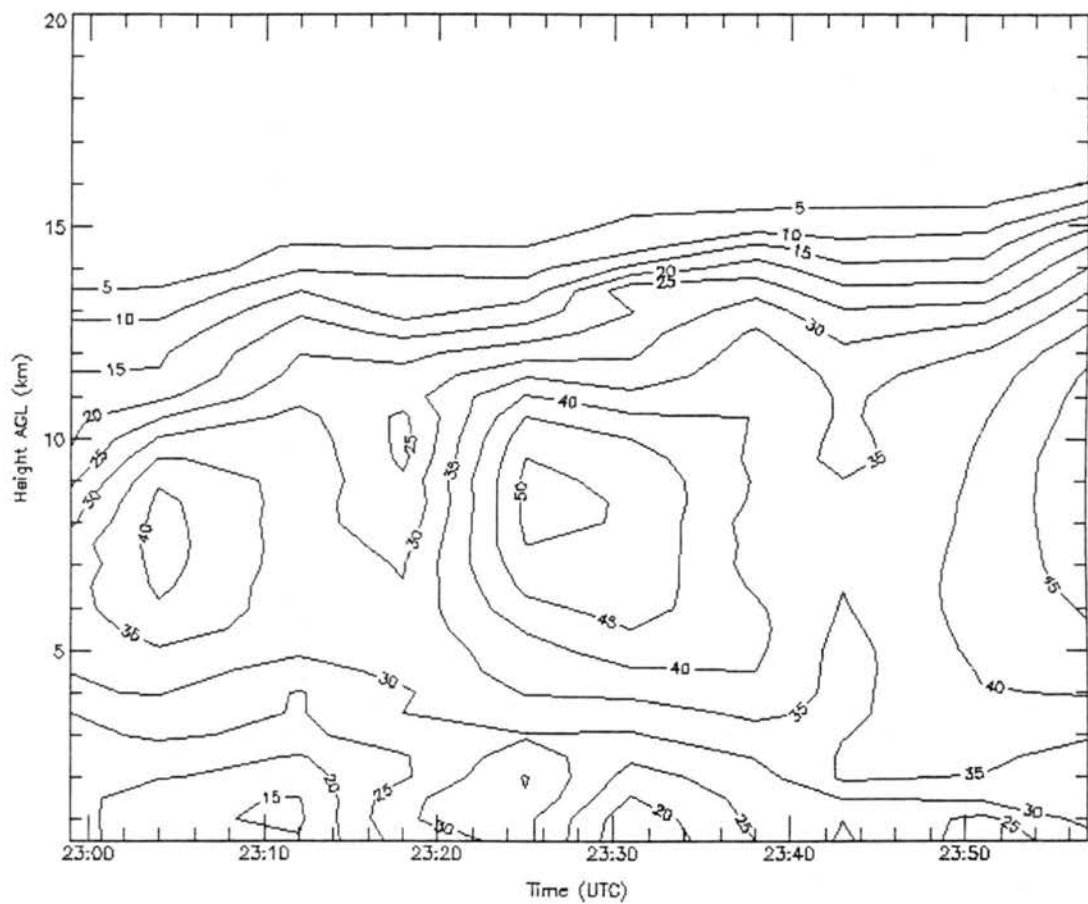


Figure 3.42: Time-height cross-section of maximum vertical velocity for the 29 June 2000 storm. Values are in  $\text{m s}^{-1}$ .

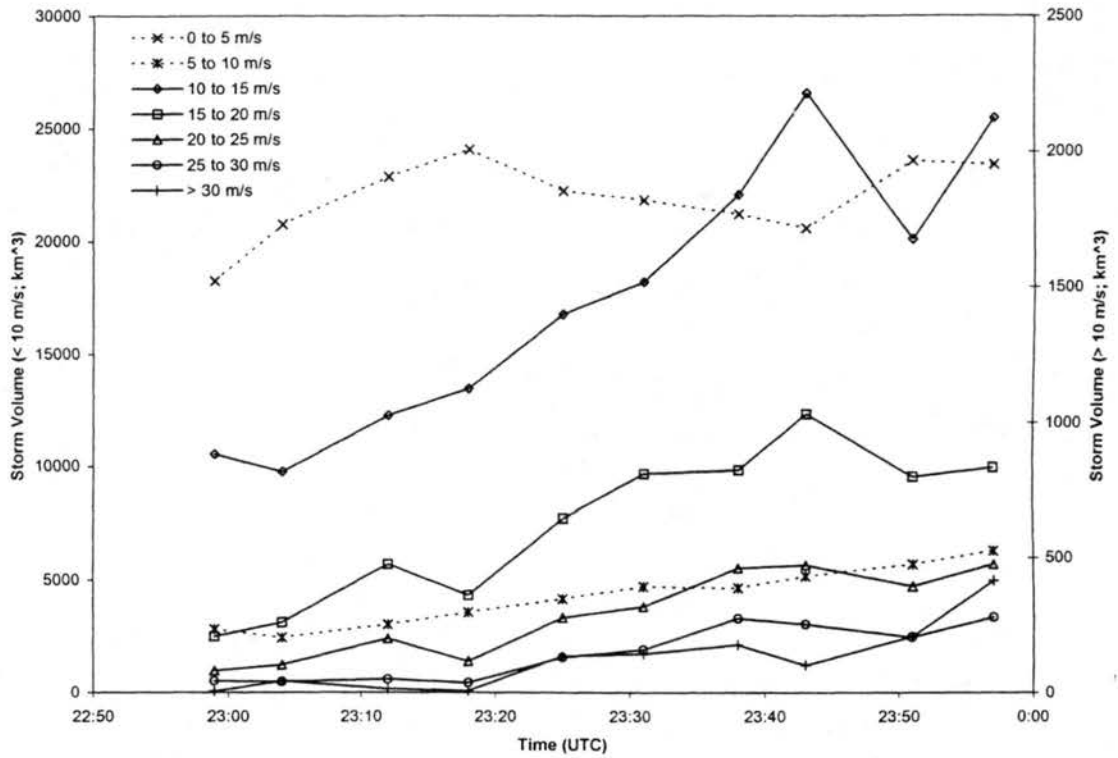


Figure 3.43: Volume of 29 June 2000 storm containing updrafts within respective bins as a function of time.

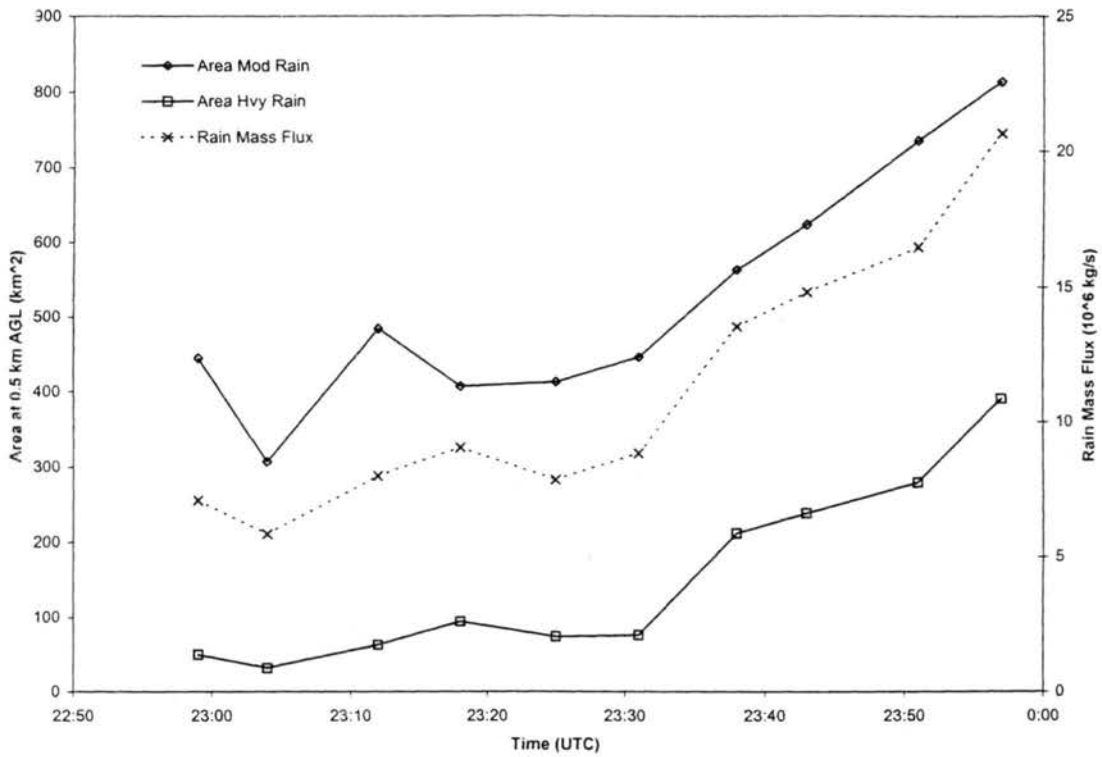


Figure 3.44: Rain production by the 29 June 2000 storm as a function of time. Values are at 0.5 km AGL. Moderate rain is 20-60 mm h<sup>-1</sup>, and heavy rain is greater than 60 mm h<sup>-1</sup>.

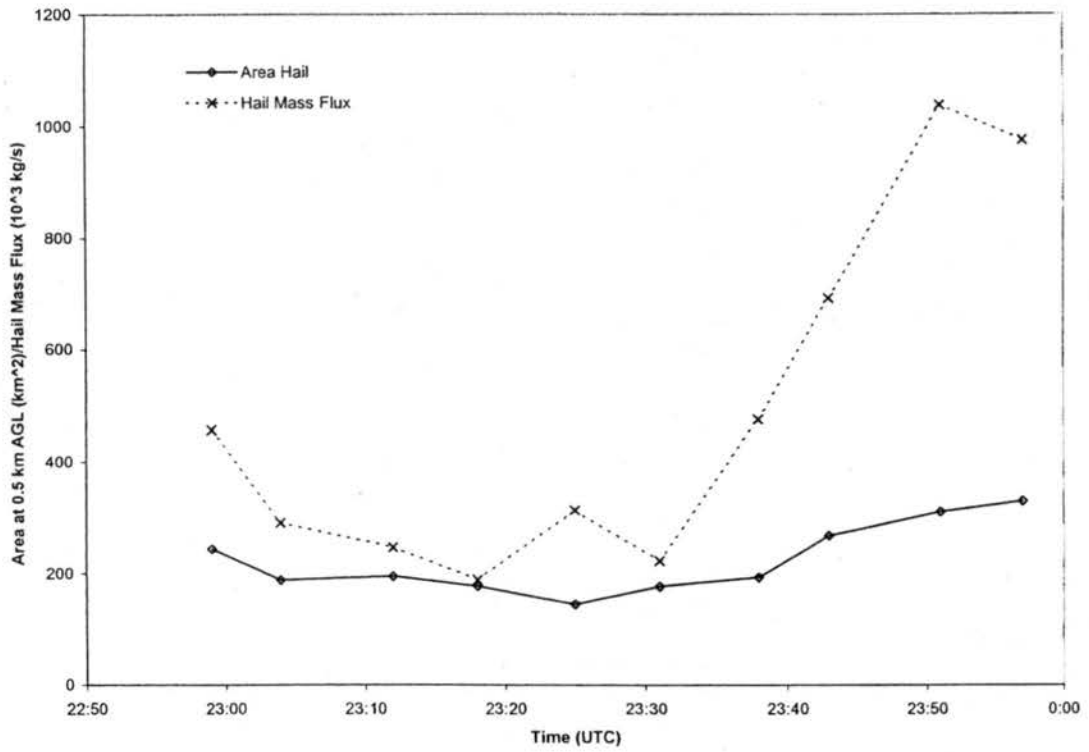


Figure 3.45: Hail production by the 29 June 2000 storm as a function of time. Values are at 0.5 km AGL.

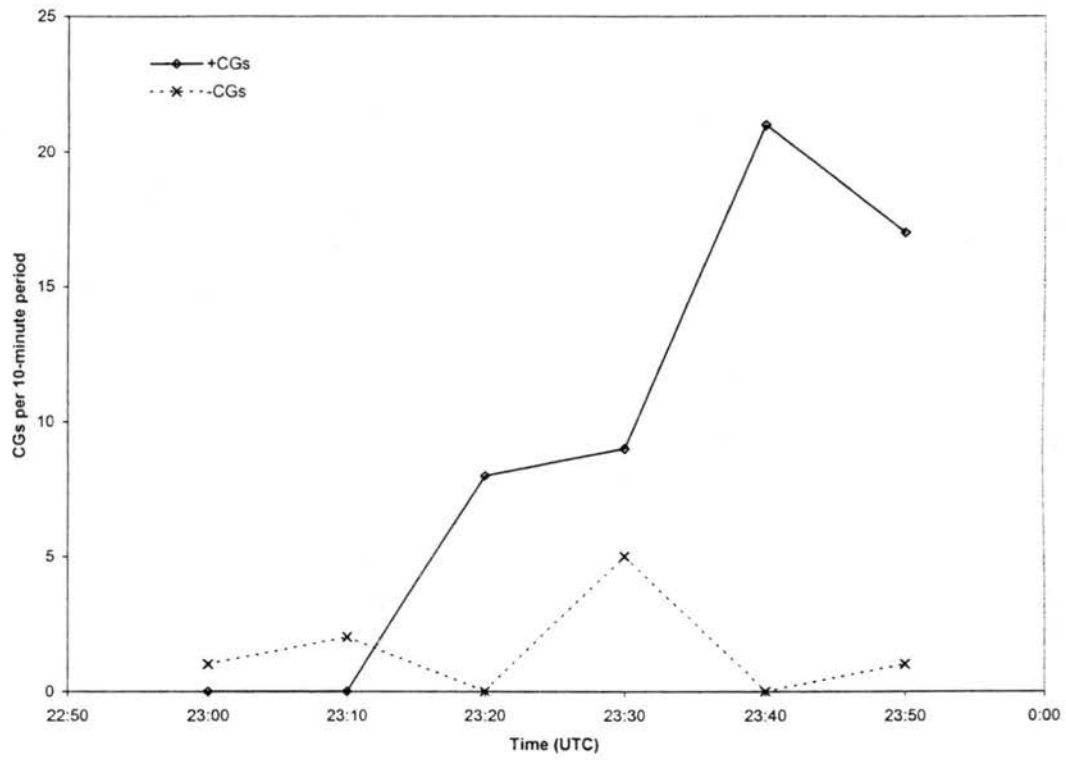


Figure 3.46: CG flash rate as a function of time for the 29 June 2000 storm.

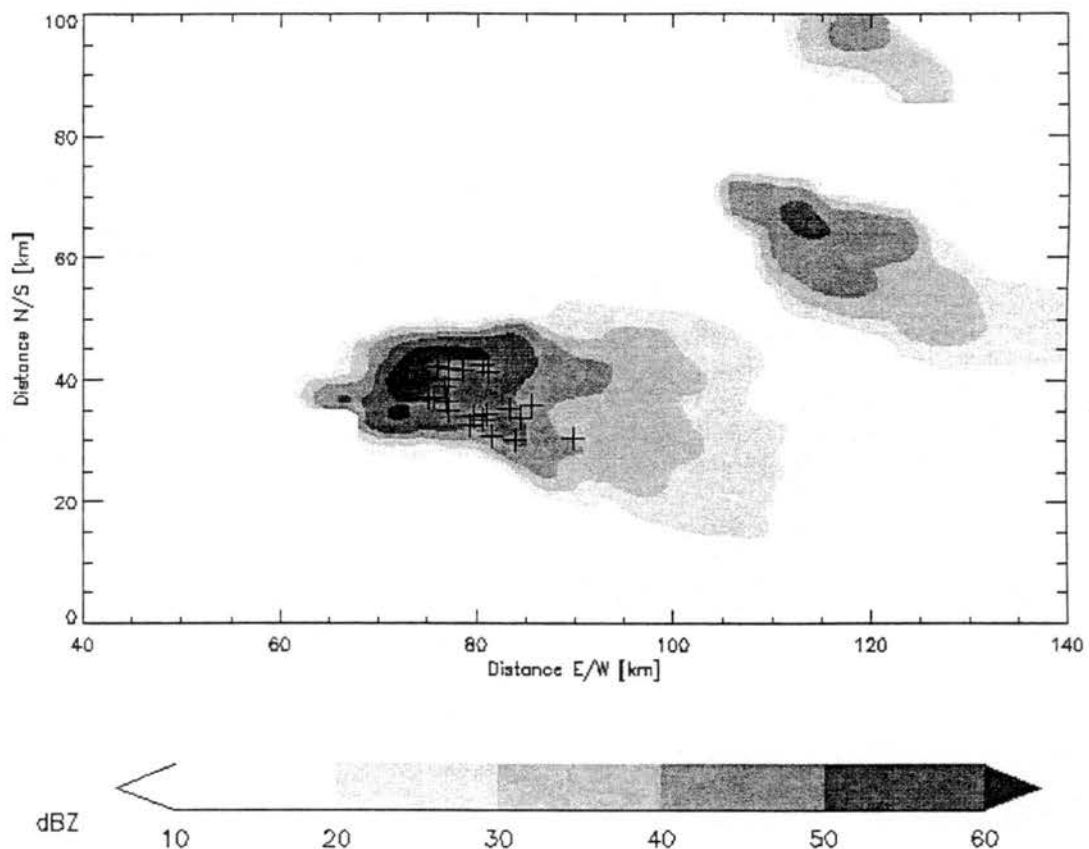


Figure 3.47: Horizontal cross-section of CHILL radar reflectivity at 0.5 km AGL, at 2343 UTC on 29 June 2000. Also shown are ground strike positions (plus signs for positives, minus signs for negatives) of NLDN CGs that occurred during 2340-2350 UTC. Distances are relative to CHILL.

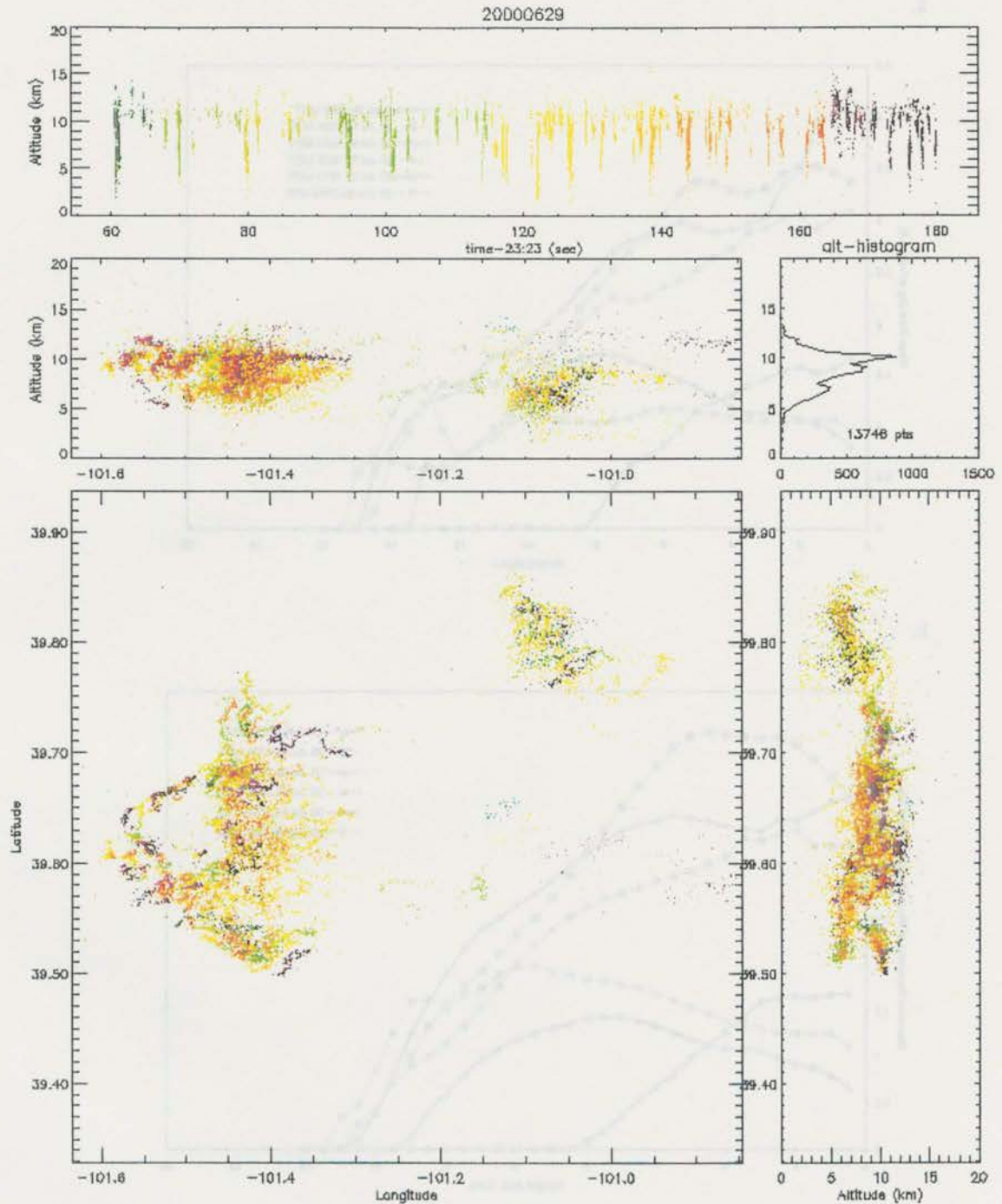
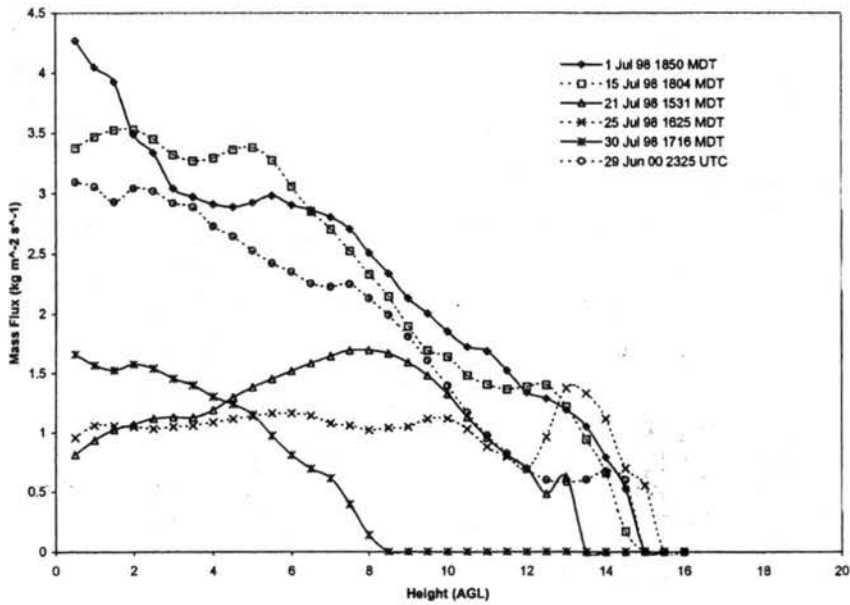


Figure 3.48: Two minutes of LMA data for the 29 June 2000 storm, centered on 23:23:54 UTC. The top panel shows VHF signals as a function of time and altitude. The bottom left panel shows a plan view of the signals. The panels immediately above and to its right show projections of the data onto vertical planes in the east-west and north-south directions, respectively. The remaining panel shows an altitude histogram of signals that occurred during the time period. Warmer colors denote more recent signals.

a.



b.

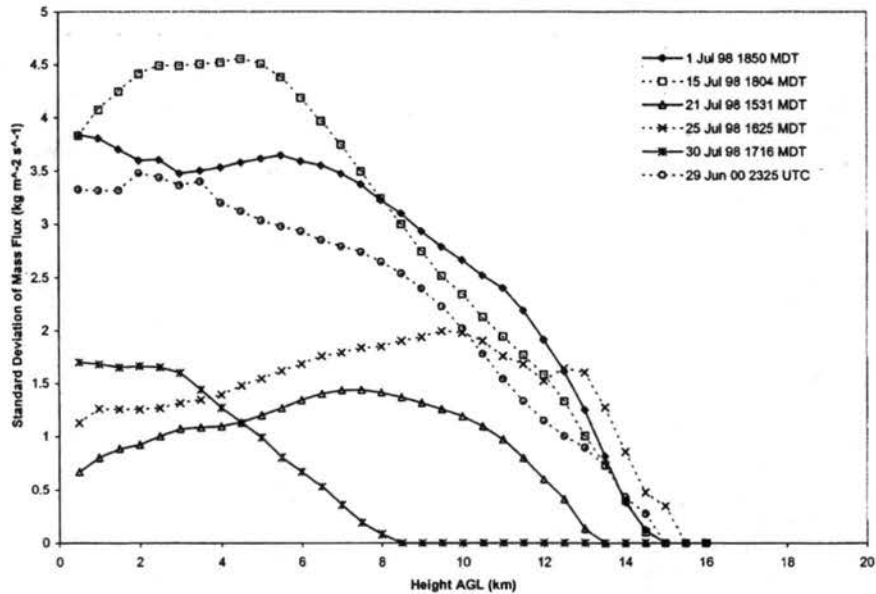
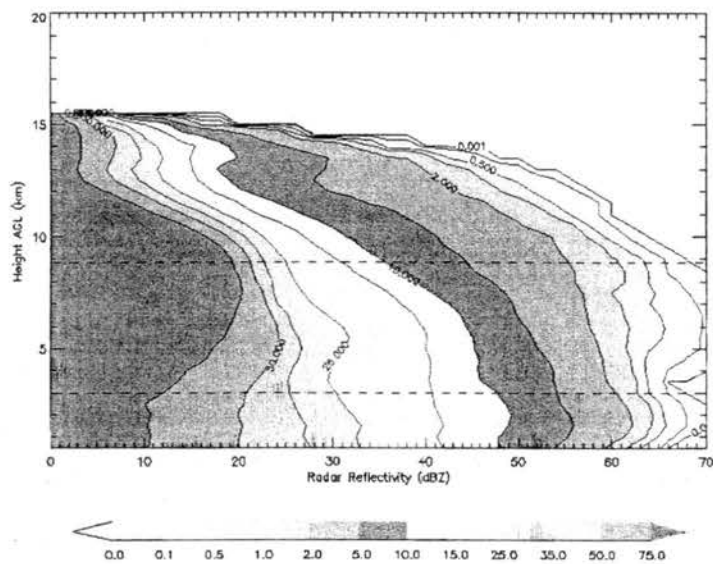


Figure 3.49: a) Average positive vertical air mass flux as a function of height at the times of peak updrafts for the mid-latitude storms. b) Standard deviation of positive vertical air mass flux as a function of height at the times of peak updrafts for the mid-latitude storms.

a.



b.

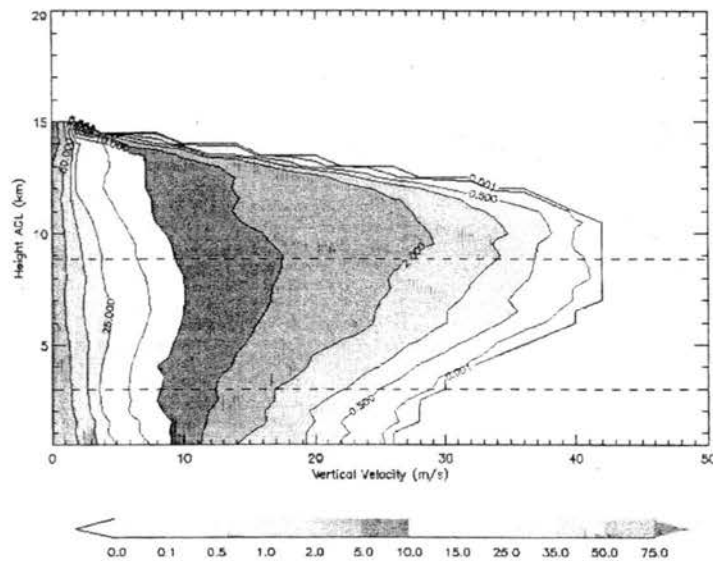
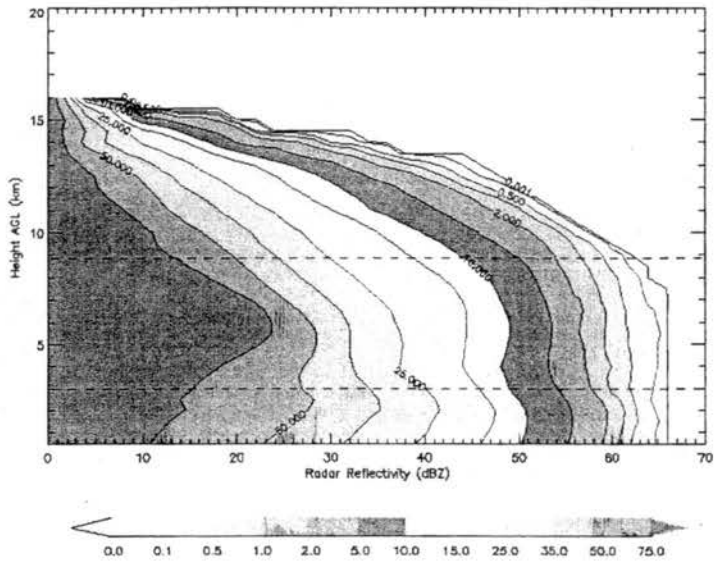


Figure 3.50: Cumulative frequency by altitude diagrams (CFADs) of CHILL radar reflectivity (a) and dual-Doppler-derived vertical velocity (b) for the 1 July 1998 storm at 1850 MDT. The dashed lines denote the approximate boundaries of the mixed phase region.

a.



b.

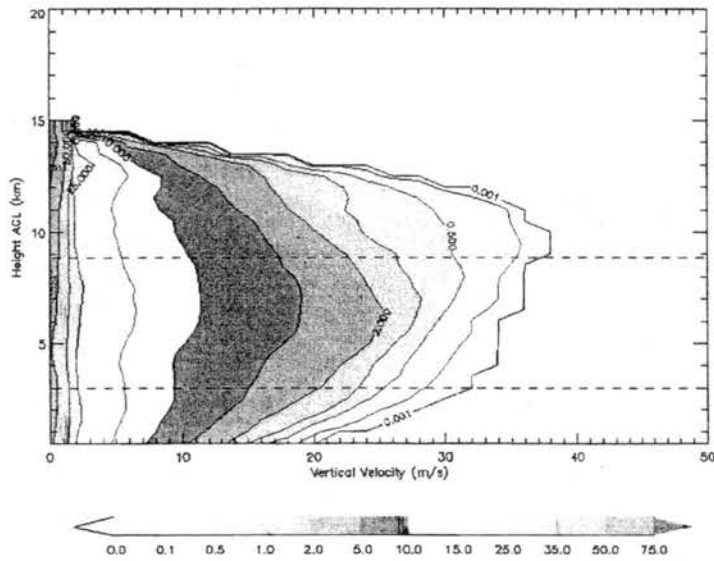
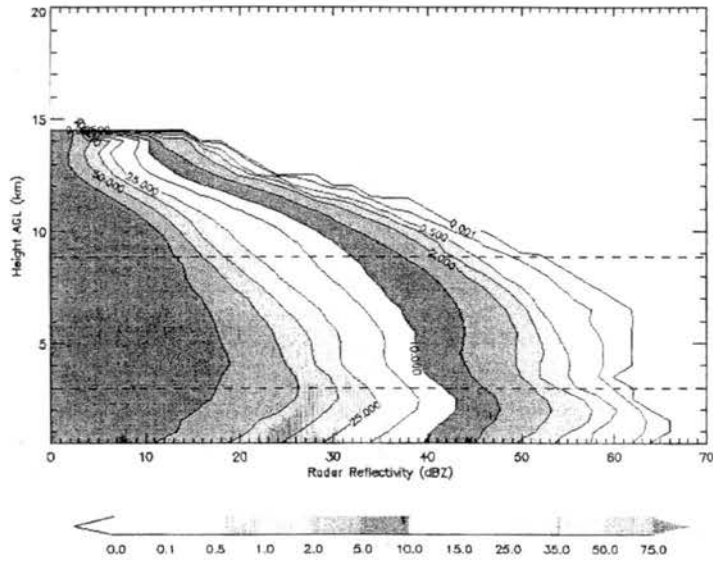


Figure 3.51: Cumulative frequency by altitude diagrams (CFADs) of CHILL radar reflectivity (a) and dual-Doppler-derived vertical velocity (b) for the 15 July 1998 storm at 1804 MDT. The dashed lines denote the approximate boundaries of the mixed phase region.

a.



b.

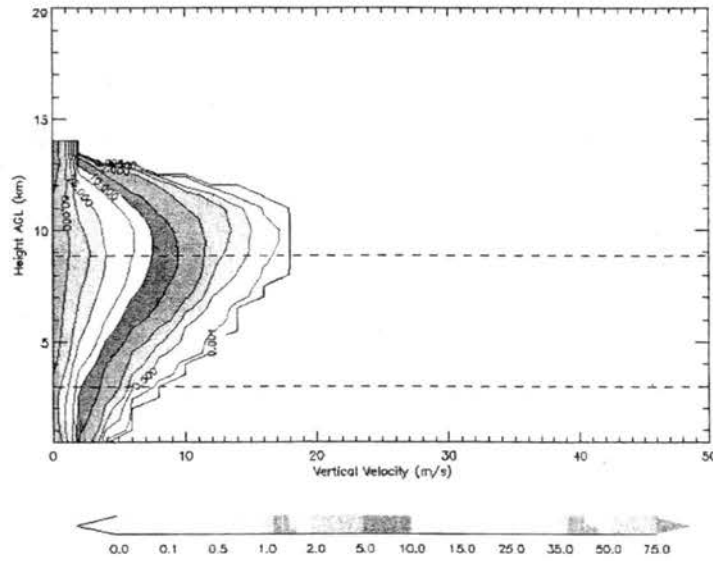
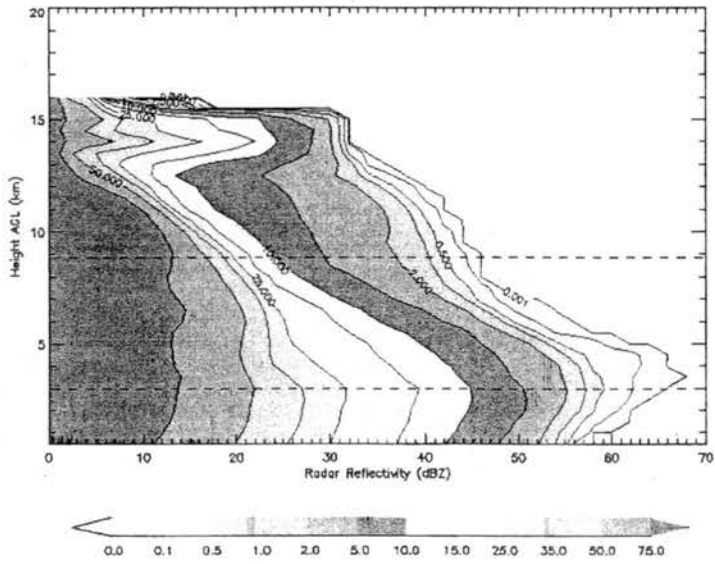


Figure 3.52: Cumulative frequency by altitude diagrams (CFADs) of CHILL radar reflectivity (a) and dual-Doppler-derived vertical velocity (b) for the 21 July 1998 storm at 1531 MDT. The dashed lines denote the approximate boundaries of the mixed phase region.

a.



b.

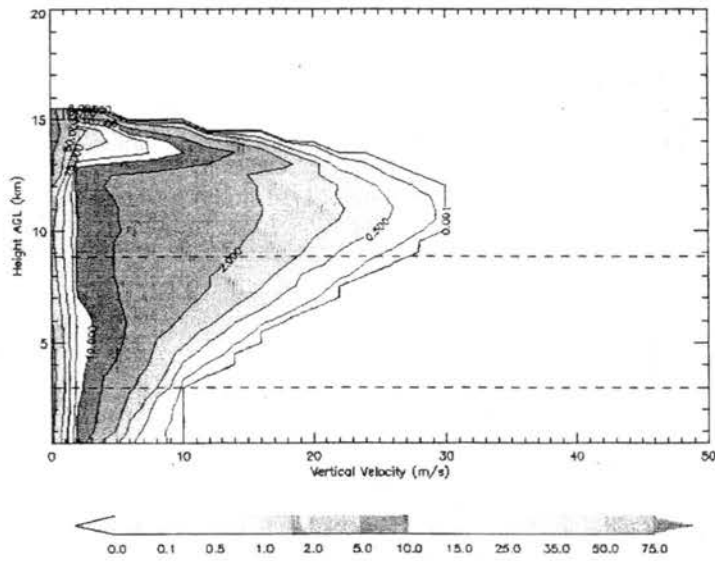
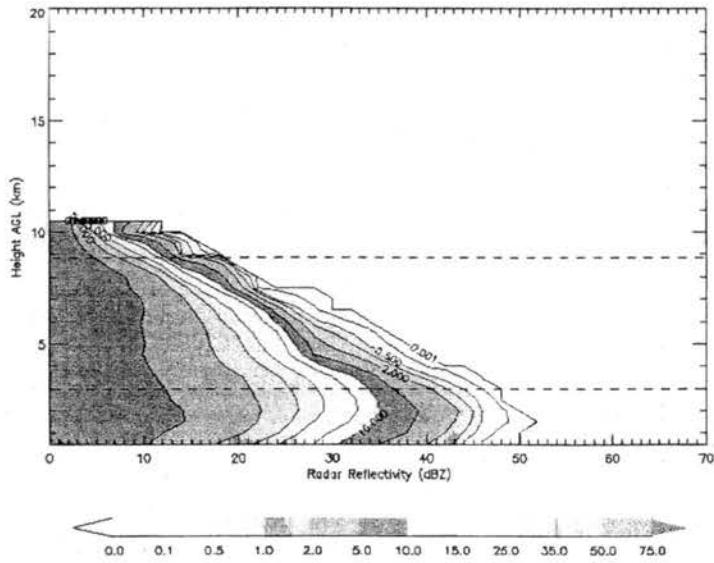


Figure 3.53: Cumulative frequency by altitude diagrams (CFADs) of CHILL radar reflectivity (a) and dual-Doppler-derived vertical velocity (b) for the 25 July 1998 storm at 1625 MDT. The dashed lines denote the approximate boundaries of the mixed phase region.

a.



b.

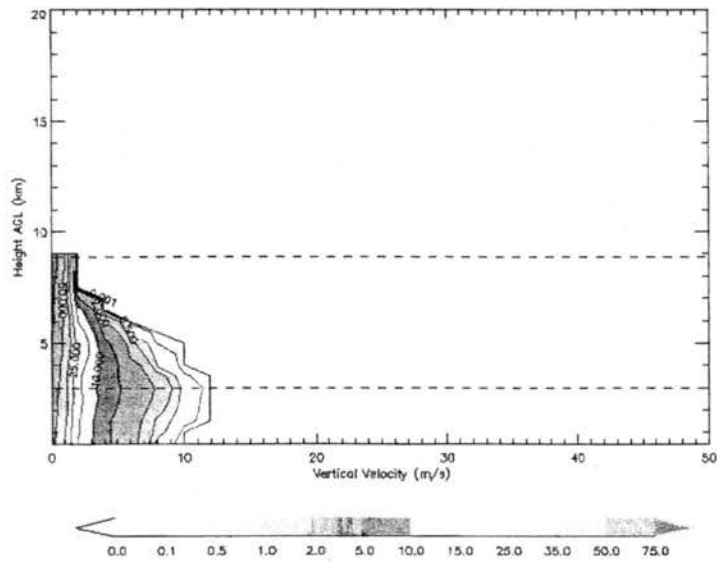
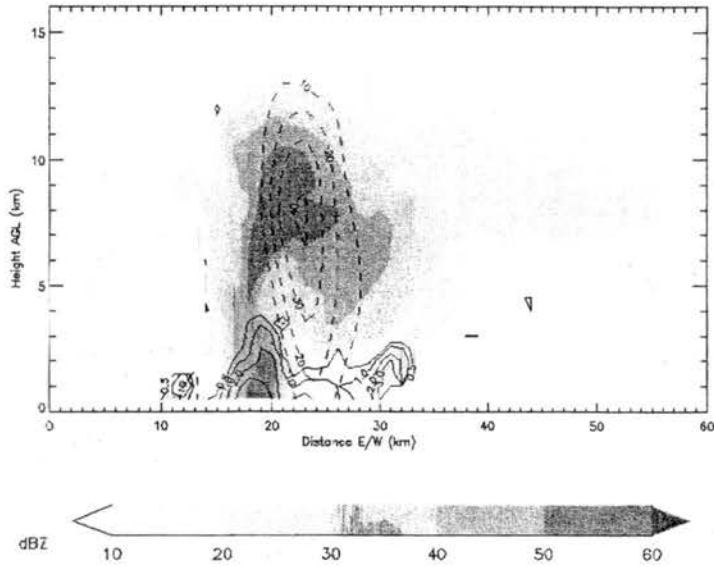


Figure 3.54: Cumulative frequency by altitude diagrams (CFADs) of CHILL radar reflectivity (a) and dual-Doppler-derived vertical velocity (b) for the 30 July 1998 storm at 1716 MDT. The dashed lines denote the approximate boundaries of the mixed phase region.



a.



b.

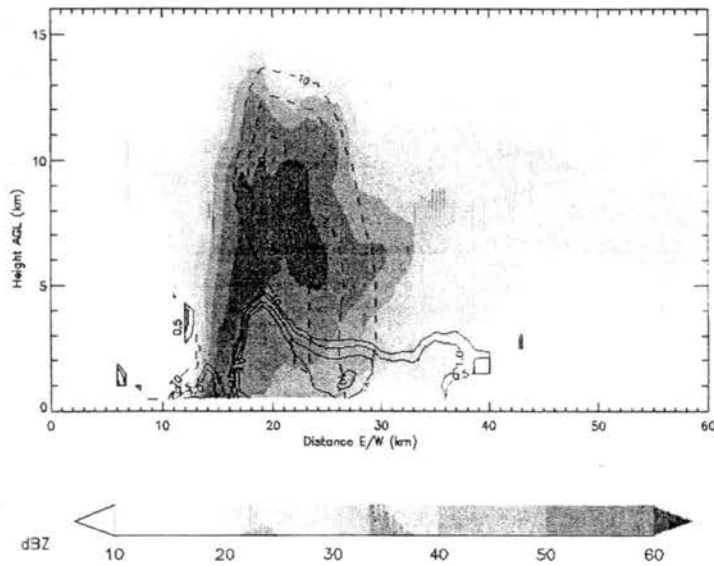
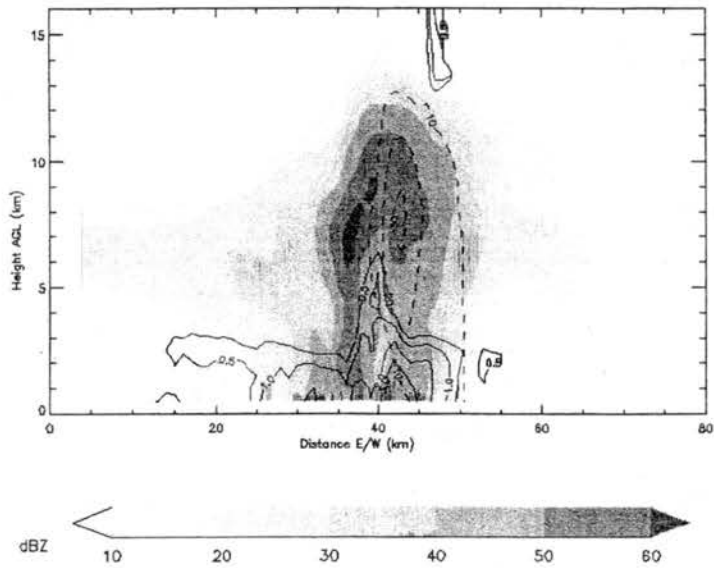


Figure 3.56: Vertical cross-sections of CHILL radar reflectivity (shaded), along with differential reflectivity (solid line) and vertical velocity (dashed). a) Cross-section taken at 16 km north, at 1850 MDT on 1 July 1998. b) Same as a) except at 21 km north. Distances are relative to CHILL.

a.



b.

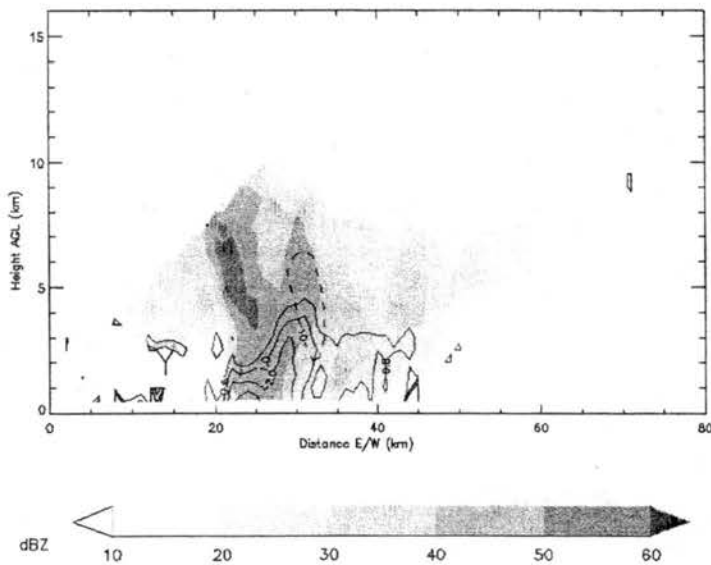


Figure 3.57: Vertical cross-section of CHILL radar reflectivity (shaded), along with differential reflectivity (solid line) and vertical velocity (dashed). a) Cross-section is taken at 30 km north, at 1804 MDT on 15 July 1998. b) Same as a) except at 8 km north. Distances are relative to CHILL.

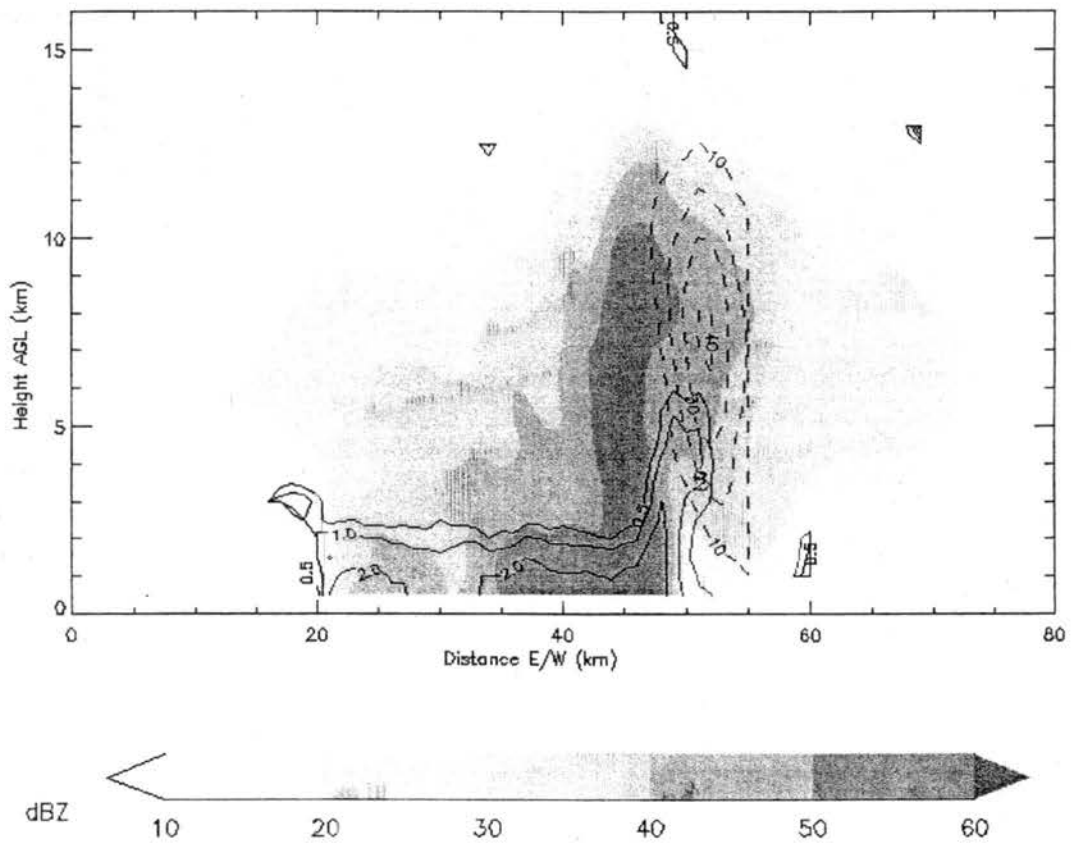


Figure 3.58: Vertical cross-section of CHILL radar reflectivity (shaded), along with differential reflectivity (solid line) and vertical velocity (dashed). Cross-section is taken at 2 km north, at 1840 MDT on 15 July 1998. Distances are relative to CHILL.

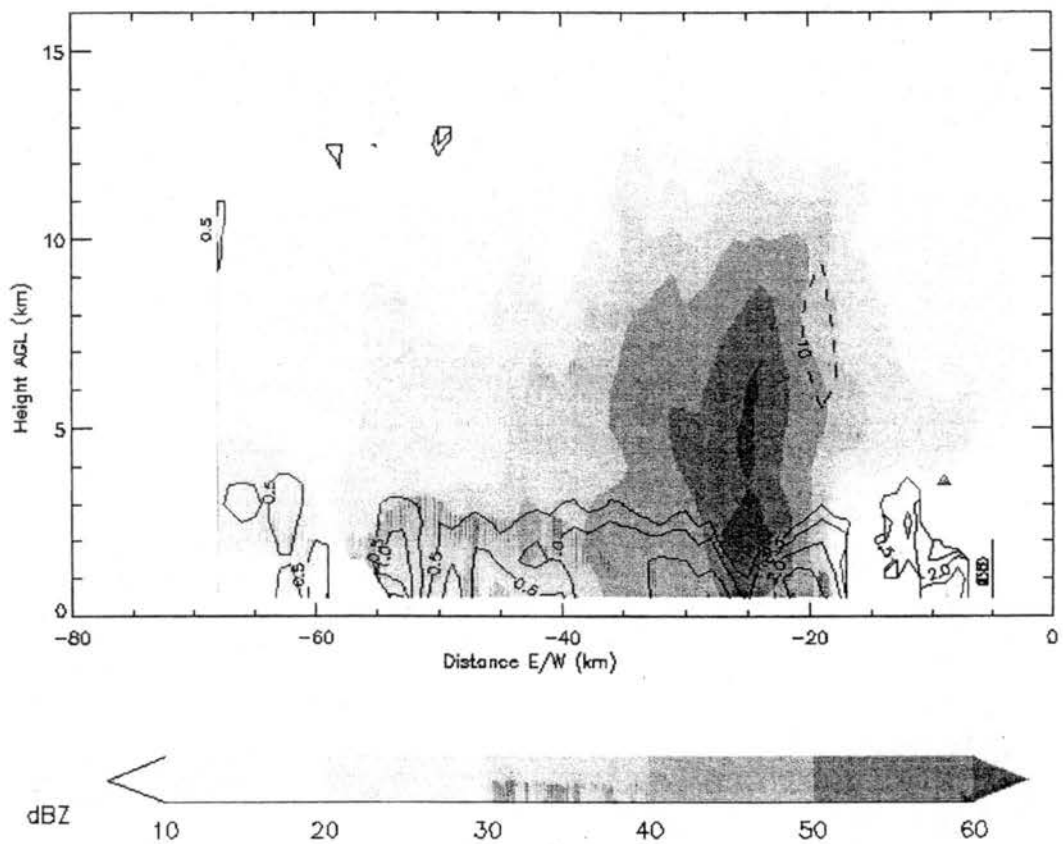
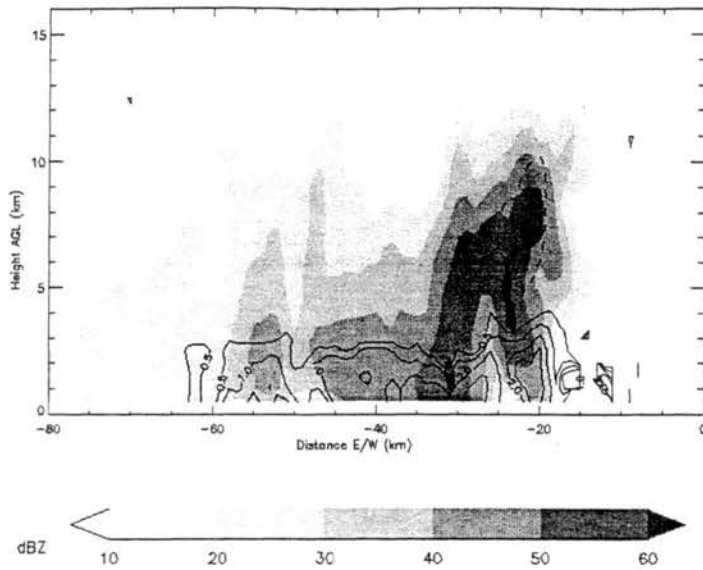


Figure 3.59: Vertical cross-section of CHILL radar reflectivity (shaded), along with differential reflectivity (solid line) and vertical velocity (dashed). Cross-section is taken at 23 km north, at 1531 MDT on 21 July 1998. Distances are relative to CHILL.

a.



b.

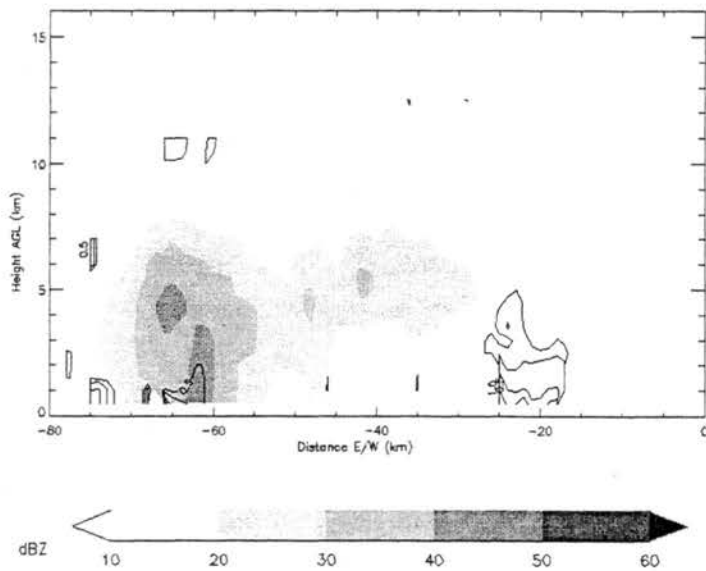


Figure 3.60: Vertical cross-section of CHILL radar reflectivity (shaded), along with differential reflectivity (solid line) and vertical velocity (dashed). a) Cross-section is taken at 24 km north, at 1516 MDT on 21 July 1998. b) Same as a) except at 50 km north. Distances are relative to CHILL.

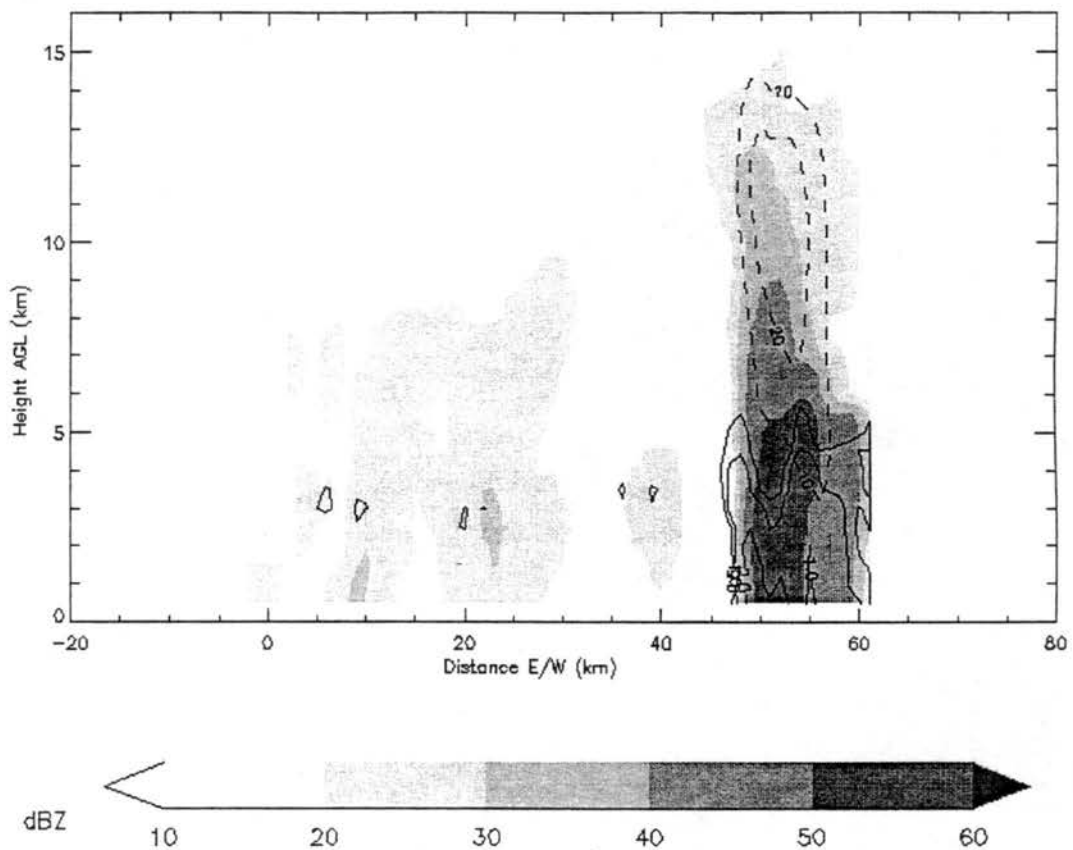
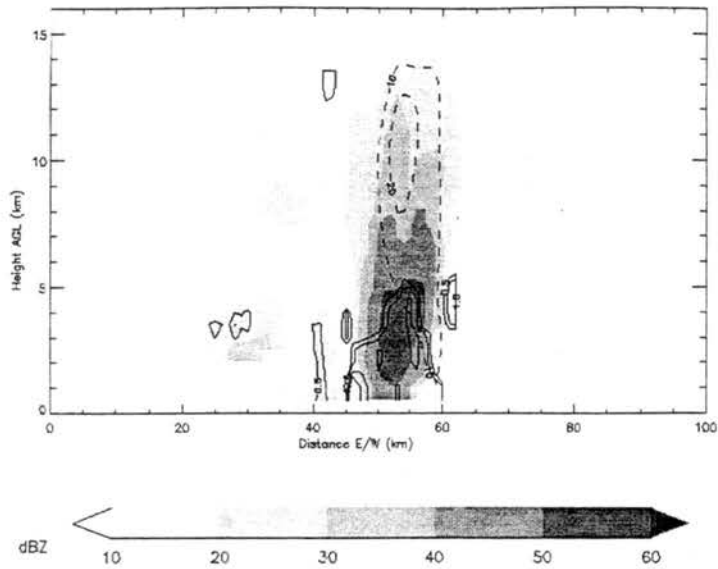


Figure 3.61: Vertical cross-section of CHILL radar reflectivity (shaded), along with differential reflectivity (solid line) and vertical velocity (dashed). Cross-section is taken at 39 km north, at 1625 MDT on 25 July 1998. Distances are relative to CHILL.

a.



b.

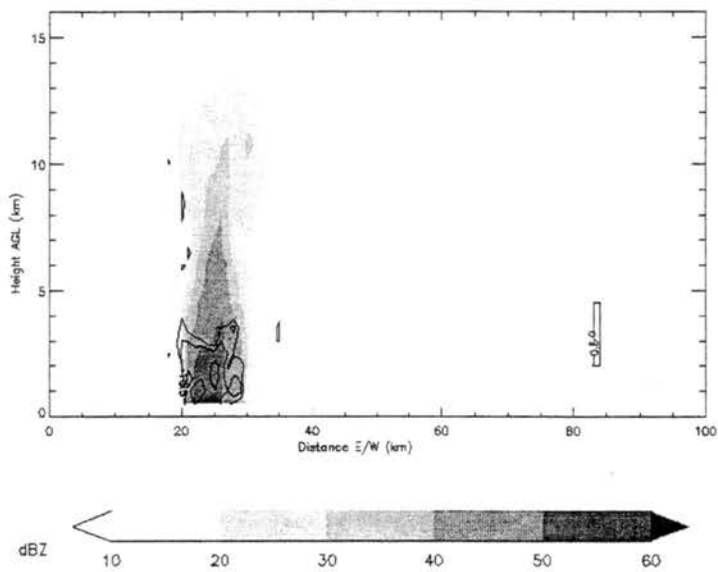


Figure 3.62: Vertical cross-section of CHILL radar reflectivity (shaded), along with differential reflectivity (solid line) and vertical velocity (dashed). a) Cross-section is taken at 27 km north, at 1640 MDT on 25 July 1998. b) Same as a) except at 11 km south. Distances are relative to CHILL.

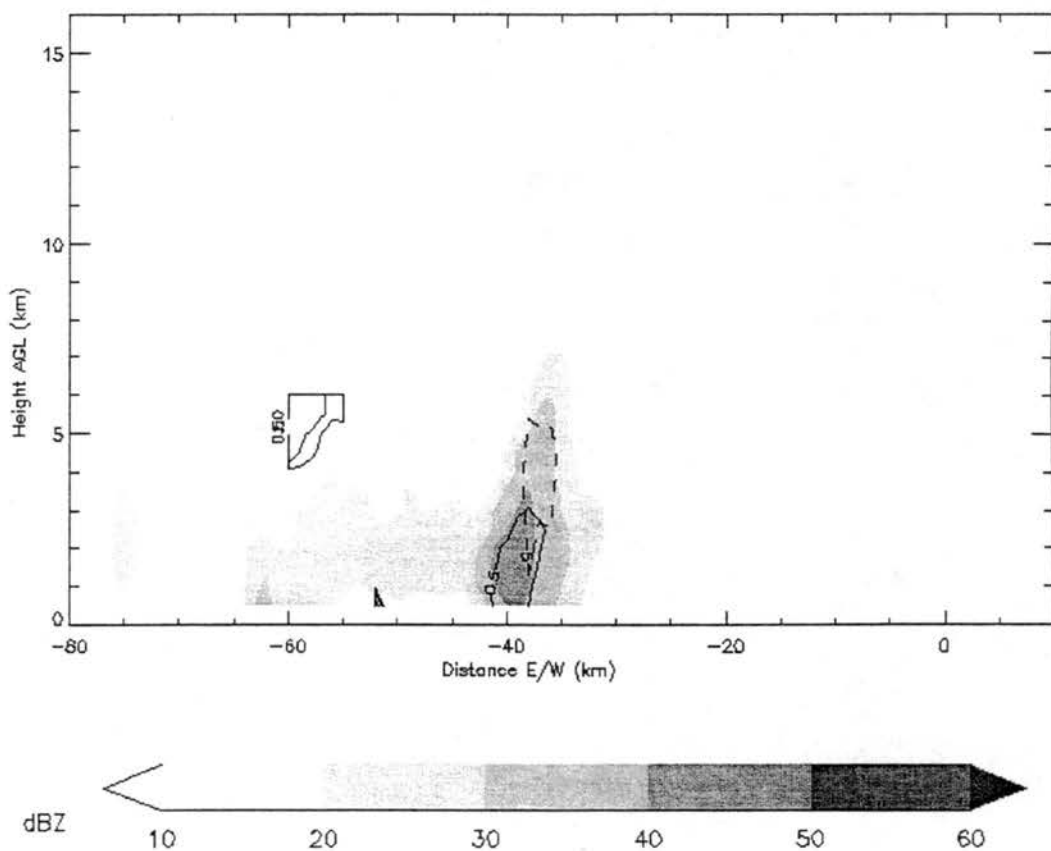
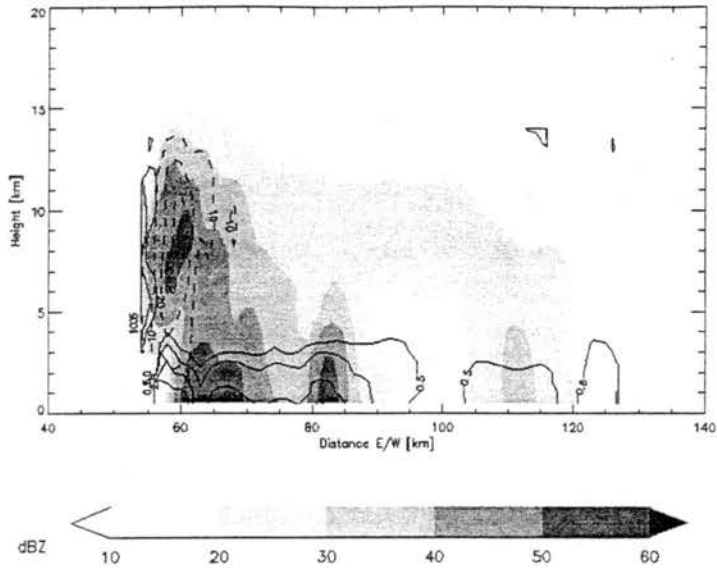


Figure 3.63: Vertical cross-section of CHILL radar reflectivity (shaded), along with differential reflectivity (solid line) and vertical velocity (dashed). Cross-section is taken at 25 km north, at 1716 MDT on 30 July 1998. Distances are relative to CHILL.

a.



b.

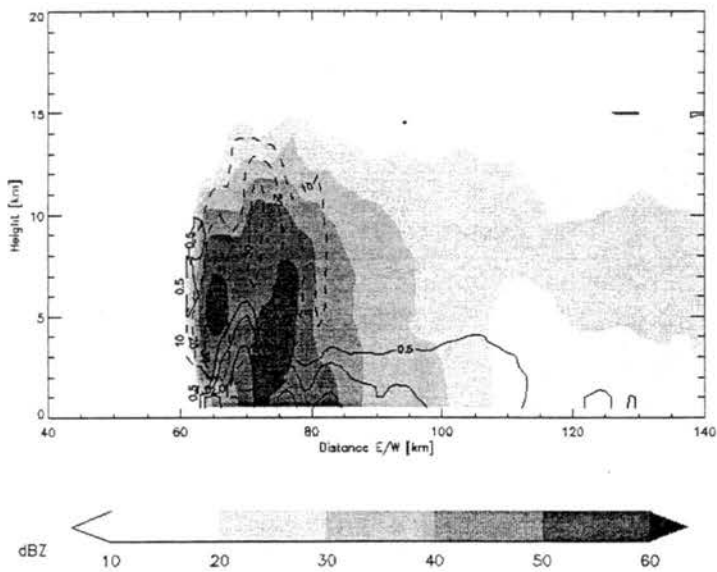
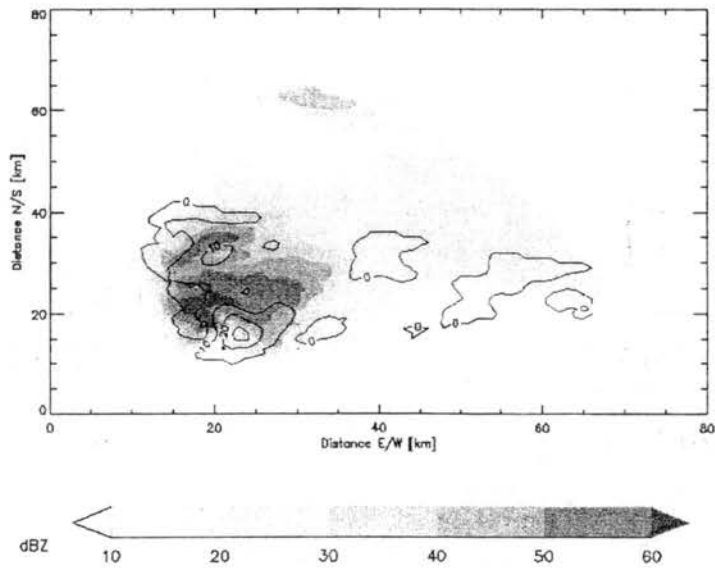


Figure 3.64: Vertical cross-section of CHILL radar reflectivity (shaded), along with differential reflectivity (solid line) and vertical velocity (dashed). a) Cross-section is taken at 51 km north, at 2312 UTC on 29 June 2000. b) Taken at 35 km north, at 2343 UTC on 29 June. Distances are relative to CHILL.

a.



b.

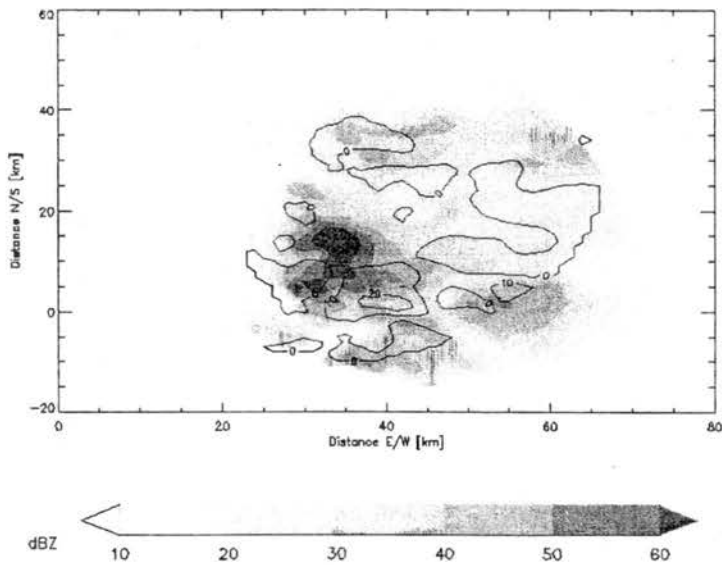
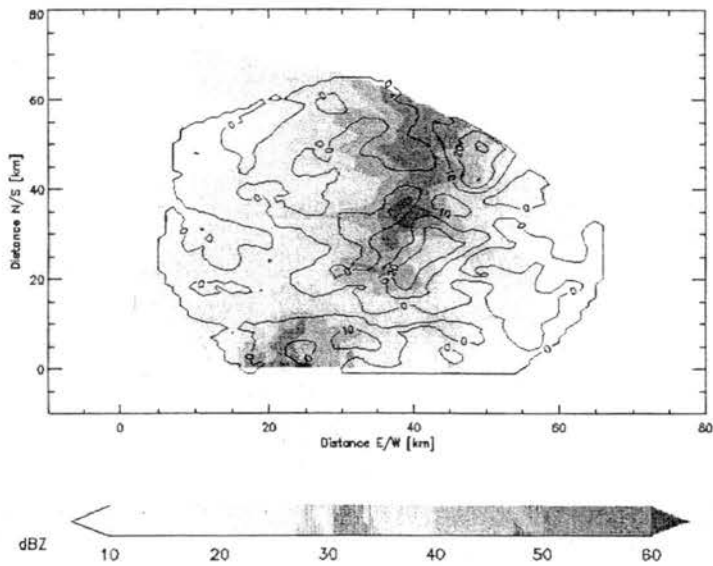


Figure 3.65: Horizontal cross-section of CHILL radar reflectivity (shaded) and vertical velocity (solid line) at 4.5 km AGL for the 1 July 1998 storm. a) At 1850 MDT. b) At 1925 MDT.

a.



b.

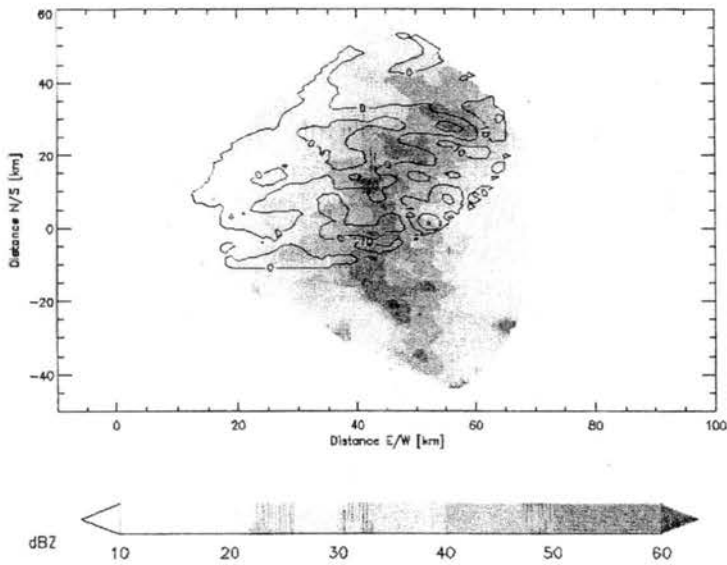
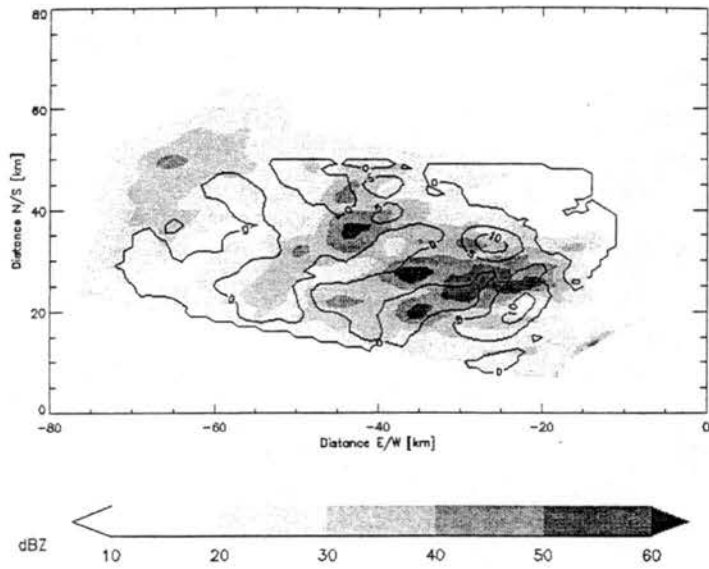


Figure 3.66: Horizontal cross-section of CHILL radar reflectivity (shaded) and vertical velocity (solid line) at 4.5 km AGL for the 15 July 1998 storm. a) At 1804 MDT. b) At 1840 MDT.

a.



b.

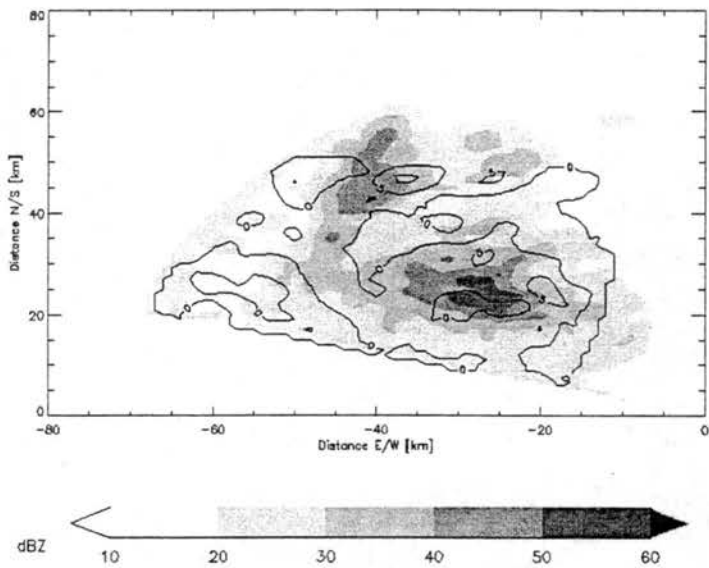
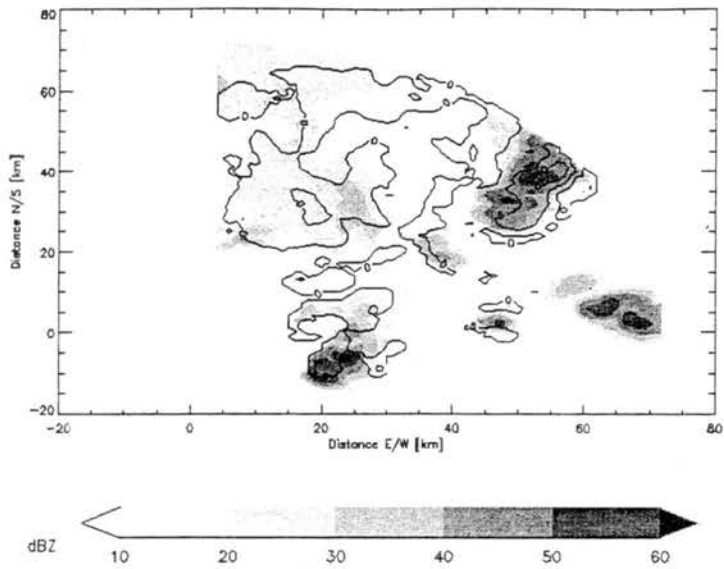


Figure 3.67: Horizontal cross-section of CHILL radar reflectivity (shaded) and vertical velocity (solid line) at 4.5 km AGL for the 21 July 1998 storm. a) At 1516 MDT. b) At 1531 MDT.

a.



b.

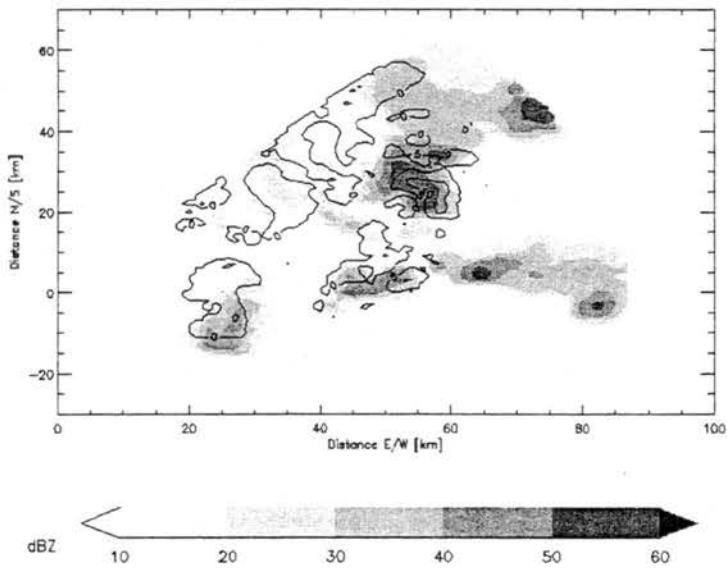


Figure 3.68: Horizontal cross-section of CHILL radar reflectivity (shaded) and vertical velocity (solid line) at 4.5 km AGL for the 25 July 1998 storm. a) At 1625 MDT. b) At 1640 MDT.

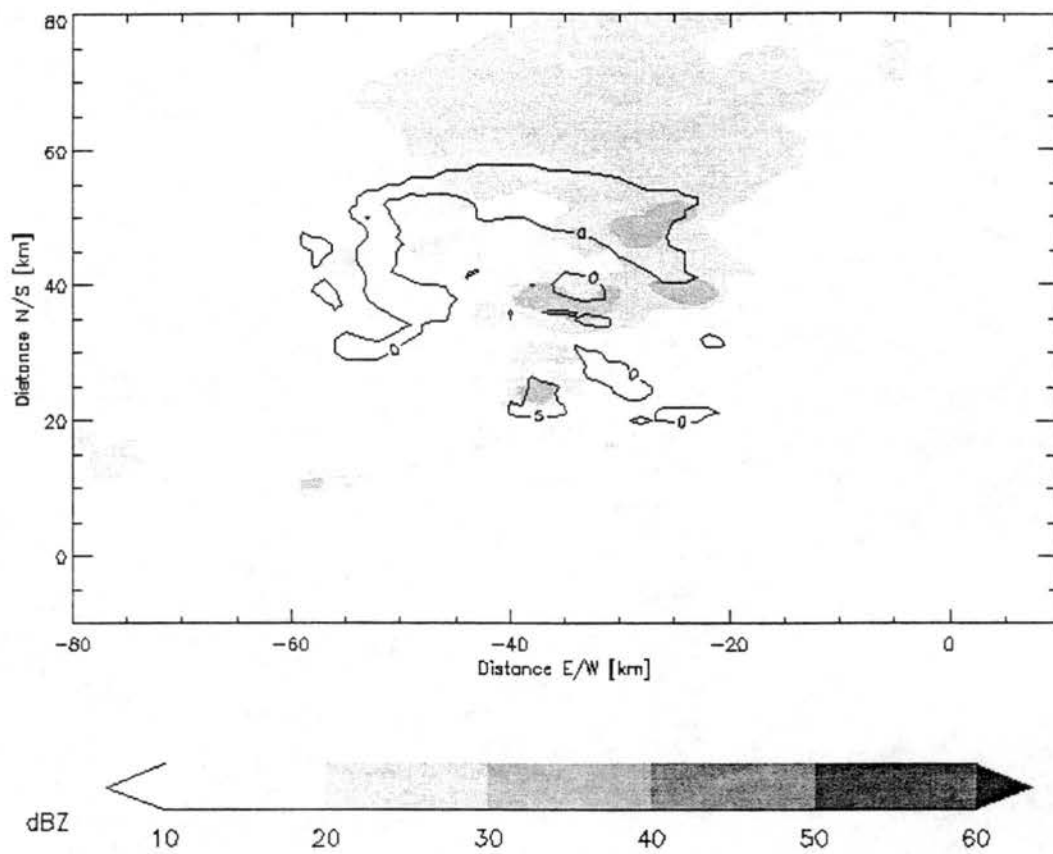


Figure 3.69: Horizontal cross-section of CHILL radar reflectivity (shaded) and vertical velocity (solid line) at 4.5 km AGL for the 30 July 1998 storm at 1716 MDT.

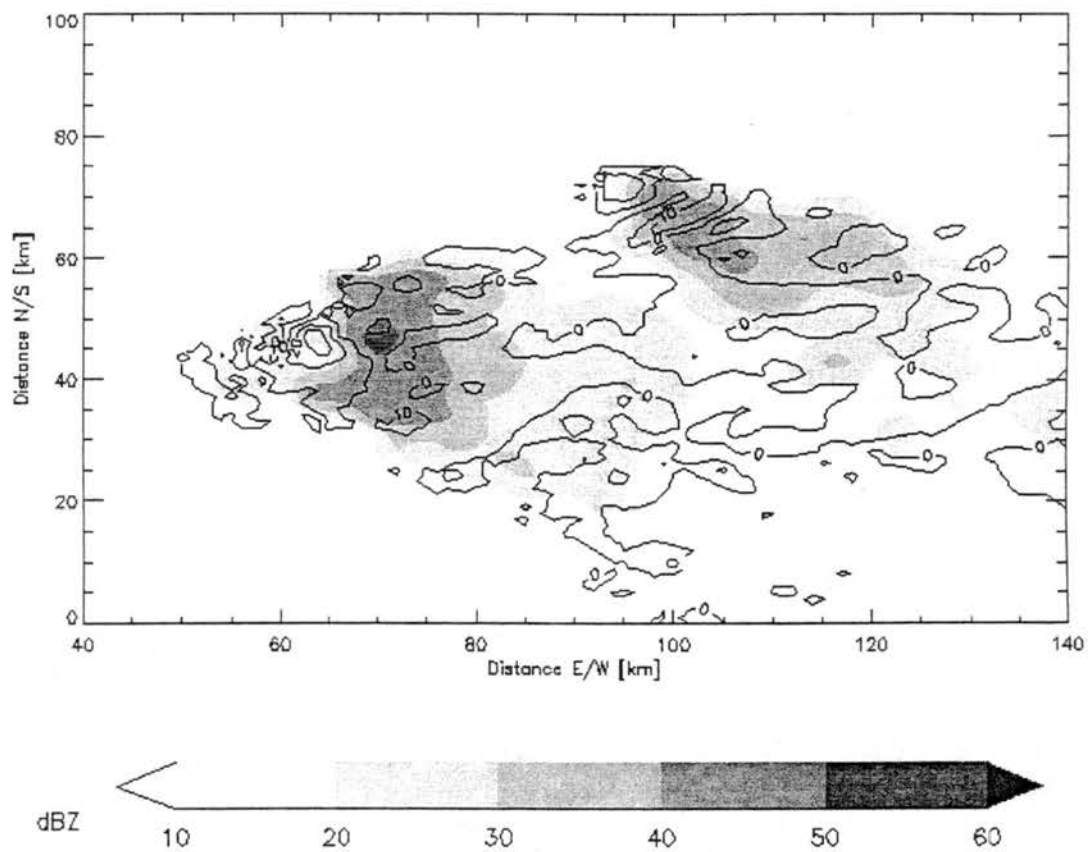


Figure 3.70: Horizontal cross-section of CHILL radar reflectivity (shaded) and vertical velocity (solid line) at 4.5 km AGL for the 29 June 2000 storm at 2325 UTC.

## CHAPTER 4

### TRMM/LBA TROPICAL THUNDERSTORMS

#### *4.1 Overview of Storms*

##### *a) 26 January 1999*

The storm of 26 January 1999 was an intense and very large squall line that propagated westward through the eastern LBA domain, eventually passing over both the SPOL and TOGA radars. While this storm was observed by radar for several hours, this study focused on the time period of 1950-2220 UTC (Local time = UTC - 4 hours), coincident with storm passage through the eastern dual-Doppler lobe. Figure 4.1 shows a horizontal cross-section of SPOL radar reflectivity at 0.5 km AGL at 2030 UTC. The linear structure and immense size of the storm are clearly evident. Figure 4.2 shows a time-height cross-section of maximum radar reflectivity for the entire analysis period of this storm. The storm was comparable to other significant land- or island-based tropical convective events (e.g., Carey and Rutledge 2000) with 50 dBZ ranging between 6 and 8 km AGL for much of the storm's lifetime. In addition, 30 dBZ extended above 13 km AGL for a large portion of its lifetime as well. The apparent weakening of the storm with time is a bit misleading, since as the line overran SPOL less of the main convective area was scanned, rather more trailing stratiform rain was covered. This was particularly true after 2140 UTC.

Figure 4.3 shows a time-height cross-section of peak updraft, as determined by the dual-Doppler syntheses. Around 2030 UTC, the maximum  $W$  exceeded  $30 \text{ m s}^{-1}$ . Immediately before and after this time, peak updrafts were more moderate. Late in the storm peak updrafts steadily declined as less of the convective line was scanned.

Figure 4.4 shows the volume of the storm containing updrafts within various bins, as a function of time. The storm was enormous, often having over  $60 \cdot 10^3 \text{ km}^3$  of volume containing updrafts between 0 and 10

$\text{m s}^{-1}$ . At the peak updraft intensity, near 2030 UTC, nearly  $10^3 \text{ km}^3$  of the storm contained updrafts between 10 and  $15 \text{ m s}^{-1}$ . However, while peak  $W$  exceeded  $30 \text{ m s}^{-1}$  around this time, the peak updrafts were limited to small volumes. In fact, well under  $100 \text{ km}^3$  of the storm contained updrafts in excess of even  $20 \text{ m s}^{-1}$  at this time.

Figure 4.5 shows rain area and rain mass flux at 0.5 km AGL as functions of time. Moderate ( $20\text{-}60 \text{ mm h}^{-1}$ ) rain covered around  $10^3 \text{ km}^2$  at the beginning of the analysis period, but then generally declined in size with time as less of the convective region was scanned by the SPOL radar. Heavy (greater than  $60 \text{ mm h}^{-1}$ ) rain covered up to  $200 \text{ km}^2$  at the beginning, but this area declined with time as well, due to storm movement relative to sample domain. Rain mass flux started off very high, around  $20 \cdot 10^6 \text{ kg s}^{-1}$ , and declined with time as the storm approached SPOL. Not surprisingly for tropical convection, this storm contained negligible hail at 0.5 km AGL (as inferred from polarimetric radar data). Hence, hail figures are not shown.

Cloud-to-ground flash rates for the 26 January storm are shown in Figure 4.6. Negative CG flash rate started out near 40 flashes in a 10-minute period, or  $4 \text{ min}^{-1}$ , but generally fell with time. This likely was due to the same reason for the decline in such variables as rain mass flux – the storm slowly moved out of the analysis region, which focused on the eastern dual-Doppler lobe. This negative CG output falls between that of the mid-latitude storms of 21 and 25 July 1998 (Figures 3.23 and 3.32), making the 26 January 1999 storm a significant producer of negative CGs. By contrast, the positive CG flash rate was well below  $1 \text{ min}^{-1}$  throughout the analysis period.

Figure 4.7 shows a horizontal cross-section of radar reflectivity from the 2010 UTC volume of the SPOL radar at 0.5 km AGL, along with ground strike positions and polarities of BLDN-detected CGs that occurred between 2010 and 2020 UTC. As can be seen, CG flash locations did not always correlate well with radar echo, due to BLDN flash location issues. However, despite the fact that some CGs could not be associated with specific cells, they certainly could be associated with specific regions of the storm. For example, in Figure 4.7 it is apparent that most of the CGs were associated with the northern half of the storm, which incidentally also was where the largest vertical velocities were found.

Figure 4.8 shows total flash rate from the SPOL FCM as a function of time. During the early portion of the analysis period, the storm was too far away for flashes to be detected. However, as it approached

SPOL, flash rates increased, peaking at over 60 flashes in a 5-minute period around 2130 UTC and later. This leads to an estimate of total flash rate on the order of  $12 \text{ min}^{-1}$  at peak, which means this storm was significantly electrified since FCM estimates were likely to be low for reasons discussed previously. From Figure 4.6, around this time the total CG flash rate was about  $1.5 \text{ min}^{-1}$ , averaged over a 10-minute period. Although CG flash rates were likely to be underestimated around this time because so much of the storm had moved out of the analysis region, this leads to an IC flash rate estimate of  $10.5 \text{ min}^{-1}$  around this time, and an IC:CG ratio of 7:1. This is a fairly high ratio, but while the FCM estimates were likely to be low, so too were the CG estimates.

In summary, the storm of 26 January 1999 was a strong tropical squall line that featured a respectable reflectivity structure, updrafts in excess of  $30 \text{ m s}^{-1}$ , and heavy rain. It was a significant producer of lightning, with a substantial total flash rate, as well as a relatively high negative CG lightning flash rate. Few positive CGs were recorded.

#### *b) 13 February 1999*

On 13 February 1999, a number of cells of varying but generally moderate intensity populated the eastern dual-Doppler lobe. This study focused on the time period of 1710-1840 UTC. Figure 4.9 shows a horizontal cross-section of SPOL radar reflectivity at 0.5 km AGL at 1733 UTC. As can be seen, convection was widely scattered with little apparent organization. The cell near 70 km east and 45 km north of SPOL was the most intense at this time. Figure 4.10 shows a time-height cross-section of maximum radar reflectivity for analysis period of this storm. For the most part, the reflectivity structure was less intense than the 26 January storm, with 50 dBZ generally below 6 km AGL and 30 dBZ generally below 10 km AGL. The storm intensified after 1745 UTC, with 30 dBZ reaching to 15 km AGL, and 50 dBZ to 7 km. However, the storm did not remain intense for long, with reflectivities mostly collapsing to previous values after 1800 UTC.

Figure 4.11 shows a time-height cross-section of peak updraft, as determined by the dual-Doppler syntheses. After 1733 UTC, peak updrafts intensified to over  $20 \text{ m s}^{-1}$ , but soon collapsed to more moderate values of 10-15  $\text{m s}^{-1}$  by 1745 UTC. Thus, the storm reached its peak in vertical velocity and collapsed by the time the reflectivity structure began to intensify. It is interesting that the peak in

reflectivity structure lagged the peak in vertical velocity by so much. However, both Figures 4.10 and 4.11 are comprised of the entire storm, which was itself composed of many individual cells. While caution is needed when interpreting the plots of peak values, it appears that particle growth tended to lag the intensification of the storm's updraft. This is different from other storms in this study, where reflectivity and updraft growth were largely coincident.

Figure 4.12 shows the volume of the storm containing updrafts within various bins as a function of time. The storm was much smaller than 26 January, with roughly  $20\text{-}25 \cdot 10^3 \text{ km}^3$  of volume containing updrafts between  $< 10 \text{ m s}^{-1}$ . At the peak in updraft intensity, around 1733 UTC, nearly  $350 \text{ km}^3$  of the storm contained updrafts between 10 and  $15 \text{ m s}^{-1}$ , and generally less than  $100 \text{ km}^3$  contained updrafts in excess of  $15 \text{ m s}^{-1}$ . Thus, less of the storm contained significant updrafts, compared to 26 January.

Figure 4.13 shows rain area and rain mass flux at 0.5 km AGL for this storm as functions of time. Moderate rain generally covered less than  $400 \text{ km}^2$  during the analysis period. Heavy rain covered well under  $50 \text{ km}^2$  for the most part. Rain mass flux was comparably modest,  $< 8 \cdot 10^6 \text{ kg s}^{-1}$  throughout the analysis period. Like 26 January, this storm contained negligible hail at 0.5 km AGL.

Figure 4.14 depicts CG lightning flash rates for 13 February. Interestingly, no CGs were detected within the analysis domain until 1800 UTC, when negative CG lightning flash rate began to increase steadily, eventually reaching 20 flashes in 10 minutes at the end of the analysis time. Positive CGs were not detected either before or after 1800 UTC, however. A simple browsing of the raw data showed that no CGs of any kind were detected within the entire BLDN domain (not just the analysis domain for the 13 February case) between roughly 1700 and 1800 UTC. Individual BLDN stations were detecting flashes during this time, but multiple stations were not, and thus no flash solutions could be made. There was likely a network malfunction during this time, so effectively, on 13 February 1999, the BLDN was down from the start of this study's analysis period until after 1800 UTC. Even after that time caution must be applied as network issues may have lingered, causing CG flash rates to be underestimated. The peak negative CG flash rate of  $2.0 \text{ min}^{-1}$  was lower than the peak negative CG flash rate from 26 January. However, it was comparable to past studies or "ordinary" convection (e.g., Peckham et al. 1984). Also, considering the state of the BLDN on this day, it would be difficult to call this a low-CG storm with any confidence.

Figure 4.15 shows a horizontal cross-section of radar reflectivity from the 1833 UTC volume of the SPOL radar at 0.5 km AGL, along with ground strike positions and polarities of CGs between 1830 and 1840 UTC. Once again, flash locations were problematic, and it was difficult to associate particular CGs with particular cells. It does appear, however, that CGs were not concentrated in any particular region of the storm at this time. Unfortunately, no FCM data were available for this storm. Thus, no estimates of total flash rate, IC flash rate, or IC:CG ratio were made.

In summary, the storm of 13 February 1999 was a collection of scattered and disorganized cells that generally featured a modest reflectivity structure, updrafts in excess of  $20 \text{ m s}^{-1}$ , and some heavy rain. Although there were problems with the BLDN on this day, this storm appeared to have produced a number of negative CGs, though significantly less than 26 January.

#### *c) 15 February 1999*

The storm of 15 February 1999 was comprised of a number of westward-propagating cells that gradually merged and formed a more mesoscale-type system. This study focused on the time period of 1820-2130 UTC, when the storm was within the eastern dual-Doppler lobe. Figure 4.16 shows a horizontal cross-section of SPOL radar reflectivity at 0.5 km AGL at 2030 UTC. At this time the storm was more mesoscale in nature, but contained significant ancillary convection as well. Figure 4.17 shows a time-height cross-section of maximum radar reflectivity for analysis period of this storm. The 50 dBZ contour generally stayed at 6 km AGL and below, although the 30 dBZ contour was more variable. During the first half of the analysis period, the 30 dBZ contour varied between 9 and 14 km AGL. But then as the cells merged later in the analysis period, a broad intensification occurred, with 30 dBZ reaching to 15 km AGL during a 40-minute period centered around 2030 UTC.

Figure 4.18 shows a time-height cross-section of peak updraft, as determined by the dual-Doppler syntheses. The first half of the analysis period contained two notable peaks in updraft speed (up to  $25\text{-}30 \text{ m s}^{-1}$ ), which correlated well with reflectivity intensifications seen Figure 4.17. Then a broad intensification in updraft occurred, with peak updrafts over  $30 \text{ m s}^{-1}$  around 2030 UTC. Unlike 13 February, peak reflectivity and peak updraft correlated well during the analysis period. Note that around the times of 1938,

1942, and 2021 UTC the SPOL and TOGA were scanning up to two minutes apart from one another, so dual-Doppler syntheses around these times may not be completely accurate.

Figure 4.19 shows the volume of the storm containing updraft speeds within various bins as a function of time. The volume of the storm containing moderate updrafts ( $0-10 \text{ m s}^{-1}$ ) steadily grew with time, eventually reaching to around  $50 \cdot 10^3 \text{ km}^3$ . During the times of peak updrafts ( $\sim 1910$  and  $\sim 2030$  UTC), around  $450 \text{ km}^3$  of the storm contained updrafts between  $10$  and  $15 \text{ m s}^{-1}$ , and up to  $400 \text{ km}^3$  contained updrafts in excess of  $15 \text{ m s}^{-1}$ . Thus, the updrafts in this storm were more intense and covered a larger volume than 13 February, were comparable to 26 January.

Figure 4.20 shows rain area and rain mass flux at  $0.5 \text{ km AGL}$  for this storm as functions of time. Moderate rain generally covered up to  $800 \text{ km}^2$  during the analysis period. Heavy rain was confined to areas below  $100 \text{ km}^2$ . Rain mass flux peaked near  $14 \cdot 10^6 \text{ kg s}^{-1}$ . These values come close to, but do not reach the level of 26 January 1999. However, they were in excess of the rain production by the 13 February storm. Again, negligible hail (at  $0.5 \text{ km AGL}$ ) was detected.

CG flash rates are shown in Figure 4.21. Much like 26 January and 13 February, the 15 February storm produced few positive CGs. However, it tended to produce a significant number of negative CGs, although flash rates were highly variable throughout the analysis period, ranging from less than 1 to about 5 per minute. However, negative CG flash rate tended to rebound quickly from its various maxima and minima, and thus there were no extended time periods where the storm was producing high or low numbers of negative CGs. This storm's peak negative CG production was greater than the preceding two storms.

Figure 4.22 shows a horizontal cross-section of radar reflectivity from the 2050 UTC volume of the SPOL radar at  $0.5 \text{ km AGL}$ , along with ground strike positions and polarities of BLDN-detected CGs that occurred between 2050 and 2100 UTC. Many CGs were situated outside of any echo due to flash location problems, however most appeared to be associated with the main echo in the southwest, which was the most intense part of the storm, reflectivity- and vertical velocity-wise.

The SPOL FCM was in a good position to capture the lightning produced by the storm at its peak near 2030 UTC. Total flash rate data are shown in Figure 4.23. Immediately before 2030 UTC, total flash rate peaked near 80 flashes in a 5 minute period, or about 16 flashes per minute. Again, while this is likely to be an underestimate for storm total flash rate, it does show that this storm produced significant lightning

near the time of its peak updraft. Around this time the storm's total CG flash rate was declining toward a minimum of  $1.5 \text{ min}^{-1}$ , which occurred at 2030 UTC. Using the 2020 UTC CG flash rate of approximately  $2.5 \text{ min}^{-1}$ , an estimate for the IC flash rate around this time would be  $13.5 \text{ min}^{-1}$ , with an IC:CG ratio of over 5:1. This IC:CG ratio was comparable to, though slightly lower than, the estimate for 26 January.

In summary, the storm of 15 February 1999 was a gradually merging set of cells that featured a reflectivity structure, updrafts, and rain production that fell between the storms of 26 January and 13 February. The storm had a significant total flash rate at its peak, and had a peak negative CG flash rate that exceeded both 26 January and 13 February.

#### *d) 17 February 1999*

The 17 February 1999 storm was a collection of loosely organized cells which populated the eastern dual-Doppler lobe. This study focused on the time period of 1720-1830 UTC. Figure 4.24 shows a horizontal cross-section of SPOL radar reflectivity at 0.5 km AGL at 1750 UTC. At this time, the southernmost elongated cell near 20 km east and 15 km north of SPOL was the most intense. Figure 4.25 shows a time-height cross-section of maximum radar reflectivity for analysis period of this storm. The storm looks very stratified in this plot but that is mostly due to the low time resolution (10 minute) between succeeding radar scans. The storm intensified somewhat around 1750 UTC, with the 50 dBZ contour reaching up to 7 km AGL after remaining near 5 km earlier. However, the 30 dBZ contour tended to levitate near 12 km AGL around 1750 UTC. It underwent a few changes during the analysis period, but generally stayed between 10 and 14 km.

Figure 4.26 shows a time-height cross-section of peak updraft, as determined by the dual-Doppler syntheses. The reflectivity peak at 1750 UTC coincided nicely with a peak in vertical velocity, with updrafts reaching over  $25 \text{ m s}^{-1}$  at this time. In addition, there was a secondary maximum in peak vertical velocity around 1730 UTC, when updrafts exceed  $20 \text{ m s}^{-1}$ .

Figure 4.27 shows the volume of the storm containing updraft speeds within various bins as a function of time. The volume of the storm containing moderate updrafts ( $0\text{-}10 \text{ m s}^{-1}$ ) was on the low end of the LBA storms in this study, less than  $25 \cdot 10^3 \text{ km}^3$ . Nearly  $300 \text{ km}^3$  of the storm contained updrafts between 10 and  $15 \text{ m s}^{-1}$  around 1730 UTC, but this value declined afterward, and was even less at 1750 UTC. At the

1750 UTC peak, however, on the order of  $150 \text{ km}^3$  of the storm contained updrafts in excess of  $15 \text{ m s}^{-1}$ . As a result, the updrafts in this storm were more intense and tended to cover a larger volume than 13 February, but were weaker overall than 15 February and 26 January.

Figure 4.28 shows rain area and rain mass flux at 0.5 km AGL for this storm as functions of time. Moderate rain generally covered nearly  $500 \text{ km}^2$  at its peak during the analysis period. However, heavy rain generally covered less than  $50 \text{ km}^2$ . Rain mass flux followed the moderate rain area and reached over  $9 \cdot 10^6 \text{ kg s}^{-1}$  at its peak. Much like with the updrafts, these values fell below the rain production by 15 February and 26 January, but exceeded that of 13 February. Once again, negligible hail (at 0.5 km AGL) was detected in this storm.

Figure 4.29 shows CG flash rates for this event. This storm produced the highest negative CG flash rates of the tropical cases examined, varying between less than 30 to almost 65 negative CGs in a 10-minute period. Positive CG production was negligible, much like the other tropical thunderstorms.

Figure 4.30 shows a horizontal cross-section of radar reflectivity from the 1730 UTC volume of the SPOL radar at 0.5 km AGL, along with ground strike positions and polarities of BLDN-detected CGs that occurred between 1730 and 1740 UTC. Significant CG flash location errors were evident on this day as well, but CGs were distributed among the three main regions of this storm, with the southernmost region apparently receiving the lion's share. This region also featured the strongest updrafts.

The SPOL FCM was operational during this storm, and total flash rate is plotted in Figure 4.31. Total flash rate tended to increase with time as the storm (and particularly its most intense southernmost portion) moved closer to SPOL. It hit its peak at the end of the analysis period, with greater than 30 flashes in a 5 minute period ( $\sim 6$  flashes per minute). This value is typical of average convection (e.g., Piepgrass et al. 1982), and while a comparison is difficult to due to detection efficiency issues, it does appear that this storm produced a lower total flash rate than either 26 January or 15 February. This is not surprising, however, given the fact that updrafts in the 17 February storm appeared to be less intense than in those events. The total CG flash rate around this time was just under 6 per minute, which implied that nearly all of the flashes the storm was producing at this time were negative CGs, with an IC:CG ratio near 0. However, this estimate could be in error if the SPOL FCM had a poor detection efficiency for this case.

In summary, the storm of 17 February 1999 was comprised of loosely organized cells. The storm tended to fall between the storms of 13 February and 15 February in terms of reflectivity structure, updraft intensity, and rain production. It was modestly electrified based on FCM data, but it produced the highest negative CG flash rates of any of the tropical cases.

*e) 20 February 1999*

The storm of 20 February 1999 storm was another collection of loosely organized cells which populated the eastern dual-Doppler lobe. This study focused on the time period of 1720-2000 UTC. Figure 4.32 shows a horizontal cross-section of SPOL radar reflectivity at 0.5 km AGL at 1848 UTC. The cell near 25 km east and 60 km north of SPOL was the most intense around this time. Figure 4.33 shows a time-height cross-section of maximum radar reflectivity for analysis period of this storm. Temporal resolution of viable radar scans was poor in the first half of the analysis period, which is why reflectivities look so stratified then. During this time, the 30 dBZ contour generally stayed between 8 and 11 km AGL, with 50 dBZ oscillating around 5 km or so. The storm intensified after 1840 UTC, however, with the 30 dBZ contour extending up to 14 km AGL. The 50 dBZ contour did not extend higher after the intensification, though, and in fact tended to decline in altitude with time.

Figure 4.34 shows a time-height cross-section of peak updraft, as determined by the dual-Doppler syntheses. The reflectivity intensification after 1840 UTC correlated with an increase in peak vertical velocity around this time. A broad peak of  $20 \text{ m s}^{-1}$  or more dominated the second half of the analysis period, with maximum vertical velocities reaching over  $25 \text{ m s}^{-1}$  for a short time.

Figure 4.35 shows the volume of the storm containing updraft speeds within various bins as a function of time. Moderate updrafts ( $0\text{-}10 \text{ m s}^{-1}$ ) filled over  $30 \cdot 10^3 \text{ km}^3$  at its peak near 1850 UTC. At this time, up to  $600 \text{ km}^3$  of the storm contained updrafts between 10 and  $15 \text{ m s}^{-1}$ , and updrafts in excess of  $15 \text{ m s}^{-1}$  filled close to  $300 \text{ km}^3$  of the storm around this peak time. Thus, while the storm contained comparatively less volume of moderate updraft at its peak, the volume of stronger updrafts compared well with the higher end storms in this tropical study, like 26 January.

Figure 4.36 shows rain area and rain mass flux at 0.5 km AGL for this storm as functions of time. Moderate rain generally covered upwards of  $400 \text{ km}^2$  at its peak, although heavy rain generally covered

less than  $50 \text{ km}^2$ . Rain mass flux peaked at over  $7 \cdot 10^6 \text{ kg s}^{-1}$ , making this storm one of the lighter rain producers in the study. Negligible hail (at 0.5 km AGL) was detected in this storm.

CG flash rates for this storm are shown in Figure 4.37. Curiously, the first half of the analysis period was marked by little CG lightning. In fact, it wasn't until after the general intensification of the storm around 1840 UTC that negative CG flash rate picked up, reaching a peak of just over  $2.5 \text{ min}^{-1}$  averaged over a 10-minute period at 1900 UTC. Unlike the "low-CG" period of 13 February, the BLDN was detecting plenty of CG flashes (within the entire BLDN domain) during the first half of the 20 February analysis period, so it would be difficult to attribute this apparent low production of CGs to a lightning network malfunction. The peak CG flash rate for this storm was within the norm for typical convection observed in past studies. Despite nearly 2 hours of observations, no positive CGs were detected in the analysis region for this storm.

Figure 4.38 shows a horizontal cross-section of radar reflectivity from the 1859 UTC volume of the SPOL radar at 0.5 km AGL, along with ground strike positions and polarities of BLDN-detected CGs that occurred between 1900 and 1910 UTC. CG flash locations once again have significant errors on this day, but around this time it appeared that most of the CGs were associated with the southern portion of the storm. Meanwhile, the strong cell near 20 km east and 55 km north of SPOL produced few CGs during this time.

The SPOL FCM was operational during this storm, but failed to detect flashes until the very end of the analysis period, when it detected 3 flashes between 1945 and 2000 UTC. This is because convection generally was too far away from SPOL for flashes to be detected with reasonable efficiency. Thus, no total flash rate data are shown for this storm.

In summary, the storm of 20 February 1999 was a loose collection of cells, similar to several other storms in this study. Compared to the other LBA storms, it had roughly average updraft intensity but below average rainfall production. Its CG production was very low during the first half of the analysis period, but gradually grew after the storm had intensified in the second half.

#### *f) Summary*

Table 4.1 summarizes some key observations of the tropical thunderstorms examined in this chapter. The 26 January 1999 storm was an intense squall line, and featured the highest peak reflectivity, over 60 dBZ in fact. It also had the most volume of updraft in excess of  $10 \text{ m s}^{-1}$ , as well as the largest area of heavy rain and the largest rain mass flux. In addition to its many firsts, it also had the second highest altitude of the 30 dBZ contour, the second fastest peak updraft, and the second highest total flash rate (of the storms for which FCM data were available). The 13 February 1999 storm, a collection of moderate cells, generally had substantially less intense observations, as well as the smallest peak negative CG flash rate. However, it did feature the greatest vertical extent of the 30 dBZ contour. The 15 February 1999 was a collection of cells that gradually merged and intensified over time, and it featured the largest peak updraft and the largest volume of updraft in excess of  $20 \text{ m s}^{-1}$ . It also had the highest total flash rate and the second highest negative CG flash rate. The 17 February 1999 storm was another collection of moderate-to-intense cells. It had overall significantly less intense storm measurements compared to the 26 January and 15 February cases, although it did produce the largest negative CG flash rate in the set. The 20 February 1999 storm was yet another collection of moderate-to-intense cells. This storm did not lead in any quantitative category shown. In fact, typically 20 February was in the middle to bottom half of all storms in any particular category, including having the second lowest peak negative CG flash rate. However, it did have the second largest volume of updraft in excess of  $20 \text{ m s}^{-1}$ . Note that over the entire tropical set the 10-minute averaged negative CG flash rate was in the range of  $2\text{-}6.5 \text{ min}^{-1}$ . This falls just below the rates seen in the moderate mid-latitude cases like 21 and 25 July 1998, but is comparable to peak CG rates observed in past studies of moderate convection (e.g., Peckham et al. 1984).

#### *4.2 Comparison of Storm Environments*

Table 4.2 shows convective available potential energy (CAPE) and wind shear for each of the tropical cases. Multiple VIZ soundings (typically one every 3-6 hours) were made each day from Abracos Hill, which was very near the TOGA radar. The 1800 UTC soundings were used for 26 January and 15 February, while for the other days the 1500 UTC soundings were analyzed. These soundings all preceded

the analysis periods on each day, and likely best represented the immediate pre-convective environment when compared with other soundings on the storm days.

The first column in Table 4.2 shows a straight calculation of CAPE for all dates, assuming no mixed layer and based on irreversible processes. That is, simply the positive area of the sounding, starting with a surface air parcel. The 26 January 1999 sounding featured around  $1600 \text{ J kg}^{-1}$  in CAPE. However, the 13 February 1999 sounding had over  $2000 \text{ J kg}^{-1}$ , but that storm generally had less intense updrafts, in terms of both peak values and volumes of significant updrafts. The 15 February 1999 sounding had only around  $500 \text{ J kg}^{-1}$  of CAPE, which is very low considering it produced comparable updrafts to 26 January. The 17 February sounding had about as much CAPE as 13 February, which is reasonable since the two storms were comparable in intensity. Finally, the 20 February sounding had over  $1600 \text{ J kg}^{-1}$  of CAPE. Excepting 15 February, all of these CAPEs were enough for moderate to intense convection (Bluestein 1993, chapter 3), and “moderate to intense” is as good a description as any for these storms. They all featured updraft statistics comparable to the 21 and 25 July 1998 storms from Colorado. Again, excepting 15 February and although a stronger storm like 26 January had a sounding with the least amount of CAPE, the CAPE values for the soundings generally were within approximately 20-25% of one another. This is consistent with the fact that the tropical thunderstorms featured updrafts statistics that were comparable to one another, at least compared to the broader spectrum observed in the mid-latitude cases.

There were three other sounding sites during LBA (Ariquemes, Rolim de Moura, and Rebio Jaru). The 1800 UTC, 15 February 1999, soundings from these sites were analyzed to see whether the Abracos Hill sounding from this day was unrepresentative of the environment, for whatever reason. The CAPEs from these soundings were very different, ranging from less than 300 to over  $2100 \text{ J kg}^{-1}$ . Combining all the CAPE estimates for this day, a regional average of  $1103.3 \text{ J kg}^{-1}$  was obtained. This was twice the energy in the Abracos Hill sounding, but was still significantly below the values for the other days. It is important to note that the LBA soundings were preliminary, so discrepancies could exist that have nothing to do with the actual environment. In addition, soundings at these different locations were not all the same type, so inter-instrumental differences could be an important factor in the different CAPE measurements.

Column 2 in Table 4.2 shows the magnitude of the shear vector between the surface and 475 mb, which is roughly 6 km AGL in the LBA domain. Thus, these values are basically the shear over the lowest 6 km,

for easy comparison to the mid-latitude environments. The environment on 15 February 1999 had the weakest shear, around  $6.5 \text{ m s}^{-1}$ . The 13 February environment had the most, nearly  $15 \text{ m s}^{-1}$ . The other three days had nearly identical low-level shears, just above  $9 \text{ m s}^{-1}$ . These low-level shears were fairly comparable to the shears in the Colorado convection, falling in between the highest and lowest shears from those cases. However, the directions of the vectors were different, since winds tended to become more easterly with height in the tropical soundings, as opposed to the westerly trend in the mid-latitude cases. Upper level shears (Column 3 in Table 4.2), defined as the magnitude of the shear vector between 475 and 200 mb (or roughly 6-12 km AGL), were nearly identical among all the tropical cases, with the exception of 17 February. Most days the upper-level shear was around  $5.5 \text{ m s}^{-1}$ , but on 17 February this value nearly doubled to about  $10.4 \text{ m s}^{-1}$ . All of these shear values were comparable to certain cases from the mid-latitudes, although overall the average was lower, consistent with their location in the deep tropics. Note that, like the mid-latitude cases, none of these shear calculations involved any pressure weighting.

Overall, it is difficult to discern any systematic differences between the soundings on the different tropical dates. With some exceptions, the environments had comparable CAPE and shear, and the exceptions weren't always correlated with notable cases. For example, the 17 February case had the highest negative CG flash rates, and its environment had the most upper-level shear. However, its CAPE was comparable to other storms, as was its low-level shear. A weak CG producer like 20 February had a nearly identical environment, in both CAPE and shear, to 26 January, which overall produced more CGs. In addition, using the formula,  $w_{\max} = \sqrt{2 * CAPE}$ , all of the adjusted CAPEs for each particular case give theoretical updraft speed maximums well in excess of what was observed.

#### 4.3 Vertical Structure

Much like with the mid-latitude storms, this study focused on 1-2 key periods in each storm's lifetime. One of those times was the time of a significant peak in updraft speed (if not the outright maximum updraft for the entire case). Radar volumes that corresponded to this time were 2030 UTC on 26 January 1999, 1733 UTC on 13 February 1999, 2030 UTC on 25 February 1999, 1750 UTC on 17 February 1999, and 1848 UTC on 20 February 1999.

Figure 4.39a shows average positive vertical air mass flux as a function of height for each storm corresponding to times of peak updraft. In general, at these times the tropical thunderstorms all had very comparable mass fluxes to one another, particularly considering the fact that the standard deviations for these fluxes (Figure 4.39b) were roughly as large as the means. In particular, averages and standard deviations of the fluxes were generally very close to one another within the mixed phase region (0 to  $-40$  °C), which spanned between 4 and 10.5 km AGL for these storms. Thus, while storms like 26 January and 15 February tended to feature more intense updrafts, overall their average (and standard deviations of) vertical air mass fluxes were comparable to the other storms. In fact, 15 February had systematically lower mass fluxes than the other storms throughout most of the vertical, although not too much should be read into this given the standard deviations observed. Overall, the tropical mass fluxes were very similar to the values posted for the mid-latitude storms of 21 and 25 July 1998 (Figure 3.49), which suggests that these tropical thunderstorms were of comparable intensity to moderate mid-latitude convection.

The next set of figures show CFADs of SPOL radar reflectivity and dual-Doppler-derived vertical velocity for these key times in each LBA storm. These CFADs were derived the same way as those in Chapter 3. Once again, particular attention was paid to the mixed phase region (4-10.5 km AGL).

Figure 4.40 shows CFADs of SPOL radar reflectivity (Figure 4.40a) and dual-Doppler-derived vertical velocity (Figure 4.40b) for the 26 January storm at 2030 UTC. Figure 4.41 shows the same but for 13 February at 1733 UTC. Figure 4.42 shows the same for 15 February at 2030 UTC, and Figure 4.43 shows the same for 17 February at 1750 UTC. Finally, Figure 4.44 shows CFADs for 20 February 1999 at 1848 UTC.

Examining the reflectivity CFADs, very little (0.1 % or less) of any storm contained a reflectivity of 50 dBZ or greater within the mixed phase region, and usually only in the extreme lower part. In addition, for all storms, the percentage of any storm containing 30 dBZ or greater varied significantly with altitude within the mixed phase region. However, the storms all had fairly similar profiles, with 30 dBZ and greater occupying over 35% of storm area at the lower altitudes within the mixed phase region, down to 1% or less near the  $-40$  °C altitude. Of all the storms, 26 January had the highest percentage of 30 dBZ and greater, with the other storms typically having only about 15% in the lower mixed phase region, although many compared favorably to 26 January near the top of the mixed phase region. The storms of 13 and 20

February probably had the weakest reflectivity CFADs overall, with 30 dBZ and greater declining to less than 0.1% of storm area near the top of the mixed phase region. These CFADs, as a whole, were less intense than those of the mid-latitude cases. They are consistent with the tropical thunderstorms having a much larger portion of their precipitation being formed through warm rain processes, rather than more ice-based microphysics in the mid-latitude cases.

The updraft CFADs also were similar among the different storms. For all storms, increasingly larger areas contained updrafts equal to or in excess of  $10 \text{ m s}^{-1}$  as altitude increased within the mixed phase region, ranging from 0.5% or less near the bottom to over 2% at the top. All storms featured  $20 \text{ m s}^{-1}$  or greater updrafts, but interestingly these updrafts tended to be situated outside the mixed phase region, in the upper portion of the storms. This was especially true on 15 February. Of all the storms, 17 February had the highest percentage of  $20 \text{ m s}^{-1}$  and larger within the mixed phase region, but still this value was at most 0.5%, which is very low compared to some of the mid-latitude storms. In addition, these updrafts were not seen in the lower mixed phase region. Of all the mid-latitude storms, the reflectivity and vertical velocity CFADs from 25 July compare the most favorably with the CFADs from the LBA thunderstorms.

The vertical structure of the tropical thunderstorms was examined in more detail. Figure 4.45a shows a vertical cross-section, at 35 km north of SPOL, of radar reflectivity, differential reflectivity, and positive vertical velocity for the 26 January storm at 2030 UTC. This is through the middle part of the observed portion of the storm, where the highest radar reflectivities were seen. Positive  $Z_{dr}$  and 50 dBZ reflectivity extended to over 5 km AGL, with the maximum in vertical velocity (over  $10 \text{ m s}^{-1}$ ) occurring above that. A vertical cross-section taken at the same time at 85 km north (Figure 4.45b) shows that the northern portion of the storm contained the highest vertical velocities, with a thin sliver of  $20 \text{ m s}^{-1}$  or greater co-located with enhanced upper level reflectivities (over 30 dBZ in fact). In this cross-section, positive  $Z_{dr}$  also extended to over 5 km AGL. Note, however, that unlike the Colorado storms, positive  $Z_{dr}$  was co-located with the highest reflectivities, so there were no indications of hail or so-called  $Z_{dr}$  columns.

Figure 4.46 is the same as Figure 4.45 except for the 13 February 1999 storm at 1733 UTC. The cross-section goes through 45 km north, the location of the main core of the storm. The easternmost cell was the most intense, with a small column of 50 dBZ, and positive  $Z_{dr}$  and 40 dBZ extending to 5 km and above. Much like 26 January, the vertical velocity maximum occurs above this, peaking at over  $20 \text{ m s}^{-1}$ . This

maximum was co-located with an elevated 30 dBZ contour, although this contour did not extend to as high and altitude as in 26 January (< 10 km versus over 13 km in 26 January).

Figure 4.47 shows a vertical cross-section of the same radar variables as before, but for 2030 UTC on 15 February 1999, at 24 km north of SPOL. The cross-section looks very similar to those from previous storms, with positive  $Z_{dr}$  in the most intense cell to 5 km AGL, and 40 dBZ to 7 km. Peak vertical velocity was over  $30 \text{ m s}^{-1}$ , and the updraft core was co-located with an elevated 30 dBZ contour, which reached to 14 km. Notice that in the weaker cell immediately to the east the lower level (< 5 km AGL) structure was similar (though with lower peak reflectivity and  $Z_{dr}$ ), but the updraft was significantly less intense, as was the upper-level reflectivity structure.

Figure 4.48 shows a vertical cross-section, at 17 km north of SPOL, of radar reflectivity, differential reflectivity, and positive vertical velocity for the 17 February 1999 storm, at 1750 UTC. Once again, positive  $Z_{dr}$  extended to roughly 5 km, with 40 dBZ reaching to around 8 km. The updraft exceeded  $20 \text{ m s}^{-1}$ , and was nearly co-located with 30 dBZ elevated to 12 km AGL.

Figure 4.49a shows a vertical cross-section, at 72 km north of SPOL, of the 20 February 1999 storm at 1739 UTC. This time corresponded to the time of minimal CG production by this storm. At this time the storm had a weaker reflectivity structure compared to the preceding storms, with reflectivities < 50 dBZ in the lower core. Also, 40 dBZ extended to just 5 km AGL, although positive  $Z_{dr}$  extended to roughly the same altitude as the other storms. Peak vertical velocity exceeded  $10 \text{ m s}^{-1}$ , but the 30 dBZ contour extended to only 7 km or so. Thus, the lack of CG lightning activity at this time may be attributed to a weaker vertical structure, which led to less electrification overall.

Figure 4.49b shows a vertical cross-section at 1848 UTC, the time of maximum updraft. The cross-section goes through the same cell as before, but by now it had moved to 60 km north of SPOL. The storm at this time had intensified, with the updraft exceeding  $20 \text{ m s}^{-1}$  and co-located with a thin sliver of a 30 dBZ contour that reached as far as 13 km AGL. However, there still was no 50 dBZ in the lower core, and 40 dBZ still extended to only 5 km AGL. Positive  $Z_{dr}$  extended to roughly the same altitude as before, about 5 km. This second cross-section was more intense than the previous one, although it still was somewhat weaker overall than previous storms.

Figure 4.50 shows one more vertical cross-section for the 20 February storm, at 25 km north of SPOL. The time is 1859 UTC, which coincides with the time of peak CG flash rate in this storm. This cross-section goes through the southern portion of this storm, which from Figure 4.38 appeared to be producing the most CGs. The easternmost cell was the most intense, and compared favorably to cross-sections for the other LBA thunderstorms. While peak vertical velocity did not exceed  $20 \text{ m s}^{-1}$  in this part of the storm, 30 dBZ did extend up to 12 km, and was co-located with the updraft core. Similar to other storms, positive  $Z_{dr}$  extended to 5 km AGL, and 40 dBZ reached 6 km.

#### *4.4 Testing of Elevated Charge Mechanism*

The elevated charge hypothesis predicts that the storms with the strongest drafts should feature the lowest negative CG lightning flash rates, and the highest IC:CG ratios. Based on the vertical velocity CFADs (Figures 4.40-4.44), vertical air mass fluxes (Figure 4.39), as well as peak updrafts (Figures 4.3, 4.11, 4.18, 4.26, and 4.34) and updraft volume statistics (Figures 4.4, 4.12, 4.19, 4.27, and 4.35), the tropical thunderstorms can be subjectively compared in terms of updraft intensity. Overall, the storms were fairly comparable to one another in terms of updraft intensity. The CFADs and vertical air mass fluxes were very similar among all the cases. The 26 January and 15 February storms had the strongest peak updrafts, while 13 February had the weakest. The storms of 17 and 20 February fell between these extremes. However, peak updrafts varied much less than was seen in the Colorado cases, from just over  $20 \text{ m s}^{-1}$  to just over  $30 \text{ m s}^{-1}$ . The volumes of significant updrafts also did not vary as much as was seen in the Colorado cases. The 13 and 17 February storms were perhaps the weakest in this category, but the other storms all compared favorably to one another.

The CG lightning flash rates (Figures 4.6, 4.14, 4.21, 4.29 and 4.37), showed more variability among the different cases from Brazil, although once again this variability was not as much as was seen in the Colorado cases. The lowest observed peak value was 20 CGs in a 10-minute period (13 February) and the highest was 64 CGs in a 10-minute period (17 February). This 3:1 ratio between highest and lowest was much lower than the 9:1 ratio seen in the mid-latitude data set. The differences in these ratios increases dramatically if one considers just the peak negative CG flash rates, as the Colorado cases included many low negative CG producers. When they were able to be estimated, the total flash rates and IC:CG ratios

from the tropical cases generally were fairly modest, particularly when compared to the peak Colorado cases.

Overall, the tropical cases were very similar to one another kinematically. On this level, they compare perhaps most favorably with the moderate mid-latitude case of 25 July 1998. Electrically, while there was some variability, there was not as much as the mid-latitude cases, and as a whole the tropical cases compare once again most favorably to the moderate 25 July case.

The 20 February case poses some potential problems. It had a period of low-CG production, but this coincided with the first half of this storm's analysis period, when the storm generally was weaker kinematically and had a weaker vertical reflectivity structure. Thus, it could be argued that the storm was not significantly electrified at this time. However, even during the storm's more intense period, CGs were not associated with the intense northern cell. While this phenomenon was consistent with other low-CG storms from the mid-latitude cases, those storms had vastly more intense reflectivity and kinematic structures, while 20 February was at best comparable to, if not weaker than, other more significant CG producers like 26 January. In addition, some of the cells in the CG-producing part of the storm were fairly intense, and had similar vertical structures to other tropical thunderstorms in this study. Thus, the 20 February storm was not all that anomalous.

While it would be difficult to discern anything like an elevated charge mechanism within the narrow kinematic spectrum that the tropical cases provided, taken in concert with the mid-latitude cases, they help to fill out the middle part of the kinematics-lightning spectrum. In this region one would expect increasing negative CG flash rates along with increasing total flash rates as kinematic strength increased. The strongest storms, kinematically speaking, like 26 January and 15 February, featured higher negative CG flash rates than the somewhat weaker 13 and 20 February storms. The 17 February case had the highest negative CG flash rates of any case, but had a weaker kinematic structure than 26 January and 15 February. Thus, it perhaps does not place as well within these narrow considerations. However, looking at the big picture and considering the probabilistic nature of lightning, some scatter is expected. In addition, BLDN flash location issues cannot be ruled out in explaining this dichotomy. Moreover, it is possible that this broad analysis could have missed some subtle differences between each case, details that could have influenced the electrification of these storms. More detailed case studies would be required to discern

whether or not this were true. In the larger frame of view, though, the radar and lightning observations from these five tropical cases are consistent with an elevated charge mechanism.

#### *4.5 Testing of PPCG Mechanisms*

None of the tropical thunderstorms in this study produced anomalously high amounts of positive CG flashes. Therefore, there is little testing of PPCG mechanisms that can be done. However, some comments can be made about the implications for the three proposed PPCG mechanisms, based on the observations of these tropical thunderstorms. Upper-level shear generally was less in the tropical cases than the mid-latitude cases, particularly the PPCG cases. This is consistent with the tilted dipole mechanism, although it hardly supports it strongly. The tropical cases all produced comparable rain to the mid-latitude cases. In fact, some cases like 26 January exceeded the rain production of many of the mid-latitude cases. However, none of these storms experienced a dramatic intensification like the 15 July 1998 and 29 June 2000 storms. Thus, the tropical observations do not necessarily contradict either the inverted dipole or the precipitation unshielding hypotheses.

#### *4.6 Testing of Separated Updraft-Downdraft Mechanism*

Similar to the mid-latitude cases, simple correlations were performed between SPOL reflectivity and vertical velocity. Correlations were performed for all volumes on all days. For a given radar volume, correlations were done in the same regions as the mid-latitude cases: over the entire radar volume, only in the region of 30 dBZ and greater, only in the region of  $-10$  to  $0$  °C, and in 30 dBZ and greater plus in the region of  $0$  to  $-10$  °C. The best correlations found are summarized in Table 4.3. Much like what was seen in the mid-latitude cases, the absolute value of the correlation coefficient generally was well under 0.6, and of varying sign. Moreover, correlations were highly variable during the lifetime of a particular storm, and at times were near zero.

These weak correlations are not surprising in the context of the separated updraft-downdraft mechanism, however, since none of the tropical thunderstorms could reasonably be called low-CG. Thus, strong negative correlations should not be seen if the mechanism were active. However, many of the best correlations for the tropical cases were negative, and often very close to the best correlations seen in the

mid-latitude cases, particularly the low producers of negative CGs (1 and 15 July 1998, 29 June 2000). It is not clear why this should be the case if the separated updraft-downdraft mechanism were operative.

The updraft-downdraft mechanism also was examined in a more subjective manner, with horizontal cross-sections taken through 5.0 km AGL, which is located within the key  $-10$  to  $0$  °C region. Figure 4.51 shows cross-sections for the key time of 2030 UTC (the time of maximum updraft) on 26 January 1999. In general, the major precipitation cores were roughly co-located with the main updraft cores. Figure 4.52 shows cross-sections for the 13 February 1999 storm, at 1733 UTC (updraft maximum). Once again, no major offset between precipitation and updraft cores was seen.

Continuing on to 15 February, Figure 4.53 shows a cross-section at 2030 UTC (updraft maximum), and once again updraft and precipitation cores were roughly in the same area as one another. Similar results were obtained for the 17 February 1999 storm, whose cross-section at 1750 UTC (updraft maximum) is shown in Figure 4.54. Finally, the storm of 20 February continued the pattern, with updraft cores very near precipitation cores, as seen in Figure 4.55, which is from 1848 UTC (updraft maximum).

Thus, overall the tropical thunderstorms showed very little offset between updraft and precipitation cores. In addition, all of these storms produced plenty of negative CGs. Thus, these results were not inconsistent with the separated updraft-downdraft mechanism, because none met the necessary requirement of offset updraft and precipitation cores, and none could be confidently termed a low-CG storm. However, these results don't necessarily support the existence of this mechanism either, as there were no true low-CG storms in this data set to contrast with these cases.

#### *4.7 Summary*

Radar, lightning, and sounding data from five tropical continental thunderstorms were analyzed, compared, and contrasted. Several proposed mechanisms to explain the observed lightning patterns were tested. The data best supported the elevated charge mechanism, as the tropical thunderstorms fell in the middle range of the kinematic spectrum, matching mid-latitude cases like 25 July 1998 with its moderate negative CG production and IC:CG ratio. The tropical cases all had very similar kinematic and reflectivity structures to 25 July 1998. Although their negative CG lightning production was significant, it fell below the peak production by 25 July 1998. However, some of the tropical cases exhibited higher IC:CG ratios

than 25 July. Thus, it appears that there is some scatter in this middle area of the kinematic-lightning spectrum, which is likely due to the probabilistic nature of lightning (or perhaps BLDN and FCM issues). Overall, however, the tropical cases fit nicely within the spectrum predicted by the elevated charge hypothesis.

The storms of 26 January and 15 February 1999 produced the most rainfall, and saw some of the higher negative CG lightning flash rates of the tropical cases. However, 13, 17, and 20 February tended to produce comparable rainfall, but 17 February had a larger negative CG lightning flash rate than even 26 January and 15 February. While there were important problems with BLDN CG flash locations, and thus CG flash rate estimates for these storms, these observations are consistent with what was seen in the mid-latitude cases: Rainfall (in terms of heavy rain area and rain mass flux) does not appear to play a significant role electrically, in the sense that it does not affect total or CG lightning flash rate.

The separated updraft-downdraft mechanism was not contradicted by the tropical observations, but neither was it heavily supported, since there was no clear low-CG storm to compare against the others. In fact, many of the tropical thunderstorms exhibited reflectivity-draft correlations comparable to low-CG storms from the mid-latitude cases. In addition, the PPCG mechanisms (tilted dipole, inverted dipole, precipitation unshielding) were not contradicted by the tropical cases, but once again there was no tropical PPCG case against which the others could be compared. Thus, the tropical data are fairly neutral with respect to these mechanisms.

Table 4.1: Summary of kinematic, microphysical, and lightning observations for the tropical cases.

	26 Jan 99	13 Feb 99	15 Feb 99	17 Feb 99	20 Feb 99
Peak $Z_h$ (dBZ)	60.2	54.9	55.7	54.7	54.7
Peak Height 30 dBZ (km AGL)	15.0	15.5	15.0	14.0	14.0
Peak $W$ ( $m s^{-1}$ )	30.3	24.5	33.7	27.6	26.4
Peak Volume $W > 10 m s^{-1}$ ( $km^3$ )	1192.0	380.5	829.5	363.5	783.0
Peak Volume $W > 20 m s^{-1}$ ( $km^3$ )	53.5	14.5	177.5	44.5	73.5
Peak Area Heavy Rain ( $km^2$ )	200.0	32.0	98.0	28.0	41.0
Peak Rain Mass Flux ( $10^6 kg s^{-1}$ )	20.1	7.4	13.4	9.1	7.3
Peak -CG Flash Rate (flashes per 10 minutes)	39	20	49	64	26
Peak Total Flash Rate (flashes per 5 minutes)	64	NA	79	32	NA

Table 4.2: CAPE (in  $\text{J kg}^{-1}$ ) and shear (in  $\text{m s}^{-1}$ ) calculations for the tropical cases.

	<b>Standard CAPE</b>	<b>Sfc-475 mb Shear</b>	<b>475-200 mb Shear</b>
<b>26 January 1999</b>	1622.6	9.43	5.49
<b>13 February 1999</b>	2078.5	14.75	5.74
<b>15 February 1999</b>	508.5	6.46	5.46
<b>17 February 1999</b>	2066.9	9.06	10.37
<b>20 February 1999</b>	1664.1	9.13	5.80

Table 4.3: Best correlation coefficients for reflectivity versus vertical wind speed, considering various regions of the tropical thunderstorms. Also shown are the times of the radar volumes in which the best correlations were found (Z – UTC).

	<b>All of Storm</b>	<b>&gt; 30 dBZ</b>	<b>0 to -10 °C</b>	<b>0 to -10 °C &amp; &gt; 30dBZ</b>
<b>26 January 1999</b>	-0.131 (1950Z)	0.263 (2150Z)	-0.230 (1950Z)	-0.415 (2040Z)
<b>13 February 1999</b>	0.351 (1730Z)	0.384 (1730Z)	0.506 (1730Z)	0.518 (1730Z)
<b>15 February 1999</b>	-0.279 (1901Z)	-0.246 (1901Z)	-0.469 (1901Z)	-0.432 (1901Z)
<b>17 February 1999</b>	-0.249 (1810Z)	0.104 (1810Z)	-0.467 (1730Z)	-0.335 (1750Z)
<b>20 February 1999</b>	-0.306 (1920Z)	-0.396 (1839Z)	-0.437 (1933Z)	-0.544 (1839Z)

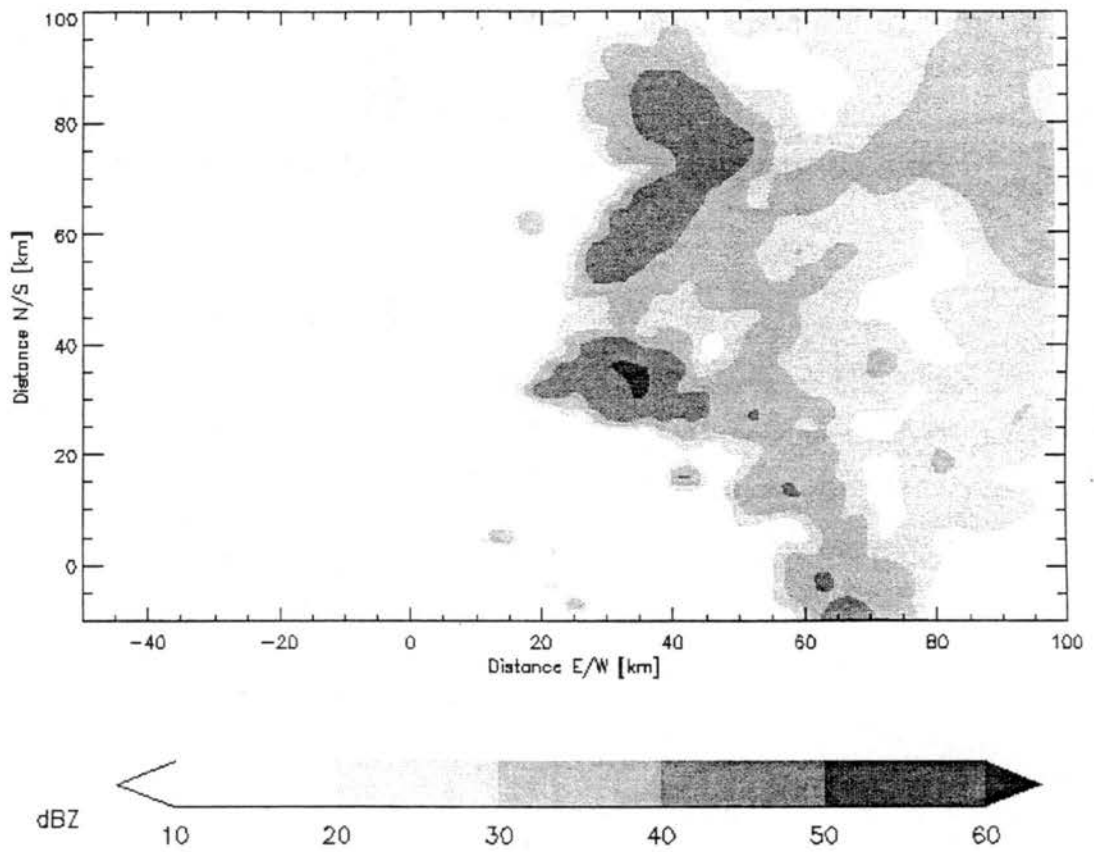


Figure 4.1: Horizontal cross-section of SPOL radar reflectivity at 0.5 km AGL, at 2030 UTC on 26 January 1999. Distances are relative to SPOL.

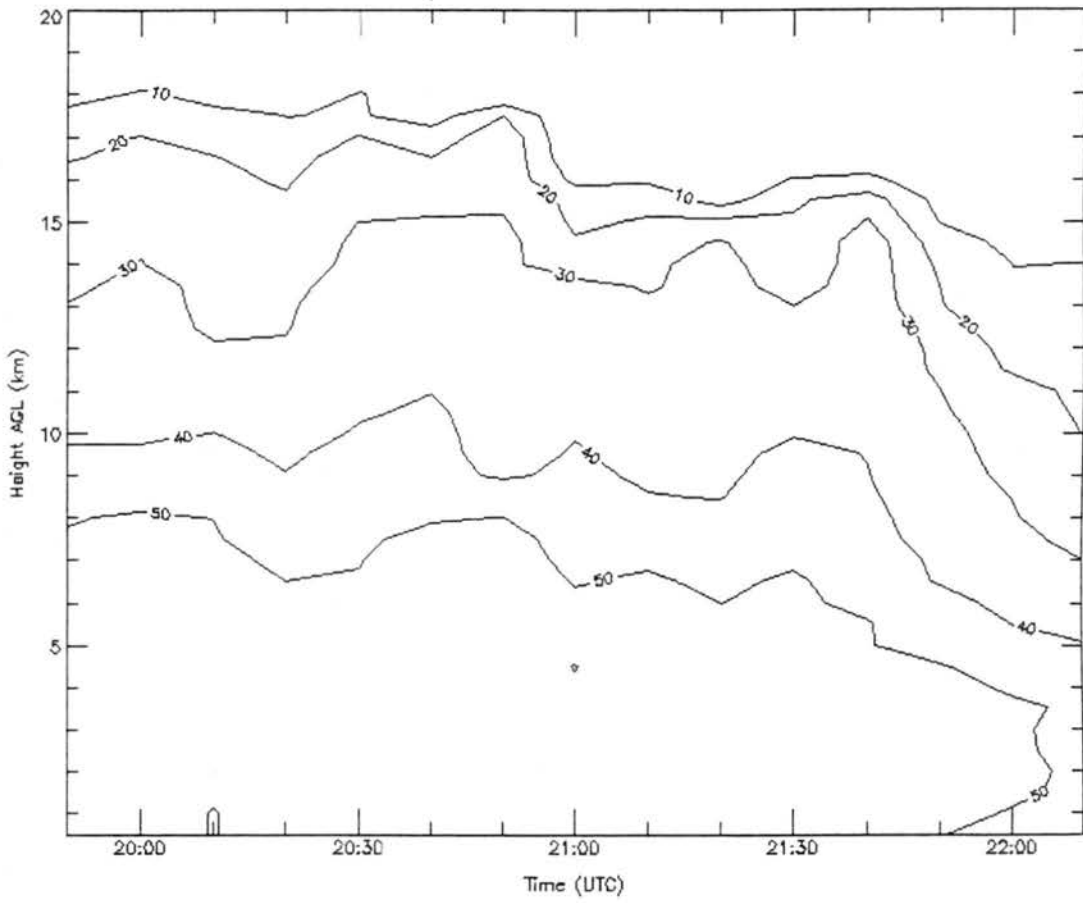


Figure 4.2: Time-height cross-section of peak SPOL radar reflectivity for the 26 January 1999 storm. Values are in dBZ.

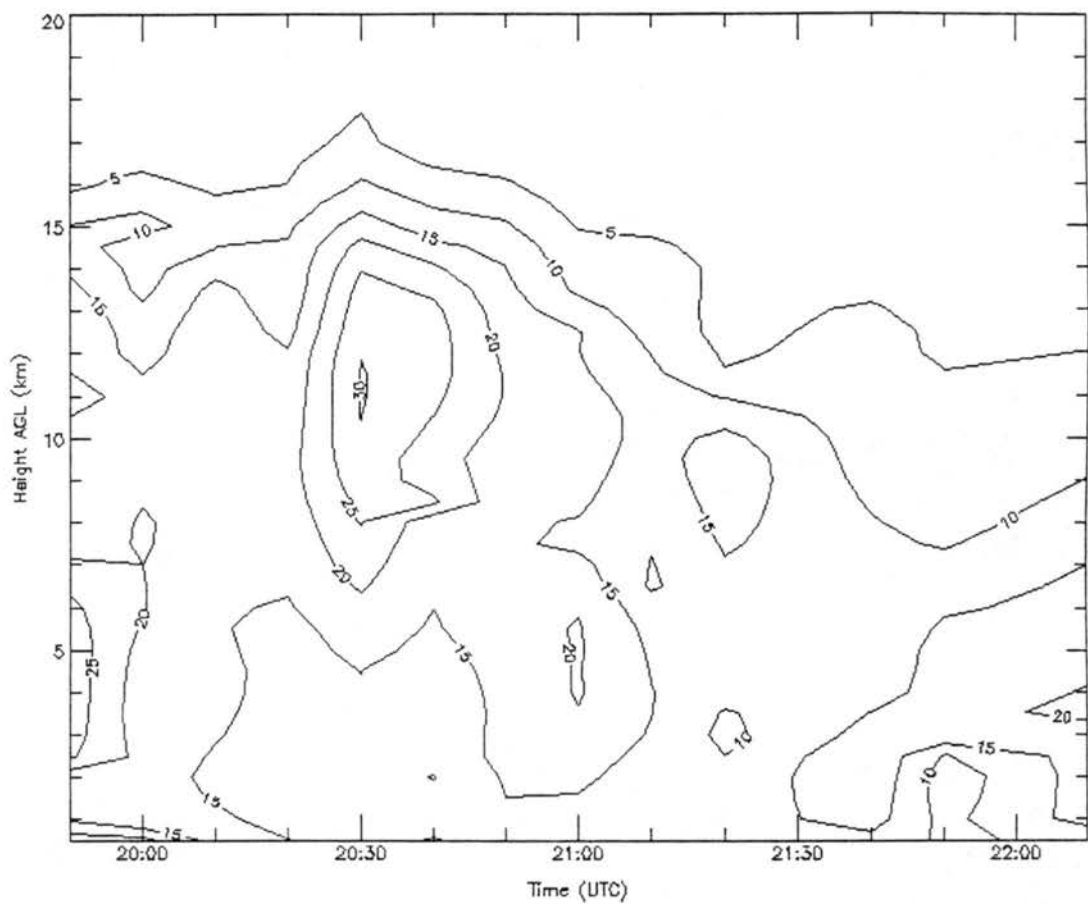


Figure 4.3: Time-height cross-section of maximum vertical velocity for the 26 January 1999 storm. Values are in  $\text{m s}^{-1}$ .

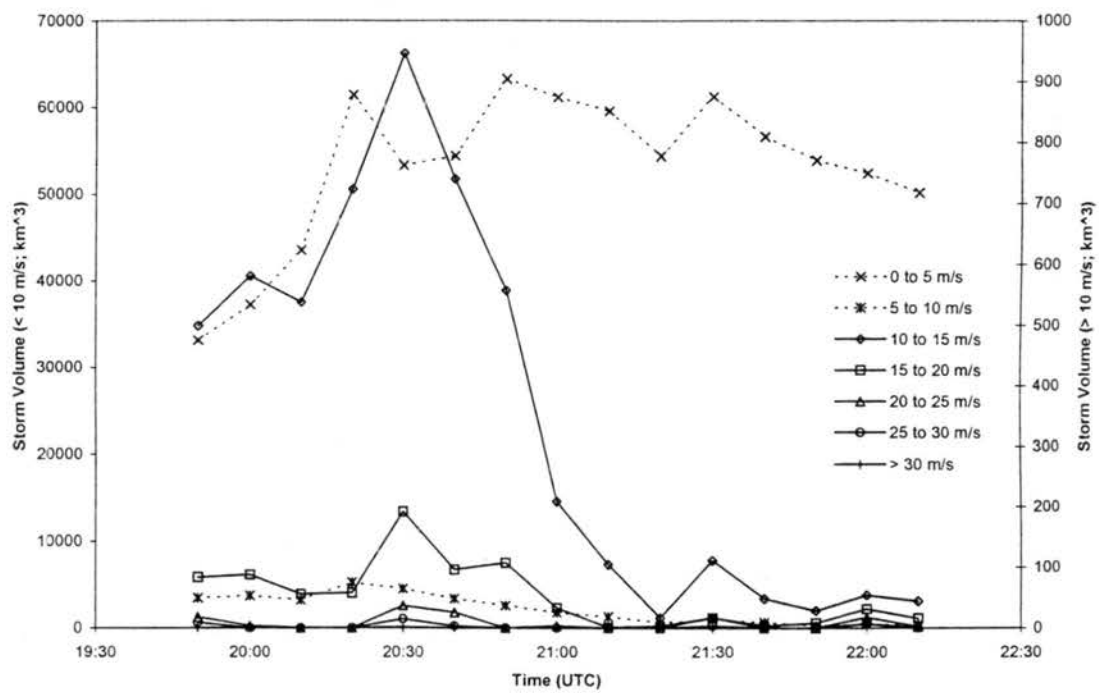


Figure 4.4: Volume of 26 January 1999 storm containing updrafts within respective bins as a function of time.

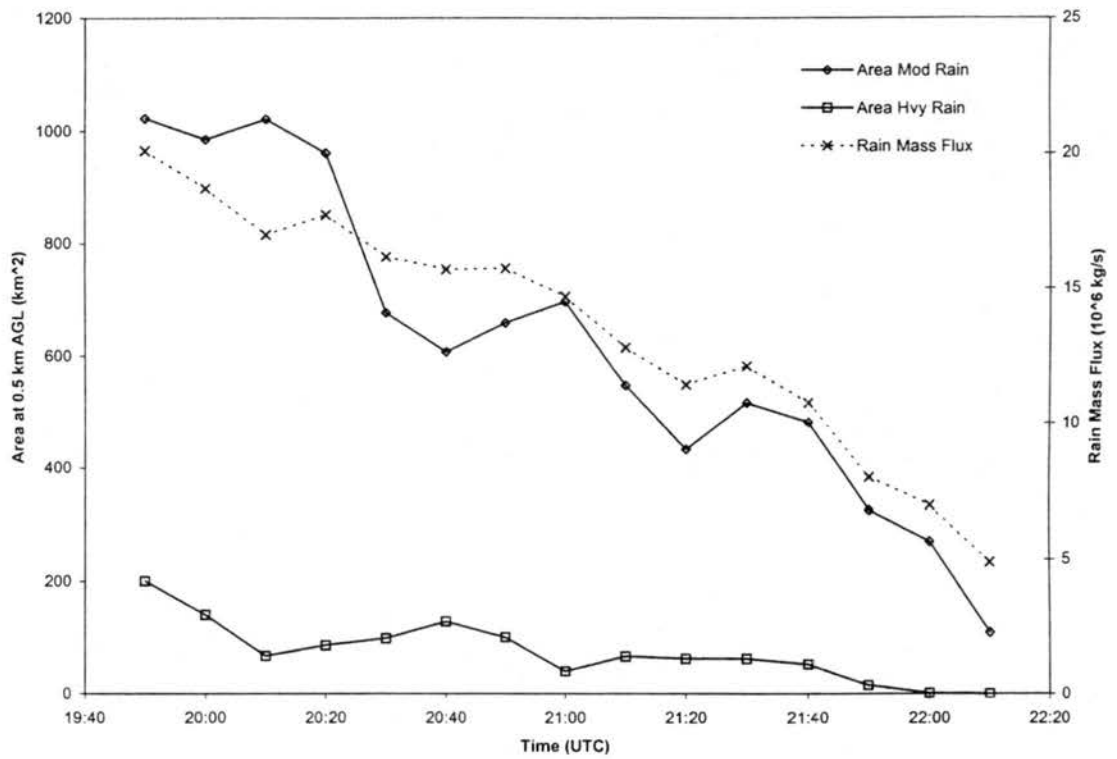


Figure 4.5: Rain production by the 26 January 1999 storm as a function of time. Values are at 0.5 km AGL. Moderate rain is 20-60 mm h<sup>-1</sup>, and heavy rain is greater than 60 mm h<sup>-1</sup>.

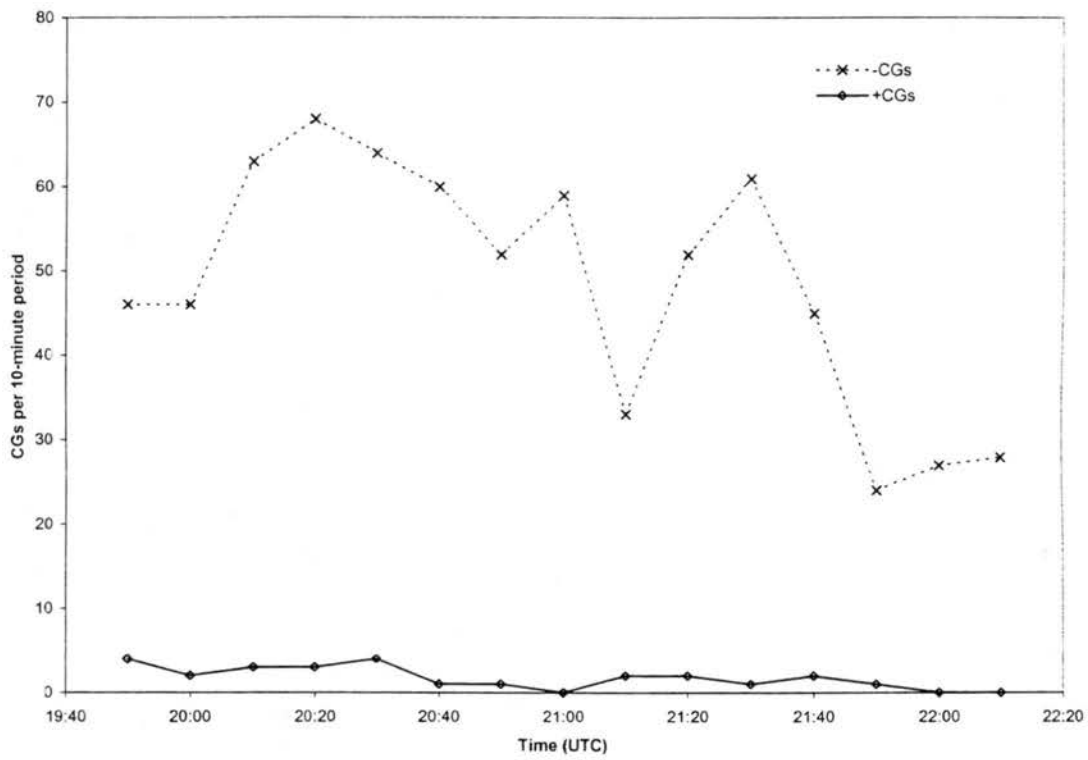


Figure 4.6: CG flash rates as functions of time for the 26 January 1999 storm.

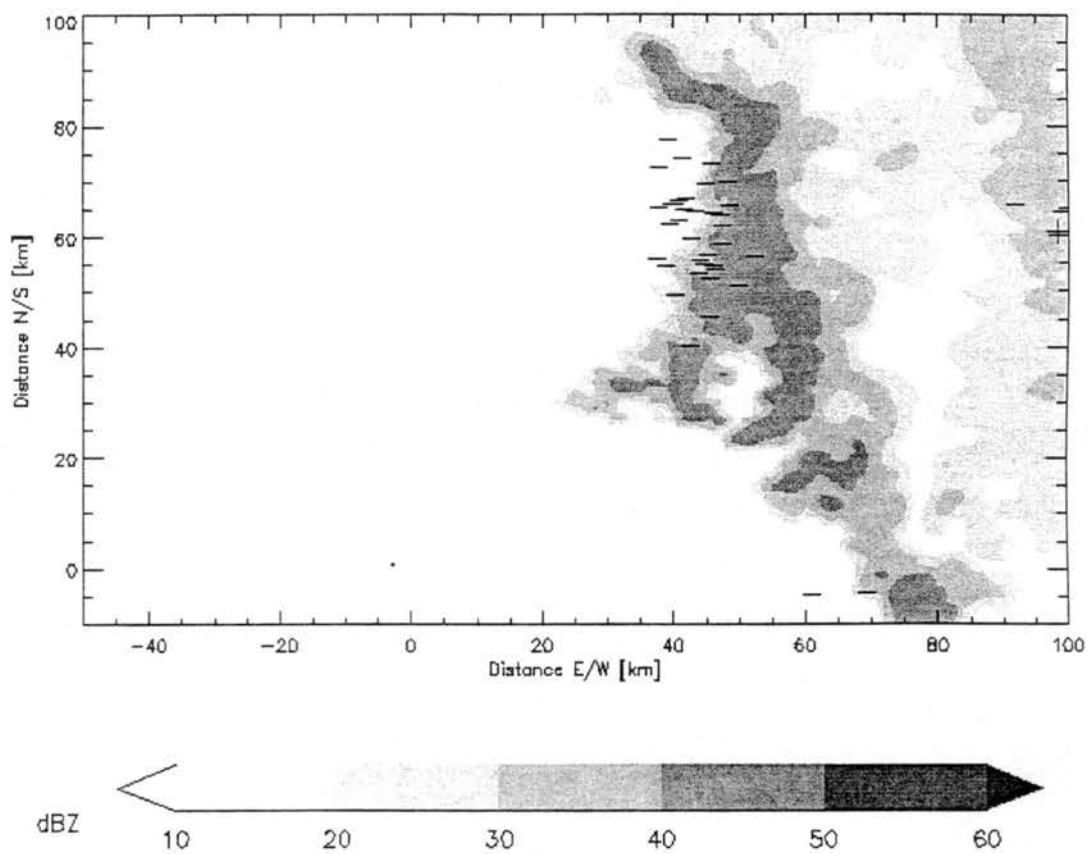


Figure 4.7: Horizontal cross-section of SPOL radar reflectivity at 0.5 km AGL, at 2010 UTC on 26 January 1999. Also shown are ground strike positions (plus signs for positives, minus signs for negatives) of BLDN CGs that occurred during 2010-2020 UTC. Distances are relative to SPOL.

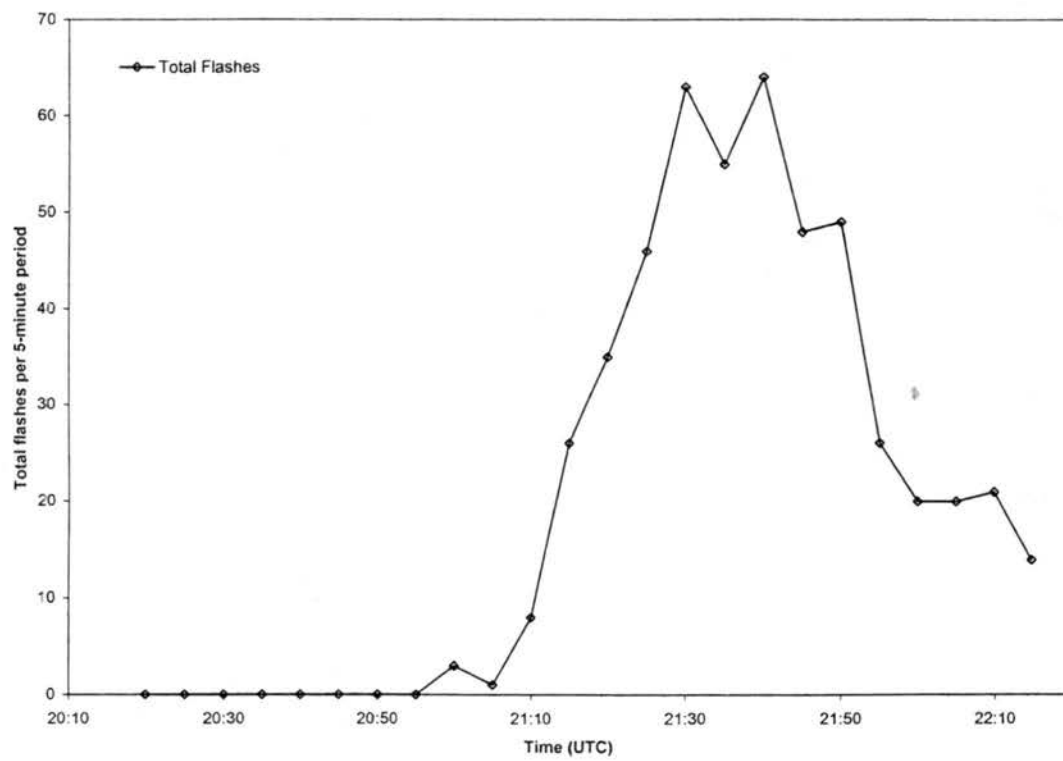


Figure 4.8: Total flash rate as a function of time for the 26 January 1999 storm.

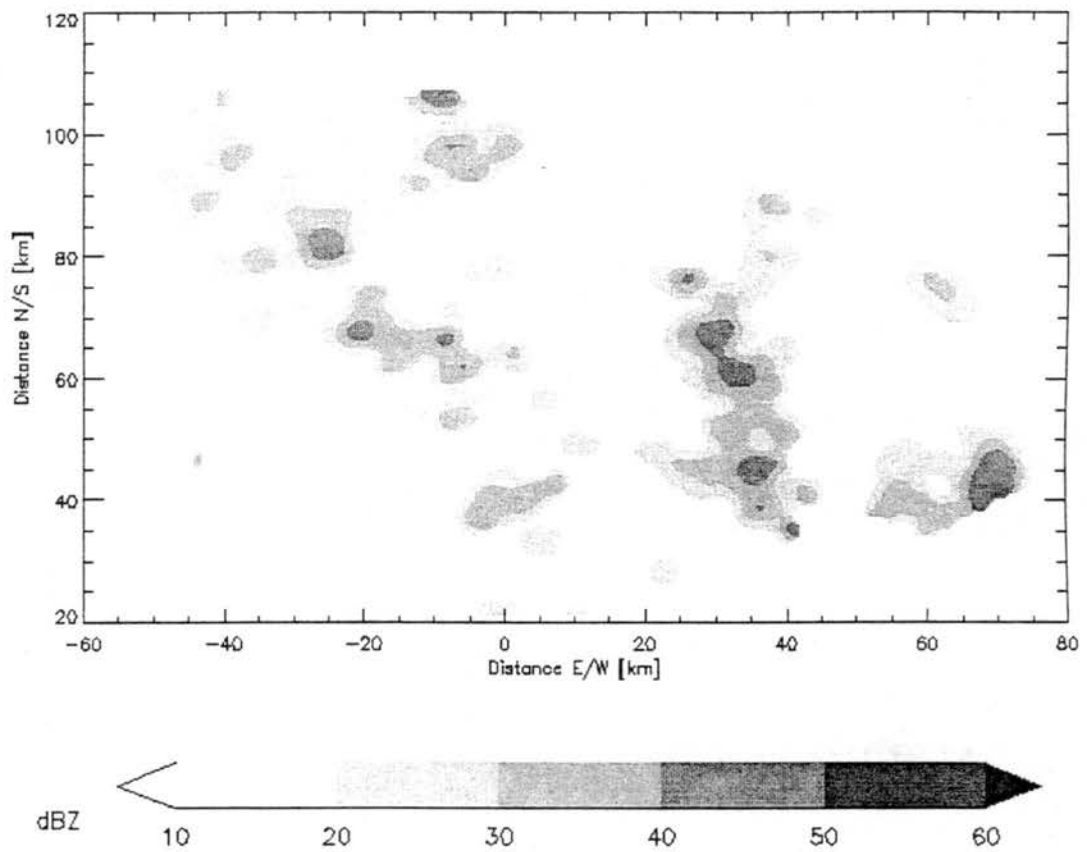


Figure 4.9: Horizontal cross-section of SPOL radar reflectivity at 0.5 km AGL, at 1733 UTC on 13 February 1999. Distances are relative to SPOL.

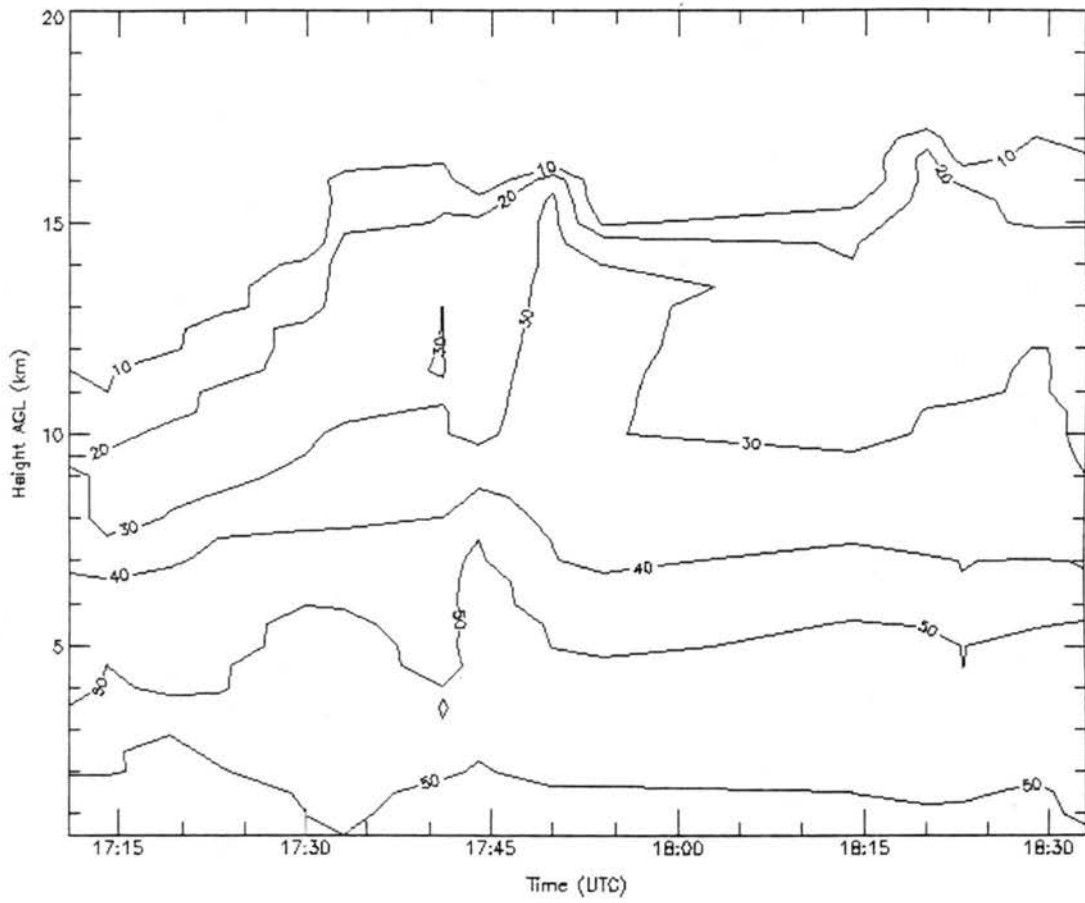


Figure 4.10: Time-height cross-section of peak SPOL radar reflectivity for the 13 February 1999 storm. Values are in dBZ.

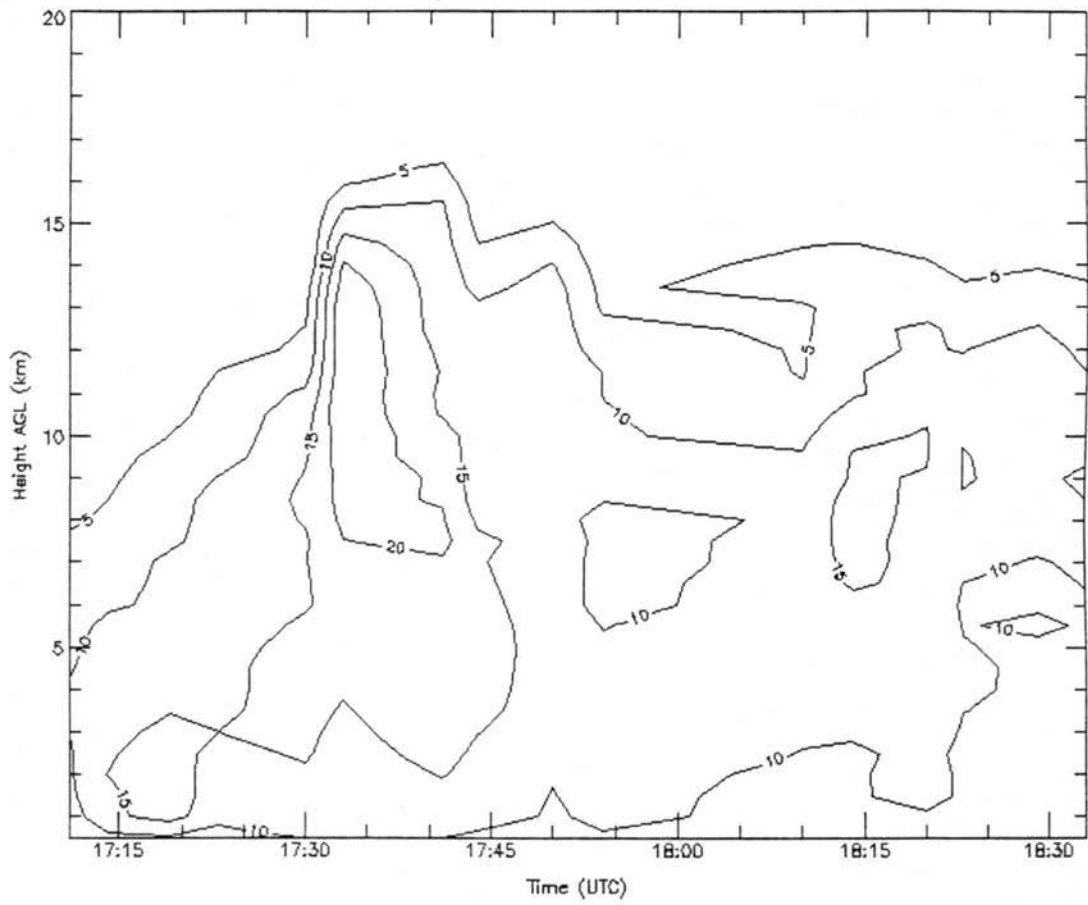


Figure 4.11: Time-height cross-section of maximum vertical velocity for the 13 February 1999 storm. Values are in  $\text{m s}^{-1}$ .

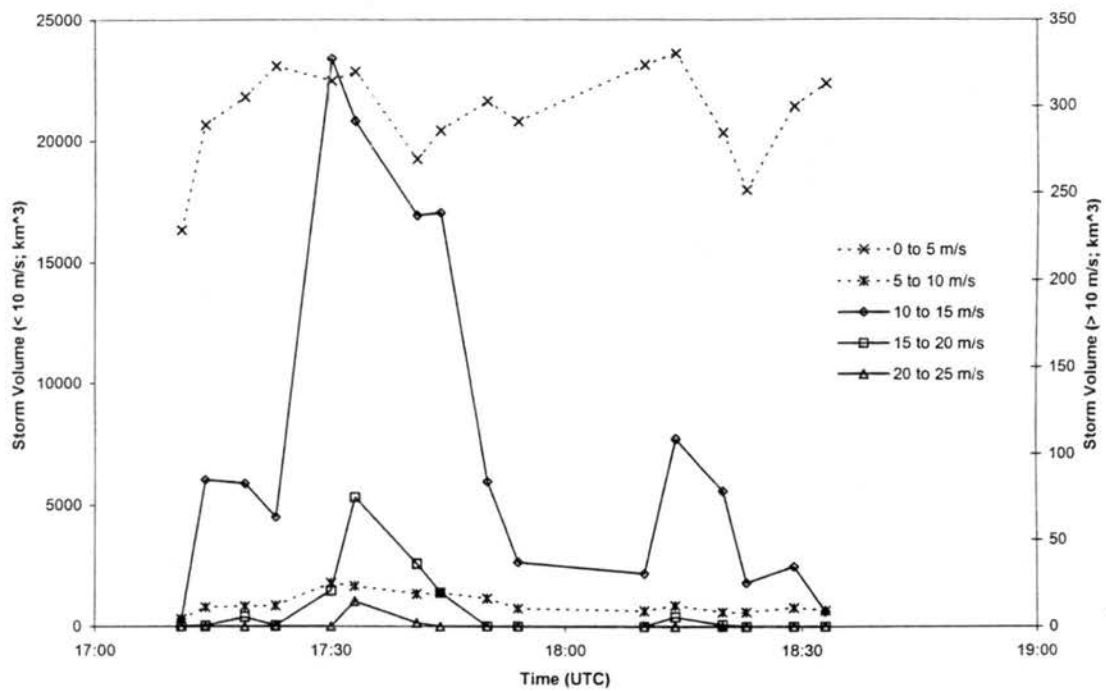


Figure 4.12: Volume of 13 February 1999 storm containing updrafts within respective bins as a function of time.

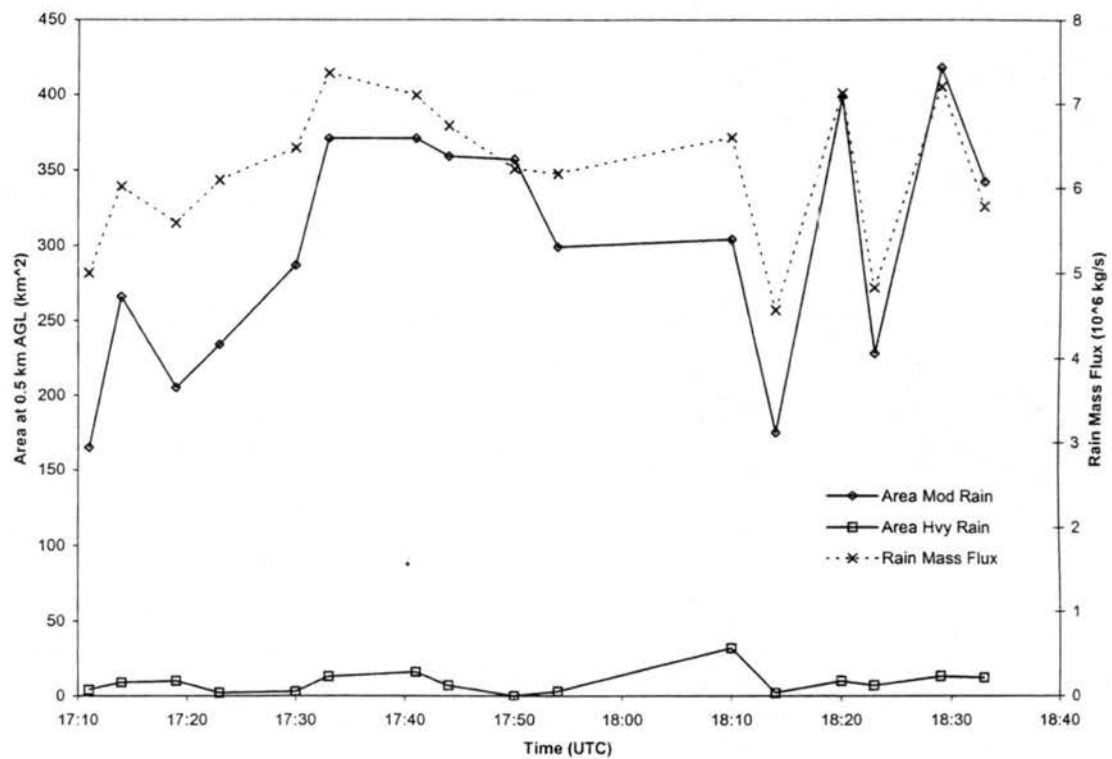


Figure 4.13: Rain production by the 13 February 1999 storm as a function of time. Values are at 0.5 km AGL. Moderate rain is 20-60 mm h<sup>-1</sup>, and heavy rain is greater than 60 mm h<sup>-1</sup>.

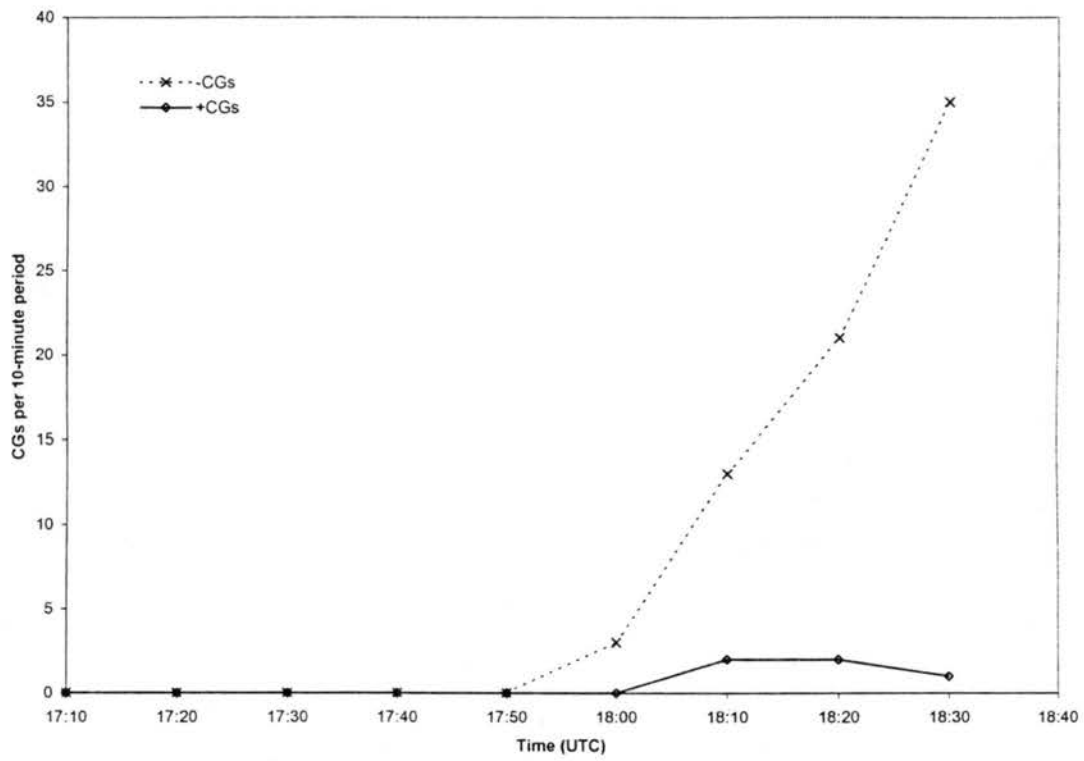


Figure 4.14: CG flash rates as functions of time for the 13 February 1999 storm.

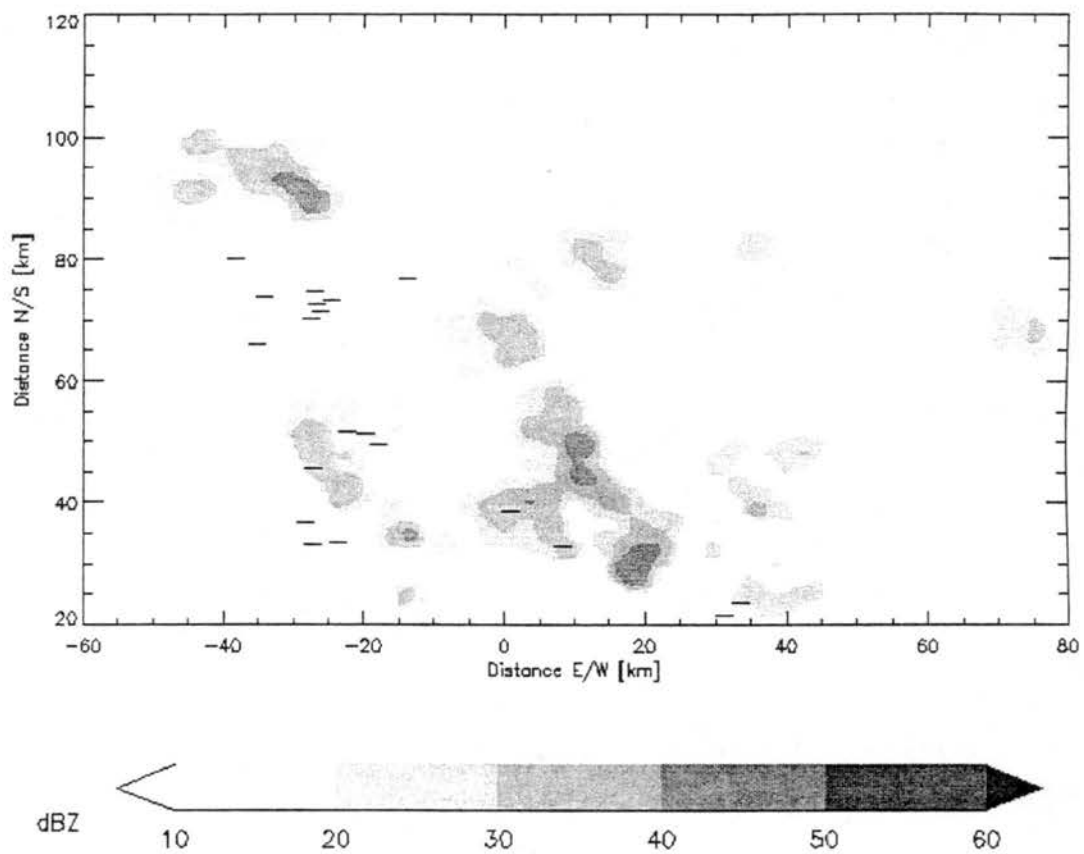


Figure 4.15: Horizontal cross-section of SPOL radar reflectivity at 0.5 km AGL, at 1833 UTC on 13 February 1999. Also shown are ground strike positions (plus signs for positives, minus signs for negatives) of BLDN CGs that occurred during 1830-1840 UTC. Distances are relative to SPOL.

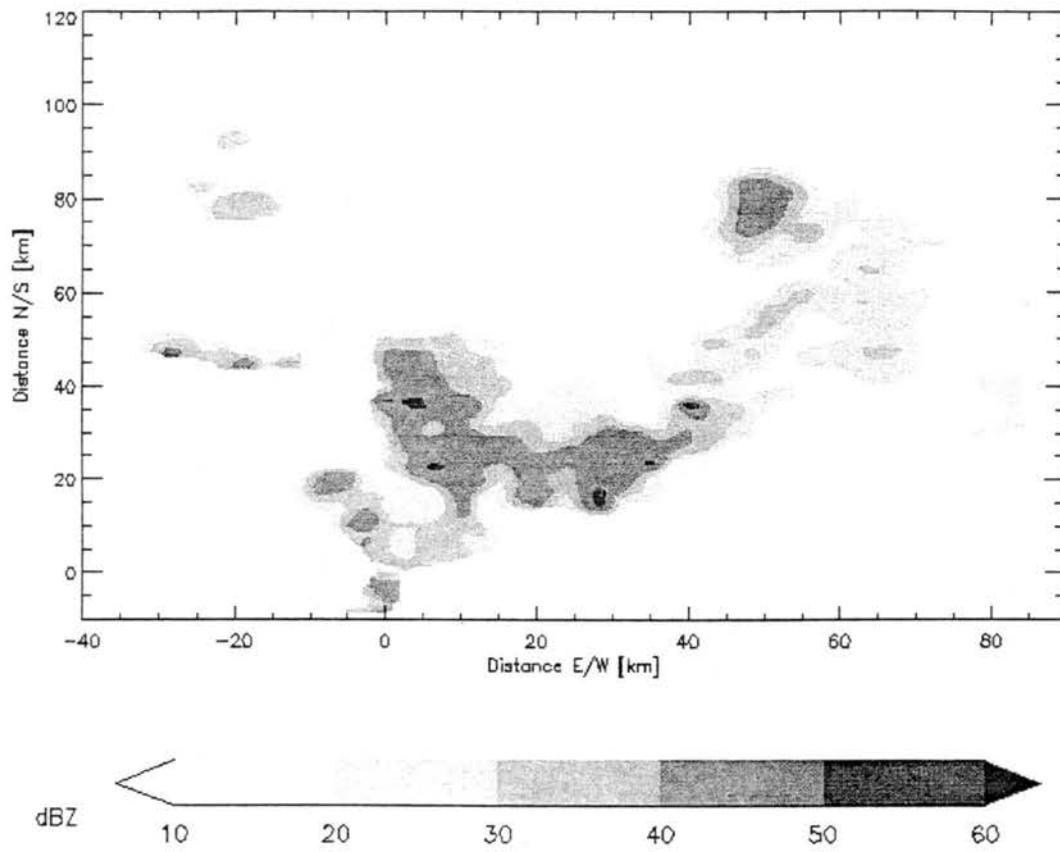


Figure 4.16: Horizontal cross-section of SPOL radar reflectivity at 0.5 km AGL, at 2030 UTC on 15 February 1999. Distances are relative to SPOL.

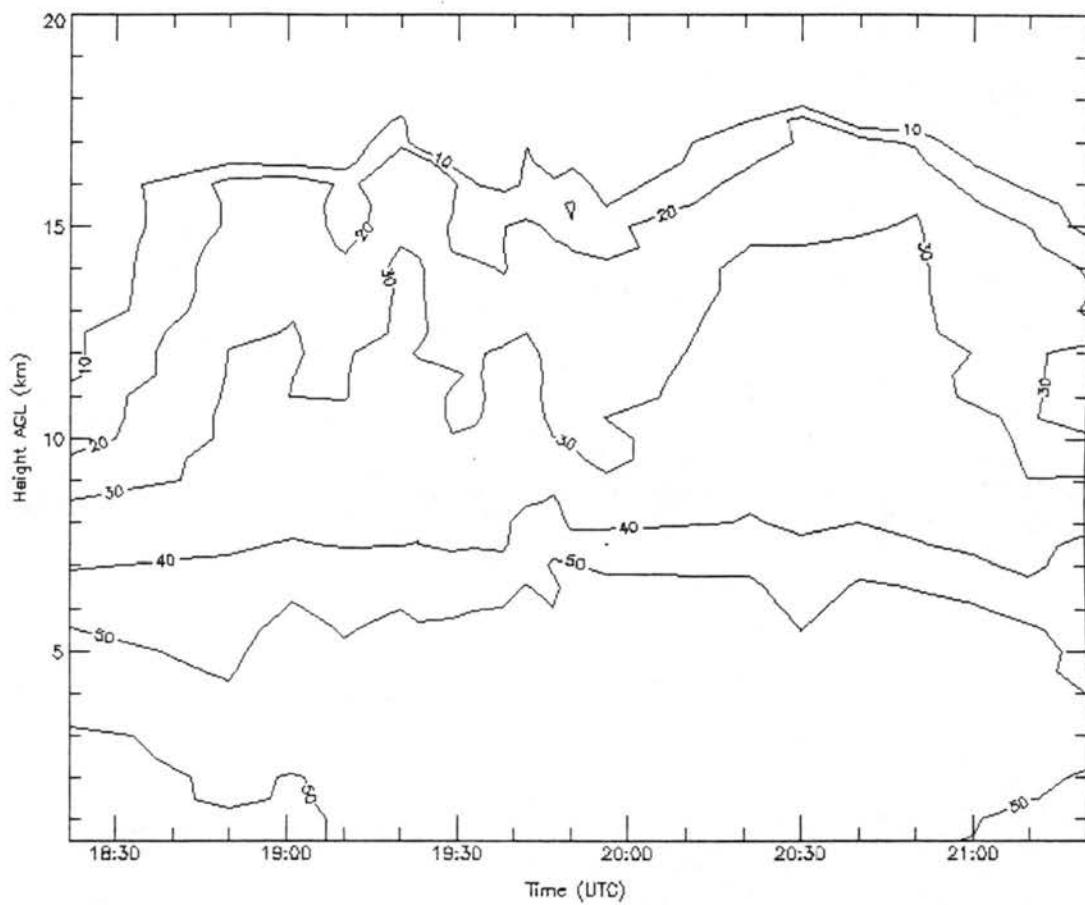


Figure 4.17: Time-height cross-section of peak SPOL radar reflectivity for the 15 February 1999 storm. Values are in dBZ.

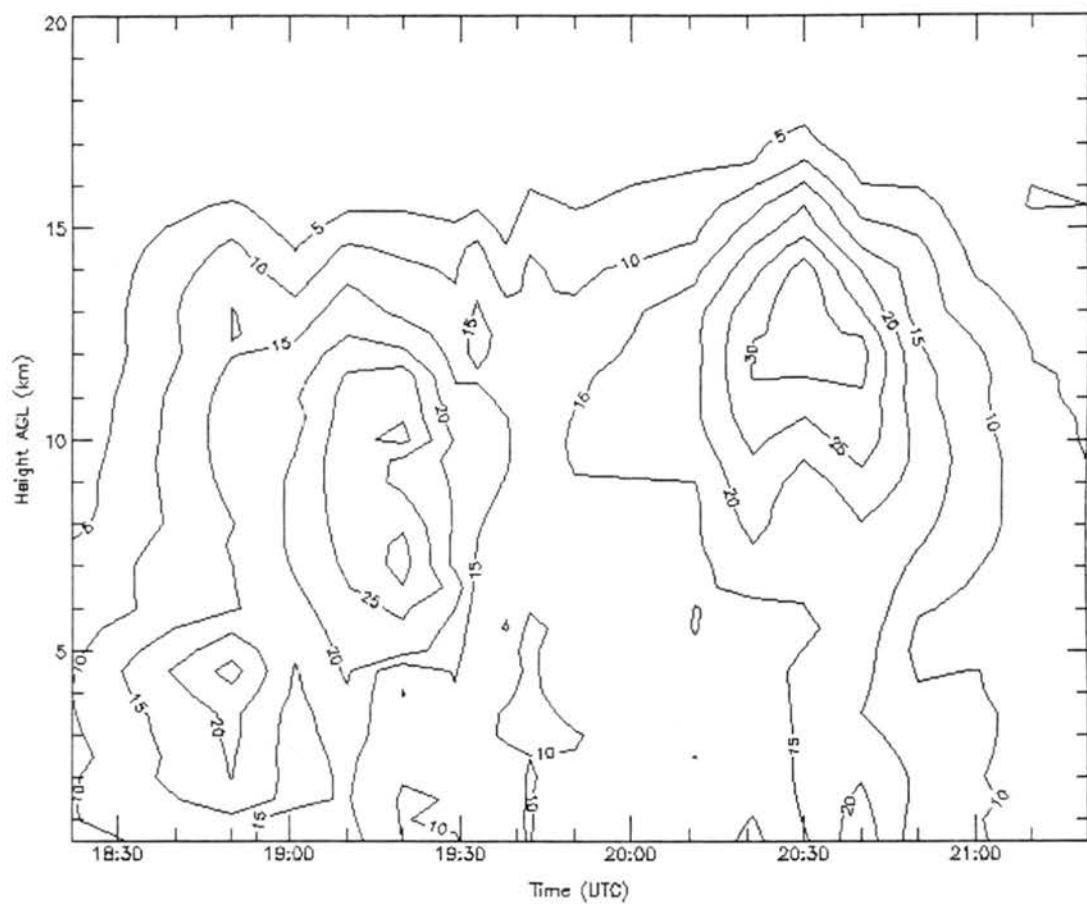


Figure 4.18: Time-height cross-section of maximum vertical velocity for the 15 February 1999 storm. Values are in  $\text{m s}^{-1}$ .

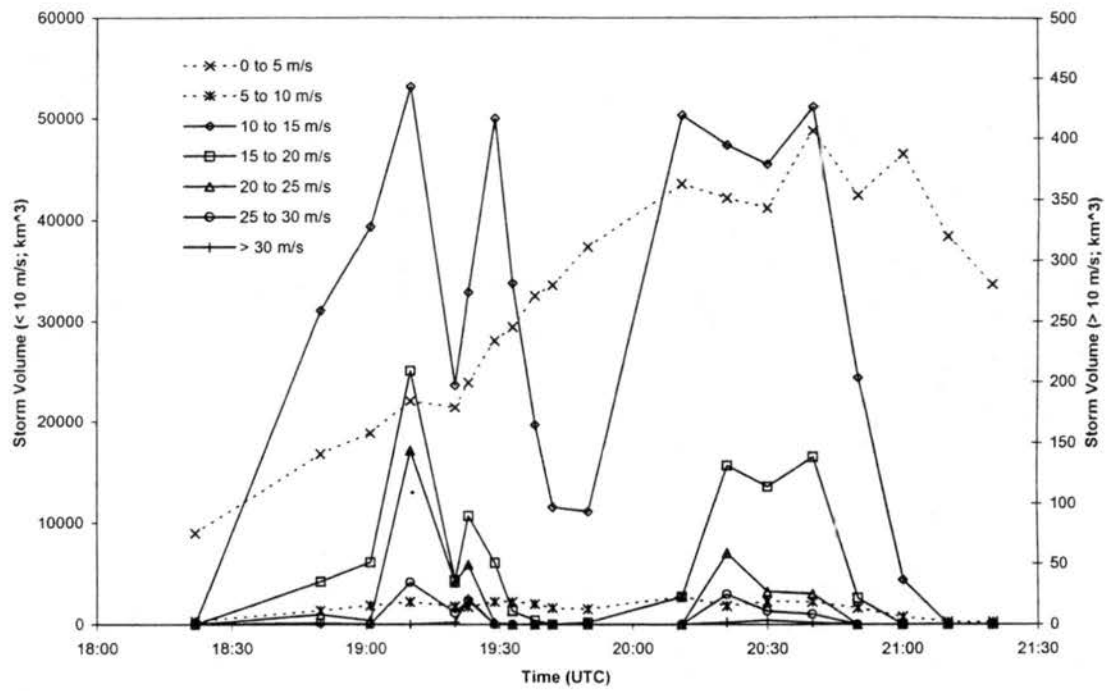


Figure 4.19: Volume of 15 February 1999 storm containing updrafts within respective bins as a function of time.

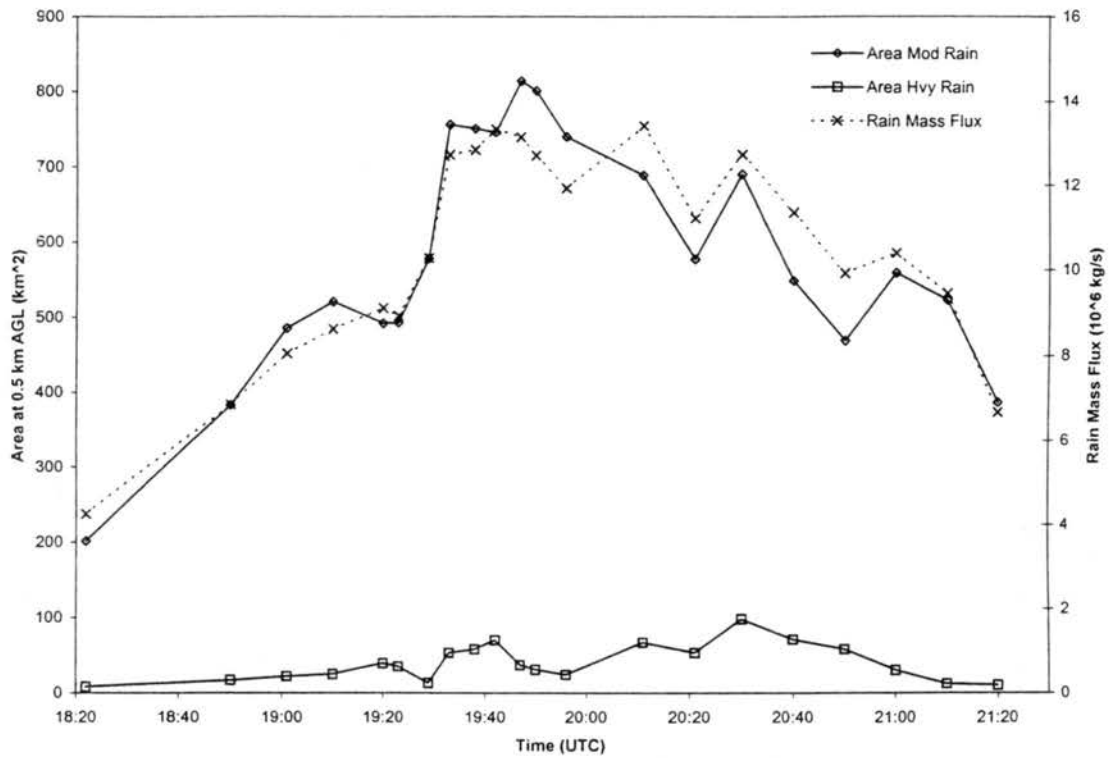


Figure 4.20: Rain production by the 15 February 1999 storm as a function of time. Values are at 0.5 km AGL. Moderate rain is 20-60 mm h<sup>-1</sup>, and heavy rain is greater than 60 mm h<sup>-1</sup>.

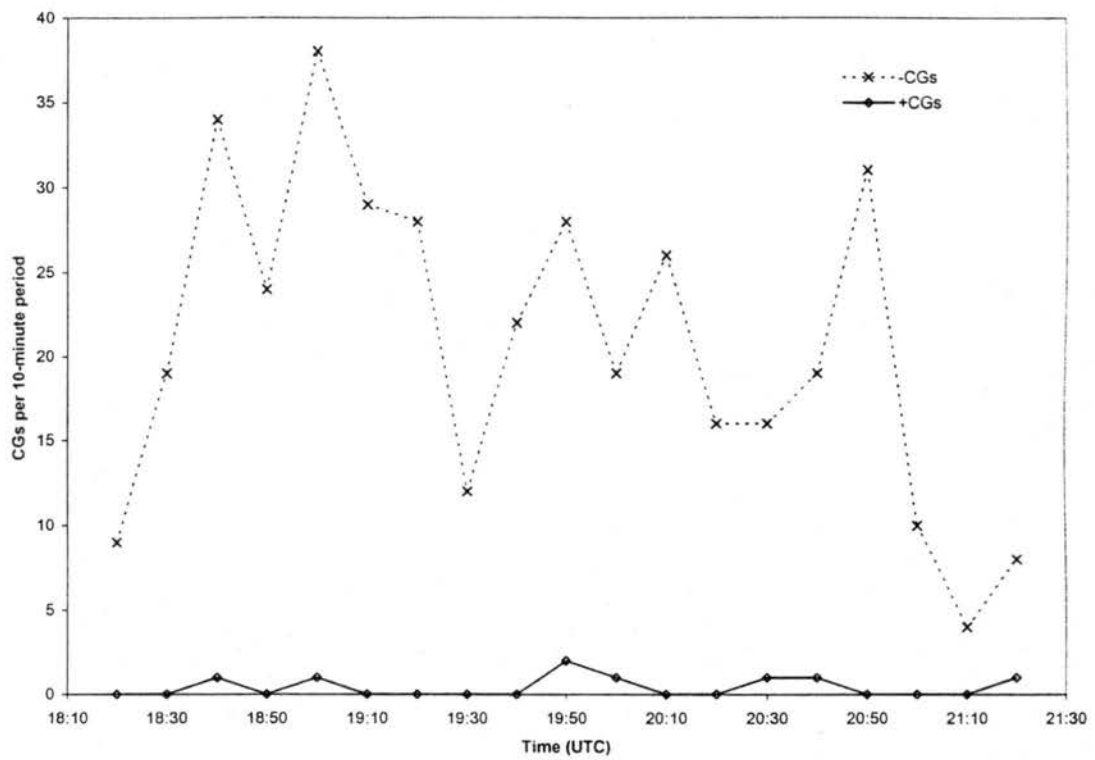


Figure 4.21: CG flash rates as functions of time for the 15 February 1999 storm.

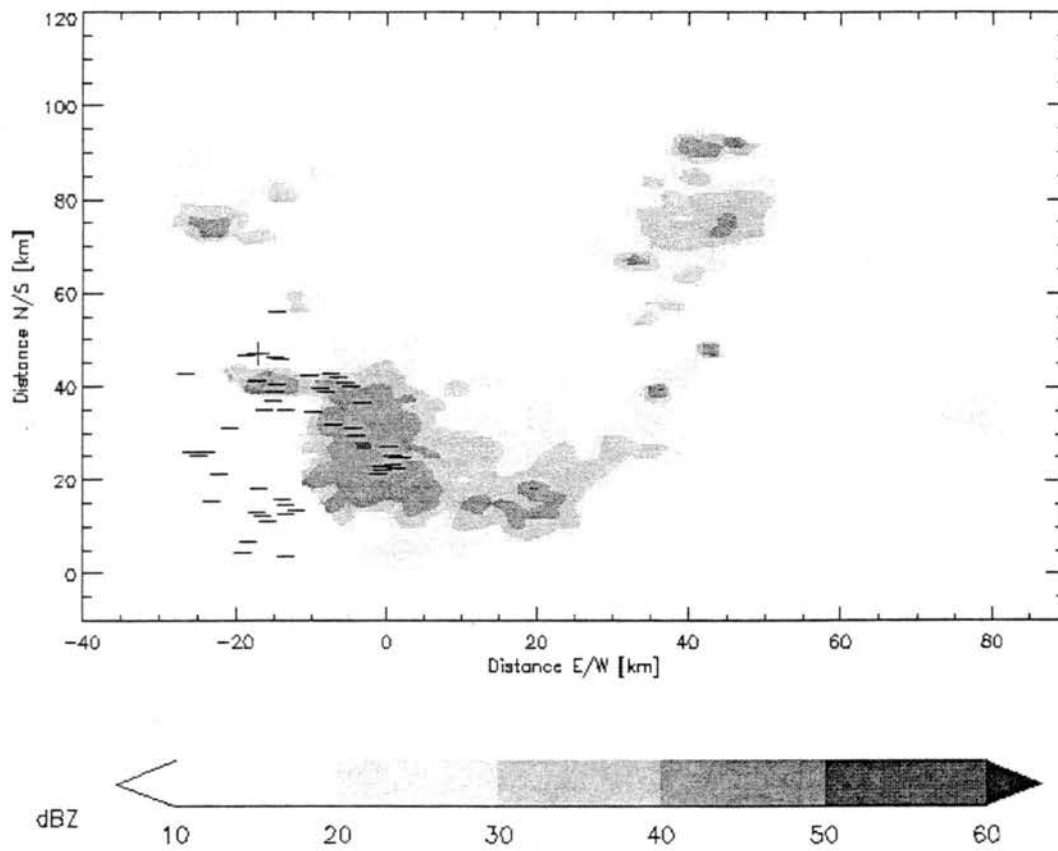


Figure 4.22: Horizontal cross-section of SPOL radar reflectivity at 0.5 km AGL, at 2050 UTC on 15 February 1999. Also shown are ground strike positions (plus signs for positives, minus signs for negatives) of BLDN CGs that occurred during 2050-2100 UTC. Distances are relative to SPOL.

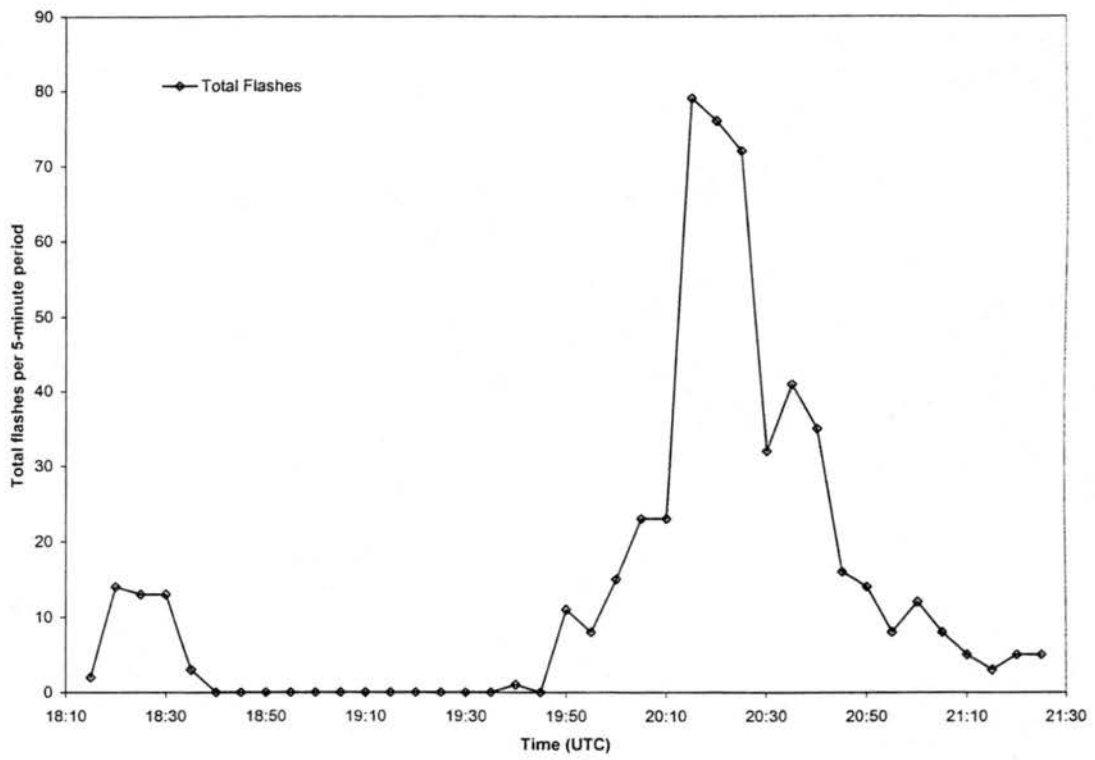


Figure 4.23: Total flash rate as a function of time for the 15 February 1999 storm.

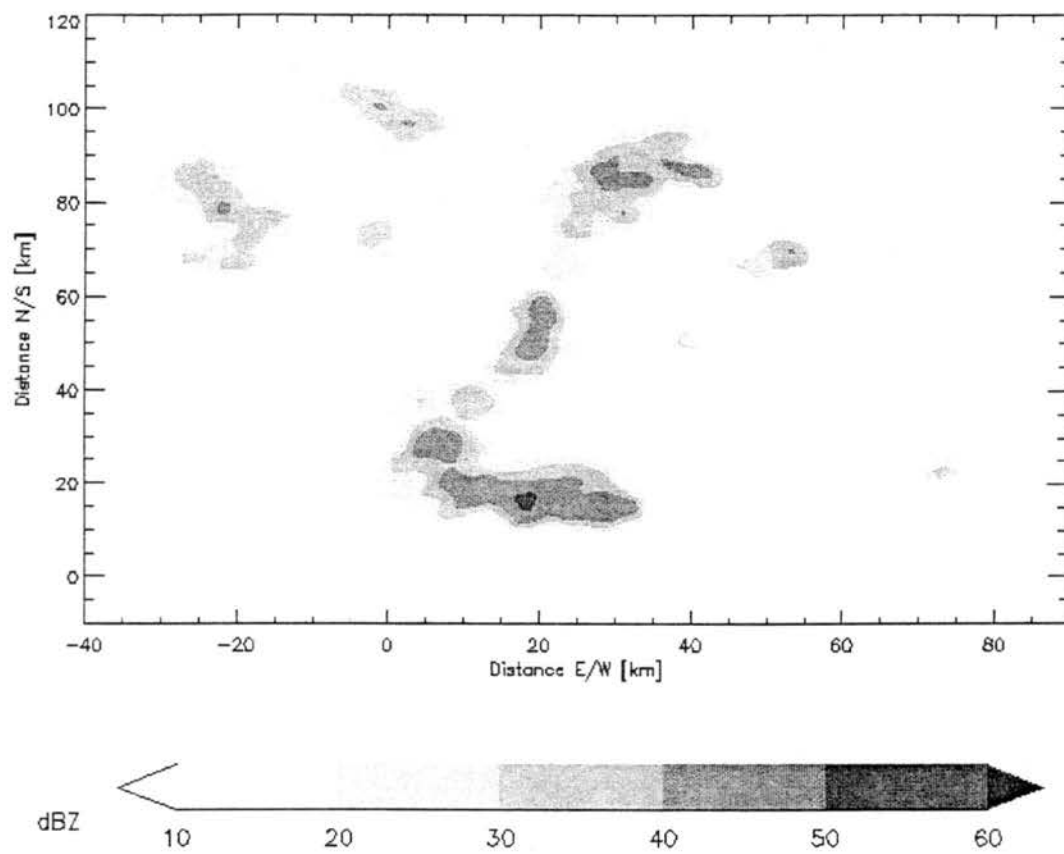


Figure 4.24: Horizontal cross-section of SPOL radar reflectivity at 0.5 km AGL, at 1750 UTC on 17 February 1999. Distances are relative to SPOL.

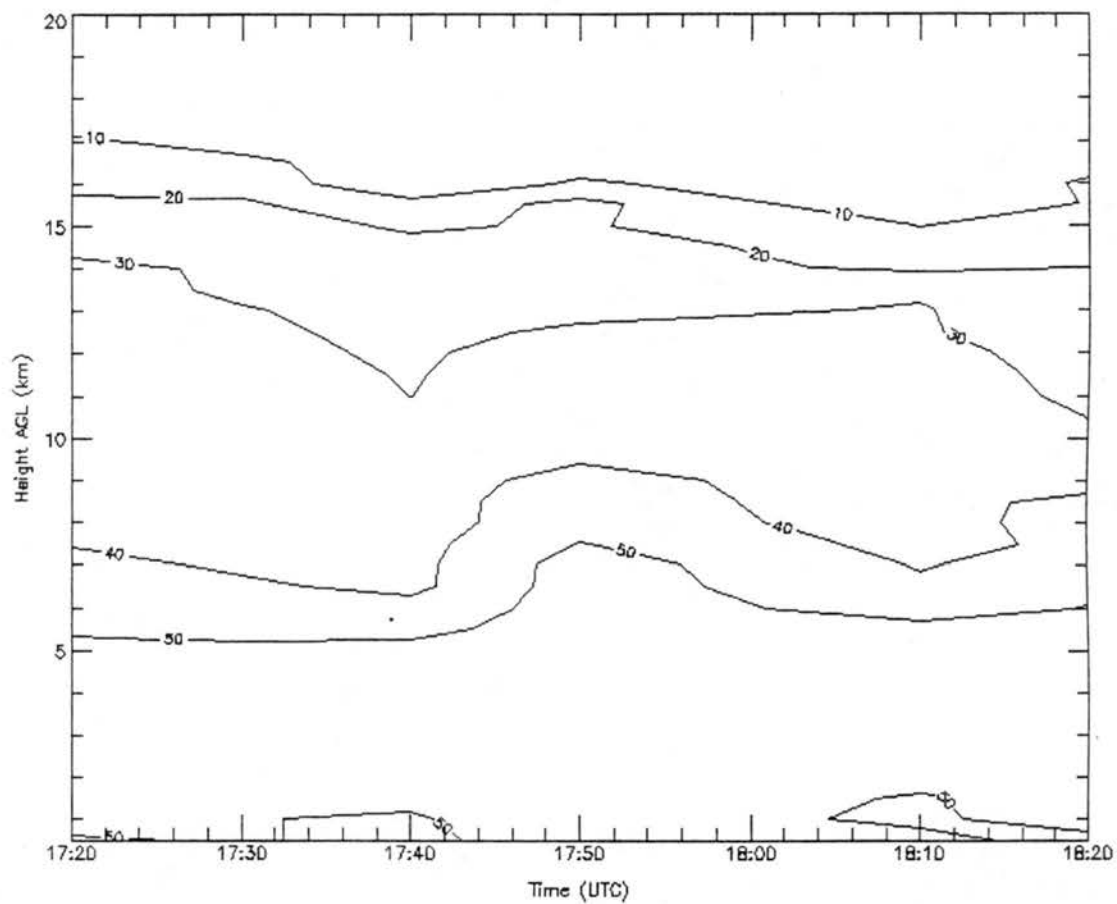


Figure 4.25: Time-height cross-section of peak SPOL radar reflectivity for the 17 February 1999 storm. Values are in dBZ.

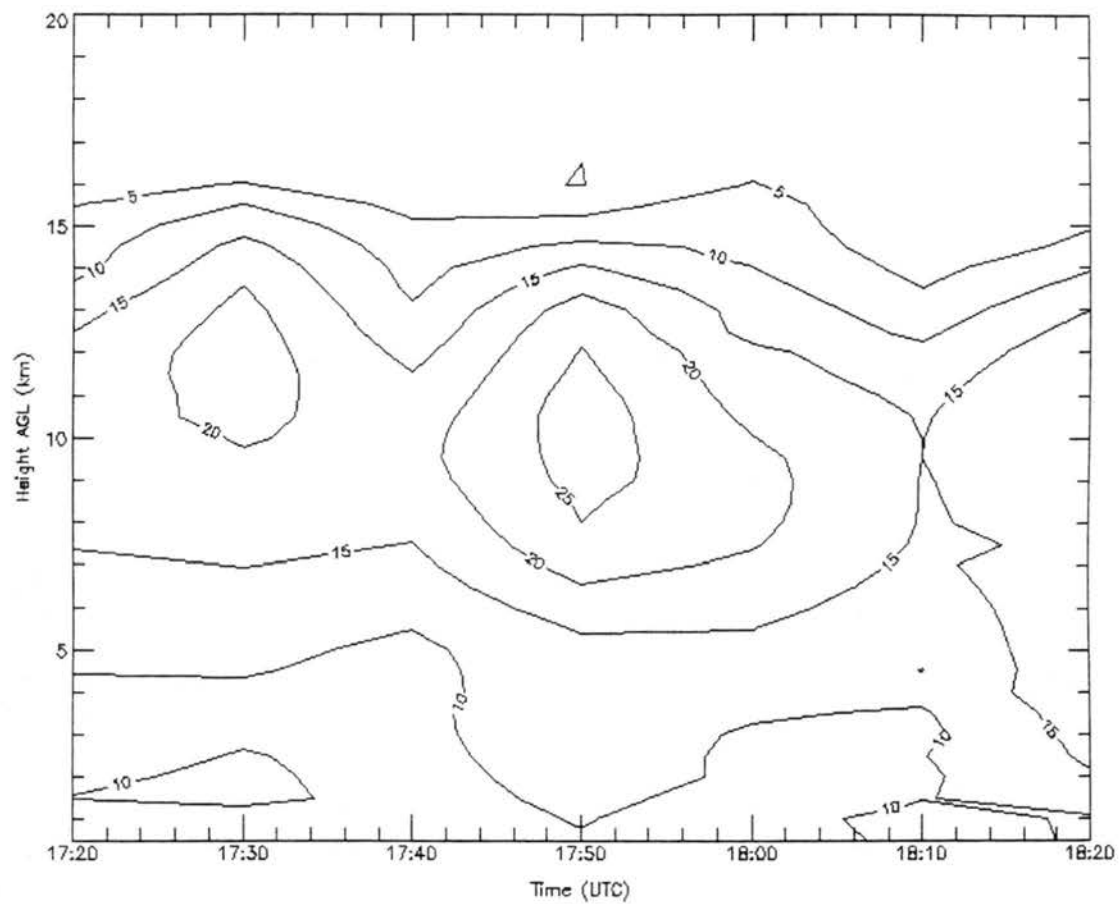


Figure 4.26: Time-height cross-section of maximum vertical velocity for the 17 February 1999 storm. Values are in  $\text{m s}^{-1}$ .

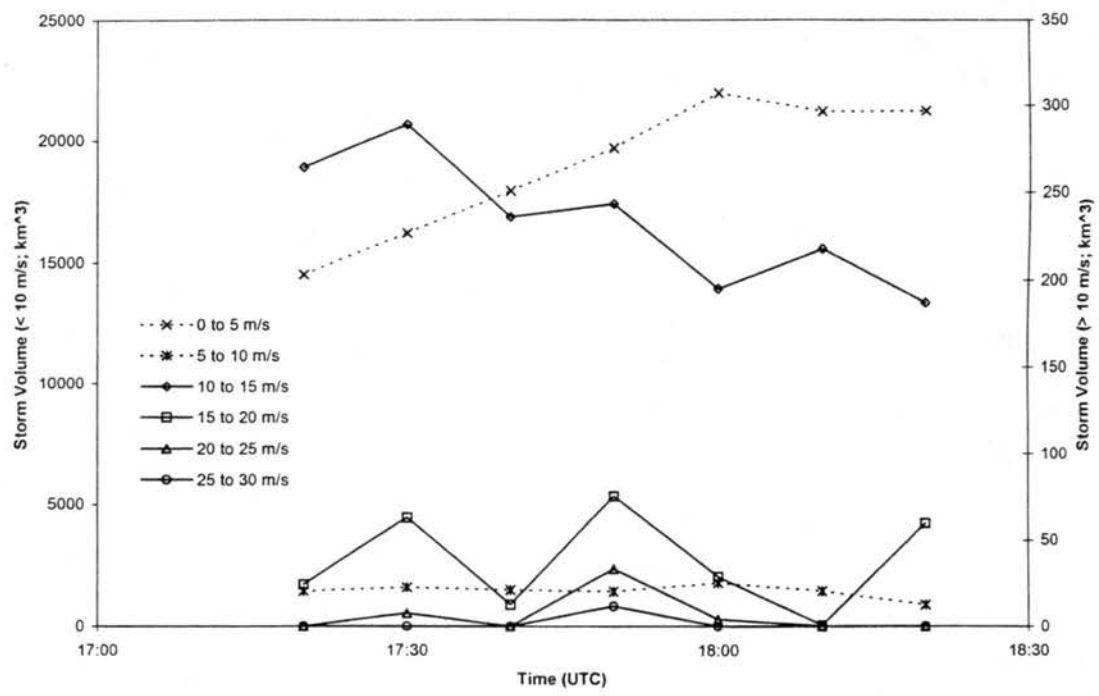


Figure 4.27: Volume of 17 February 1999 storm containing updrafts within respective bins as a function of time.

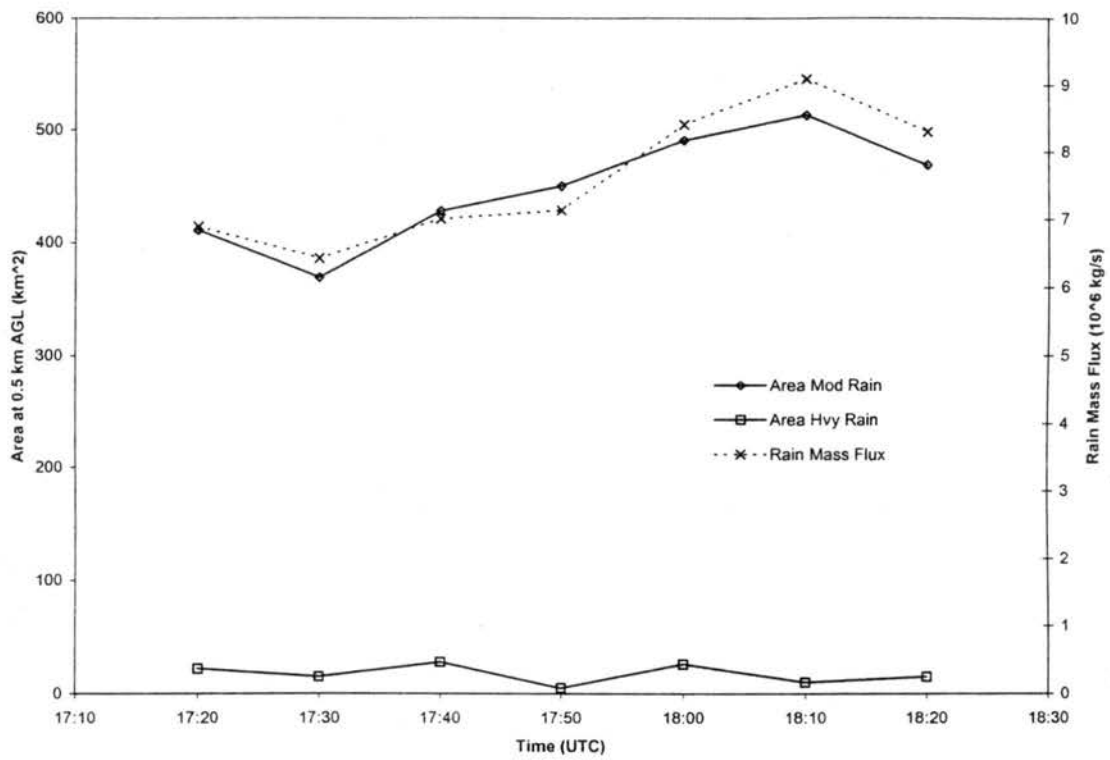


Figure 4.28: Rain production by the 17 February 1999 storm as a function of time. Values are at 0.5 km AGL. Moderate rain is 20-60 mm h<sup>-1</sup>, and heavy rain is greater than 60 mm h<sup>-1</sup>.

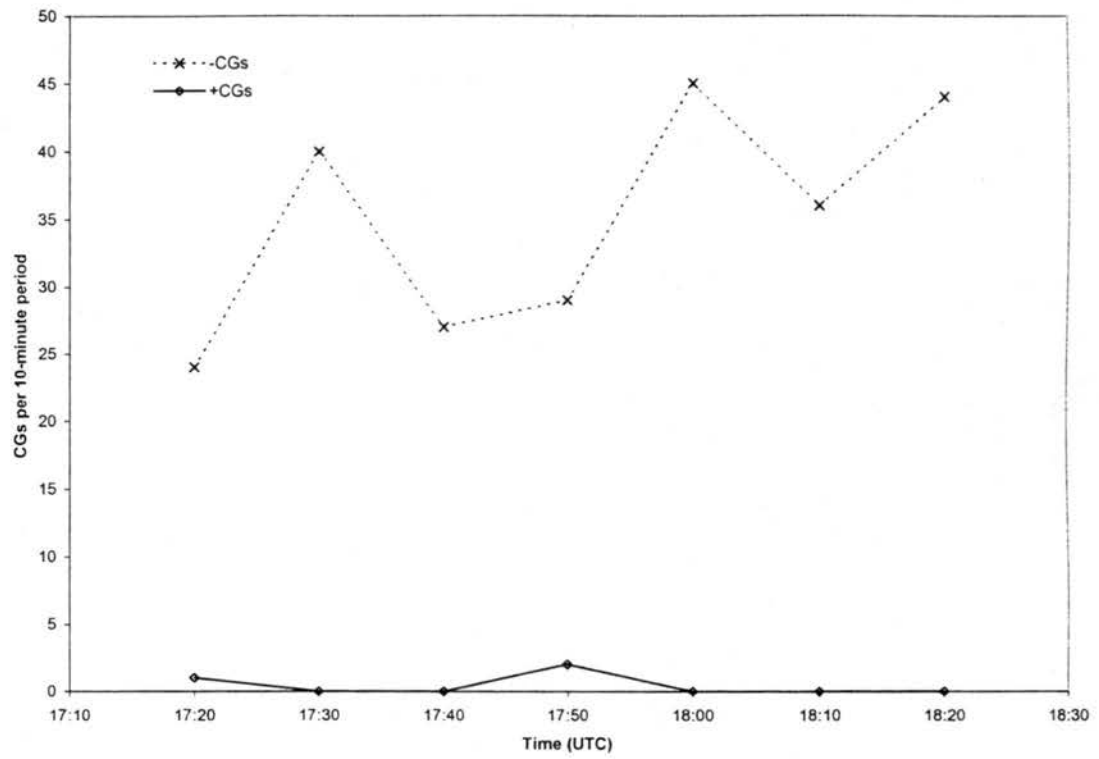


Figure 4.29: CG flash rates as functions of time for the 17 February 1999 storm.

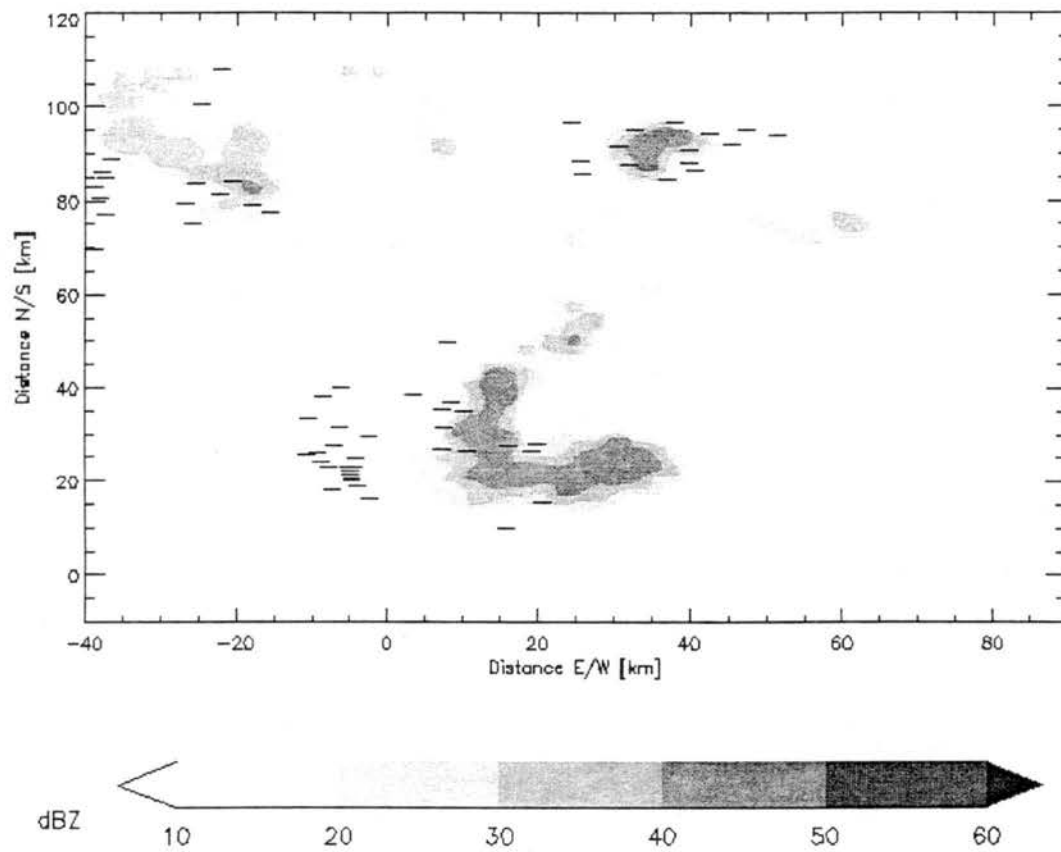


Figure 4.30: Horizontal cross-section of SPOL radar reflectivity at 0.5 km AGL, at 1730 UTC on 17 February 1999. Also shown are ground strike positions (plus signs for positives, minus signs for negatives) of BLDN CGs that occurred during 1730-1740 UTC. Distances are relative to SPOL.

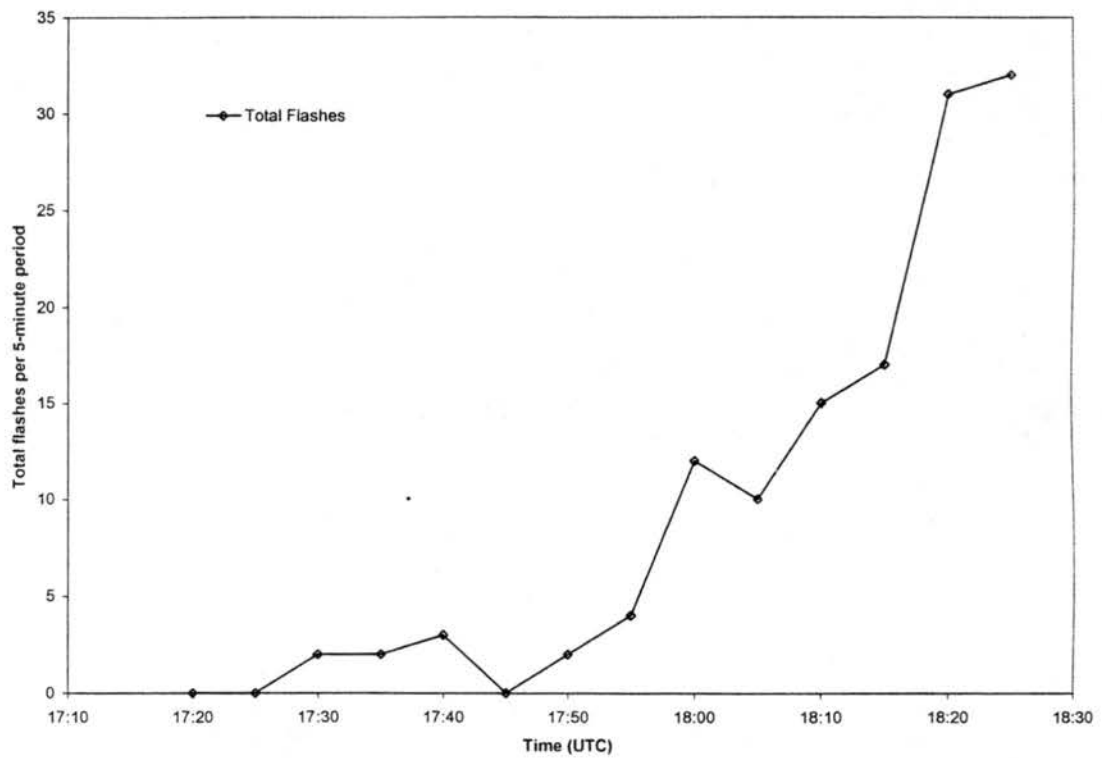


Figure 4.31: Total flash rate as a function of time for the 17 February 1999 storm.

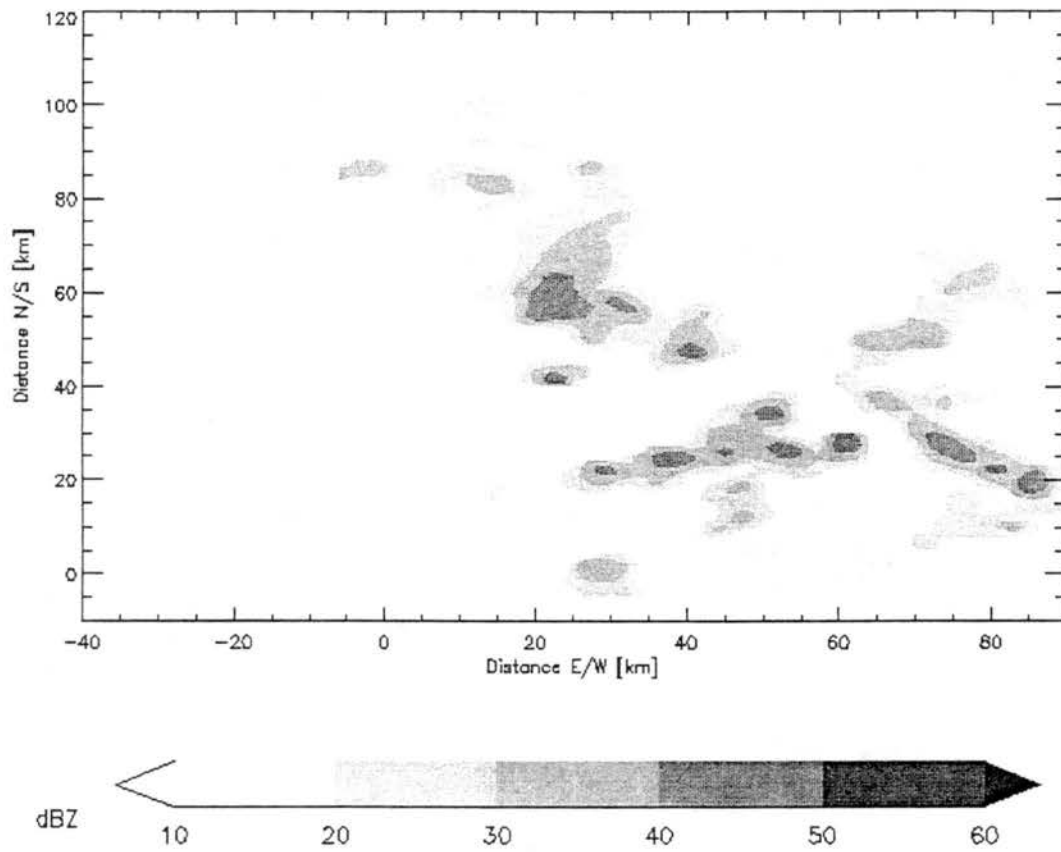


Figure 4.32: Horizontal cross-section of SPOL radar reflectivity at 0.5 km AGL, at 1848 UTC on 20 February 1999. Distances are relative to SPOL.

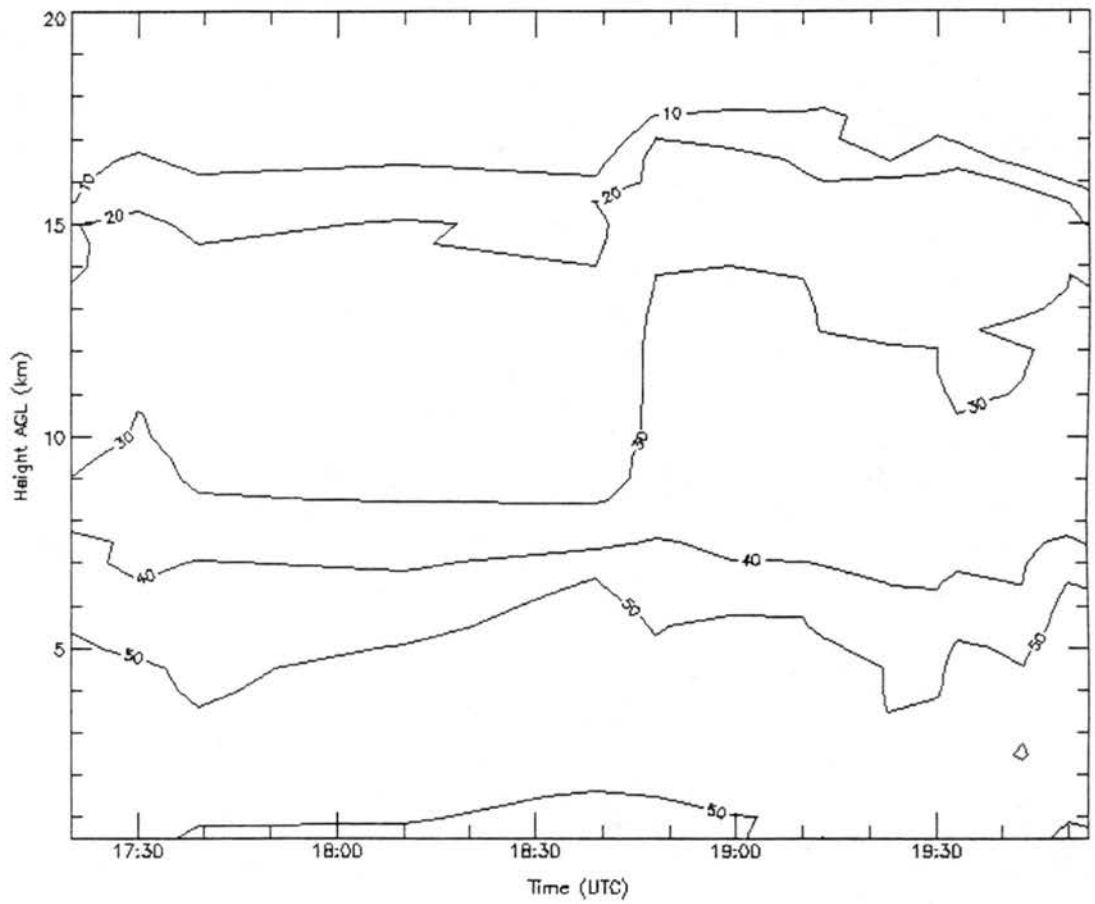


Figure 4.33: Time-height cross-section of peak SPOL radar reflectivity for the 20 February 1999 storm. Values are in dBZ.

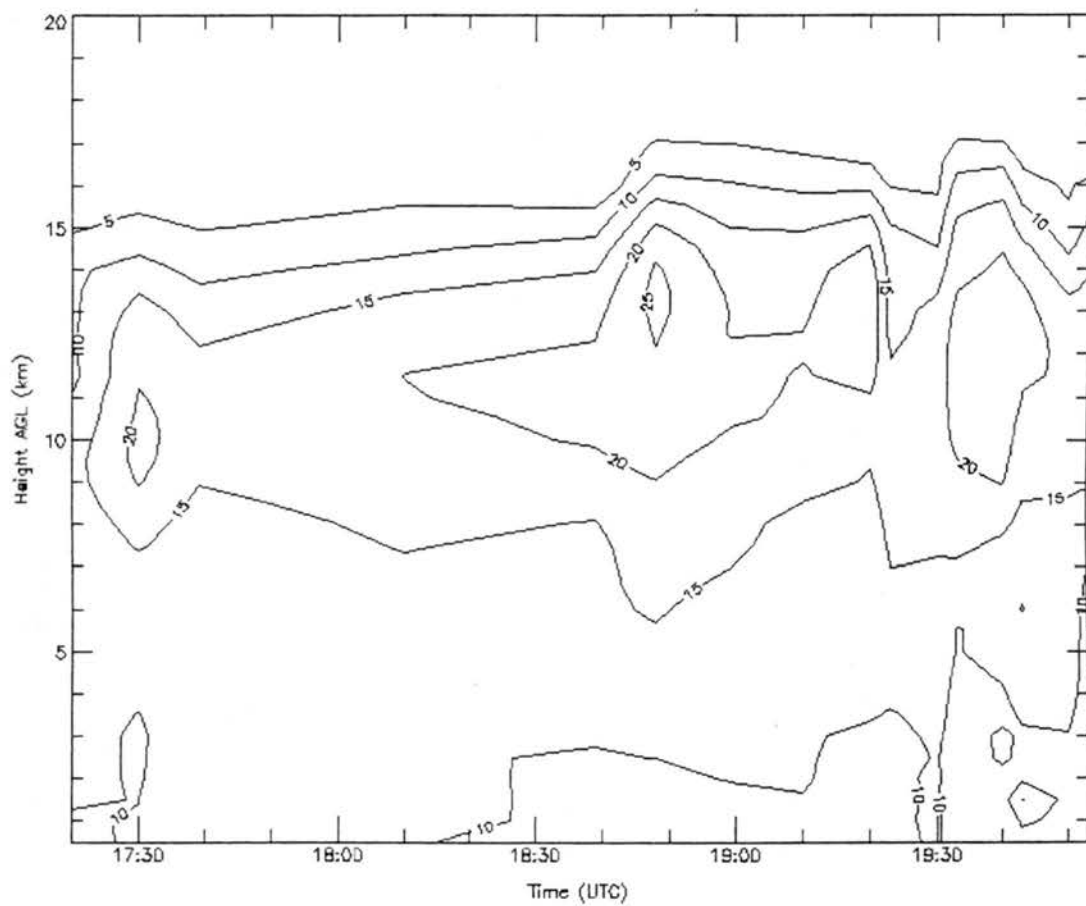


Figure 4.34: Time-height cross-section of maximum vertical velocity for the 20 February 1999 storm. Values are in  $\text{m s}^{-1}$ .

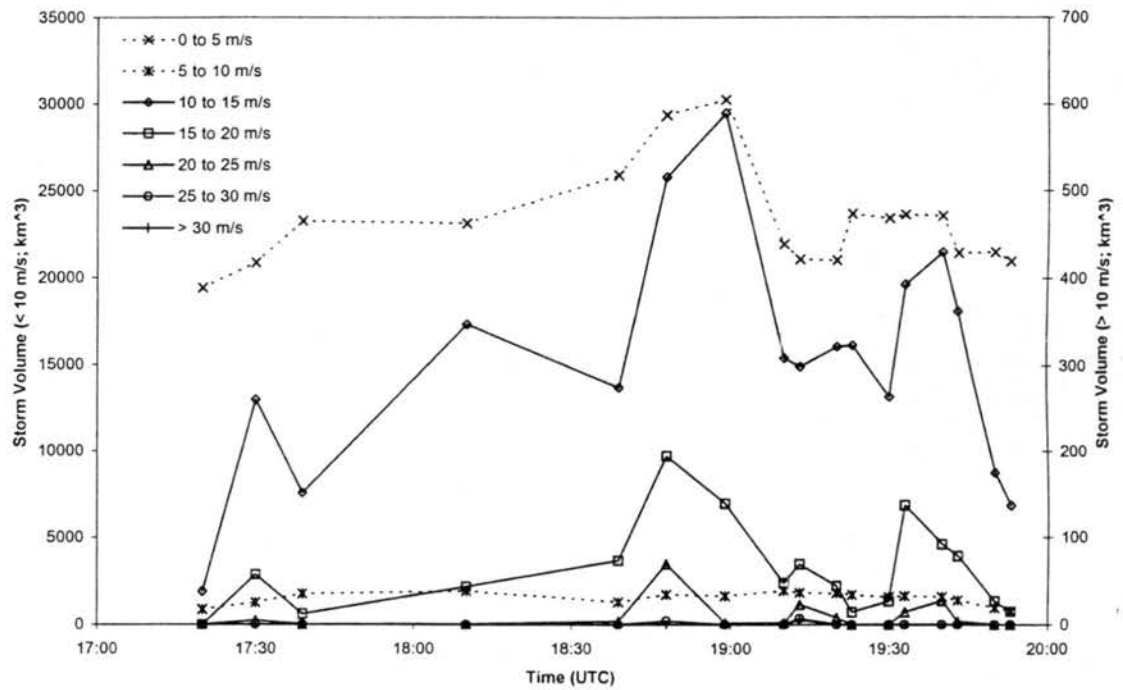


Figure 4.35: Volume of 20 February 1999 storm containing updrafts within respective bins as a function of time.

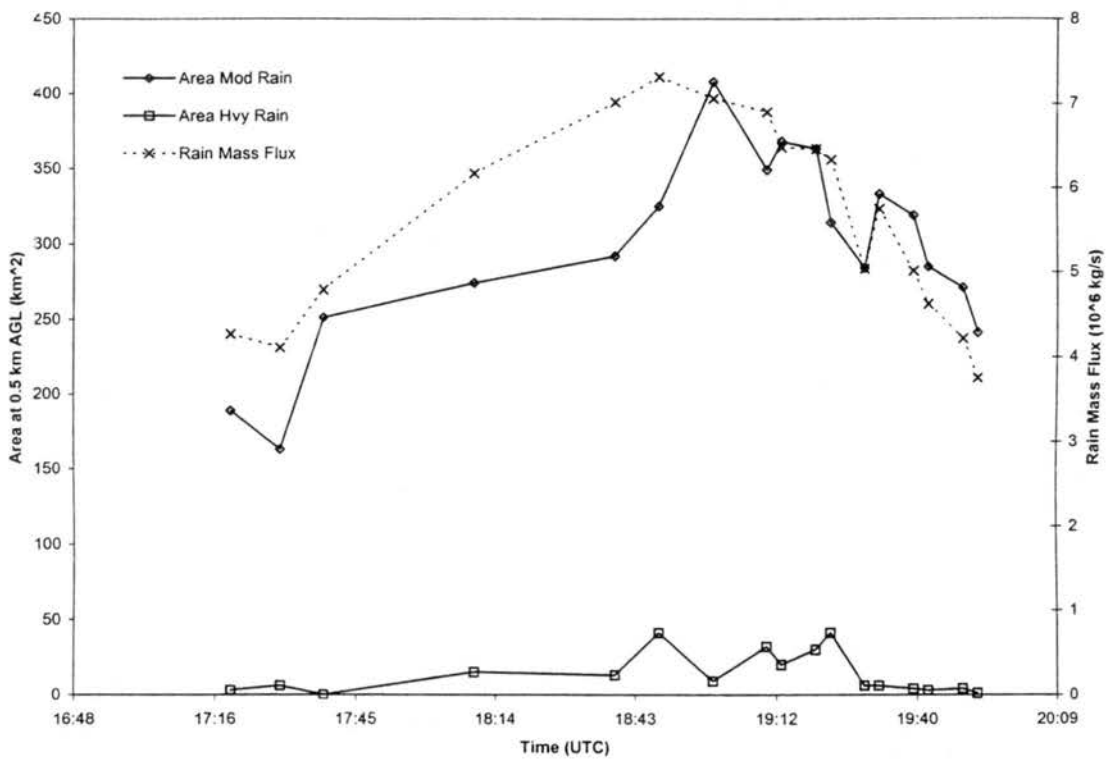


Figure 4.36: Rain production by the 20 February 1999 storm as a function of time. Values are at 0.5 km AGL. Moderate rain is 20-60 mm h<sup>-1</sup>, and heavy rain is greater than 60 mm h<sup>-1</sup>.

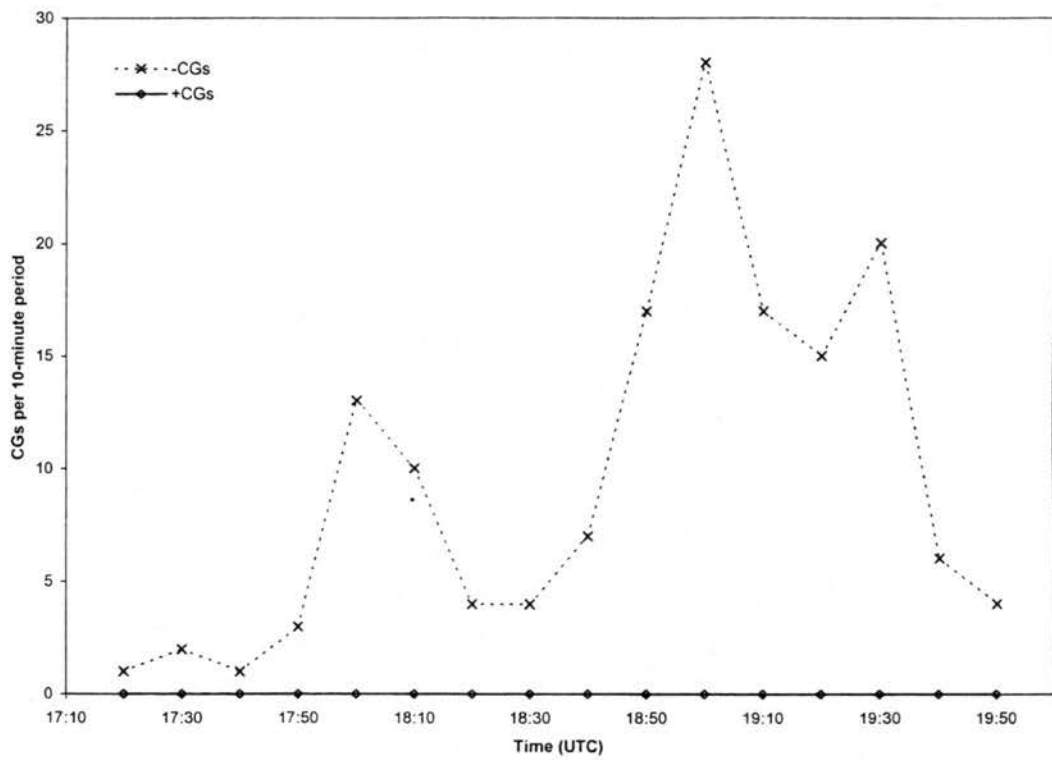


Figure 4.37: CG flash rates as functions of time for the 20 February 1999 storm.

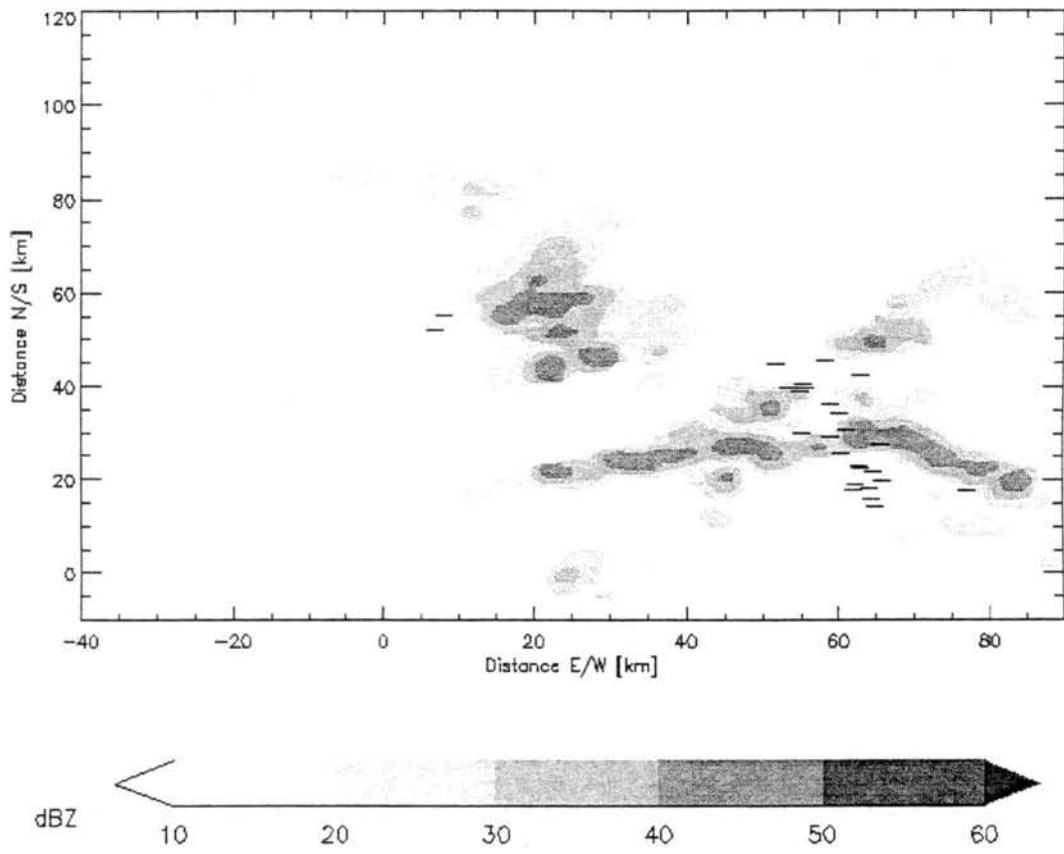
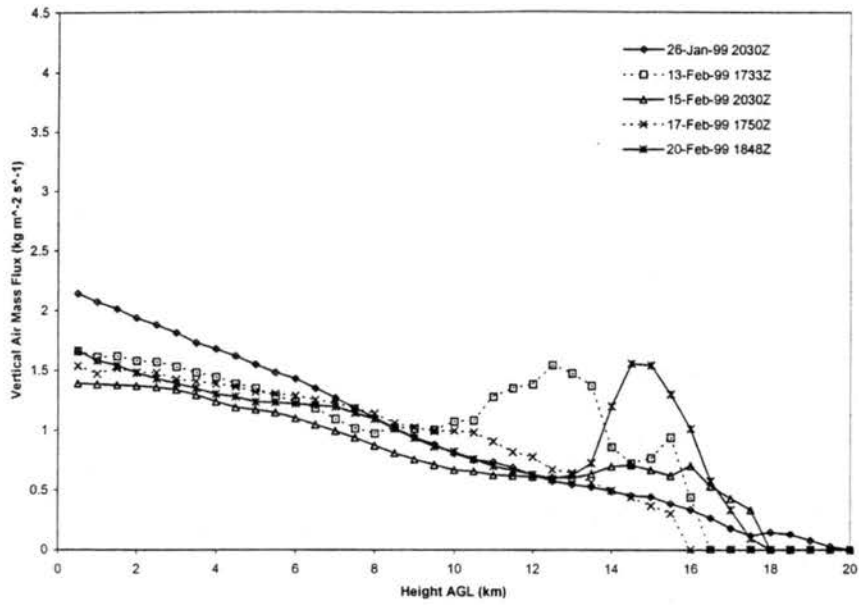


Figure 4.38: Horizontal cross-section of SPOL radar reflectivity at 0.5 km AGL, at 1859 UTC on 20 February 1999. Also shown are ground strike positions (plus signs for positives, minus signs for negatives) of BLDN CGs that occurred during 1900-1910 UTC. Distances are relative to SPOL.

a.



b.

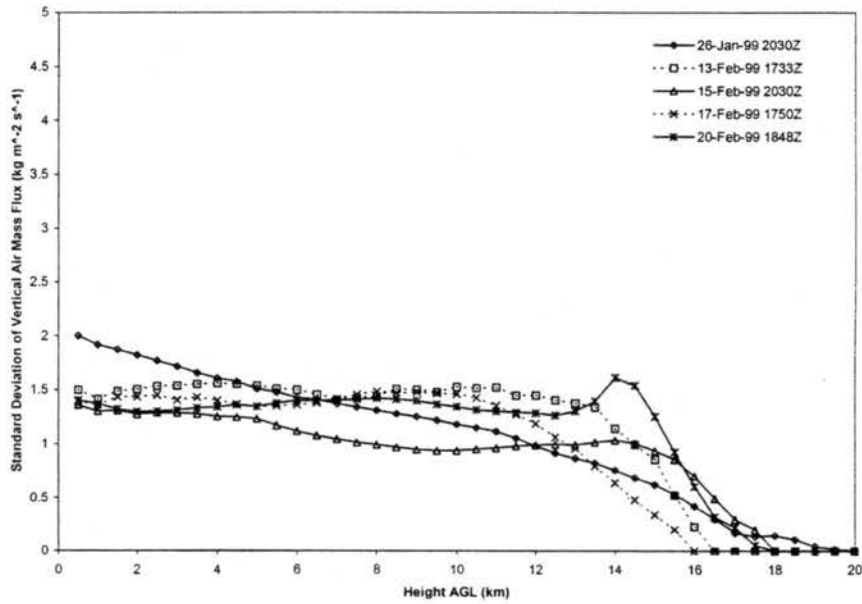
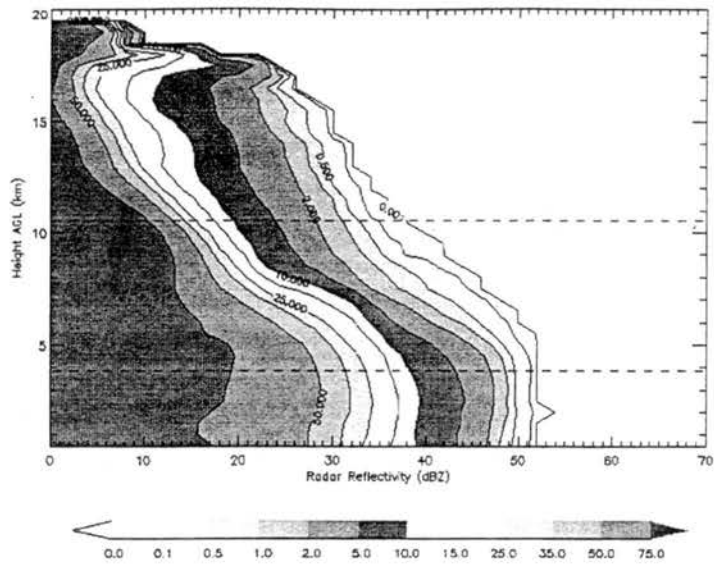


Figure 4.39: a) Average positive vertical air mass flux as a function of height at the times of peak updrafts for the tropical storms. b) Standard deviation of positive vertical air mass flux as a function of height at the times of peak updrafts for the tropical storms.

a.



b.

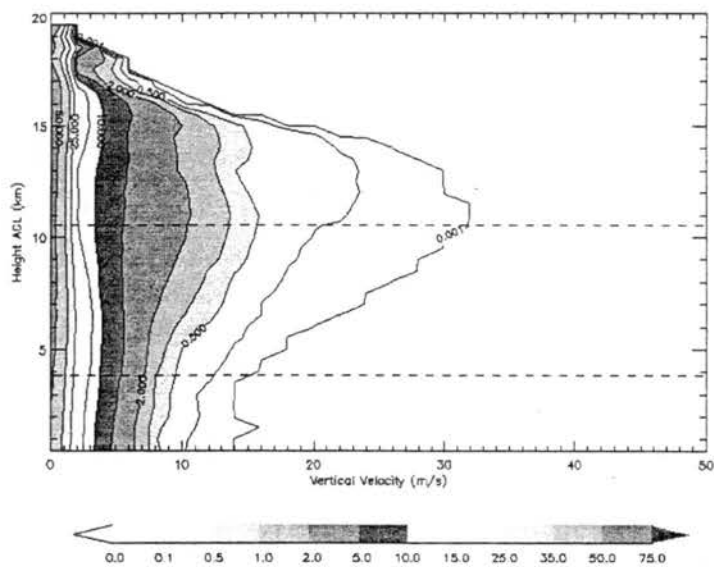
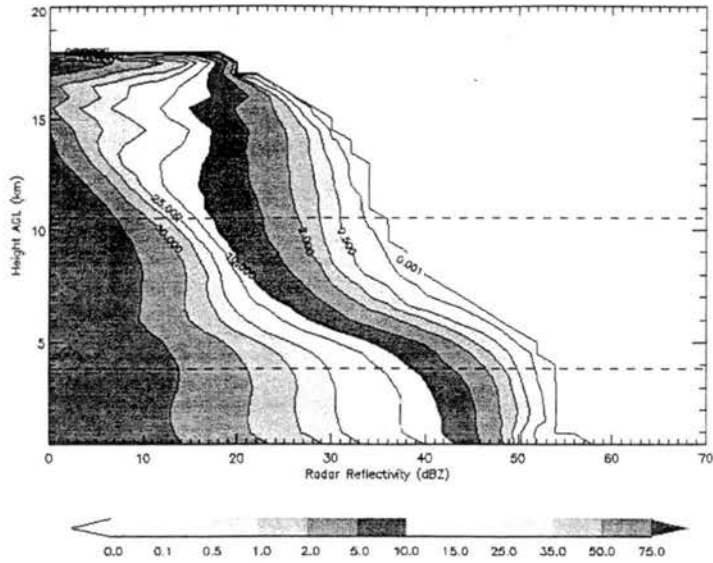


Figure 4.40: Cumulative frequency by altitude diagrams (CFADs) of SPOL radar reflectivity (a) and dual-Doppler-derived vertical velocity (b) for the 26 January 1999 storm at 2030 UTC. The dashed lines denote the approximate boundaries of the mixed phase region.



a.



b.

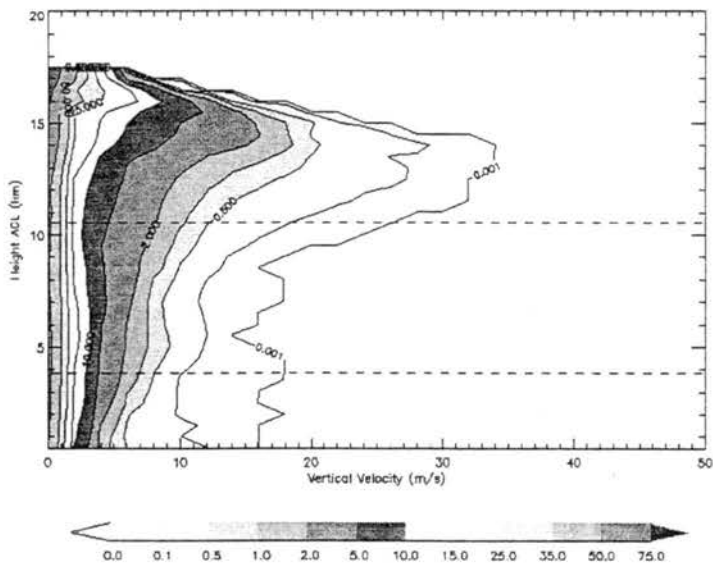
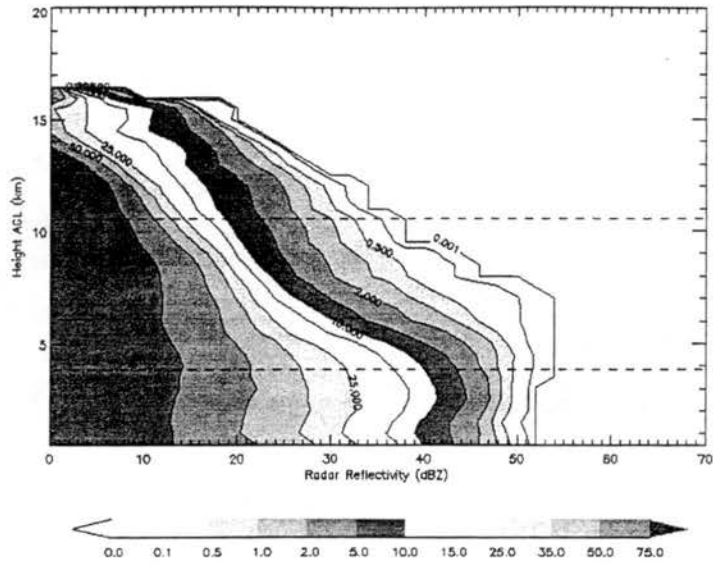


Figure 4.42: Cumulative frequency by altitude diagrams (CFADs) of SPOL radar reflectivity (a) and dual-Doppler-derived vertical velocity (b) for the 15 February 1999 storm at 2030 UTC. The dashed lines denote the approximate boundaries of the mixed phase region.

a.



b.

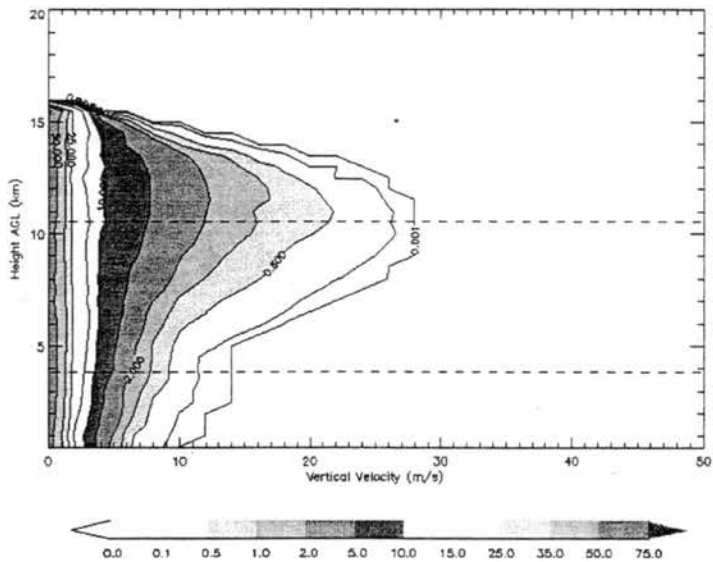
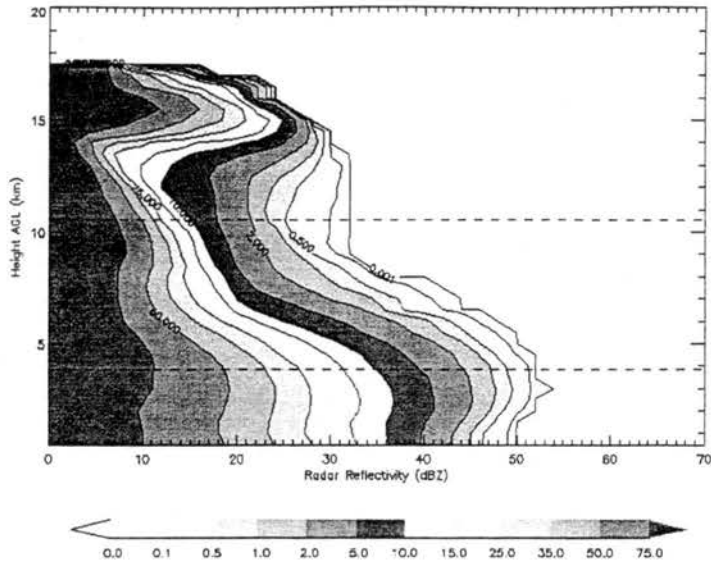


Figure 4.43: Cumulative frequency by altitude diagrams (CFADs) of SPOL radar reflectivity (a) and dual-Doppler-derived vertical velocity (b) for the 17 February 1999 storm at 1750 UTC. The dashed lines denote the approximate boundaries of the mixed phase region.

a.



b.

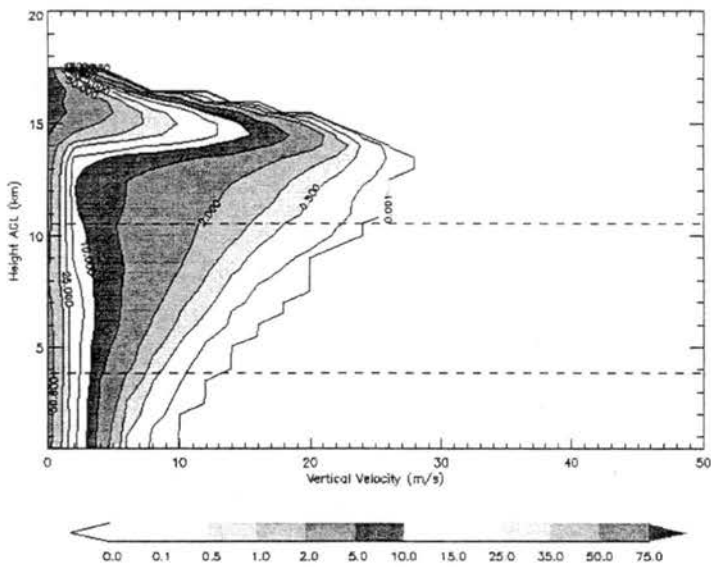
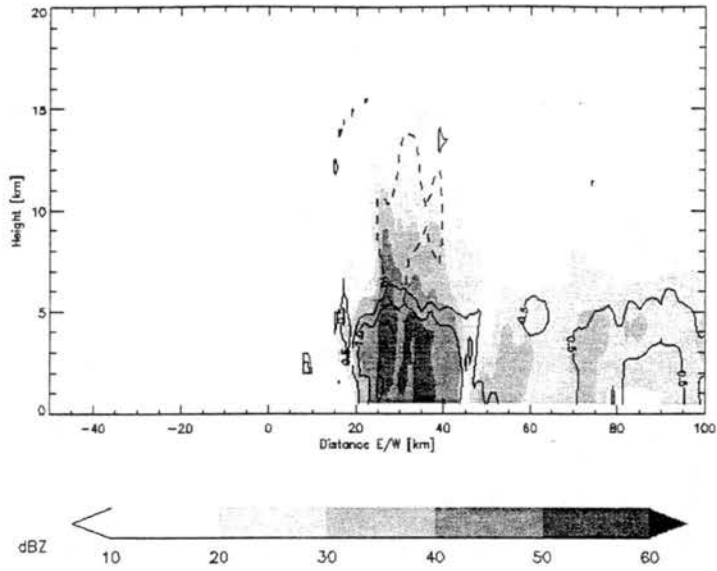


Figure 4.44: Cumulative frequency by altitude diagrams (CFADs) of SPOL radar reflectivity (a) and dual-Doppler-derived vertical velocity (b) for the 20 February 1999 storm at 1848 UTC. The dashed lines denote the approximate boundaries of the mixed phase region.

a.



b.

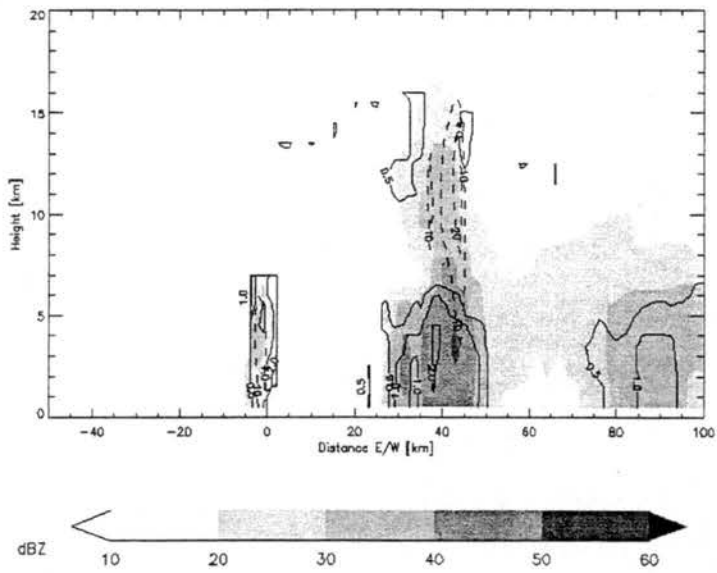


Figure 4.45: Vertical cross-section of SPOL radar reflectivity (shaded), along with differential reflectivity (solid line) and vertical velocity (dashed). a) Cross-section taken at 35 km north, at 2030 UTC on 26 January 1999. b) Same as a) except at 85 km north. Distances are relative to SPOL.

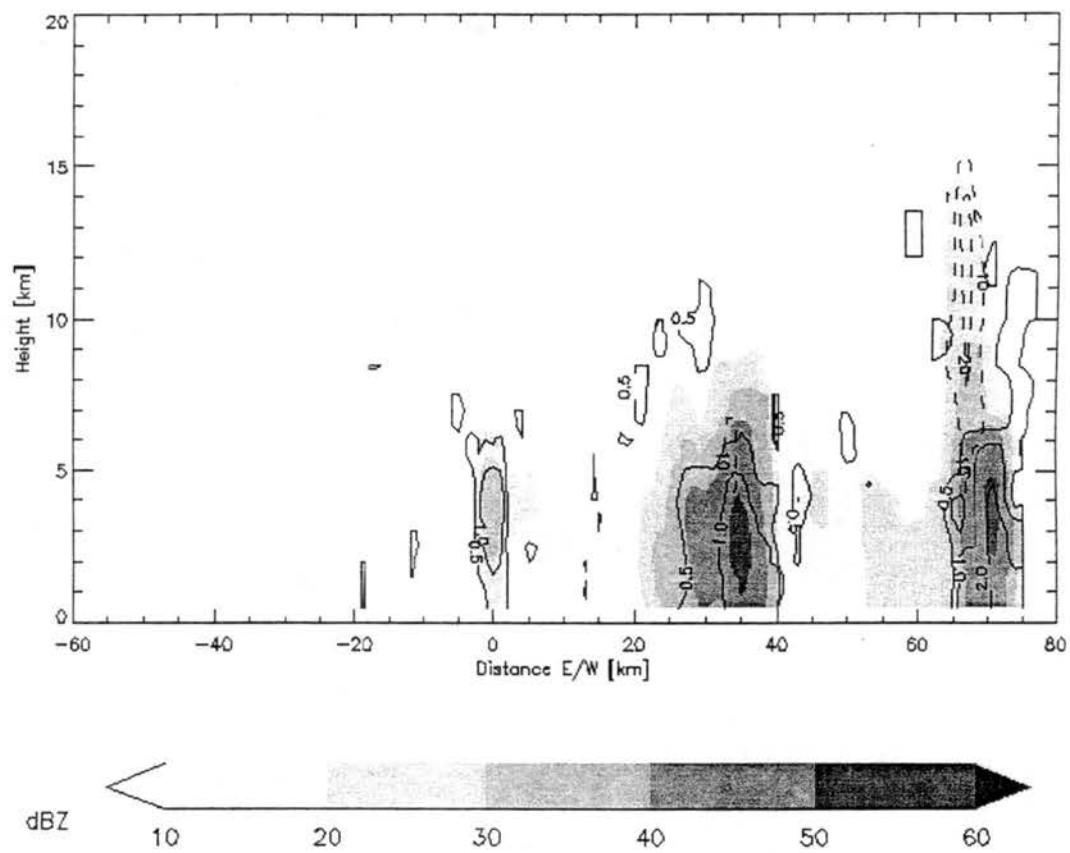


Figure 4.46: Vertical cross-section of SPOL radar reflectivity (shaded), along with differential reflectivity (solid line) and vertical velocity (dashed). Cross-section taken at 45 km north, at 1733 UTC on 13 February 1999. Distances are relative to SPOL.

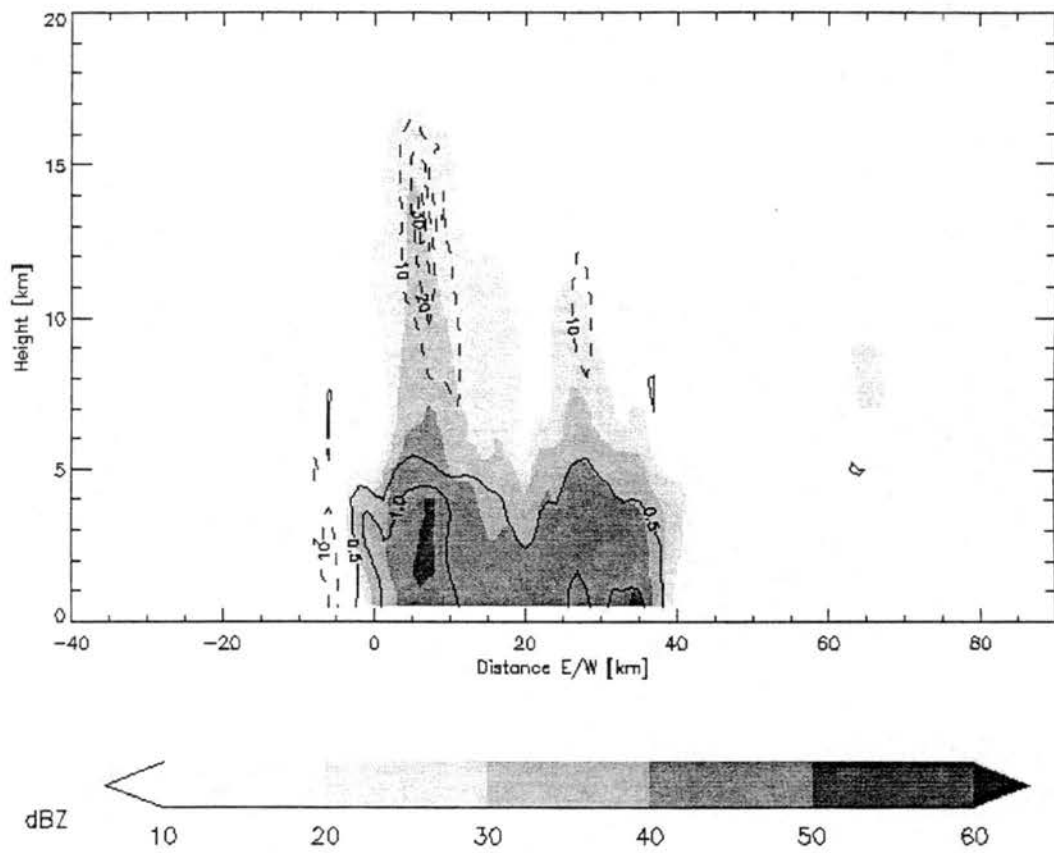


Figure 4.47: Vertical cross-section of SPOL radar reflectivity (shaded), along with differential reflectivity (solid line) and vertical velocity (dashed). Cross-section taken at 24 km north, at 2030 UTC on 15 February 1999. Distances are relative to SPOL.

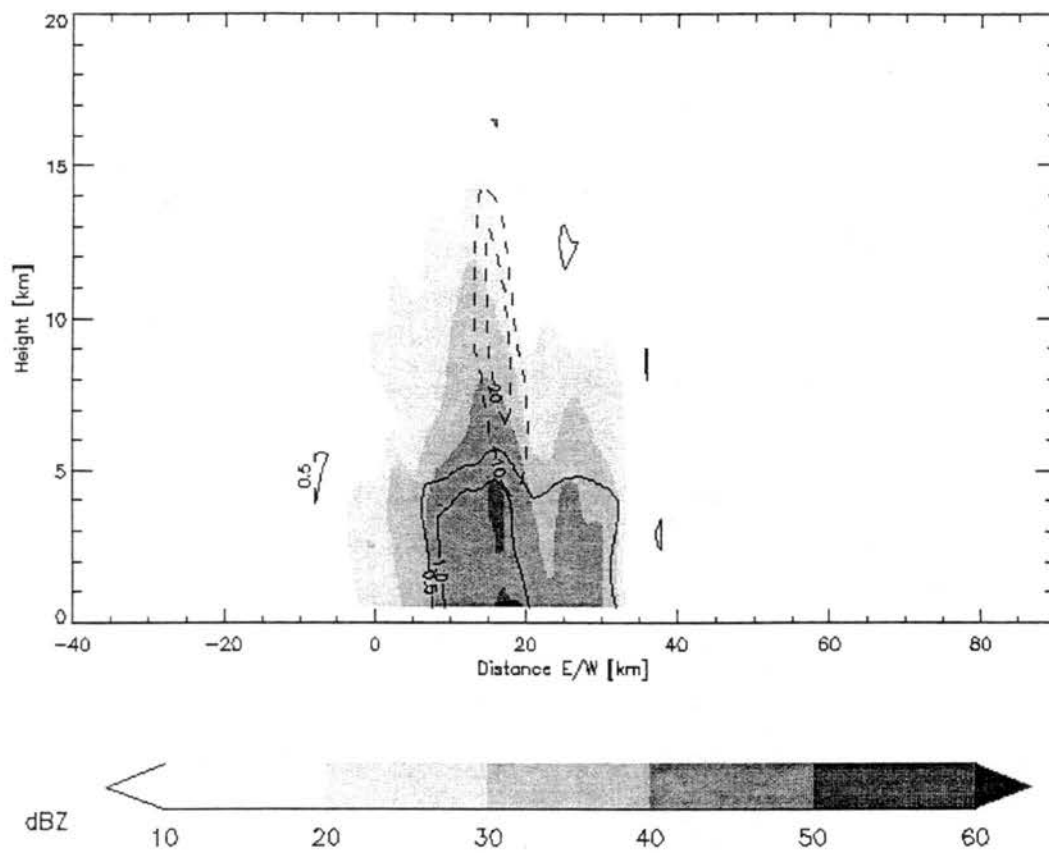
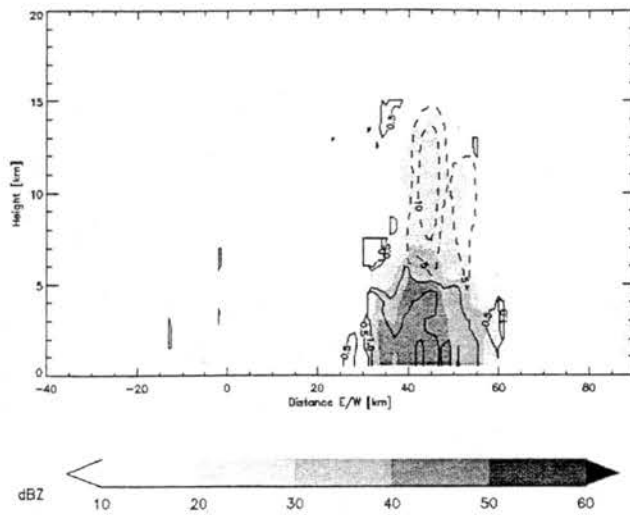


Figure 4.48: Vertical cross-section of SPOL radar reflectivity (shaded), along with differential reflectivity (solid line) and vertical velocity (dashed). Cross-section taken at 17 km north, at 1750 UTC on 17 February 1999. Distances are relative to SPOL.

a.



b.

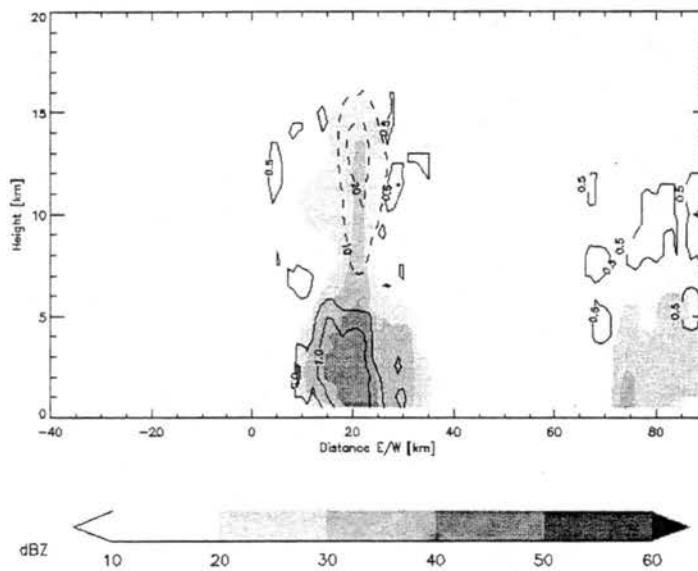


Figure 4.49: Vertical cross-section of SPOL radar reflectivity (shaded), along with differential reflectivity (solid line) and vertical velocity (dashed). a) Cross-section taken at 72 km north, at 1739 UTC on 20 February 1999. b) Same as a) except at 60 km north, at 1848 UTC. Distances are relative to SPOL.

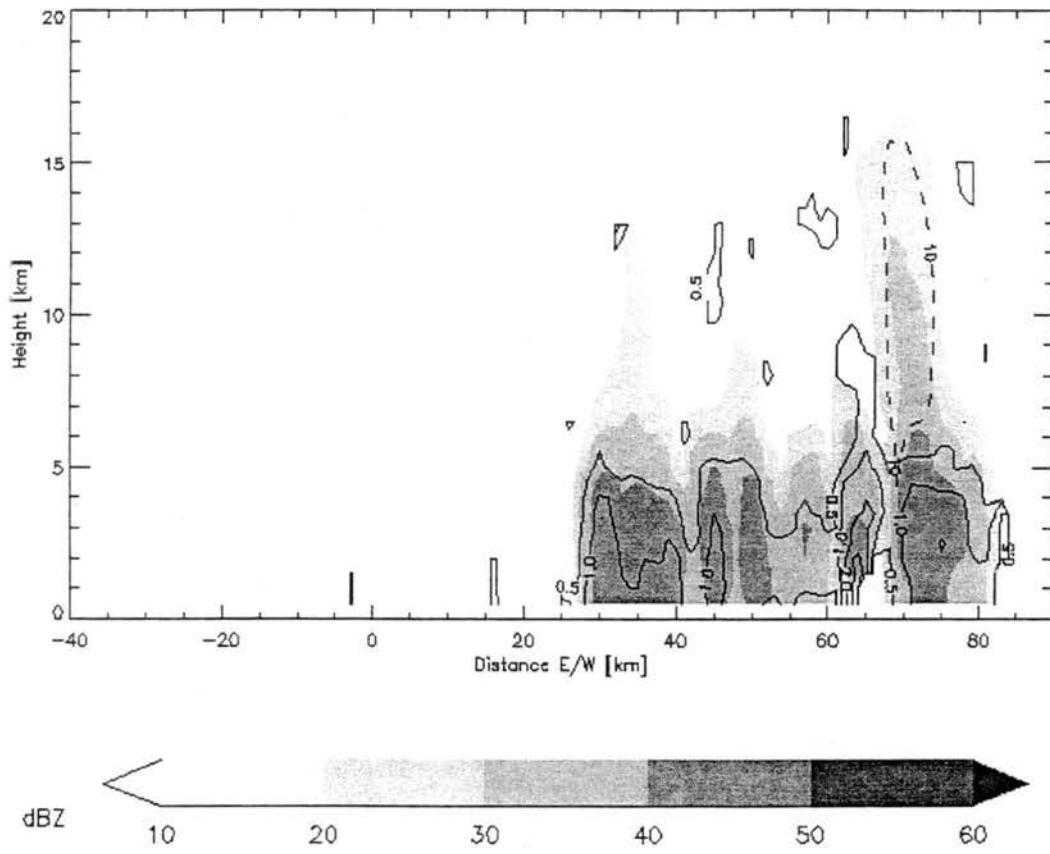


Figure 4.50: Vertical cross-section of SPOL radar reflectivity (shaded), along with differential reflectivity (solid line) and vertical velocity (dashed). Cross-section taken at 25 km north, at 1859 UTC on 20 February 1999. Distances are relative to SPOL.

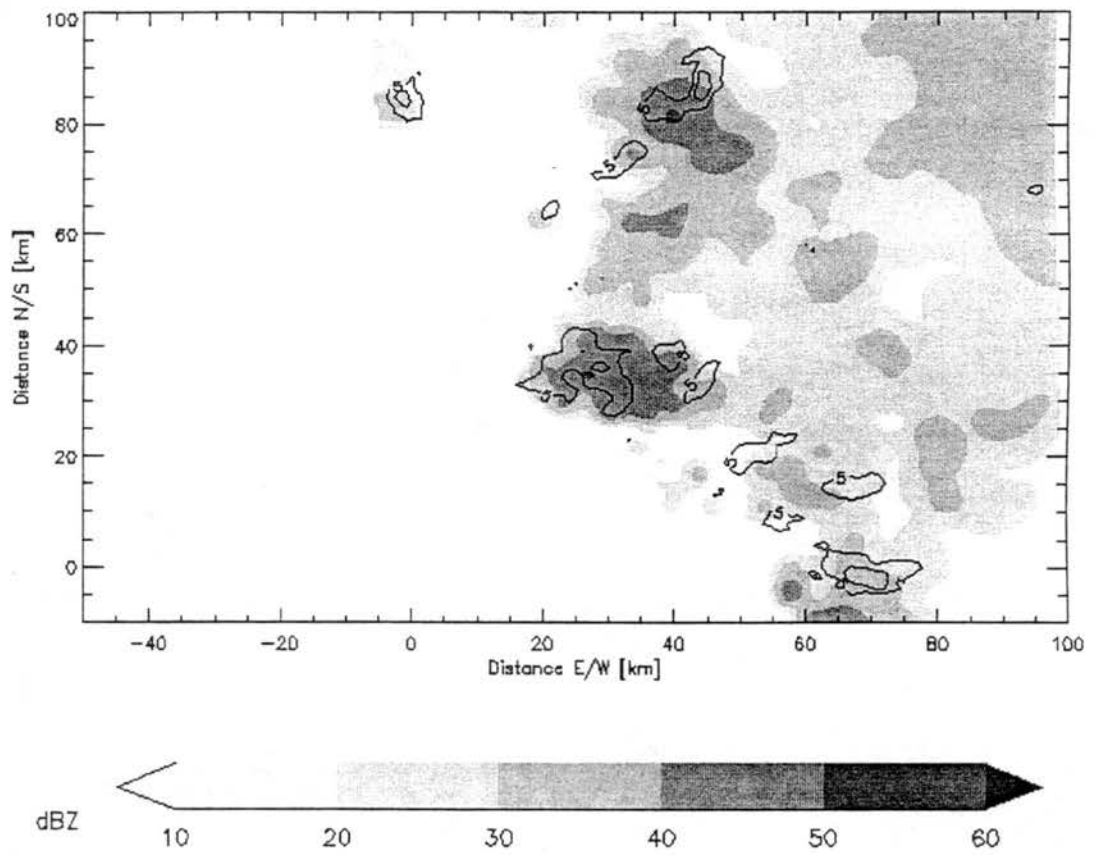


Figure 4.51: Horizontal cross-section of SPOL radar reflectivity (shaded) and vertical velocity (solid line) at 5.0 km AGL for the 26 January 1999 storm at 2300 UTC.

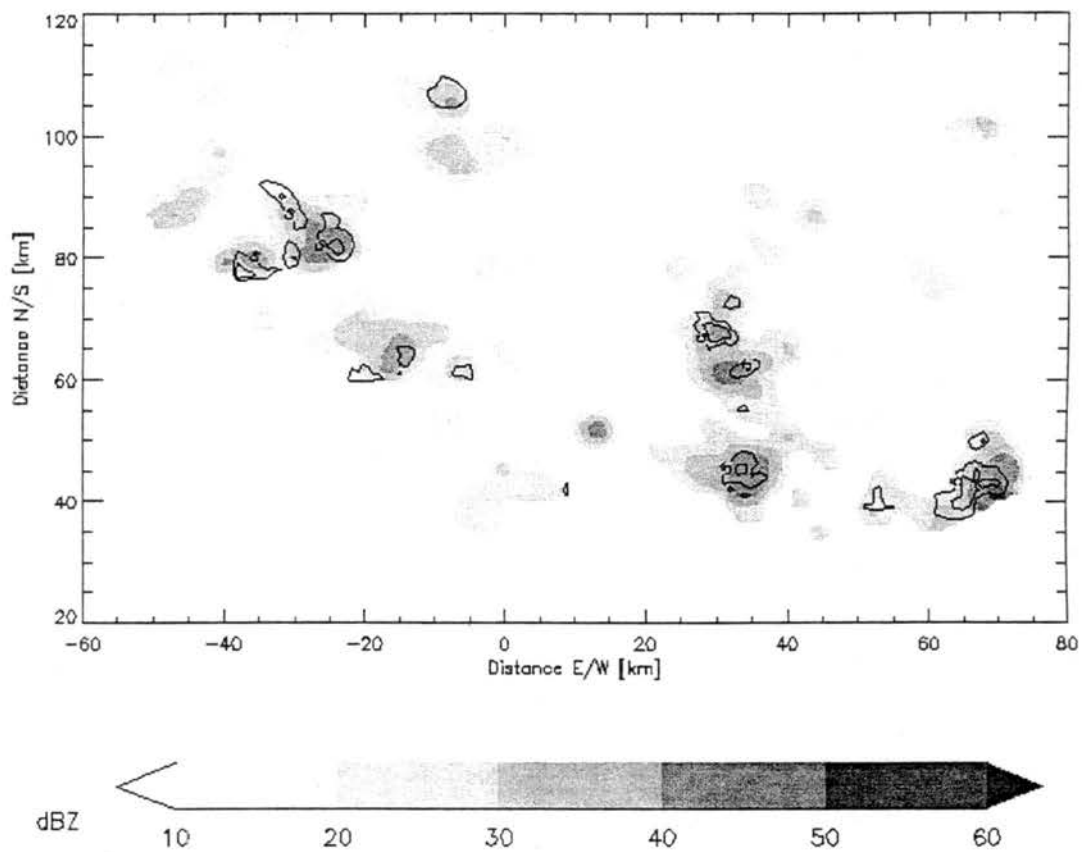


Figure 4.52: Horizontal cross-section of SPOL radar reflectivity (shaded) and vertical velocity (solid line) at 5.0 km AGL for the 13 February 1999 storm at 1733 UTC.

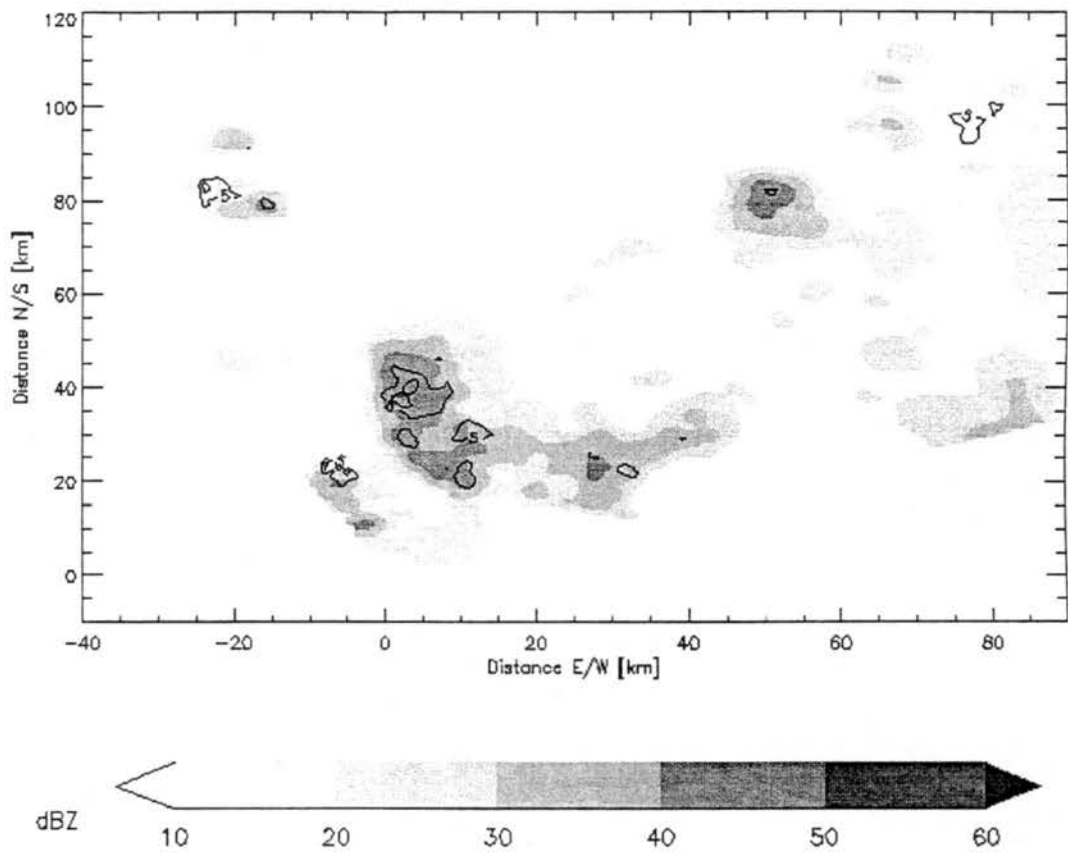


Figure 4.53: Horizontal cross-section of SPOL radar reflectivity (shaded) and vertical velocity (solid line) at 5.0 km AGL for the 15 February 1999 storm at 2030 UTC.

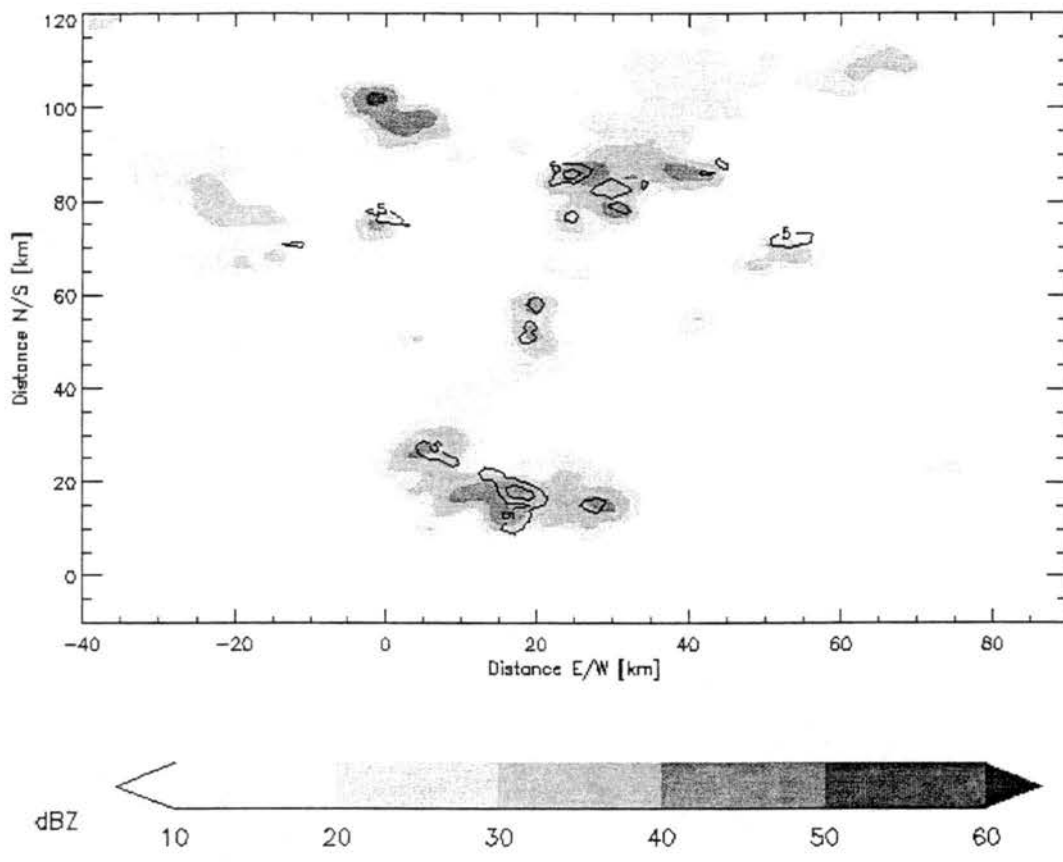


Figure 4.54: Horizontal cross-section of SPOL radar reflectivity (shaded) and vertical velocity (solid line) at 5.0 km AGL for the 17 February 1999 storm at 1750 UTC.

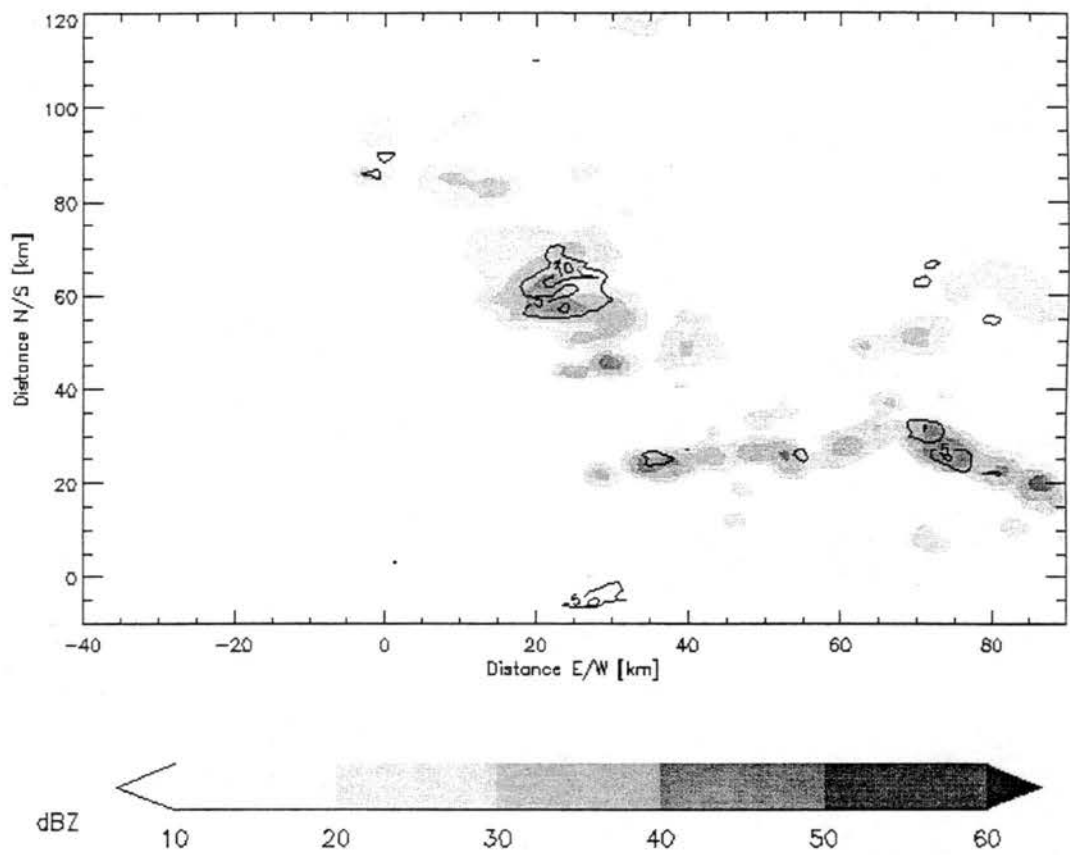


Figure 4.55: Horizontal cross-section of SPOL radar reflectivity (shaded) and vertical velocity (solid line) at 5.0 km AGL for the 20 February 1999 storm at 1848 UTC.

## CHAPTER 5

### SYNTHESIS AND DISCUSSION

#### *5.1 Synthesis of Mid-Latitude and Tropical Results*

This study sought to test mechanisms that purport to explain some of the relationships between convective storm kinematics, microphysics, and lightning. Observations of 6 mid-latitude and 5 tropical thunderstorms have been collected and heretofore analyzed separately. In this chapter, the analyses of these 11 events will be combined into a single set, so that a more robust testing of the proposed mechanisms can be developed.

##### *a) Kinematic Intensity versus Cloud-to-Ground Lightning Production*

If the elevated charge mechanism is valid, then one would expect a plot similar to Figure 1.1 when plotting kinematic intensity versus negative CG flash rate for these storms. Recall that in Figure 1.1, negative CG flash rate rose with kinematic intensity, but only for a time, and then as kinematic intensity continued to increase negative CG flash rate began to decrease. The question is, what quantity should be used as the measure of kinematic intensity (KI)? Peak vertical velocity is a common measure, but perhaps is not the best since it only reflects the value of a single grid point at a particular time. Volume occupied by significant updrafts is another potential measure, as this would include more data points. Still another measure could be vertical air mass flux, in particular mass flux in the mixed phase region.

In this study, it was found that a combination of all three of these measurements provided the best estimate of overall kinematic intensity, as there was a lot more scatter in plots of KI versus other storm measurements (e.g., flash rates, precipitation amounts) when only one or two were used. Thus, these measurements were combined to form a kinematic intensity index. In particular, for each storm, peak

vertical velocity, peak volume of the storm containing updrafts in excess of  $10 \text{ m s}^{-1}$ , peak volume of the storm containing updrafts in excess of  $20 \text{ m s}^{-1}$ , and peak average vertical air mass flux within the mixed phase region ( $0$  to  $-40 \text{ }^\circ\text{C}$ ) were all normalized to the respective values for the 25 July 1998 storm, and then averaged together to form the kinematic intensity (KI) index. The 25 July 1998 storm selected since it was representative of the middle region of kinematic intensity for the thunderstorms in this study.

The advantage of an index defined as above is that it is not completely sensitive to any one measure of kinematic intensity. Thus, the storm which dominates only a single category, and is weak in others, likely will be lower on the index scale than a storm which does well in each category. In such a situation, the latter storm can more reliably be called the most intense storm, kinematically speaking, since it performs well in a variety of different measures. Using a composite index also has advantages as it was found that it tended to reduce scatter compared to plotting one single kinematic measure versus things like flash rates and precipitation amounts. That is, for the most part, no one single kinematic measure was significantly more correlated to lightning production than another. Thus, using a single measure of kinematic intensity, or weighting one more strongly than another, was not needed.

Peak values were used to construct the index because each of the cases generally had only 30 minutes or less of optimum dual-Doppler geometry. Thus, doing averages over storm lifetime could be very misleading, since storms which were not well placed within the dual-Doppler lobes for a majority of their lifetimes would appear to be less intense than those that were, regardless of their true updrafts.

Figure 5.1 shows plots of kinematic intensity index versus peak negative (a) and positive (b) CG flash rate for each storm in this study. In Figure 5.1a, the three low negative CG storms (1 and 15 July 1998, 29 June 00) stand out in the right side of the plot, with their high kinematic indices yet low peak negative CG flash rates. Note how the kinematic index for 29 June 2000 exceeds the indices for the other two intense storms by a large margin, especially 1 July 1998. This was mainly due to the large volume of intense updrafts observed in 29 June 2000. Peak vertical velocity and vertical air mass flux were much less distinctive. Most of the remaining storms fell within a kinematic intensity index range of 0.5 to 1.5, or within 50% of the 25 July 1998 storm. However, in this range of moderate intensities, peak negative CG flash rates varied significantly, and there was no obvious one-to-one correspondence between kinematic intensity index and peak negative CG flash rate. However, there is a definite tendency for storms within

this moderate intensity range to exhibit peak negative CG flash rates that are greater than those for storms with larger KI. This is true whether those storms are tropical or mid-latitude, suggesting that the elevated charge mechanism is valid in both tropical and mid-latitude settings. This is not surprising, since the mechanism is based on basic physical principles that should be valid no matter what the climatic region is. Note that the weak monsoonal storm, 30 July 1998, was very low on the intensity scale and produced no negative CG lightning. This is consistent with it not having strong enough updrafts to electrify significantly.

There is a tendency, within the 0.5-1.5 kinematic intensity range, for tropical convection to have lower peak negative CG flash rates than corresponding mid-latitude convection. However, this is not necessarily just because the tropical convection was less electrified overall. In fact, 15 February 1999 had a nearly identical kinematic index to 25 July 1998, and while 15 February produced a lower peak negative CG flash rate than 25 July 1998, as far as the FCMs could detect it did have a significantly greater total flash rate (cf. Tables 3.1 and 4.1). The same was true for 26 January 1999. Thus, these tropical thunderstorms could have had greater IC:CG ratios than 25 July 1998. This is once again consistent with the elevated charge mechanism, since the typical location of the main negative charge region, around  $-20^{\circ}\text{C}$ , would have been at a higher altitude (in the AGL sense, which is what would be important for CG lightning) in the tropical environment than in the mid-latitude environment, in fact 1.5-2 km higher based on the thermodynamic soundings in this study. In general, the higher altitude should tend to favor ICs over CGs in tropical thunderstorms versus mid-latitude thunderstorms, given the same kinematic intensity. This observation is broadly consistent with those of Pierce (1970) and Prentice and Mackerras (1977), who found that IC:CG ratio decreased with increasing latitude. However, although the results of this study are favorable for this interpretation, caution is advised since the FCMs had significant detection issues for every storm they observed, and at best only gave a limited snapshot of current IC:CG ratio, not necessarily the peak value.

Figure 5.1b shows that the two PPCG storms, 15 July 1998 and 29 June 2000, both had significantly higher kinematic intensity indices than any other storm, even 1 July 1998. However, as mentioned above, the discrepancy in KI between the low-CG 1 July 1998 storm and the PPCG storms was mainly due to the vastly greater volumes of intense (i.e.,  $> 20 \text{ m s}^{-1}$ ) updrafts in the latter storms, when compared to 1 July. The other components of the index were not as different between these storms. Given such a small sample

size, it is difficult to draw any firm conclusions, but one key difference between low-CG and PPCG storms may be that, although both types of storms can have comparable peak vertical velocities and vertical air mass fluxes, PPCG storms have far larger volumes containing intense updrafts. That is, in PPCG storms the updrafts aren't necessarily any stronger than in low-CG storms, but strong updrafts occupy a greater storm volume. A larger volume of very fast updrafts would imply significantly greater production of positive charge, which could be tapped for subsequent positive CG flashing.

Note that the PPCG storms featured much larger KI than the more moderate (and non-PPCG) convection centered around 25 July 1998. Considering past studies, it may seem redundant to point this out, but this study clearly shows that PPCG severe storms are much stronger kinematically than non-severe, non-PPCG storms.

#### *b) Precipitation Intensity versus Cloud-to-Ground Lightning Production*

Along the same lines as the KI index, a rain intensity index was constructed for each storm. This index was comprised of peak area of heavy ( $> 60 \text{ mm h}^{-1}$ ) rain at 0.5 km AGL and peak rain mass flux, both of which were normalized to their respective values for 25 July 1998, and then averaged together. Once again, 25 July 1998 was an arbitrary choice, but it was a fairly moderate rain producer. And obviously, based on the definition, its rain intensity index was 1.

The rain index is advantageous over any one particular measure of rain intensity because it balances very heavy rain producers (heavy rain area) against storms which overall produce large rain totals despite the absence of large rain rates (rain mass flux). Peak values were used for similar reasons to the kinematic index. Storms were not always entirely scanned and so peak values give better estimates of rainfall intensity than average values would.

Figure 5.2 shows rain intensity index versus peak negative and peak positive CG flash rate for each storm in this study. The 15 July 1998 and 29 June 2000 storms were by far the most intense rain producers. Note also that a kinematically intense storm like 1 July 1998 fell near the middle of the distribution in terms of rain production. In Figure 5.2a, no well-defined relationship between rainfall intensity and peak negative CG flash rate is evident. However, it does appear that the PPCG storms featured the highest rainfall intensities, and in Figure 5.2b the PPCG storms stand out at the high end of the spectrum,

suggesting that very intense rainfall is related to enhanced positive CG flashing. This is broadly consistent with both the inverted dipole and precipitation unshielding mechanisms. However, it does not appear that rainfall alone (through precipitation current) can explain low production of negative CGs, since a low-CG storm like 1 July 1998 actually had a lower rainfall intensity index than more prolific negative CG producers such as 21 and 25 July 1998.

A hail intensity index was constructed for the mid-latitude cases. It was comprised of peak hail area at 0.5 km AGL and peak hail mass flux, both normalized to 25 July 1998 and averaged together. A hail index was not calculated for the tropical cases since they produced negligible hail.

Figure 5.3 show hail intensity index versus peak negative and peak positive CG flash rate for each mid-latitude storm. Figure 5.3a is very similar to the mid-latitude portion of Figure 5.1a, suggesting that kinematic intensity and hail intensity are strongly related. Moderate hail producers like 21 and 25 July 1998 featured significantly higher negative CG flash rates than more intense hail producers. In Figure 5.3b, which is very similar to the mid-latitude portion of Figure 5.1b, the most distinctive feature is that the PPCG storms produced vastly more hail than other storms, even 1 July. However, given the apparent strong relationship between kinematic and hail intensities discussed further below, it would be difficult to decouple the two enough to state unambiguously that hail was a driving factor in causing PPCG storms. In addition, hail is not likely produced in high enough number concentrations (Cheng and English 1983), even in storms like 15 July 1998 and 29 June 2000, to be significant from an electrical perspective compared to graupel. Moreover, observations of a PPCG storm by Carey and Rutledge (1998) suggest that may be electrically neutral in such storms, in that it does not carry enough aggregate charge to affect lightning production significantly.

### *c) Radar Reflectivity Intensity versus Cloud-to-Ground Lightning Production*

Finally, a reflectivity intensity index was developed for all of the case studies. The index contained contributions from peak reflectivity, peak height of the 30 dBZ contour, and peak height of the 50 dBZ contour, each normalized to 25 July 1998, and then averaged together. Thus, the reflectivity intensity index is a measure of the vertical structure of each storm, and is an alternative to other reflectivity intensity measures such as vertically integrated liquid water (VIL; Greene and Clark 1972).

Figure 5.4 shows reflectivity index versus peak negative (a) and peak positive (b) CG flash rates for every storm in the study. In Figure 5.4, the most obvious inference is that the storms did not vary significantly in reflectivity intensity, as almost all are within 20% or so of the base index for 25 July 1998. The tropical thunderstorms tended to have lower reflectivity intensities than the mid-latitude thunderstorms. This was mainly due to the fact that their 50 dBZ contour did not extend to as high an altitude, which can be attributed to the lack of hail in the tropical thunderstorms, particularly hail aloft. The more intense hailstorms like 1 July 1998 and the PPCG storms, tended to have higher reflectivity indices, probably because they had more hail aloft than more moderate storms like 21 and 25 July 1998. In general, the storms with the most intense reflectivities tended to have lower peak negative CG flash rates than other storms, but there is no obvious correspondence between positive CG flash rate and reflectivity intensity. Certainly the most intense storms were capable of being PPCG, but a low-CG storm like 1 July 1998 actually had a slightly more intense reflectivity structure than a PPCG storm like 15 July 1998. Note that the shallow 30 July 1998 storm had the lowest reflectivity intensity index. A reflectivity-based index can be very ambiguous, however, since radar reflectivity is more strongly weighted to the largest particles, rather than particle concentrations. An index that included more polarimetric variables, such as  $K_{dp}$  and LDR, would be more suitable, but many of these variables were used to deduce precipitation type at the lowest grid level (and thus already included in the precipitation indices), so such an index was not developed in this study.

#### *d) Kinematic Intensity versus Precipitation and Reflectivity Intensities*

It is interesting to compare the various intensity indices not only to CG rates, but also to each other, thus elucidating the relationships between convective storm kinematics and microphysics. Figure 5.5 shows kinematic intensity index versus rain intensity index for every storm in this study. While there is a broad tendency for rain intensity to increase with kinematic intensity, there is a lot of scatter in this relationship. For example, a kinematically intense storm like 1 July 1998 produced less rainfall than kinematically weaker storms like 21 and 25 July 1998, and 26 January 1999. Thus, the relationship between convective storm kinematics and rain production is not as simple as: stronger updraft, more rain. While condensation

rate is roughly proportional to updraft speed, one must also consider such complicating factors as entrainment, particle collisions, and evaporation before relating kinematic strength to rain production.

Figure 5.6 shows kinematic intensity index versus hail intensity index for the mid-latitude storms. Here, a much more obvious relationship is seen than with rain intensity. For the most part, the stronger the storm is kinematically, the more hail it produces. There does appear to be a plateau that hail intensity reaches at the extreme end of kinematic intensity (29 June 2000), but this should be interpreted with caution since analysis of 29 June 2000 was terminated even though its hail production was continuing to increase. Basic microphysics suggests that precipitation fallout should lag its production (which is fueled by ascending air), and thus it is entirely possible that the 29 June storm's true hail peak was not contained within the analysis time. Recall that the most important reason for the difference in kinematic intensity index between 1 July 1998 and the PPCG storms was that the latter contained significantly larger volumes of very fast updrafts. Since hail production is fueled by fast updrafts, it seems natural that a larger volume of such updrafts should result in larger fallout of hail at the surface.

Figure 5.7 shows kinematic intensity index versus reflectivity intensity index for all the mid-latitude and tropical thunderstorms. While there is a tendency for reflectivity intensity to increase with kinematic strength, at the high end this relationship flattens out, such that storms like 1 and 15 July 1998, and 29 June 2000, have very similar reflectivity intensities, yet very different kinematic strengths. This could be due to the way the reflectivity index was defined, since it contained no area or volume measures, as opposed to the kinematic index.

## *5.2 Energy and Charge Considerations*

Table 5.1 lists maximum total kinetic energy contained within the vertical motions of the storms in this study, for both the entirety of each storm and also just within the critical mixed-phase region. The two PPCG storms, 15 July 1998 and 29 June 2000, had by far the largest energy resources to tap for charging. Whether within the entire storm or just the mixed-phase region, their kinetic energy exceeds by a factor of two even the low-CG 1 July 1998 storm. Interestingly, however, the 26 January 1999 tropical squall line had the third largest kinetic energy totals, although 26 January did not contain as large a fraction of its total kinetic energy within the mixed-phase region as in the mid-latitude low-CG and PPCG storms.

It is clear that the PPCG storms were by far the most energetic. This is largely due to their increased size, which means more mass to contain energy, and not necessarily because of their vertical motions, which were comparable in magnitude to the low-CG 1 July 1998 storm. Since a fraction of a thunderstorm's kinetic energy ultimately is converted to electrical energy through charge separation, it seems possible that some of this extra energy could be tapped for enhanced positive charge production. This increased positive charge then could lead to increased positive CG flash rates.

It is important to demonstrate that enhanced positive charge can account for the positive CG flash rates observed in these PPCG storms. Typical observed concentrations within charge layers are on the order of 1-10 C km<sup>-3</sup>, and charge layers usually are on the order of 1 km thick (MacGorman and Rust 1998). Consider a 10 km x 10 km updraft, giving an area of 100 km<sup>2</sup>. Given that the PPCG storms in this study had significant updraft volumes well in excess of 1000 km<sup>3</sup> at peak, and were 15 km high or taller, this is an acceptable order of magnitude estimate for updraft area at any particular vertical level. This leads to an estimate of enhanced positive charge on the order of 100-1000 C. An order of magnitude estimate for peak positive CG flash rates in these storms is about 10 per 10 minute period (1 per minute). Given that typical flashes transfer on the order of 10-100 C of charge (Uman 1987), this means that positive CGs will deplete 100-1000 C of charge in 10 minutes. In other words, the enhanced positive charge region would be completely eliminated in 10 minutes. This is more than enough time for charge regeneration to occur, since typical electric fields recover within seconds after a lightning flash (MacGorman and Rust 1998). Note that this argument works for either the upper or lower positive charge regions.

### *5.3 Discussion and Conclusions*

With 11 cases spanning mid-latitude and tropical convective regimes, this was likely the largest combined dual-Doppler, multiparameter radar, and lightning study performed to date. Despite its breadth, however, the sample size was still relatively small, preventing comprehensive statistical conclusions. Nonetheless, some key insights can be made into the relationships between convective storm microphysics, kinematics, and lightning, insights.

The elevated charge mechanism was well supported by the observations. Storms that featured strong kinematics, such as 1 and 15 July 1998, and 29 June 2000, consistently featured smaller peak negative CG

flash rates compared to storms that were kinematically less intense, whether the latter storms were tropical or mid-latitude. This conclusion is strengthened by the fact that it was independent of the particular kinematic descriptor. The low negative CG producers had higher peak updrafts, greater average (and standard deviations of) updrafts, greater average (and standard deviations of) vertical mass fluxes, larger volumes containing updrafts greater than virtually any arbitrary threshold (e.g.,  $20 \text{ m s}^{-1}$ ), CFADs that showed greater percentages of strong vertical velocities at nearly every altitude, and so on. Various combinations of these measures (such as the kinematic intensity index) showed the same pattern. Even just simple vertical cross-sections through the dual-Doppler data showed the low negative CG producers to be more intense kinematically in a subjective sense.

Hail production was found to be highly correlated to kinematic intensity (at least for the mid-latitude cases), and thus the most significant hail producers were also the lowest producers of negative CGs (save for a weakly electrified case like 30 July 1998). This implies that future mid-latitude thunderstorm analyses without access to dual-Doppler data, but perhaps with access to multiparameter radar data (and thus the means to quantify hail production), can identify the kinematically strongest storms by looking for the storms which produce the largest hail areas and hail mass fluxes.

Unlike hail, rain production was only loosely correlated to kinematic intensity, and also negative CG production. Thus, one cannot identify probable low negative CG storms by simply looking for the storms that produce the largest rain mass fluxes or heavy rain areas. This also implies that rain is not a significant factor in reducing negative CG lightning production, through mechanisms such as enhanced precipitation current.

Radar reflectivity intensity showed some correlation with kinematic intensity, and potentially can be used as a proxy for updraft strength. In this study, low negative CG producers were distinguished by the 50 dBZ contour extending to significant altitudes, approximately 14 km above mean sea level (MSL) or higher. Also, in low negative CG producers, up to 5% or more of storm area contained 50 dBZ or greater throughout almost every altitude within the mixed phase region.

Less evidence was found for the other mechanism proposed to explain reduced negative CG flash rates, the separated updraft-downdraft mechanism. In particular, it was difficult to find a robust negative correlation between precipitation cores and updraft cores in storms that produced low negative CG flash

rates, the necessary criterion for this mechanism to be active. Subjective perusals of the data did show some offsets between updrafts and precipitation shafts in such storms. However, such offsets were also seen in more prolific negative CG producers, like 21 July 1998.

This data set contained two PPCG storms (15 July 1998 and 29 June 2000) and one low-CG storm (1 July 1998). From a kinematic perspective, both of these types of storms were very similar. They had similar peak updrafts and similar average (as well as standard deviations of) updrafts and vertical air mass fluxes. CFADs of vertical velocity were comparable, as were vertical cross-sections of storm updrafts. Reflectivity intensities (in terms of peak reflectivities and peak heights of notable reflectivity contours, as well as reflectivity CFADs) were also very close to one another. In fact, the only true differences between these two storm types from a kinematic perspective was that the PPCG storms had greater volumes of significant updrafts (e.g.,  $> 20 \text{ m s}^{-1}$ ). Given the observed strong correlation between kinematic strength and hail production in this study, this implies that the PPCG storms also produced more hail than the low-CG storm. Also, each PPCG storm featured rapid and significant intensifications (in terms of both their kinematics and reflectivities), during which positive CG flash rates increased to their peak values. The low-CG storm of 1 July 1998 showed no such intensification.

While the sample size is too small to make definitive conclusions, one can examine the implications of these observed differences in terms of the proposed PPCG mechanisms. First of all, positive CGs obviously transfer positive charge from ground. Given the Stolzenburg et al. (1998c) thunderstorm charge model, this charge must come from some part of the thunderstorm, whether the lower positive charge region (inverted dipole mechanism) or the upper positive charge region (tilted dipole and precipitation unshielding mechanisms). Simply put, a larger volume of significant updrafts should result in a greater reservoir of positive charge in both of these regions. Based on non-inductive charging theories, a larger volume of significant updrafts would result in more condensate and more opportunities for charge-separating collisions. Hence, more positive charge (and also more negative charge as well).

Balancing this out of course is that this charge would be produced over a larger volume, so charge densities would not necessarily be reduced in theory. In practice, however, charge densities could increase, at least temporarily and locally in small regions, given turbulence within the thunderstorm. That may be all that is needed to initiate positive CG flashes.

The intensification may be what separates the low-CG storms from the PPCG storms. Both are certainly kinematically intense, but it appears that if a storm intensifies even more, such that its volume of significant updrafts increases, then it can begin to produce more positive CGs. That is, a further intensification could cause the positive charge densities within the storm to be capable of reaching the threshold for positive breakdown. The 29 June 2000 storm provides a good example of this, as the storm was low-CG prior to its intensification in the middle of the analysis period. After this intensification, as updraft volumes steadily grew, so did positive CG flash rates.

The question then is, where is the origin of these positive flashes. That is, which region of positive charge is responsible for positive CGs, and which PPCG mechanism is valid. Without in situ charge measurements, it is difficult to do anything but speculate about these issues. In a general sense, this idea of enhanced positive charge caused by larger updraft volumes is consistent with any of the proposed PPCG mechanisms, as they don't necessarily deal with the issue of producing the charge in the first place. They merely seek to describe how this positive charge is exposed to ground. However, based on the observations in this study, a so-called "inverted dipole" may be the best candidate, in the following sense. First of all, by inverted it is not meant that the charge structure within the thunderstorm is simply reversed. It is unclear based on the kinematic observations in this study why this should occur. However, the elevated charge mechanism suggests that, in intense updrafts, the entire thunderstorm charge structure is elevated (Stolzenburg et al. 1998c), not just the main negative charge region. In such a storm, a further intensification in the volume of significant updrafts could cause an increase in the amount of charge in the lower positive charge region, making the initiation of positive CGs from this region more likely. While the main negative charge and upper-level positive charge also would increase, potential CGs from these regions would be less favored by the greater distance between them and ground. Enhanced lower positive charge could also explain the apparent inverted nature of IC lightning seen in preliminary LMA observations from STEPS (Dr. P. Krehbiel, personal communication). In essence, the lower positive charge region could grow large enough that ICs between it and the main negative charge region were favored, in addition to initiating positive CGs.

A schematic depiction of these processes can be found in Figure 5.8. In low-CG storms the charge structure is elevated when compared to an ordinary thunderstorm, due to the stronger updrafts. In addition,

there is more charging overall due to stronger updrafts, and a greater volume containing strong updrafts. A low-CG storm has about the same updraft speeds as a PPCG storm, and similar altitudes of major charge regions, but the greater volume of strong updrafts causes more charging overall, and enhances lower positive charge.

The inverted dipole as conceived as an elevated charge structure with enhanced lower positive charge has advantages over other possible explanations for positive CGs. For example, the precipitation unshielding and tilted dipole mechanisms posit that the upper positive charge region is responsible for most positive CGs. However, it is unclear why it should necessarily be favored over lower positive charge, since it is farther from ground. Moreover, such mechanisms are somewhat at odds with the elevated charge mechanism, since the main negative charge region also should be closer to ground. In fact, the tilted dipole mechanism completely fails to explain the observed dearth of negative CGs in PPCG storms, because whether or not the upper positive charge is exposed to ground through a sheared anvil, the main negative charge region still is closer to ground than it, even if the negative charge were at a higher altitude than in ordinary convection. Thus, negative flashes, though perhaps reduced in number, should still dominate over positive flashes.

The precipitation unshielding mechanism seeks a way around this issue by suggesting that enhanced precipitation currents tend to neutralize the main negative charge, but observations from this study contradict this idea. If enhanced precipitation currents do significantly reduce negative CG flash rates, then why did a low-CG storm like 1 July 1998 produce comparable rainfall to more prolific negative CG producers? Furthermore, no significant correlations were found between CG lightning characteristics and rain amounts from the storms examined.

In summary, an “inverted dipole” brought about by an elevated thunderstorm charge structure and enhanced lower positive charge provides perhaps the simplest and most coherent explanation for the PPCG storms in this study. The elevated charge structure is brought about by intense updraft strength, and is a phenomenon also common to low-CG intense or severe storms. It is suggested that an increase in the volume of intense updrafts enhances lower positive charge, and is possibly what sets apart PPCG storms from low-CG storms. It is important to note that PPCG storms do not necessarily have stronger updrafts than low-CG storms; in fact, the two types of storms appear to be very similar in an average sense (i.e.,

CFADs, vertical air mass fluxes, etc.). PPCG storms merely have a greater volume of intense updrafts. That is, compared to low-CG storms, PPCG storms aren't any stronger, just bigger.

From the forecasting perspective, this has important implications, as CG data become more widely available for "nowcasting" applications. It has been noted in past studies (e.g., Carey and Rutledge 1998) that there is a one-way correlation between enhanced positive CG activity and the occurrence of severe weather. That is, most PPCG storms are severe, but not all severe storms are PPCG. Now, low-CG storms are capable of being severe, just like PPCG storms. For example, 1 July 1998 produced large hail and possibly a tornado. Thus, low-CG storms may help to fix the discrepancies in the PPCG-severe weather correlation. It is possible that most anomalously low negative CG producing storms are severe, and most severe storms produce anomalously low negative CG lightning, at least during a significant portion of their lifetimes (~30 minutes or more).

Given the probabilistic nature of thunderstorm electrification and lightning, and the three-dimensional nature of thunderstorm wind fields and turbulence, the simple slab models of thunderstorm charge structure are likely incomplete. However, they are useful in an average sense. While not every intense thunderstorm will feature elevated negative charge, most could. Thus, what could distinguish intense or severe convection from more ordinary convection is not necessarily enhanced positive CG flash rates, but instead a dearth of negative CGs, and a high IC:CG ratio. This implies that forecasters equipped with CG lightning data could look for anomalously low negative CG lightning flash rates when attempting to "nowcast" severe weather.

### *5.3 Suggestions for Future Research*

The sample of storms in this study was the most robust to date, but still small from a statistical perspective. To move to the next level of insight, studies with far more cases are needed. The basic barrier to this, however, is the time required to analyze all the radar and lightning data for each case. Future studies need to develop sophisticated techniques to completely automate data processing, particularly radar data editing such as velocity unfolding and sidelobe removal.

The other key ingredients for new insight are in situ data on thunderstorm charge structure as well as more reliable intracloud lightning measurements. Both of these measurements were available in STEPS,

and should be incorporated into future radar/lightning studies. Future thunderstorm field projects will need these measurements as well.

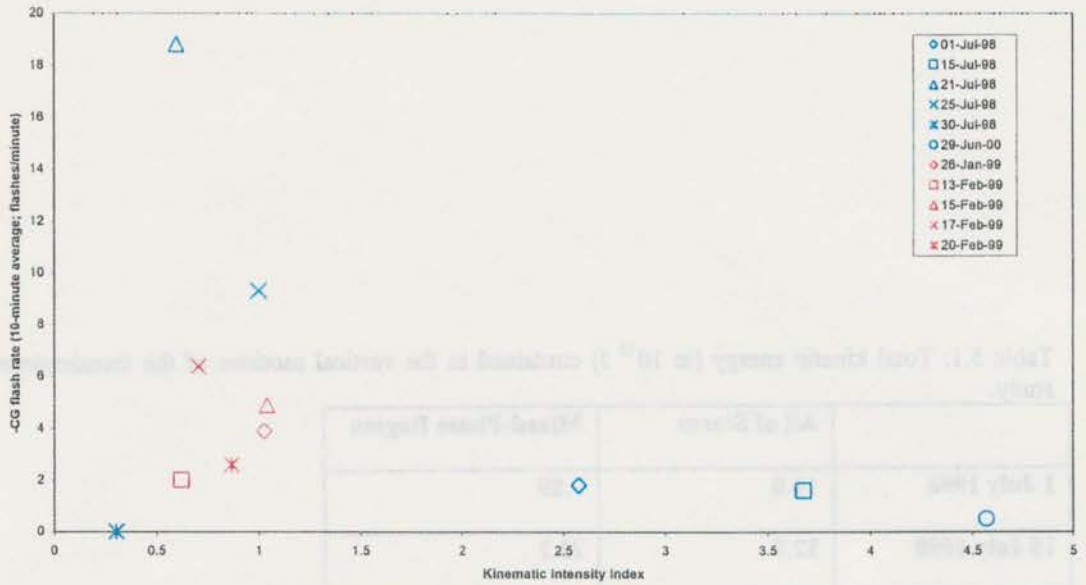
The results presented here have some implications for current and future numerical model lightning flash rate parameterizations. For example, Wang and Prinn (2000) use a parameterization for total lightning flash rate in their thunderstorm chemistry model that is based on the difference between the maximum updraft and maximum downdraft in the storm. Though not presented here, it was found in this study that downdrafts tracked updrafts very well, such that storms with the fastest updrafts also had the fastest downdrafts. In fact, this is why downdraft data for the most part were not presented, as they were superfluous. In this sense, the Wang and Prinn (2000) parameterization could be somewhat redundant. Either maximum updraft or maximum downdraft, instead of both, could have been used with minimal loss in accuracy. The Price and Rind (1992) parameterization bases total flash rate on cloud top height, which could be somewhat inaccurate based on the results from this study. Based on radar reflectivity data, a storm with a very high flash rate like 29 June 2000 had reflectivity contour (in particular the 0 or 10 dBZ contours) heights similar to less electrified storms like 25 July 1998 or several of the tropical cases. In fact, based on the results of the CFADs, vertical cross-sections, and reflectivity intensity index plots, this study's results tend to imply that the altitudes of high reflectivity contours (30 or 50 dBZ, for example) would be more important from a lightning flash rate perspective, in line with the results of Ryan (1999). Finally, developers of future flash parameterizations may want to consider including vertical air mass flux and volume of significant updrafts, as these show potential in modulating flash rates.

In summary, the atmospheric electricity community should start moving away from case studies and small data sets to more robust statistical analyses. These analyses need to incorporate measurements from the full suite of available platforms: multiparameter and dual-Doppler radar, CG lightning detection networks, three-dimensional lightning mappers, and in situ charge measurements, among others. However, this does not necessarily mean just new field projects. In particular, researchers should revisit past studies and see how they can be improved upon by incorporating available data that was not initially included. One example might be combining the Stolzenburg et al. (1998a,b,c) thunderstorm charge measurements with NEXRAD radar data and NLDN CG flash data, to see how the different charge structures compared to radar and lightning data for the same cases.

Table 5.1: Total kinetic energy (in  $10^{13}$  J) contained in the vertical motions of the thunderstorms in this study.

	All of Storm	Mixed-Phase Region
1 July 1998	16.0	9.89
15 July 1998	32.8	23.2
21 July 1998	4.59	3.02
25 July 1998	6.09	3.25
30 July 1998	1.41	0.61
29 June 2000	35.6	24.2
26 January 1999	23.1	12.1
13 February 1999	8.30	4.41
15 February 1999	11.8	6.11
17 February 1999	7.13	4.30
20 February 1999	10.7	5.77

a.



b.

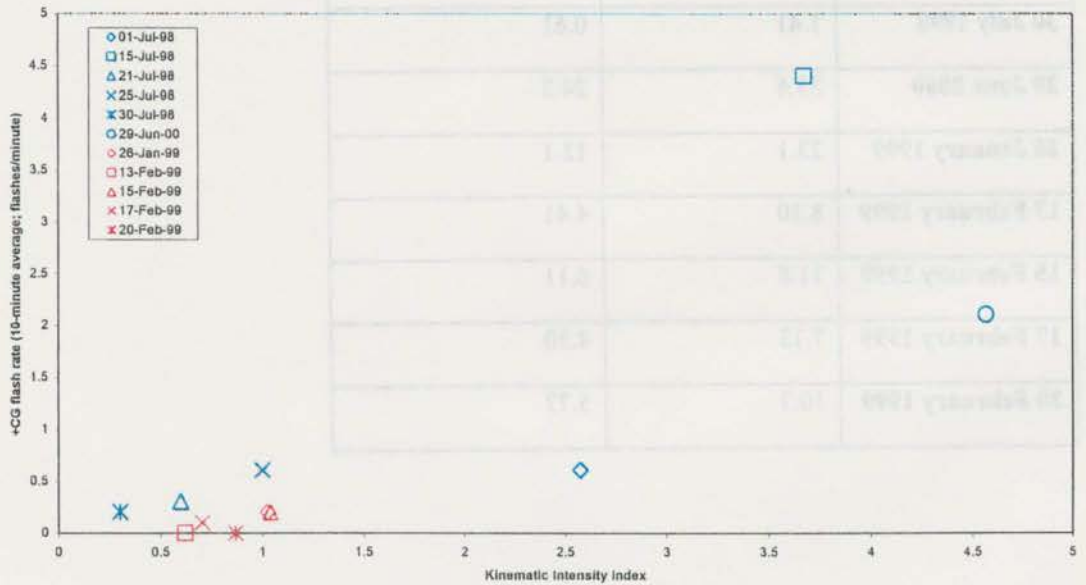
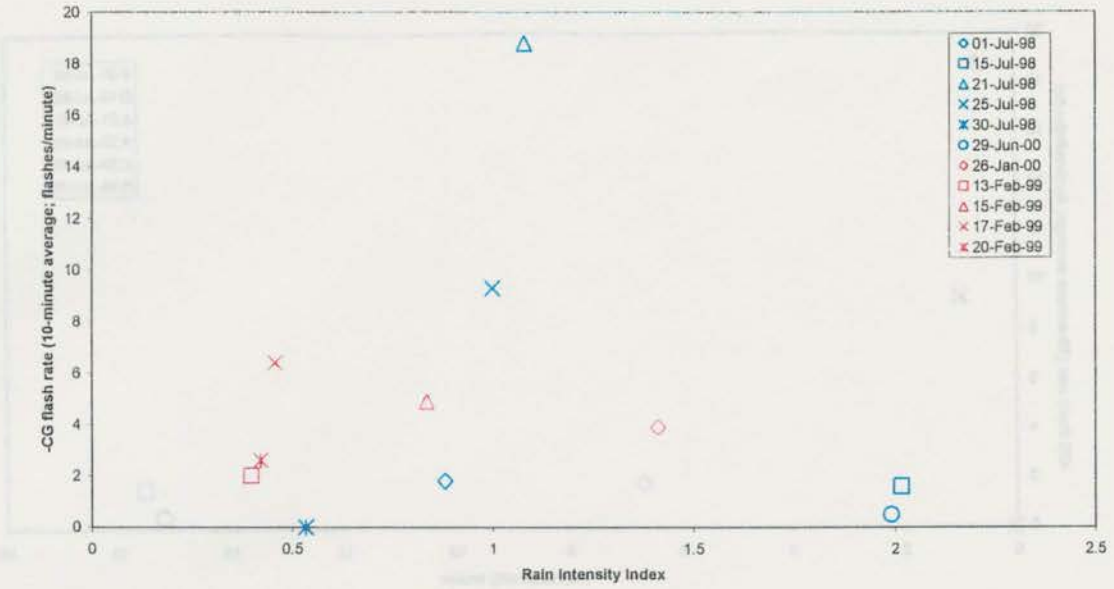


Figure 5.1: a) Kinematic intensity index versus peak negative CG flash rate for all the storms in this study. b) Same as a) except for positive CG flash rate. Blue points denote mid-latitude cases, red points denote tropical cases.

a.



b.

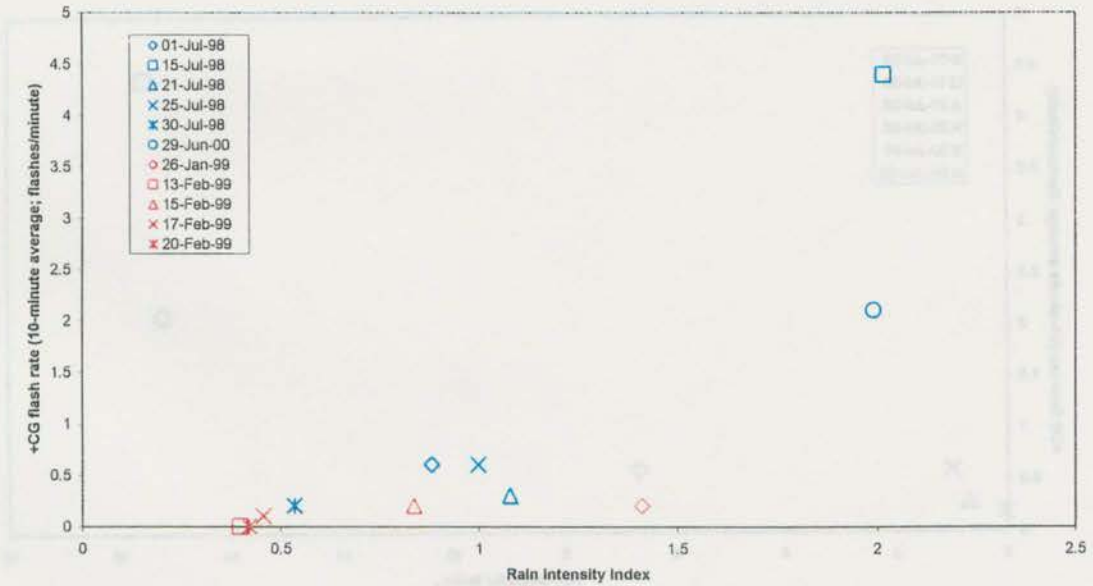
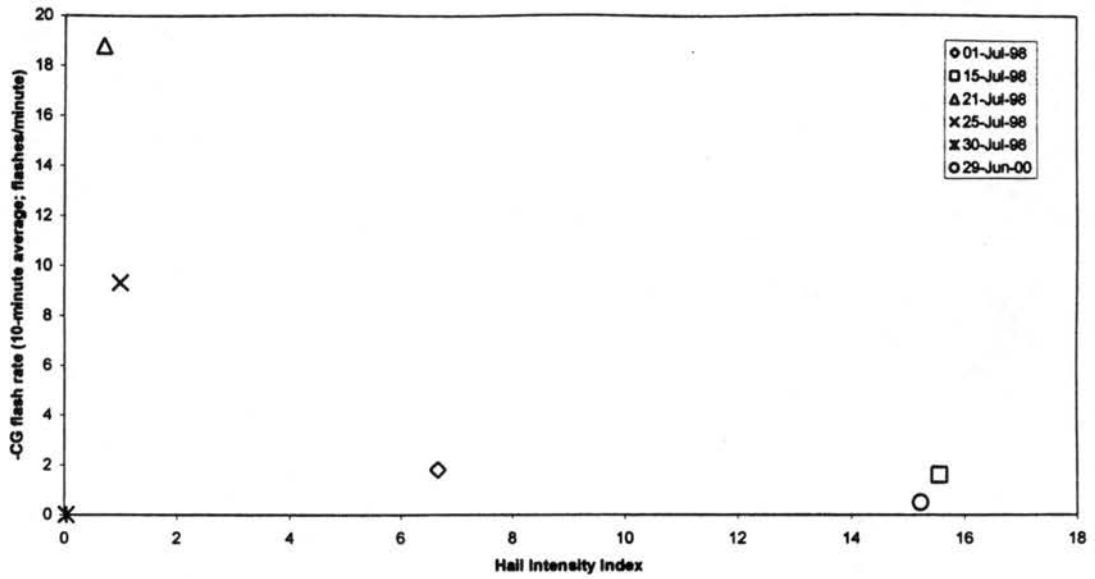


Figure 5.2: a) Rain intensity index versus peak negative CG flash rate for all the storms in this study. b) Same as a) except for positive CG flash rate. Blue points denote mid-latitude cases, red points denote tropical cases.

a.



b.

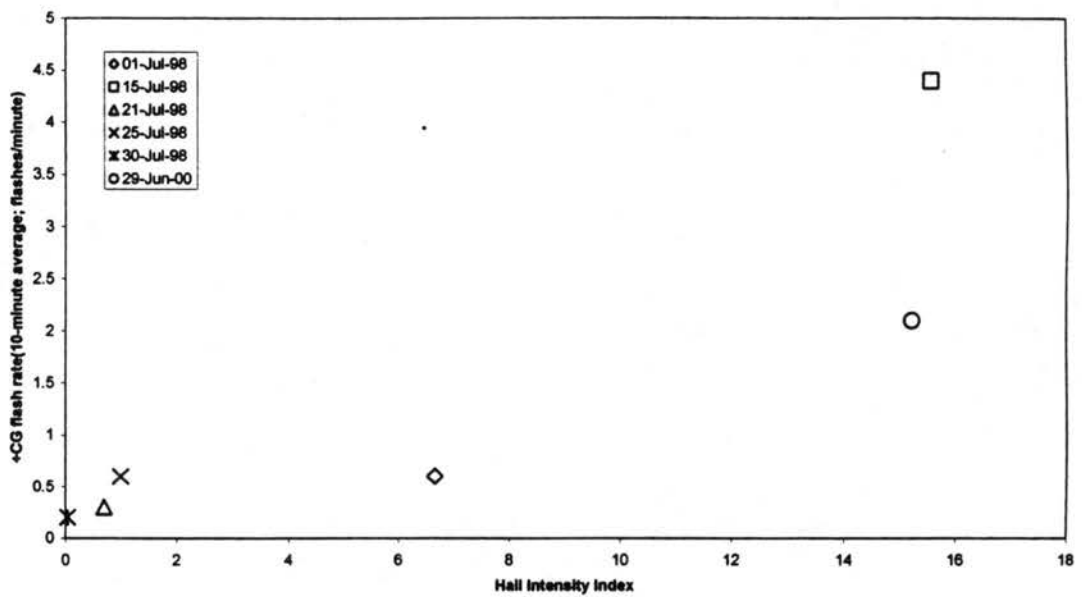
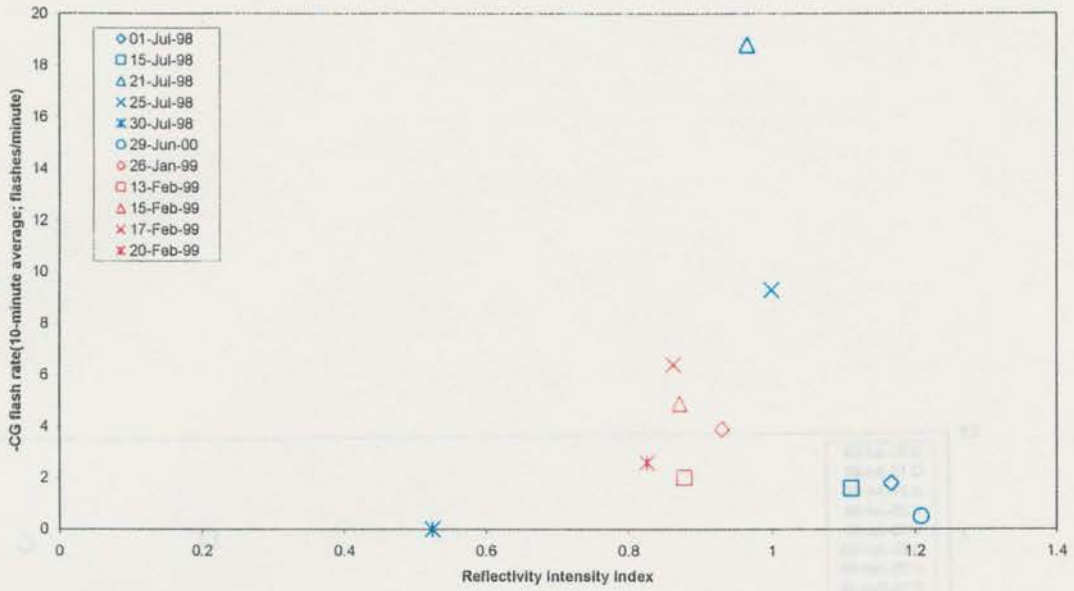


Figure 5.3: a) Hail intensity index versus peak negative CG flash rate for the mid-latitude storms in this study. b) Same as a) except for positive CG flash rate.

a.



b.

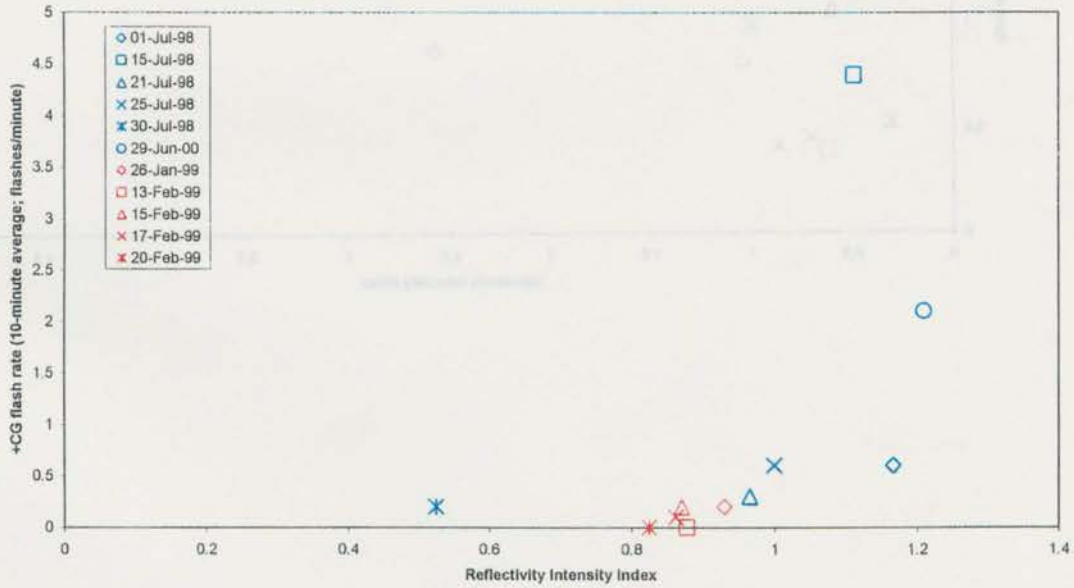


Figure 5.4: a) Reflectivity intensity index versus peak negative CG flash rate for all the storms in this study. b) Same as a) except for positive CG flash rate. Blue points denote mid-latitude cases, red points denote tropical cases.

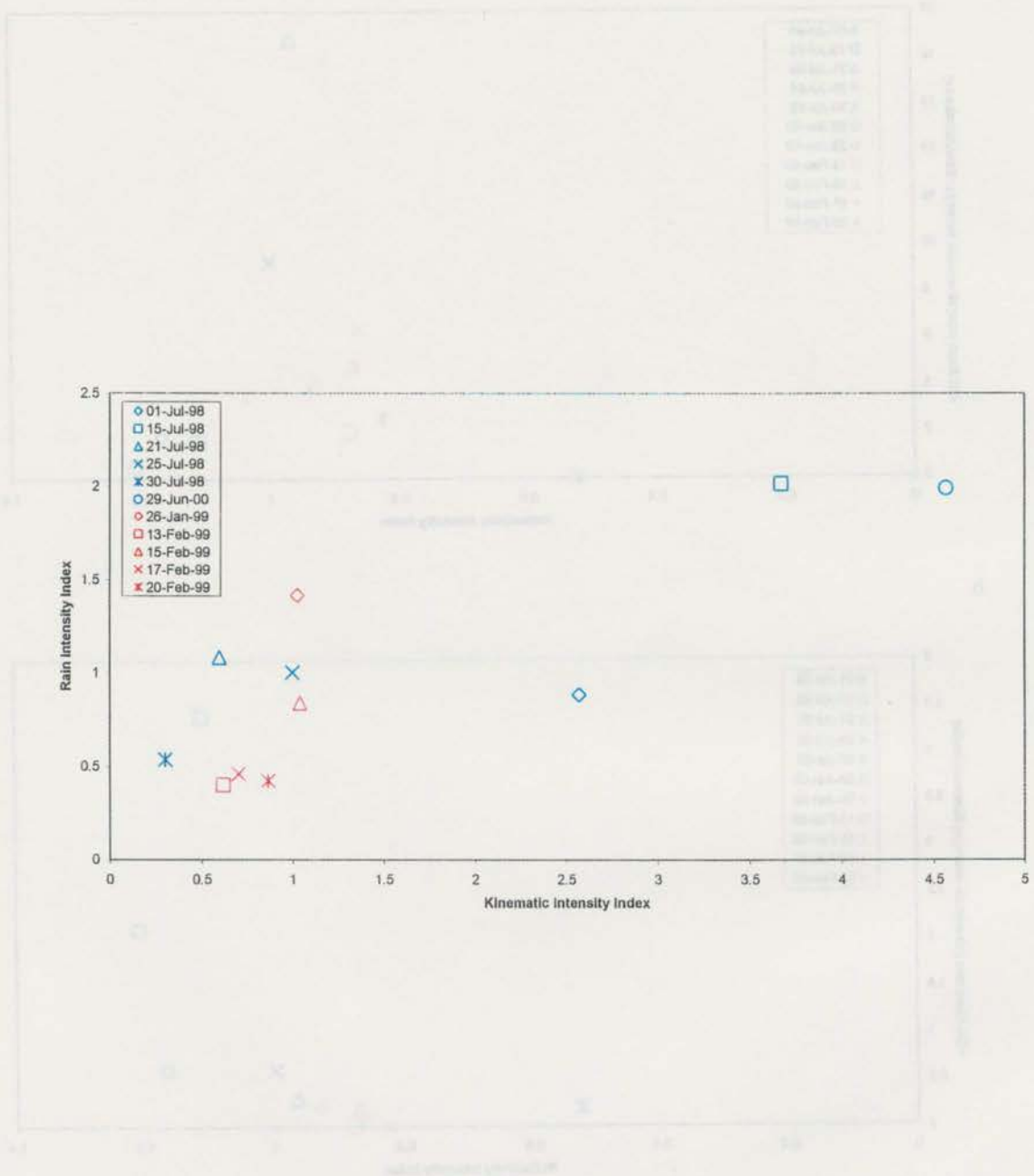


Figure 5.5: Kinematic intensity index versus rain intensity index for all the storms in this study. Blue points denote mid-latitude cases, red points denote tropical cases.

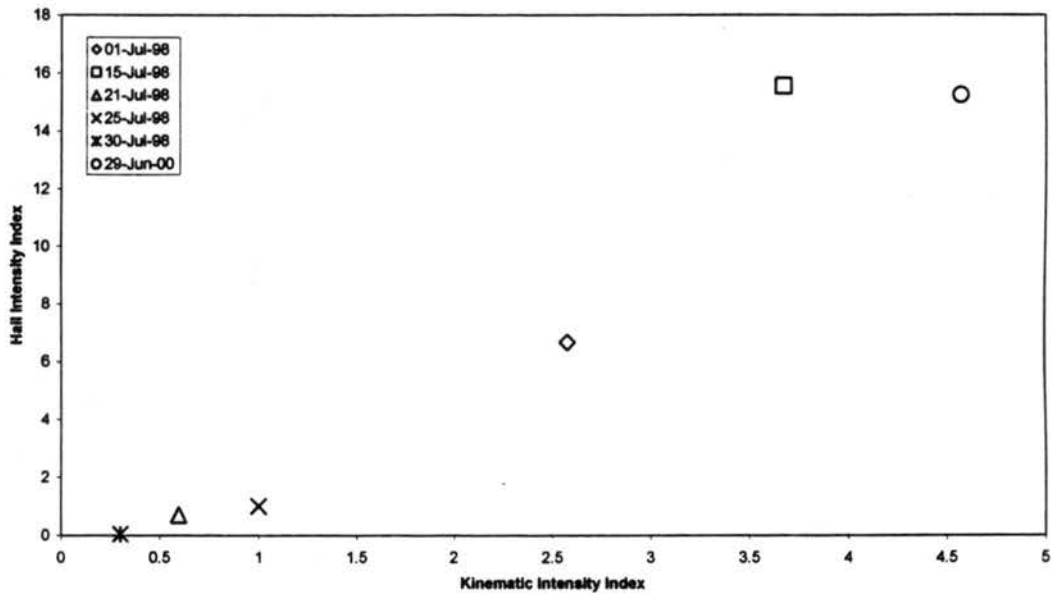


Figure 5.6: Kinematic intensity index versus hail intensity index for the mid-latitude storms in this study.

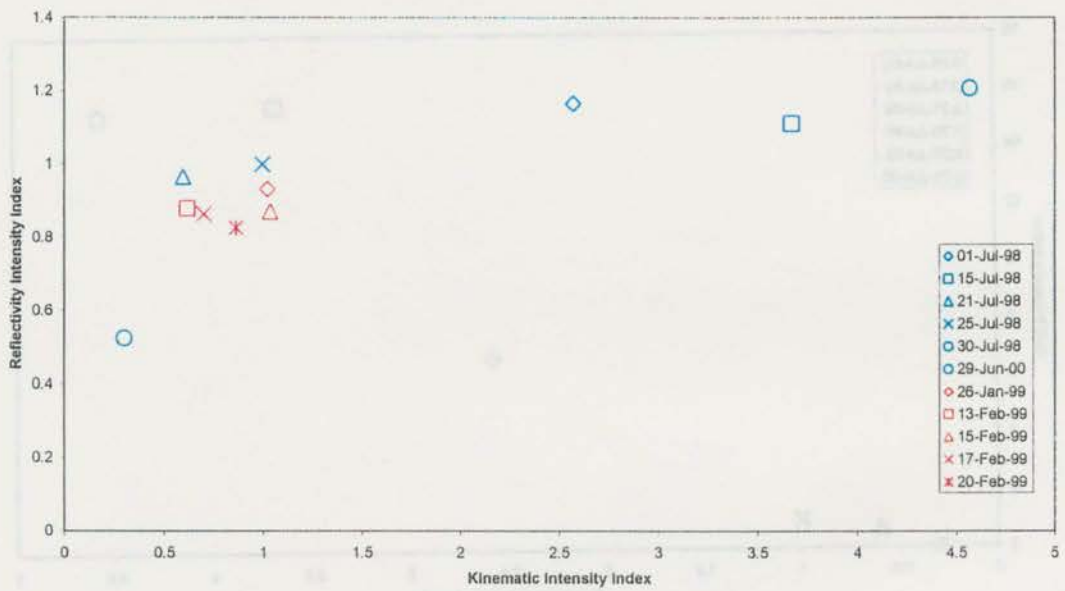


Figure 5.7: Kinematic intensity index versus reflectivity intensity index for all the storms in this study. Blue points denote mid-latitude cases, red points denote tropical cases.

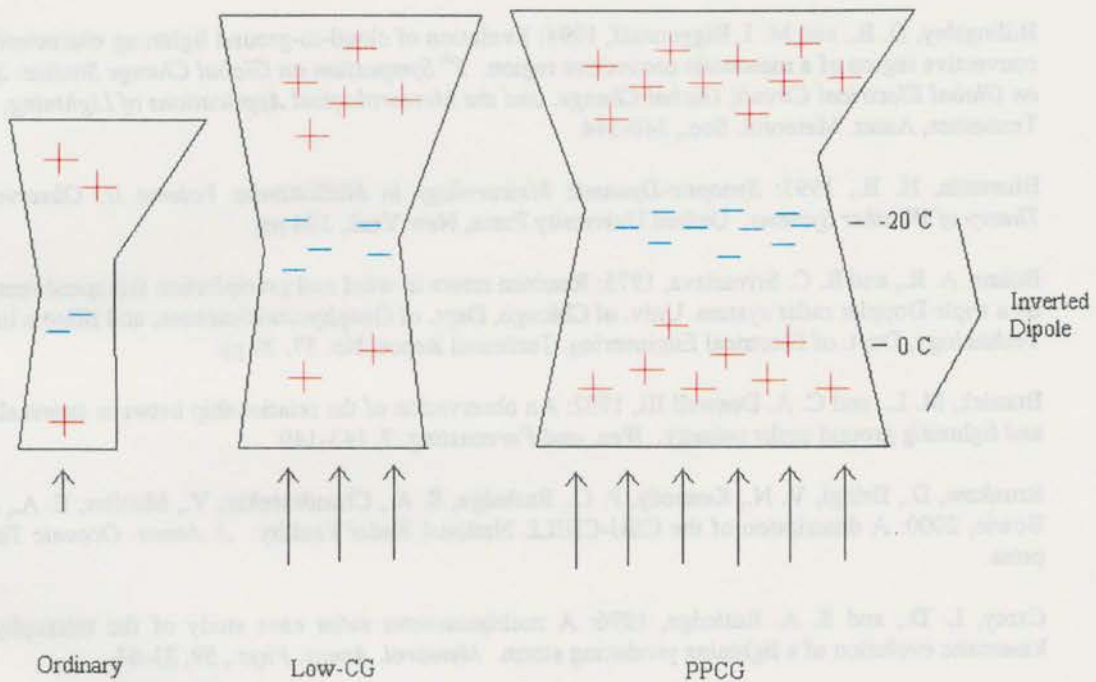


Figure 5.8: Schematic diagram of possible charge structures within the updraft regions of ordinary, low-CG, and PPCG thunderstorms. Negative charge is denoted by blue negative signs, positive charge by red plus signs. Updrafts are denoted by vector arrows, with the length of the arrow corresponding to the strength of the updraft.

## BIBLIOGRAPHY

- Balakrishnan, N., and D. S. Zrníc, 1990: Estimation of rain and hail rates in mixed-phase precipitation. *J. Atmos. Sci.*, **47**, 565-583.
- Billingsley, D. B., and M. I. Biggerstaff, 1994: Evolution of cloud-to-ground lightning characteristics in the convective region of a mesoscale convective region. *5<sup>th</sup> Symposium on Global Change Studies: Symposium on Global Electrical Circuit, Global Change, and the Meteorological Applications of Lightning*, Nashville, Tennessee, Amer. Meteorol. Soc., 340-344.
- Bluestein, H. B., 1993: *Synoptic-Dynamic Meteorology in Midlatitudes Volume II: Observations and Theory of Weather Systems*. Oxford University Press, New York, 594 pp.
- Bohne, A. R., and R. C. Srivastava, 1975: Random errors in wind and precipitation fall speed measurement by a triple Doppler radar system. Univ. of Chicago, Dept. of Geophysical Sciences, and Illinois Institute of Technology, Dept. of Electrical Engineering, Technical Report No. 37, 28 pp.
- Branick, M. L., and C. A. Doswell III, 1992: An observation of the relationship between supercell structure and lightning ground strike polarity. *Wea. and Forecasting*, **7**, 143-149.
- Brunkow, D., Bringi, V. N., Kennedy, P. C., Rutledge, S. A., Chandrasekar, V., Mueller, E. A., and R. K. Bowie, 2000: A description of the CSU-CHILL National Radar Facility. *J. Atmos. Oceanic Technol.*, In press.
- Carey, L. D., and S. A. Rutledge, 1996: A multiparameter radar case study of the microphysical and kinematic evolution of a lightning producing storm. *Meteorol. Atmos. Phys.*, **59**, 33-64.
- Carey, L. D., and S. A. Rutledge, 1998: Electrical and multiparameter radar observations of a severe hailstorm. *J. Geophys. Res.*, **103**, 13979-14000.
- Carey, L. D., and S. A. Rutledge, 2000: On the Relationship Between Precipitation and Lightning in Tropical Island Convection: A C-band Polarimetric Radar Study. *Mon. Wea. Rev.*, **128**, 2687-2710.
- Chandrasekar, V., Bringi, V. N., Balakrishnan, N., and D. S. Zrníc, 1990: Error structure of multiparameter radar and surface measurements of rainfall. Part III: Specific differential phase. *J. Atmos. Oceanic Technol.*, **7**, 621-629.
- Cheng, L., and M. English, 1983: A relationship between hailstone concentration and size. *J. Atmos. Sci.*, **40**, 204-213.
- Clarence, N. D., and D. J. Malan, 1957: Preliminary discharge processes in lightning discharges to ground. *Q. J. R. Meteorol. Soc.*, **83**, 161-172.
- Cressman, G. P., 1959: An operational objective analysis system. *Mon. Wea. Rev.*, **87**, 367-374.

- Cummins, K. L., Murphy, M. J., Bardo, E. A., Hiscox, W. L., Pyle, R. B., and A. E. Pifer, 1998: A combined TOA/MDF technology upgrade of the U. S. National Lightning Detection Network. *J. Geophys. Res.*, **103**, 9035-9044.
- Curran, E. B., and W. D. Rust, 1992: Positive ground flashes produced by low-precipitation thunderstorms in Oklahoma on 26 April 1984. *Mon. Wea. Rev.*, **120**, 544-553.
- Doviak, R. J., and D. S. Zmic, 1993: *Doppler Radar and Weather Observations*, 2<sup>nd</sup> Ed., Academic Press, San Diego, California, 562 pp.
- Goodman, S. J., Buechler, D. E., Wright, P. D., and W. D. Rust, 1988: Lightning and precipitation history of a microburst-producing storm. *Geophys. Res. Lett.*, **15**, 1185-1188.
- Goodman, S. J., Buechler, D. E., Wright, P. D., Rust, W. D., and K. E. Nielsen, 1989: Polarization radar and electrical observations of microburst producing storms during COHMEX. *24th Conf. on Radar Meteorology*, Amer. Meteorol. Soc., 190-112.
- Herzogh, P. H., and R. E. Carbone, 1984: The influence of antenna illumination function characteristics on differential reflectivity measurements. *22<sup>nd</sup> Conf. Radar Meteor.*, Zurich, Switzerland, Amer. Meteorol. Soc., 281-286.
- Hubbert, J., and V. N. Bringi, 1995: An iterative filtering technique for the analysis of copolar differential phase and dual-frequency radar measurements. *J. Atmos. Oceanic. Technol.*, **12**, 643-648.
- Jones, D. M. A., 1955: 3 cm and 10 cm wavelength radiation backscatter from rain. *Proc. 5<sup>th</sup> Wea. Radar Conf.*, Boston, Massachusetts, Amer. Meteorol. Soc., 281-285.
- Klemp, J. B., 1987: Dynamics of tornadic thunderstorms. *Annual Review of Fluid Mechanics*, **19**, 369-402.
- Lang, T. J., 1997: Relationship between storm structure and lightning activity in Colorado convection observed during STERAO-A. Master's Thesis, Colorado State University, 167 pp.
- Lang, T. J., Rutledge, S. A., Dye, J. E., Venticinque, M., Laroche, P., and E. Defer, 2000: Anomalously low negative cloud-to-ground lightning flash rates in intense convective storms observed during STERAO-A. *Mon. Wea. Rev.*, **128**, 160-173.
- Larson, H. R., and E. J. Stansbury, 1974: Association of lightning flashes with precipitation cores extending to height 7 km. *J. Atmos. Terr. Phys.*, **36**, 1547-1553.
- Livingston, J. M., and E. P. Krider, 1978: Electric fields produced by Florida thunderstorms. *J. Geophys. Res.*, **83**, 385-401.
- MacGorman, D. R., and D. W. Burgess, 1994: Positive cloud-to-ground lightning in tornadic storms and hailstorms. *Mon. Wea. Rev.*, **122**, 1671-1697.
- MacGorman, D. R., Burgess, D. W., Mazur, V., Rust, W. D., Taylor, W. L., and B. C. Johnson, 1989: Lightning rates relative to tornadic storm evolution on 22 May 1981. *J. Atmos. Sci.*, **46**, 221-250.
- MacGorman, D. R., and K. E. Nielsen, 1991: Cloud-to-Ground lightning in a tornadic storm on 8 May 1996. *Mon. Wea. Rev.*, **119**, 1557-1574.
- MacGorman, D. R., and W. D. Rust, 1998: *The Electrical Nature of Storms*. Oxford University Press, 422 pp.
- Maddox, R. A., Howard, K. W., and C. L. Dempsey, 1997: Intense convective storms with little or no lightning over Central Arizona: a case of inadvertent weather modification? *J. Appl. Met.*, **36**, 302-314.

- Maier, L. M., and E. P. Krider, 1986: The charges that are deposited by cloud-to-ground lightning in Florida. *J. Geophys. Res.*, **91**, 13275-13289.
- Maier, M. W., and E. P. Krider, 1982: A comparative study of the cloud-to-ground lightning characteristics in Florida and Oklahoma thunderstorms. *12th Conf. on Severe Local Storms*, San Antonio, Texas, Amer. Meteorol. Soc., 334-337.
- Mazur, V., Gerlach, J. C., and W. D. Rust, 1986: Evolution of lightning flash density and reflectivity structure in a multicell thunderstorm. *J. Geophys. Res.*, **91**, 8690-8700.
- Nachamkin, J. E., McAnelly, R. A., Weiland, M., Daugherty, K., Copeland, D., and W. R. Cotton, 1999: Predictability and structure of an intense orographic snowfall event in eastern Wyoming. *8<sup>th</sup> Conf. on Mesoscale Processes*, Boulder, Colorado, Amer. Meteorol. Soc., 357-360.
- Orville, R. E., 1994: Cloud-to-ground lightning flash characteristics in the contiguous United States: 1989-1991. *J. Geophys. Res.*, **99**, 10833-10841.
- Orville, R. E., and A. C. Silver, 1997: Lightning ground flash density in the contiguous United States: 1992-1995. *Mon. Wea. Rev.*, **125**, 631-638.
- Oye, R., and R. E. Carbone, 1981: Interactive Doppler editing software. *Preprints, 20<sup>th</sup> Conf. Radar Meteor.*, Boston, Massachusetts. Amer. Meteorol. Soc., 683-689.
- Peckham, D. W., Uman, M. A., and C. E. Wilcox, Jr., 1984: Lightning phenomenology in the Tampa Bay area. *J. Geophys. Res.*, **89**, 11789-11805.
- Pielke, R. A., Cotton, W. R., Walko, R. L., Tremback, C. J., Lyons, W. A., Grasso, L. D., Nicholls, M. E., Moran, M. D., Wesley, D. A., Lee, T. J., and J. H. Copeland, 1992: A comprehensive meteorological modeling system – RAMS. *Meteor. and Atmos. Phys.*, **49**, 69-91.
- Piegras, M. V., Krider, E. P., and C. B. Moore, 1982: Lightning and surface rainfall during Florida thunderstorms. *J. Geophys. Res.*, **87**, 11193-11201.
- Pierce, E. T., 1970: Latitudinal variation of lightning parameters. *J. Appl. Met.*, **9**, 194-195.
- Prentice, S. A., and D. Mackerras, 1977: Ratio of cloud to cloud-ground lightning flashes in thunderstorms. *J. Appl. Met.*, **16**, 545-550.
- Price, C., and D. Rind, 1992: A simple lightning parameterization for calculating global lightning distributions. *J. Geophys. Res.*, **97**, 9919-9933.
- Price, C., and D. Rind, 1993: What determines the cloud-to-ground lightning fraction in thunderstorms? *Geophys. Res. Lett.*, **20**, 463-466.
- Proctor, D. E., 1981: VHF radio pictures of cloud flashes. *J. Geophys. Res.*, **86**, 4041-4071.
- Ray, P. S., 1978: Triple-Doppler observations of a convective storm. *J. Appl. Met.*, **17**, 1201-1212.
- Ray, P. S., 1980: Single- and multiple-Doppler radar observations of tornadic storms. *Mon. Wea. Rev.*, **108**, 1607-1625.
- Reap, R. M., and D. R. MacGorman, 1989: Cloud-to-ground lightning: Climatological characteristics and relationships to model fields, radar observations, and severe local storms. *Mon. Wea. Rev.*, **117**, 518-535.

- Rutledge, S. A., Petersen, W. A., Cifelli, R. C., and L. D. Carey, 2000: Early results from TRMM-LBA: kinematic and microphysical characteristics of convection in distinct meteorological regimes. *24th Conf. on Hurricanes and Tropical Meteorology*, Fort Lauderdale, Florida, Amer. Meteorol. Soc., 137-138.
- Ryan, J. J., 1999: Relationship between lightning flash rates and radar observations from Colorado and Australia. Master's Thesis, Colorado State University, 134 pp.
- Ryzhkov, A. V., and D. S. Zrnich, 1998: Polarimetric rainfall estimation in the presence of anomalous propagation. *J. Atmos. Oceanic Technol.*, **15**, 1320-1330.
- Sachidananda, M., and D. S. Zrnich, 1987: Rain rate estimates from differential polarization measurements. *J. Atmos. Oceanic Technol.*, **4**, 588-598.
- Seimon, A., 1993: Anomalous cloud-to-ground lightning in an F5 tornado-producing supercell thunderstorm on 28 August 1990. *Bull. Amer. Meteorol. Soc.*, **74**, 189-203.
- Stolzenburg, M., 1994: Observations of high ground flash densities of positive lightning in summertime thunderstorms. *Mon. Wea. Rev.*, **122**, 1740-1750.
- Stolzenburg, M., Rust, W. D., Smull, B. F., and T. C. Marshall, 1998a: Electrical structure in thunderstorm convective regions. Part I: Mesoscale convective systems. *J. Geophys. Res.*, **103**, 14059-14078.
- Stolzenburg, M., Rust, W. D., and T. C. Marshall, 1998b: Electrical structure in thunderstorm convective regions. Part II: Isolated storms. *J. Geophys. Res.*, **103**, 14079-14096.
- Stolzenburg, M., Rust, W. D., and T. C. Marshall, 1998c: Electrical structure in thunderstorm convective regions. Part III: Synthesis. *J. Geophys. Res.*, **103**, 14097-14108.
- Takahashi, T., 1978: Riming electrification as a charge generation mechanism in thunderstorms. *J. Atmos. Sci.*, **35**, 1536-1548.
- Uman, M. A., 1987: *The Lightning Discharge*. Academic Press, 377 pp.
- Wang, C., and R. G. Prinn, 2000: On the roles of deep convective clouds in tropospheric chemistry. *J. Geophys. Res.*, **105**, 22269-22297.
- Weber, M. R., Boldi, R., Laroche, P., Krehbiel, P., and X. Shao, 1993: Use of high resolution lightning detection and localization sensors for hazardous aviation weather nowcasting. *17th Conf. on Severe Local Storms*, Amer. Meteorol. Soc., 739-744.
- Williams, E. R., Cooke, C. M., and K. A. Wright, 1985: Electrical discharge propagation in and around space charge clouds. *J. Geophys. Res.*, **90**, 6059-6070.
- Williams, E. R., Weber, M. E., and R. E. Orville, 1989a: The relationship between lightning type and convective state of thunderclouds. *J. Geophys. Res.*, **94**, 13213-13220.
- Williams, E. R., Weber, M. E., and C. D. Engholm, 1989b: Electrical characteristics of microburst producing storms in Denver. *24th Conf. Radar Meteor.*, Tallahassee, Florida, Amer. Meteorol. Soc., 89-92.
- Williams, E. R., Zhang, R., and J. Rydock, 1991: Mixed-phase microphysics and cloud electrification. *J. Atmos. Sci.*, **48**, 2195-2203.
- Williams, E. R., 2000: The electrification of severe storms. Contribution to *AMS Severe Storms Monograph*, in press.

Workman, E. J., and S. E. Reynolds, 1949: Electrical activity as related to thunderstorm cell growth. *Bull. Amer. Meteorol. Soc.*, **30**, 142-144.

Yuter, S. E., and R. A. Houze, Jr., 1995: Three-dimensional kinematic and microphysical evolution of Florida cumulonimbus. Part II: Frequency distributions of vertical velocity, reflectivity, and differential reflectivity. *Mon. Wea. Rev.*, **123**, 1941-1963.

Ziegler, C. L., and D. R. MacGorman, 1994: Observed lightning morphology relative to modeled space charge and electric field distributions in a tornadic storm. *J. Atmos. Sci.*, **51**, 833-851.